LA-14249-T
Thesis

Radiation Damage and Fission Product Release in Zirconium Nitride

Los Alamos
NATIONAL LABORATORY
EST. 1943

The World's Greatest Science Protecting America

Funding provided by the Advanced Fuel Cycle Initiative Program, an Agency of the Department of Energy.

This thesis was accepted by the Department of Materials Science and Engineering, New Mexico Institute of Mining and Technology, Socorro, New Mexico, in partial fulfillment of the requirements for the degree of Doctor of Philosophy. The text and illustrations are the independent work of the author, and only the front matter has been edited by the IM-1 Writing and Editing Staff to conform with Department of Energy and Los Alamos National Laboratory publication policies.

LA-14249-T
Thesis
Issued: September 2005

Radiation Damage and Fission Product Release in Zirconium Nitride

Gerald W. Egeland

Los Alamos
NATIONAL LABORATORY
EST.1943

The World's Greatest Science Protecting America

Radiation Damage and Fission Product Release in Zirconium Nitride

by

Gerald W. Egeland

Submitted in Partial Fulfillment of the Requirements for the

Doctorate of Philosophy in Materials Science

New Mexico Institute of Mining and Technology

Department of Materials and Metallurgical Engineering

Socorro, New Mexico, 87801

August 29, 2005

Abstract

Zirconium nitride is a material of interest to the AFCI program due to some of its particular properties, such as its high melting point, strength and thermal conductivity. It is to be used as an inert matrix or diluent with a nuclear fuel based on transuranics. As such, it must sustain not only high temperatures, but also continuous irradiation from fission and decay products. This study addresses the issues of irradiation damage and fission product retention in zirconium nitride through an assessment of defects that are produced, how they react, and how predictions can be made as to the overall lifespan of the complete nuclear fuel package.

Ion irradiation experiments are a standard method for producing radiation damage to a surface for observation. Cryogenic irradiations are performed to produce the maximum accumulation of defects, while elevated temperature irradiations may be used to allow defects to migrate and react to form clusters and loops. Cross-sectional transmission electron microscopy and grazing-incidence x-ray diffractometry were used in evaluating the effects that irradiation has on the crystal structure and microstructure of the material. Other techniques were employed to evaluate physical effects, such as nanoindentation and helium release measurements.

Results of the irradiations showed that, at cryogenic temperatures, ZrN withstood over 200 displacements per atom without amorphization. No significant change to the lattice or microstructure was observed. At elevated temperatures, the large amount of damage showed mobility, but did not anneal significantly. Defect clustering was possibly observed, yet the size was too small to evaluate, and bubble formation was not observed.

Defects, specifically nitrogen vacancies, affect the mechanical behavior of ZrN dramatically. Current and previous work on dislocations shows a distinct change in slip plane, which is evidence of the bonding characteristics. The stacking-fault energy changes dramatically with lowered nitrogen stoichiometry, resulting in widely spaced partial dislocations in ZrN with high nitrogen vacancy concentration.

The wide range of nitrogen stoichiometry in the phase field shows that ZrN may accept nitrogen defects readily. Explanations for this are suggested based upon the bonding structure of these cubic nitrides. This structure allows for a solid framework to remain on one sublattice, while at the same time allowing defects on the other sublattice. This allowance for defects allows significant damage from irradiation yet also decreases the drive for cluster growth. This is evidence that the structure will be acceptable for long-term use as a nuclear reactor fuel.

Acknowledgements

I would like to acknowledge the main individuals that helped me get to this point in my career. Dr. Gillian Bond, who as an academic adviser has always been helpful. I would also like to acknowledge the individuals at Los Alamos that have helped guide me through many difficulties. Stuart Maloy has been very patient, helpful, and very insightful. Kurt Sickafus has been a very knowledgeable teacher and has provided substantial input and help. James Valdez, Chris Wetteland, Greg Swadener, and Chris Stanek and as always, Kenneth McClellan, have been available for help, guidance., and occasional beer drinking.

The other committee members, Bhaskar Mujumdar and David Burleigh, should be also thanked for reading this paper as well as for sitting through the long presentations.

I would also like to thank the Advanced Fuel Cycle Initiative program (AFCI) for funding this project, for without monies no data would ever be had. The AFCI project has evolved and changed names, from ATP, ATW, AAA, and now AFCI, where I hope it stays. Due to the multinational and multiple national lab cooperation of this project, politics are always present. This, however, did not stop the project from finishing.

Special thanks go out to those that helped me get this document produced, being Chris Stanek, Andrea Dangelwicz, and Darrin Byler. Others that are not mentioned are in my heart and will be remembered. This document compiled and formatted with LaTeX[1].

[1] LaTeX document preparation system was developed by Leslie Lamport as a special version of Donald Knuth's TeX program for computer typesetting. TeX is a trademark of the American Mathematical Society. The LaTeX macro package for the New Mexico Institute of Mining and Technology thesis format was adapted from Gerald Arnold's modification of the LaTeX macro package for The University of Texas at Austin by Khe-Sing The.

Contents

List of Figures

List of Tables

List of Algorithms

List of Abbreviations

Organizations

LANL	Los Alamos National Laboratory
ORNL	Oak Ridge National Laboratory
ANL	Argonne National Laboratory
INEEL	Idaho National Engineering and Environmental Laboratory (now INL)
AFCI	Advanced Fuel Cycle Initiative
WIPP	Waste Isolation Pilot Plant
IBML	Ion Beam Materials Laboratory
EML	Electron Microscopy Laboratory
NMT	New Mexico Technical Institute of Mining and Technology
ASU	Arizona State University
UNLV	University Nevada Las Vegas

Nuclear Reactors, Processes and Fuels

TRIM	TRansport of Ions in Matter
SRIM	Stopping Range of Ions in Matter
LWR	Light Water Reactor

FBR	Fast Breeder Reactor
ADS	Accelerator Driven Reactor
HTGR	High Temperature Gas cooled Reactor
LMFBR	Liquid Metal Fast Breeder Reactor
UREX	Uranium based fuel reprocessing
PUREX	Plutonium based fuel reprocessing
TRU-N	Transuranic Nitride ((Cm, Pu, Np, Am)N)
MOX	Mixed Oxide
ZrN	Zirconium Nitride
UO_2	Uranium Oxide
UN	Uranium Nitride
PuN	Plutonium Nitride

Radiation Emitted Particles

α	Helium core (fission energy $\approx$ 5 MeV)
β	Electron (fission energy $\approx$ 7 MeV)
γ	Photon from nuclear core (1 to 0.1 nm wavelength, fission energies $\approx$ 8 MeV)
Neutron	From 7 MeV to 0.27 eV (thermal)

Characterization Equipment and Terms

TEM	Transmission Electron Microscope
SEM	Scanning Electron Microscope
AFM	Atomic Force Microscope
CBED	Condensed Beam Electron Diffraction
SAD	Selected Area Electron Diffraction
EDS	Electron Dispersion Spectroscopy
EELS	Electron Energy Loss Spectroscopy
RBS	Rutherford Backscatter Spectroscopy
RBS/C	Rutherford Backscatter Spectroscopy Channeling
RGA	Residual Gas Analyser
XPS	X-ray Photo Spectroscopy
GIXRD	Grazing Incidence X-Ray Diffractometer
HIP	Hot isostatic Press
CIP	Cold Isostatic Press
eV	Electron Volt
keV	Kilo-Electron Volt (10^3eV)
MeV	Mega-Electron Volt (10^6eV)
χ_{min}	Relative difference in backscatter in RBS/C experiments. A measure of radiation damaged induced disorder

Elements and Compounds

Xe	Xenon
He	Helium
Kr	Krypton
Ne	Neon
Zr	Zirconium
Pu	Plutonium
Np	Neptunium
Am	Americium
Cm	Curium
N	Nitrogen
Cs	Cesium
I	Iodine
Sr	Strontium
TiN	Titanium Nitride
GaN	Gallium Nitride
AlN	Aluminum Nitride
Si_3N_4	Silicon Nitride
LN_2	Liquid Nitrogen (boiling point $\approx$77 K)
CO_x	Carbon Oxides
SO_x	Sulfur Oxides
NO_x	Nitrous Oxides
N_A	Avogadro's number

Math Variables from Equations

Diffusion

D	Diffusion Coefficient
C	Concentration
J	Flux of atoms
Q	Activation Energy
k	Boltzmann's Constant
T	Temperature in Kelvin

Radiation Damage

LSS	Lindhard, Scharff and Schiott
KP	Kinchin-Pease
ZBL	Ziegler, Biersack and Littmark
σ	Cross-section
ρ_s	Surface density of atoms
ρ_a	Atomic density
$\varphi_\circ$	Particle flux
$\Phi_\circ$	Fluence
PKA	Primary knock-on atom

SKA	Secondary knock-on atom
i-v	Interstitial-vacancy pair
SRV	Spontaneous recombination volume
RCV	Replacement collision sequence
C	Concentration
T	Target energy
E	PKA energy
E_d	Displacement threshold energy
CM	Center of mass coordinates
$\overrightarrow{v}$	Lab coordinate vector
$\overrightarrow{u}$	Center of mass coordinates vector
Λ	Kinematic efficiency factor
$V(r)$	Interatomic potential
ε or $S(E)$	Stopping power
I	Binding energy of an electron
v	Velocity
m_e	mass of electron
m	mass of particle

Z	Atomic number
a	screening radius
P	Production rate
M	Mobility
ξ	Defect production efficiency
δ	Jump distance
ν	Vibrational frequency
Γ	Jump frequency
Z_1	SRV
Z_3	Unspecified parameter
L	Length of loop

Crystallography

sc	Simple Cubic
bcc	Base Centered Cubic
fcc	Face Centered Cubic
ccp	Cubic Close Packed
hcp	Hexagonal close packed
h,k,l	Indices of a crystal plane

u,v,w	Indices of a crystal direction
U,V,W	Indices of a zone axis
g	A vector normal to the reflecting plane with magnitude 1/inter-planar spacing
b	Burgers vector of a dislocation
R	Measured distance in mm
d	Inter-planar spacing
L	Camera Length
λ	Diffraction wavelength (300 keV electron = Å)
SRO	Short-Range Order
NaCl	B1, rocksalt or halite structure, fcc with all octahedral interstices filled, space group # 225 ($FM\bar{3}M$)
SFE	Stacking Fault Energy
$\perp$	Dislocation
X_i	Element "X" in an interstitial site
V_x	Vacancy of an "X" lattice site

This dissertation is accepted on behalf of the
Faculty of the Institute by the following committee:

Advisor

8/29/05

8-29-05

9-8-05

8/29/2005
Date

I release this document to the New Mexico Institute of Mining and Technology.

29 Aug '05
Student's Signature Date

CHAPTER 1

Introduction

The use of nuclear power is an emotional issue. It began with the first atomic bomb produced by the Manhattan Project at Los Alamos in 1945. Since then, nuclear energy has carried with it the stigma of the fear of nuclear warfare, and the Cold War escalation of nuclear warhead destructive power did not help. Peaceful use of nuclear power is the concern of many scientists as the potential for clean energy is immense. But accidents such as those at Three Mile Island or Chernobyl have hindered its growth. Public opinion has been the number one obstacle to the nuclear industry and, although its safety record is on a par with other forms of energy production, the average person still fears a nuclear accident.

Even as energy requirements are increasing with population growth and world industrialization, it is the general populace the has blocked production of new nuclear power plants. The state of California, for example, will not allow a new nuclear power plant to be built and yet, because of its huge energy demand, it still buys nuclear energy from across the border from Arizona's Palo Verde nuclear power plant. With the power blackouts of 2001 in California and the sudden east-coast blackout of 2003, public opinion of nuclear power has, however, become far less negative. Current use of electric power by the American public is always increasing because of the increase in electronic appliances as well as industrial electronic use. Figure 1.1 shows the global usage of electricity during the years 2000 through 2002. One may say that the usage by is a tremendous amount of electricity with respect to the rest of the planet.

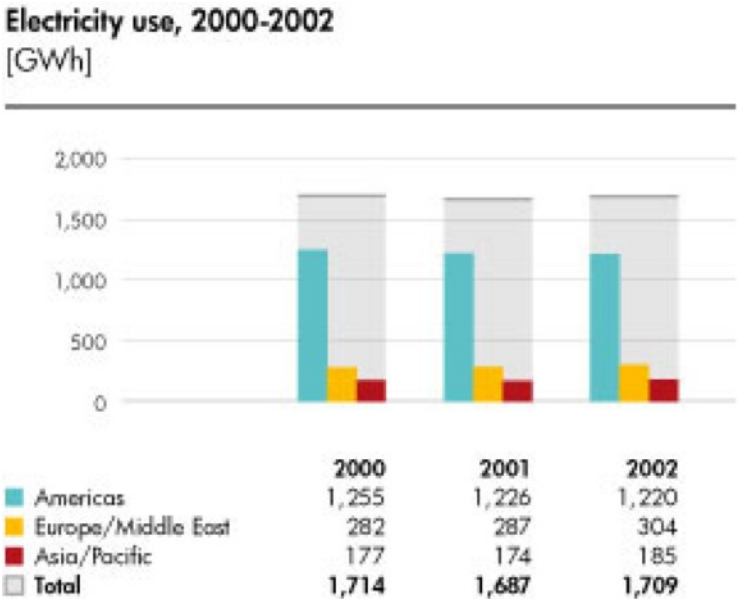

(a) Total elecricity usage

Figure 1.1: Global electricity usage during 2000 to 2002 [1]

The one sticking point against the use of nuclear power that is inarguable is the waste stream produced. The spent fuel rods, as they are removed from the reactor core, are stored in above-ground containment ponds on site as they are too “hot”, or radioactive, to handle. After ten years they have “cooled” enough to be transported to temporary underground storage facilities. The only place for them after this is at permanent storage facilities such as the Yucca Mountain deep underground nuclear-waste repository. The current state of affairs has not allowed any long-term storage facility to accept any shipments and, as a result, all fuel rods (at least in the United States) are stored in the short-term facilities on a semi-permanent basis.

The spent fuel rods are very toxic and dangerous. The fission-product waste contained within them is highly radioactive and, if released into the environment, has the potential to cause an immense amount of harm to both local ecological systems and public health. Some people fear that these long-term repositories will someday rupture and release the waste

into an aquifer, spreading it in a wide plume throughout the local area. Transportation to storage sites is as much an emotional issue as the power plants themselves. Many lawsuits are continuing to block any transportation of high-level waste across state lines. Although the design, construction, and safety records of waste transportation are exceptional, the public's fear remains.

An important long-range goal therefore is to close the fuel cycle in a way that will not allow proliferation of plutonium, and that will greatly reduce the toxicity of the waste generated. The ideal is that the high-level waste would never have to leave the nuclear power plant. It would be remanufactured into a new fuel for re-burning. Alternatively, the new fuel could be manufactured on-site and burned elsewhere. The final waste would be much less toxic and radioactive. This is the goal for the Advanced Fuel Cycle Initiative.

1.1 World Power Production

Nuclear reactors have produced power all over the world for decades. Over 17 % of the world's electricity and 6 % of commercial power is produced by nuclear power (Table 1.1). Power production is over 1000 TWatts/year. There are over 500 active nuclear power plants operating or under construction in 31 countries. Plans for future construction of conventional and advanced power plants are going forward in many countries, including South Africa, Iran, Russia, China and Japan. Nuclear energy is very inexpensive to produce, plentiful with respect to uranium ore, and clean with respect to emission gases. With the rising population and improving standards of living in the developing world, power consumption continues to increase, as seen in Figure 1.2. Many of the existing reactors will close due to age by 2020, and so with the increasing demand for power over 500 new reactors will have to be built to maintain the 17 % figure [2].

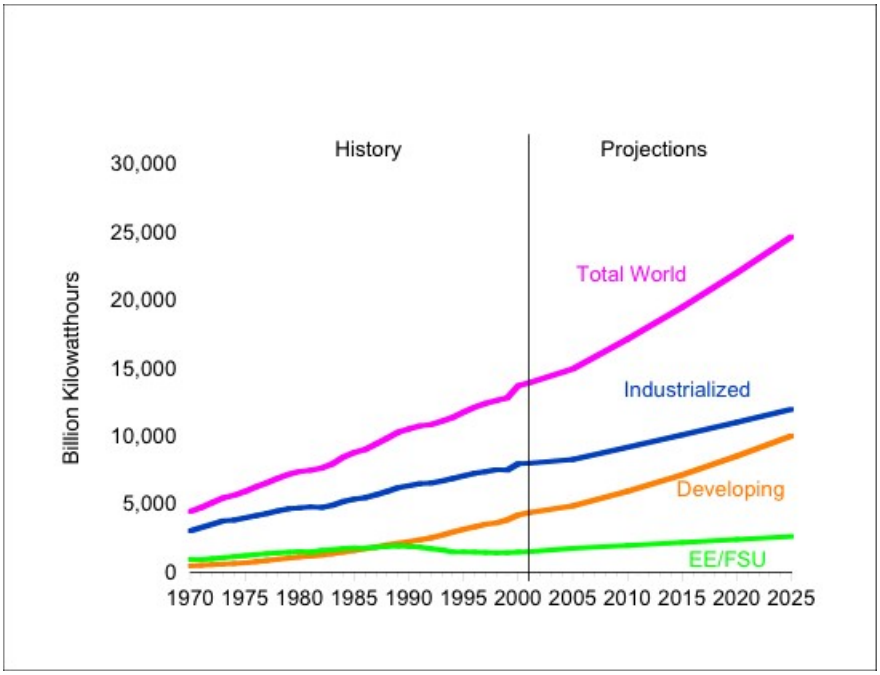

Figure 1.2: Preliminary world electricity consumption by fuel type, 1970-2025 [3]

Although nuclear power is common, coal-and-gas fired power plants continue to dominate the power production landscape (refer to Table 1.1). They are cheaper to design and construct, which makes them attractive to developing countries. The long-term cost of their use, however, is increasing and possibly higher than for nuclear energy production. A

Table 1.1: Fuels for Electricity Generation by % Supply as of 1990 [2]

	Industrialized World	Developing World	Total World
Coal	44	33	42
Oil	9	17	10
Natural Gas	12	13	12
Hydroelectric	16	33	18
Nuclear	18	4	17
Other	1	-	1
Total	100	100	100

major factor here is that greenhouse gas emission is being regulated at an increasing rate which raises the costs of coal power futures.

Natural-gas-fired power plants are much cleaner than coal-fired types, but the limiting factor for natural gas power is the transport of the fuel. Most of the world's natural gas production is in the Middle East and Siberia, which poses a challenge both to transport the fuel, and to keep it from political control. The OPEC oil crisis of the early 1970's proved that the economies of the western nations, especially the United States, have a strong dependence on middle-eastern oil. Oil is used to power motor vehicles and is not considered viable option for future electric power, but the OPEC oil crisis shows what can happen when a nation allows itself to become dependent on a commodity it cannot control.

Water power is by far one of the oldest forms of renewable energy. Water wheels were produced a thousand years ago to help grind grain or to work iron. By damming a river, it was found that an energy reservoir was formed for consistent power. In the last century, large dams were constructed and water turbines replaced the wheels of the past. These turbines turned generators for electric power. Eighteen percent of the world's power is generated by hydroelectric plants [2]. They do not produce any waste or consume any fuel. The damage done is by the dams themselves. By forming huge reservoirs they change the local ecosystem, filling a valley, and restricting the river system below. The ecological effects can be immense and although hydropower is completely clean and waste free, environmentalists do not always accept them.

Other forms of renewable energy sources, such as wind, solar, wave, biomass, etc., have their place and possible future, yet contribute little to the overall world energy production. Advocates for these energy sources claim that they could provide up to 50% of the projected energy usage in 2050. The real problem with this outlook is that this assumes that the public and energy companies are willing to risk the overhead of producing such large-

scale experiments. Although promising, such energy sources have yet to be proved on a commercial scale.

Nuclear power is greenhouse-gas-free and a relatively clean form of energy. It is not a combustion process, and therefore there are no SO_x, CO_x or NO_x effluents produced. It does not destroy or alter an ecosystem like hydroelectric or wind power. Its fuel is small, compact and relatively inexpensive. The nuclear fuel cycle, however, is "open" in that the fuel is consumed and the waste stored for future disposal. Uranium ore is processed to extract the raw uranium metal and oxide. Natural uranium is composed of ^{238}U with about 0.7 % ^{235}U, the fissile isotope. By different processes, ^{238}U is enriched with ^{235}U to 3 to 5 %. At this enriched concentration, fuel will fission easily under the right conditions. After many years of use, the fuel rod is "spent" in that the ^{235}U has been fissioned down below 3 %.

Unfortunately, the spent fuel rods are very toxic and radioactive and have waste isotopes with long half-lives. These fuel rods may be reprocessed to extract the remaining ^{238}U and re-enrich it with more ^{235}U for reuse. Different processes can be used for reprocessing the fuel rods to extract the ^{238}U but weapons-grade plutonium can be extracted from this waste as well, and the Non-Proliferation Treaty that the United States has signed has made reprocessing unacceptable. Other countries, such as France, have advanced reprocessing capabilities. Currently, The Democratic Peoples Republic of Korea (DPRK), or North Korea, has begun to reprocess spent fuel rods, not only in an effort to reinvigorate their nuclear power industry but also to threaten the United States with the capability of producing weapons grade plutonium. To date, the production of spent fuel rods is much greater than the capability of the available reprocessing facilities. World wide, the spent fuel-rod production is over 9000 t/year with even more waste produced from the military infrastructure [2].

Currently, the spent fuel rods are removed from the reactors and stored in on-site cooling ponds. The water moderates and cools the "hot" fuel rods as the short half-life elements go through radioactive decay. These rods are stored for an average of about ten years, until they have "cooled" enough to be handled with a degree of safety. They are then transfered to "temporary" underground storage sites. Waste produced for the last fifty years is still being stored in these temporary sites, awaiting the construction of suitable repositories, such as Yucca Mountain.

Long-term storage of the waste rods poses a special problem. Due to their extremely dangerous nature, the waste has a stigma that, although it is produced, it cannot be transported. Common fear is that there could be an automobile accident that may release this waste. After the 9/11 terrorist attacks, the security viewpoint is that transport vehicles would be an ideal target for terrorists. A conventional rocket or bomb striking these vehicles could produce a "dirty" bomb in which the nuclear industry supplies the radioactive elements. Currently, the state of Nevada has produced numerous lawsuits in an attempt to stop the transport and disposal of waste. The state of New Mexico is the site of the Waste Isolation Pilot Plant (WIPP), where low-level radioactive waste is stored. WIPP was planned decades ago, but was tied up in similar lawsuits that prevented its opening for many years. The "not in my back yard" feeling is very common among most or all States and populations. Therefore, high-level waste, as of this date, is still being stored in temporary underground storage facilities. Spent fuel rods from decades of use accumulate in these storage facilities with no end in sight.

The Yucca Mountain project is a nuclear repository that is being developed to store this waste in deep underground caverns. Yucca Mountain is considered to be a long-term storage facility, yet it can only contain a discrete amount of waste. Without reprocessing, the maximum a repository can hold is a predicted 70,000 metric tons [2]. This is due to

the heat produced from decay and not the size of the repository. The construction of more deep underground repositories is under consideration by the United States.

The vast quantity of legacy waste is astonishing, leading the world super-powers to fear production of plutonium to build more nuclear weapons, terrorist attacks to strike a storage facility to produce a radioactive waste cloud, or theft of such waste to proliferate weapons-grade material in certain outlaw countries. Since the 9/11 terrorist attacks the United States began truly to believe that such attacks are not only possible, but highly likely given our current state of security. Securing the waste from an easy air strike is only the start from a security stand point. The waste must be secured and the hazards reduced as much as possible.

1.2 Advanced Fuel Cycle Initiative

The Advanced Fuel Cycle Initiative (AFCI) has taken a different approach to the waste problem. The main goal of AFCI is to close the fuel cycle. Instead of burying the waste, a form of reprocessing of the waste, on site, to extract the transuranic elements is being introduced. These transuranics, specifically plutonium, neptunium, americium, and curium, are to be extracted and placed into a fuel form for "re-burning", or transmuting to a more stable form, in a reactor environment. The type of reactor, whether accelerator driven or conventional, is still debated, yet the theoretical basis remains the same in each type. The transuranic elements are transmuted via neutron capture to a less stable form. They can either decay to less hazardous elements or remain in this unstable form. The goal for this fuel is to have the resultant spent fuel waste have a half-life of less than 1000 years.

The fuel will be of a certain form. Transuranic elements will be the main component, with the rest an inert matrix. Uranium is controlled in the fuel due to the capability of ^{238}U

transmuting to plutonium. The exact amount of each component depends on the type of reactor system and fuel form.

The fuel type to be used in this reactor is being heavily debated. One candidate is the nitride-based fuel form. Actinide nitride and carbide ceramics have been studied for use in breeder and space reactor systems. Carbides, similar in many properties to the nitrides, are ruled out due to incompatibility with some of the coolants used in some reactors. Oxide fuels have been used for decades and are the most well known. Mixed OXide fuels (MOX) are one type that attempts to use the transuranics as an energy form. MOX fuels originated in the 1970s when breeder reactors were considered the answer to waste energy needs.

Metal-based fuels are currently under study due to some good qualities. Dispersed-matrix fuels, which are a composite of fuel in a metallic matrix, are another option. Vibra-pack, a form with closely packed powders of select size ratios, achieves very high density with out sintering processes and still has open porosity. TRISO fuel, a coated powder, is used in special pebble-bed reactors.

Each fuel has its pros and cons. Metal fuels have high thermal conductivity yet low melting points. Oxide fuels have insulating thermal characteristics which result in lower efficiency and very high fuel-pellet core temperatures. Dispersed-matrix fuels are more difficult to engineer due to the very different physical and chemical properties of the components.

Nitride fuels, however, have a multitude of positive characteristics. They are thermally conductive, very strong, highly refractory, and are chemically inert in most environments. Transuranic nitrides (TRU-N), however, have a few problems that must be resolved in order to be feasible. Processing of the fuel pellets is one area of concern. The sintering temperature must be below 1400°C to avoid americium nitride vaporization during sintering. Americium, and its alloy nitrides, have high vapor pressure, and begin to decompose

and vaporize the americium at about 1400°C [4, 5]. Loss of americium poses health risks at the point of processing as well as changing the overall transuranic ratio. Since the melting temperatures are greater than 2500°C, sintering of these ceramics at such low temperatures is quite difficult.

Fuels for transmutation have different physical requirements than those for a conventional reactor. The amount of fissile material is reduced or diluted with a non-fertile matrix. This matrix, combined with the fissile fuel, is processed into a structural pellet and stacked into a fuel rod. These fuel rods are placed into a nuclear reactor and taken to high burn-up, at which time they are removed for reprocessing. The reprocessing is similar to the (P)UREX process, which dissolves the fuel in acid and sorts the elements. The transuranics produced are remixed with the next batch of fuel to be re-burned. This process continues until the transuranics have been completely transmuted.

The inert matrix must be compatible with all conditions that the fuel must withstand. This includes the nuclear reactor temperature, thermal cycling, pellet manufacture and processing. It must be able to withstand several years of constant high temperatures while being constantly bombarded with neutrons and heavy fission products. It must be able to contain these fission elements or expel them as designed.

1.3 ZrN as an Inert Matrix and Surrogate

Zirconium nitride was chosen as a primary candidate for the inert matrix not only for its physical properties but also because it is somewhat of a surrogate for a TRU-N. Due to the similar atomic radii and chemical similarities between the actinide elements and zirconium the radiation tolerance of ZrN may be used as a predictor for the tolerance of TRU-N to fission products and irradiation displacement damage [6, 7, 8].

Its physical properties either meet or exceed those required for AFCI, and it is chemically compatible with TRU-N. It has similar physical qualities such as its coefficient of thermal expansion, thermal conductivity, etc. It is similar in its chemical profile and thermodynamic stability and is a good match for TRU-N. As a fuel matrix it will help transfer heat away form the fuel core and is very strong. It is also compatible with the processing specifications.

The radiation and fission product tolerance of ZrN are unknown, which is the reason for the present study. Not only will this study help to determine the candidacy of ZrN for the matrix material, it may also be used to predict these effects for the TRU-N fuel in a reactor environment.

1.4 Methodology

The goal of this study is a characterization of the radiation tolerance and fission product retention of ZrN. A systematic approach has been taken to determine these characteristics and produce design criteria for the TRU-N fuel form proposed. The information provided will help to determine the viability of ZrN for the inert matrix to engineer the final fuel product.

The characteristics that need to be understood are:

- The intrinsic defects in zirconium nitride
  - their effects on irradiation damage accumulation and fission product retention.
- the ability to accommodate the extrinsic defects produced during processing and irradiation

  - The high-energy fission product irradiation effects on the crystal structure and microstructure.

- Fission product retention and diffusion characteristics.

- The physical property changes that characterizes and tie together the above properties.

This is a ground-up approach to characterizing ZrN as a capable fuel matrix and surrogate for the AFCI program. Different facets of the material properties are observed for changes, both microscopic and macroscopic in nature. Correlations between the fission product damage and changes in the physical properties of the inert matrix are established and used as a predictor for the lifetime of the resultant TRU-N fuel at high burn-up.

As a basis for this study, ion implantation for damage production with TEM and GIXRD were used extensively as characterization techniques. Although not a truly high-energy irradiation such as an in-pile experiment or even a high-energy neutron irradiation, keV energy ion implantation is an accepted method for determining the effects of damage accumulation [9]. The defects and disparities between an actual fuel irradiation and the experimental conditions must always be remembered. Other techniques are used to assess other properties such as the effects of helium.

It is assumed that the results are applicable to the mixed TRU-N fuel form, as well as ZrN as a diluent/matrix, since many of the properties of the cubic nitrides are very similar. Proof, however, will come from a true in-pile experiment, such as the Futurix fuels irradiation in the Phoenix reactor.

CHAPTER 2

Literature Review

2.1 AFCI

The Advanced Fuel Cycle Initiative (AFCI) is a program that is attempting to help close the nuclear fuel cycle. The system is designed such that the power reactor fuel is reprocessed and re-burned to remove, by transmutation, the more dangerous and long-lived transuranic isotopes. Remaining isotopes will have much shorter half-lives and as such produce a hotter waste stream. This waste stream decays rapidly into a much less radioactive stream during storage. The high radioactivity of neptunium and americium isotopes make the fuel much more difficult to handle for those who may attempt to steal, transport, or use the waste in nefarious ways. In this way, the fuel is safer to be stored both in short and long-term repositories. A theoretical waste stream from a transmuter can be summarized in Figure 2.1.

Continued production of nuclear waste produces both toxic waste stream and weapons-grade plutonium. With the current political state of the planet, there is a strong push to decrease the production of plutonium so that weapons of such power are limited in number and control. Fuel reprocessing is not performed in the United States due to the Non Proliferation Treaty. Yet plutonium is produced and stored in temporary repositories. Typical figures for waste production by nuclear power plants are shown in Figure 2.2. As can be seen, the continued use of nuclear power either has to decrease radically, or the waste must

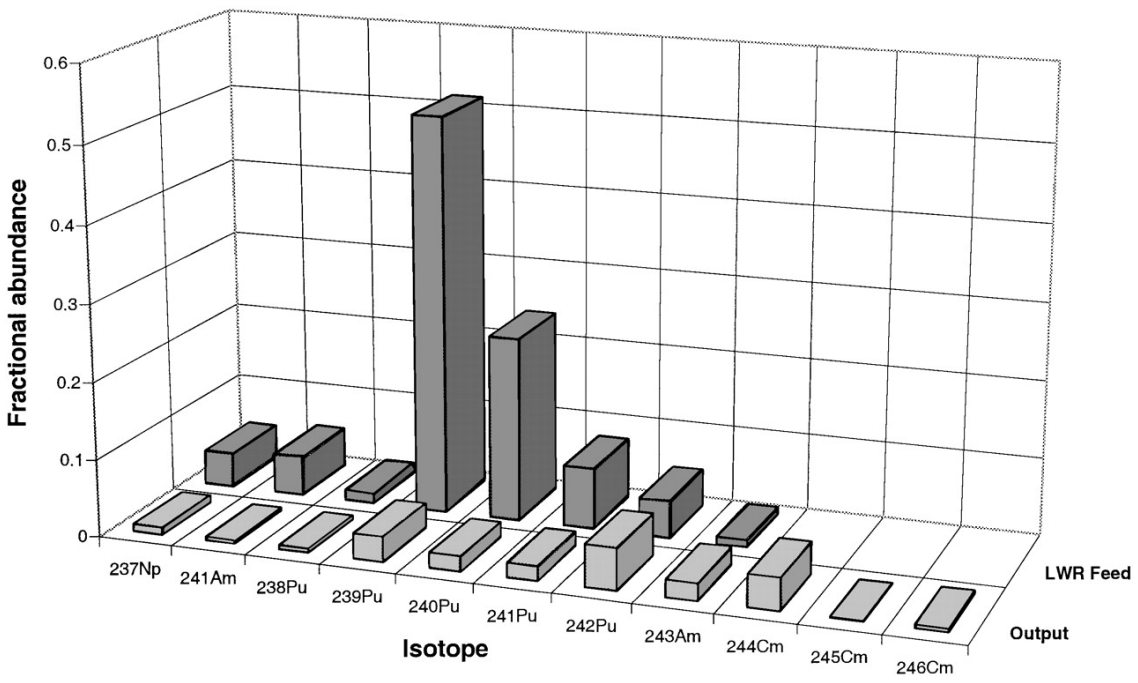

Figure 2.1: Pre and post-transmutation waste transuranics [10]

be altered. Shutting down all world-wide nuclear power reactors now would only hold the waste quantity constant, and thus do nothing to address the problem of the current waste.

As a fuel is burned in a typical power reactor, the fission reaction produces fission products, and neutrons. These neutrons are moderated and controlled in number such that the fission events are kept at the critical level yet in control. From the initial fission event until they are moderated they can interact or be absorbed by other nuclei. If the isotope is fertile, such as $^{238}\mathrm{U}$, the isotope is transmuted by accepting the neutron and becoming $^{238}\mathrm{Pu}$. This cycle continues during the fuel's life, producing transuranic isotopes with long half-lives. Figure 2.3 shows a typical power-reactor fuel break up of the transuranics by weight percent vs. time.

These transuranics produce radiation for many thousands of years, such that their long-term storage in a repository produces a risk of accidental environmental contamination.

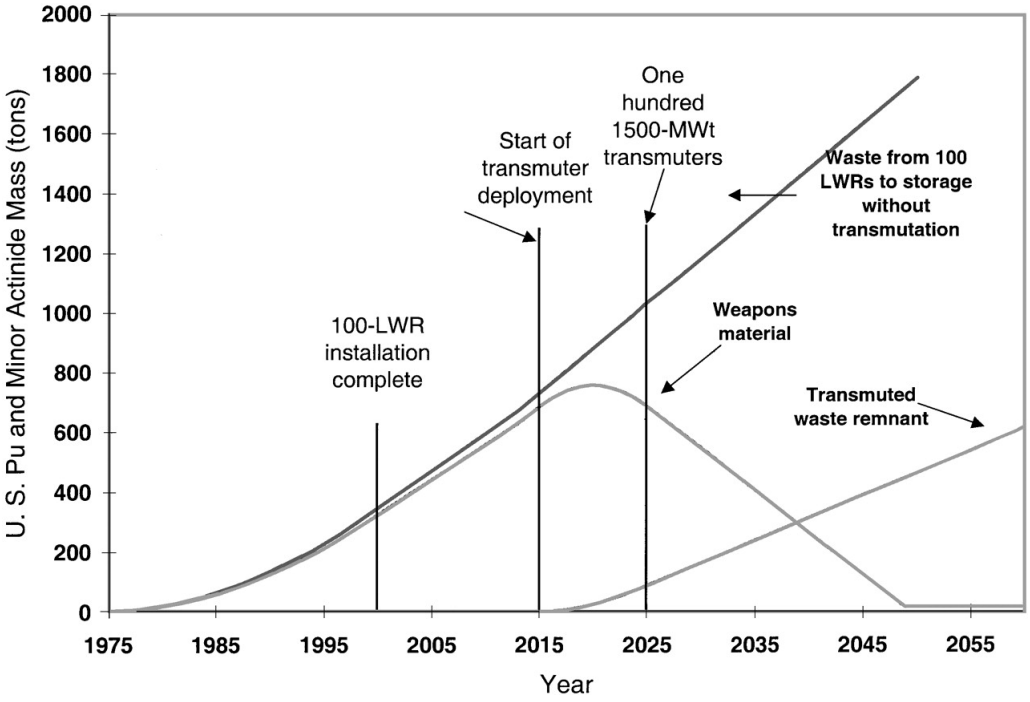

Figure 2.2: Nuclear waste predictions with and without typical transmuters [10]

AFCI, by design, attempts to reduce this danger by reducing the spent fuel's radioactive half-life to less than 1000 years. Possible schemes are single, or possibly numerous, tiers of transmutation through a specially designed reactor (refer to Figure 2.4). All schemes require that, after the reactor's fuel rod is spent and removed, the fuel is recycled such that the transuranics are removed for re-burning while the rest is set up for geologic storage. In general, the closed fuel loop follows the logic below:

- Spent fuel is "recycled" to remove transuranics.
  - Transuranic-reduced fuel is placed in queue for long-term storage.
- A fuel is produced with a high content of transuranics.
- The transuranic fuel is burned up by transmuting the transuranics.

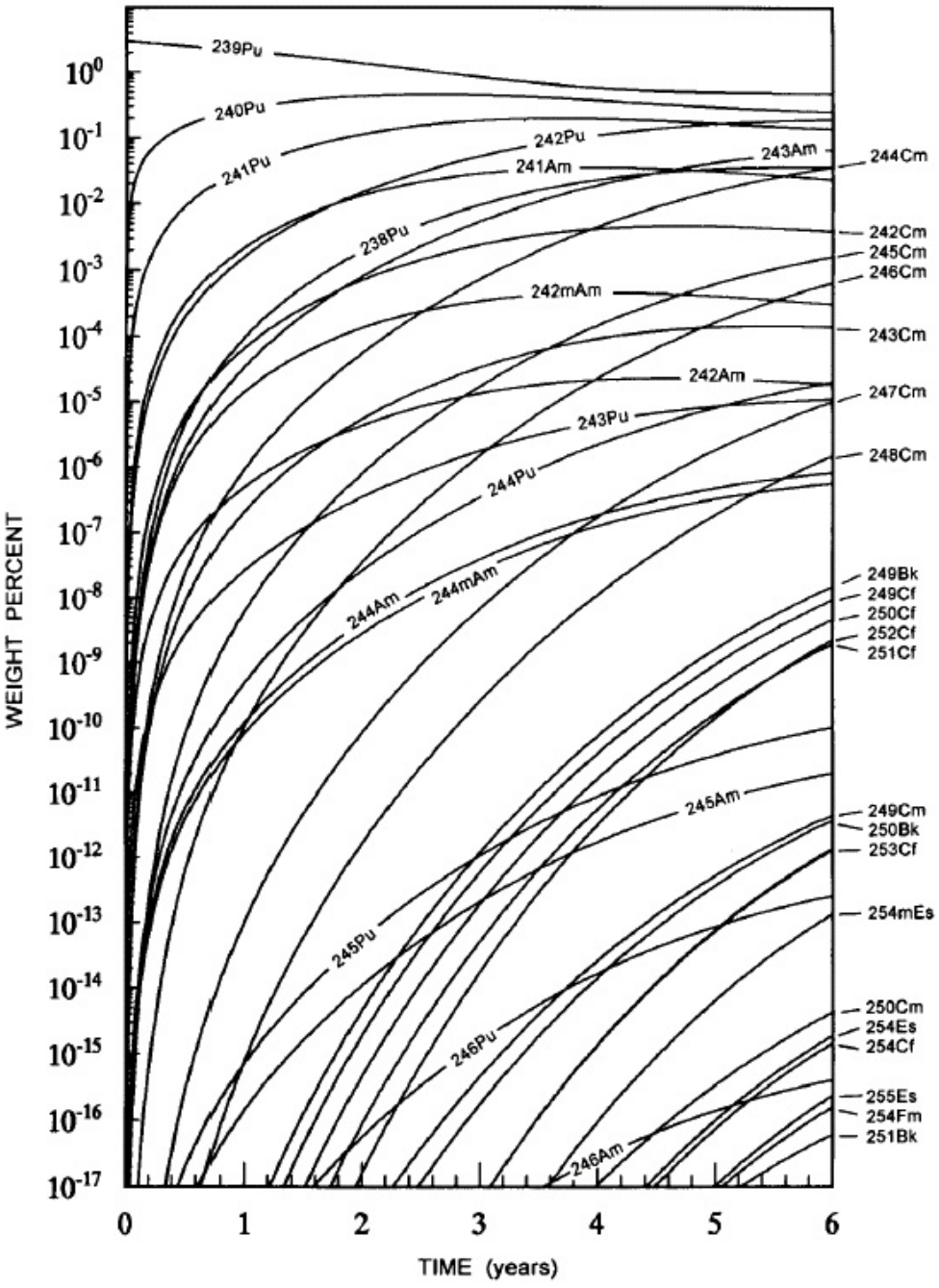

Figure 2.3: Production of transuranic isotopes by weight percent vs. fuel life. (3% ^{239}Pu with depleted U in boiling water reactor) [11]

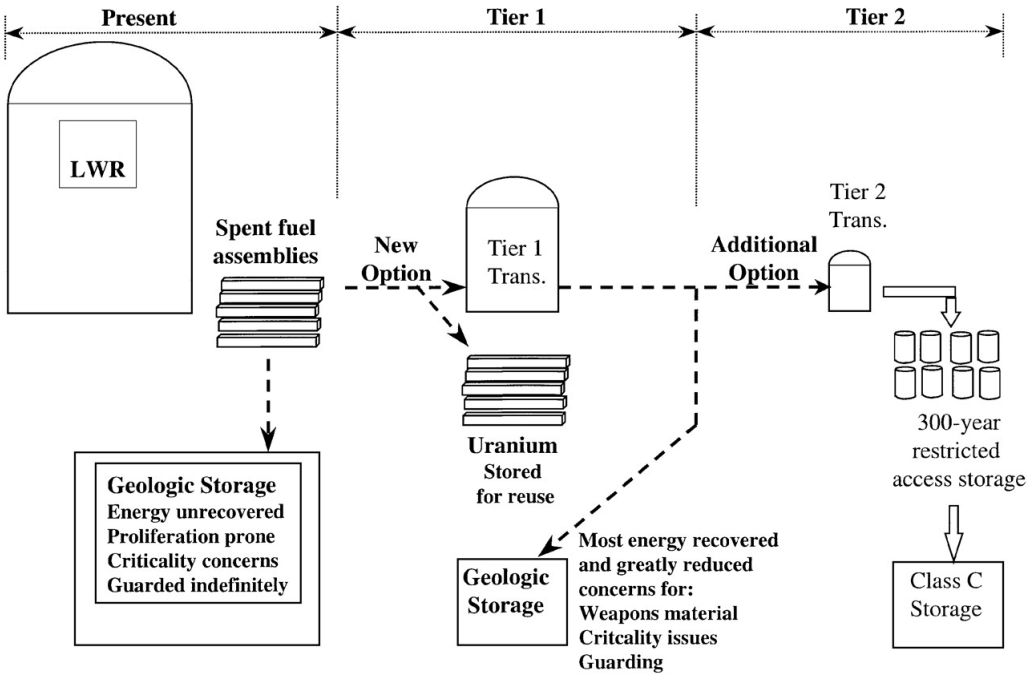

Figure 2.4: Possible transmutation scheme for AFCI [10]

  - The transmuted isotopes rapidly decay into isotopes that pose much less radiological and toxic risk.

- The reduced-radioactive fuel is then placed in queue for a long-term geologic repository.

Transmutation reactors are of varied designs. One possible configuration is shown in Figure 2.5.

2.2 Nuclear Reactor Theory

Nuclear power is based upon the extraction of heat energy derived from consistent nuclear reactions. These reactions are produced from within a fuel form which is enriched

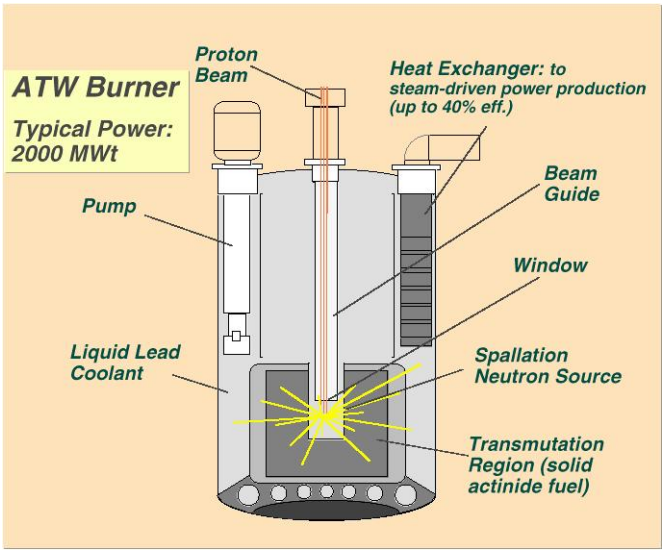

Figure 2.5: Possible AFCI reactor scheme [10]

such that the density of fissile isotopes will cause a self-sustaining nuclear reaction. Neutrons of higher energy tend to be absorbed more readily by fertile isotopes and as such can transmute these into other isotopes. Plutonium is produced from uranium this way in a breeder reactor.

2.2.1 Reactor Types

There are two main types of a nuclear reactors; thermal and fast flux (breeder). These are based upon the neutron energy spectrum used and intended purpose. Thermal reactors produce heat from enhanced fission of the fissile isotope of the fuel, while fast-spectrum reactors, while efficient at power production, are more intended to produce transmutation products such as ^{239}Pu from the fertile isotope ^{238}U.

2.2.1.1 Thermal Reactors

Thermal reactors are designed with moderators to slow down, or "thermalize" the neutrons to enhance their capture by isotopes such as ^{235}U. Thermal neutrons are slowed by the moderators. This enhances the fission process by increasing the interaction cross-section, or the probability of neutron-atom interaction, of the fissile isotopes. Water is the most common moderator, although graphite is also commonly used [12].

UO_2 has been the most common fuel form for this type of reactor. The enriched UO_2 is made into fuel pellets that are packed into fuel rods. These fuel rods, when packed and configured, produce the reactor core. These rods are then placed into a reactor core configured to be cooled by water. Water is used as a coolant and a moderator while graphite or boron control rods are used to limit the neutron flux and thus total fission.

The light water reactor (LWR) is the most common type of commercial power reactor. They evolved from the first U.S. Navy submarine power plants. There are two main types, pressurized or boiling water reactors. The water used is "light" water, as opposed to heavy water with deuterium or tritium.

Neutrons are produced during some natural decay of the radioactive isotopes. General thermal reactor theory specifies that these neutrons, moving with energies in the MeV range, need to be slowed to "thermal" velocities to be absorbed by a fissile nucleus. Thermal energy is essentially $\frac{1}{2}\left(\frac{1}{k}\right)$, or 0.27 eV. Thermal neutrons are slowed by a light element such as carbon or hydrogen. At this velocity, the nucleus of the fissile isotope, such as ^{235}U, can accept the neutron, which produces a very unstable condition within the nucleus. The nucleus, to find a more stable state, fissions in half with tremendous energy, sending these two halves, or fission products, in separate directions at very high velocities. Gamma rays are released as well as an average of three neutrons per reaction.

The fission products move about 10 to 20 μm through the fuel lattice, causing atom

displacement as they pass. This displacement may or may not break the bonds, but only "jiggle" the atoms and release some momentum energy. This energy is lost to the lattice until the fission product comes to rest. Neutrons with sufficient collision vectors can cause some lattice vibrations as well. All the energy (about 70 MeV on average) for each fission product as well as some of the neutron energy (about 1 MeV) is absorbed by the lattice as heat. This heat is then transferred through the cladding to the coolant to produce steam energy. This, of course, turns turbines on generators, thus producing electric power.

For this thermal power reactor, the three crucial components are the:

1. moderator,
2. control rod,
3. fuel.

The moderator is generally graphite or water, both of which have a high cross-section for neutrons and thus slow their velocity. The velocity must be slowed from MeV velocities to eV velocities within the reactor core for efficient, self-sustaining fission reactions to occur. Light elements tend to have a high cross-section for inelastic nuclear collisions with neutrons and thus slow them quite efficiently.

Control rods are made of elements that have a high cross-section for neutrons, yet do not slow but capture them. In this way they remove neutrons from the reactor core. The fuel needs to be enriched sufficiently that, with three neutrons, at least one is captured and a secondary fission event occurs. Generally, 3 to 5% ^{235}U in ≈95% ^{238}U is used.

Fuel is depleted when the proportion of ^{235}U becomes <3%. The expended rods are removed and placed in a "cooling pond", which is a tank that holds the spent fuel rods for about 10 years. During this time the short-half-lived fission products and transmutation

products are reduced such that the immediate radiation hazard is removed. These are then placed into temporary-storage facilities waiting for a long-term repository to hold them. The repository is designed such that the fuel rods are allowed to "cool" for thousands of years away from civilization. It is possible to reprocess the fuel rods and extract the uranium for re-enriching more fuel. The fear is that plutonium can be removed at the same time, which although has power applications, plutonium also has significant nuclear weapon applications.

2.2.1.2 Fast Reactors

Breeder or fast neutron reactors do not use moderators, and therefore the neutron velocities are very high. These use a high concentration of fissile isotopes of uranium and plutonium in the range of 30 %. Since water is a moderator, the coolant is usually liquid sodium, which heats water for steam production with the use of heat exchangers.

If there is a large concentration of fertile isotopes, such as ^{238}U, the neutrons can produce ^{239}Pu, which can capture another neutron to produce ^{240}Pu, and so on. When this occurs, the product has been "transmuted", or transformed into another element. The alchemist's dream is to produce gold from lead through the Philosopher's stone; a reactor is the modern form of alchemy. This "breeding" of plutonium produces more heat than just the ^{235}U fission events and thus is very efficient. ^{239}Pu can fission under these conditions as well. The downside is that ^{239}Pu can be used to make nuclear weapons. One promising answer to decrease plutonium production is to reprocess the spent fuel rods into a mixed oxide form of (U,Pu)O_2, or MOX (mixed oxide fuel). The fissile plutonium would be reburned in a specially configured reactor [2, 12, 13]. Although the MOX program is not dead, the production of plutonium from a breeder reactor is not politically feasible at the present time.

The Nonproliferation Treaty that the United states signed eliminates reprocessing as an option so that plutonium availability is limited to that which is already in the weapons stockpile. World-wide, reprocessing plants in operation or under construction have only a small capacity and could not provide the capacity to reprocess the legacy waste that has been accumulated. They were designed to produce the fuel needed for the breeder reactors in use and only have this limited capacity.

2.2.1.3 Advanced Reactors

There are many forms of nuclear reactors. Many are test reactors that are designed to test the feasibility of advanced designs. Others are used to produce transuranics for study, while some are designed for power yet are of the fast-neutron design. Two advanced types are listed below for their possible use with AFCI.

2.2.1.3.1 High-Temperature Gas-Cooled Reactors The High-Temperature Gas-cooled Reactor (HTGR) is a radical departure from the standard design. It is a pebble bed design,with packing of fuel, in the form of spheres and not pellets, and is cooled by helium flowed from bottom to top. The reactor core temperature may be run to near the melting point of the fuel which increases overall heat extraction. The efficiency of this design is about 15% greater than that of the conventional LWR and, although it has not yet been proved on the commercial scale, the design is being pursued by a few countries such as Japan, China, and South Africa [2].

The fuel is of the TRISO design: UO_2 with a double layer of pyrolitic carbon covered by a SiC outer layer. The small TRISO particles have a high surface area that allows maximum heat transfer to the helium. The helium flows through the pebble bed, which offers the high surface area of the TRISO fuel particles, and then transfers heat through a heat exchanger

to water for steam production.

One novel concept of the fuel is the designed retention of all the fission products. The particles were designed as small spherical pressure vessels that can withstand the buildup of fission gas pressure. They are small enough to contain the gas and fission products produced at high burn-up. Fission gas and other products that diffuse to the surface are contained by the pyrolitic carbon layers and/or SiC outer shell.

Germany's nuclear program excelled in this area of fuel production until the mid 1980s when the Green party took over and eliminated nuclear power in Germany. Many of the leading reactor scientists from Germany are now being employed by other countries to help advance their own HTGR projects.

2.2.1.3.2 Accelerator-Driven Reactors The Accelerator-Driven System (ADS) is the reactor that differs the most from the conventional. It uses a high-power accelerator to produce the neutron flux of the proper spectrum. The fuel is placed in a reactor environment at the end of the beam line where it is irradiated with the neutrons and cooled with a liquid metal such as lead-bismuth. The lead-bismuth coolant acts as neutron target as well, multiplying the neutrons by spallation from a high-energy proton beam, which are then available for capture and transmutation.

Spallation is a process in which the high-energy protons from the accelerator strike the target, in this case the liquid metal, and eject protons and neutrons in the forward direction with reduced energy. This produces a cascade of spallation that continues until the proton's energy is spent. The proton cascade produced is about one meter in depth for a 1 GeV proton beam. Many of the collisions are elastic such that energy is transferred to the nucleus. The nucleus in such cases may "boil-off "neutrons to attain the ground state. About 90% of the neutrons produced by spallation are from boil-off. About 30

neutrons are produced per one GeV proton, although the boil-off neutrons are emitted in all directions. As such, proper geometry of the fuel rods is required to capture as many spallation neutrons as possible. Fission is possible with the proper fuel composition and neutron energy spectrum [10].

Fission events provide the energy required to power the accelerator. These types of reactors run "sub-critical" such that the neutrons produced by fission within the fuel configuration are not enough to maintain a fissile reaction without the external source. Thus, the accelerator drives the reaction and there is no need for control rods in the configuration. Both the United States and Japan are developing ADS reactors [14, 15, 16, 17, 18, 19, 20].

2.2.2 Reactors for AFCI Use

AFCI relies mostly on fast-moving neutrons for fission or to transmute the transuranics to less stable isotopes [18, 13, 21, 22, 23], although thermal neutrons can also be used. The less stable isotopes then decay rapidly to a more stable form through a decay cascade. This produces a more stable and less radioactive waste form in 100 - 1000 years rather than > 10000 years if no reprocessing is performed.

Many designs have been proposed for transmutation. Most are based upon the fast spectrum of neutrons required for transmutation of the fission products in the special fuel. The spectrum is tuned such that the cross-section for neutron capture is maximized.

Thermal neutrons can be used as well if a reactor is properly configured. Both thermal, fast, and ADS reactors are considerations for the AFCI fuel cycle [10]. Power production is not of primary design although a self-sustaining reactor is idealized. Thermal efficiency is not of primary concern as the temperature of the reaction is to be kept fairly low for a breeder reactor. At 700 ° to 800 °C, the corrosive effects of the coolant and the long-term corrosion of the cladding may be controlled.

2.2.3 Nuclear Fuel Environment

The environment that a nuclear fuel must endure is very harsh. Within the core of a reactor there are thermal cycles and gradients, fission products and neutrons penetrating throughout the fuel, gas pressure buildup, etc. For the AFCI envisioned reactors, the fuel must survive years of constant battering by this environment to high burn-up. The transuranics must be largely transmuted, and the fuel must survive not only the environment but also the accumulation of the transmutation products of the original lattice. The fuel must be compatible with the coolant in case the cladding ruptures. In such a case, the fuel should not react to form an environmentally mobile species.

2.2.3.1 Temperature

The thermal environment is dependent upon the reactor type to be used. It is most often stated that the fuel will see an approximate temperature of 700°C, but one type of reactor studied for AFCI requires the fuel to be at over 1200°C (GFR) [2, 12]. LWR temperatures cannot exceed 900°C by design. TRU-N fuels are able to handle temperatures approaching 1400°C with ease. With the removal of americium, the useful temperature could be increased another 500°C or more.

Reactors are constantly cycling temperature, either by moderating the neutron flux, altering the coolant flow, fission spikes, or by compensating for fuel-rod depletion and change out. Thermal cycling, even at high temperatures, can produce thermal fatigue, bubble nucleation and growth, and eventual crack formation.

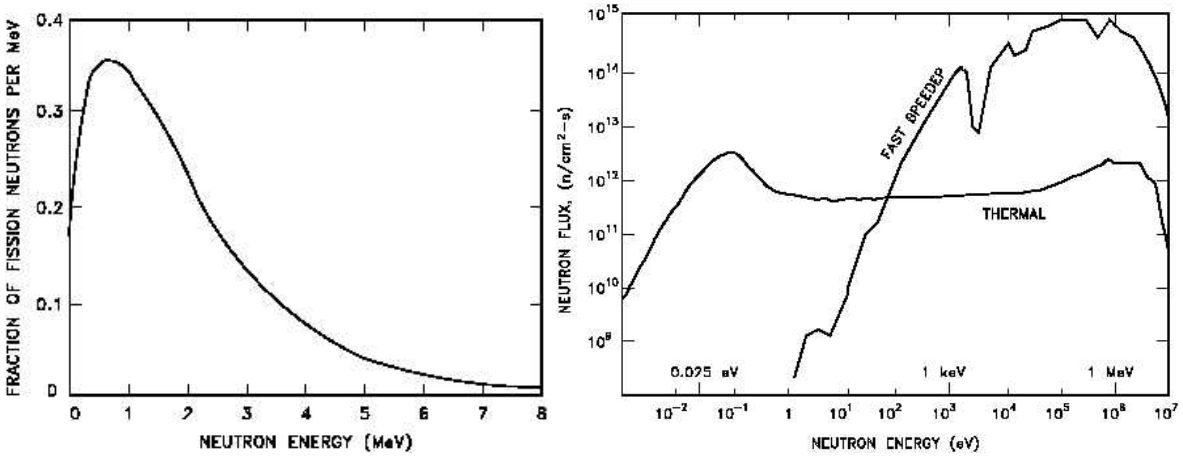

(a) Energies of neutrons from fission events.

(b) Neutron flux vs. energy spectra representative of both thermal and fast reactors.

Figure 2.6: Neutron energy spectrum [24]

2.2.3.2 Neutron Flux

A nuclear reactor, regardless of the type, produces neutrons in quantity. Figure 2.6 (a) shows an energy spectrum of neutrons produced from fission. Each nuclear fission event produces an average of three neutrons of very high energy. These neutrons can penetrate very far and most are lost outside the fuel. The high take-off energy of the neutrons reduces the cross-section of ^{235}U. Sustained fission requires that each fission event produces another fission event, and thus moderators are introduced. By the use of materials such as graphite or boron, the neutron flux is slowed down to "thermal equilibrium" with the fuel (about 0.27 eV). This "thermal spectrum" of neutrons increases the cross-section of ^{235}U and the probability of sustained fission.

The neutron flux is greater the of fission product flux by a ratio of three neutrons to two fission products. Neutrons can penetrate throughout the fuel with ease, and much of the time escape to the outer cladding. Energetic collisions of a neutron with elements of the fuel can cause displacive damage if the neutron has been slowed enough and/or the

neutrons ballistic collision angle is low. Neutrons, not having any electronic charge, will not have any electronic collision potential.

The high energy of the fission-produced neutrons, about 1 MeV, is too high for probable cross-sections of nuclear stopping collisions. Moderators and control elements slow the neutrons to produce higher cross-sections of reaction. As the neutron slows, the nuclear collision cross-section increases and the neutron will cause its displacive damage [25].

Fast-spectrum breeder reactors use higher-velocity neutrons and thus do not use moderators. Neutrons are allowed to penetrate throughout the fuel, and the high energies produce a higher cross-section for uptake by fertile isotopes. The fuel requires a highly enriched fuel to sustain the nuclear reaction. The advantage of the fast flux is that the less fissionable transuranics can be fissioned or transmuted to isotopes with shorter half-lives.

From Figure 2.6 (b), the neutron flux is about $10^{13} \frac{neutrons}{cm^2 second}$ for a thermal reactor and about $10^{15} \frac{neutrons}{cm^2 second}$ for a fast-spectrum reactor. These numbers are general representations for the types of reactors, and may be changed based on fuel type and configuration. As can be observed, the breeder reactor has a wide spectrum of fast neutrons, while the thermal reactor has a "hump" at the low end of the spectrum correlating to the "thermalized" neutrons from the moderators.

Neutrons are scattered by atoms in the lattice from both elastic and inelastic scattering such that the neutrons lose energy. At lower velocities, the cross-sections for a fission or transmutation event increase. Figure 2.7 shows the "resonance peaks" observed due to quantum effects such that the neutron absorption cross-section is increased. The effect is that neutron uptake is increased as neutron energy decreases. At very low energy, or velocity, a neutron's cross-section is proportional to $\frac{1}{v}$ where v is the velocity in eV.

The neutron flux is important for radiation damage as neutrons, although having little mass and no electronic stopping effects, still have a high velocity and nuclear collisions

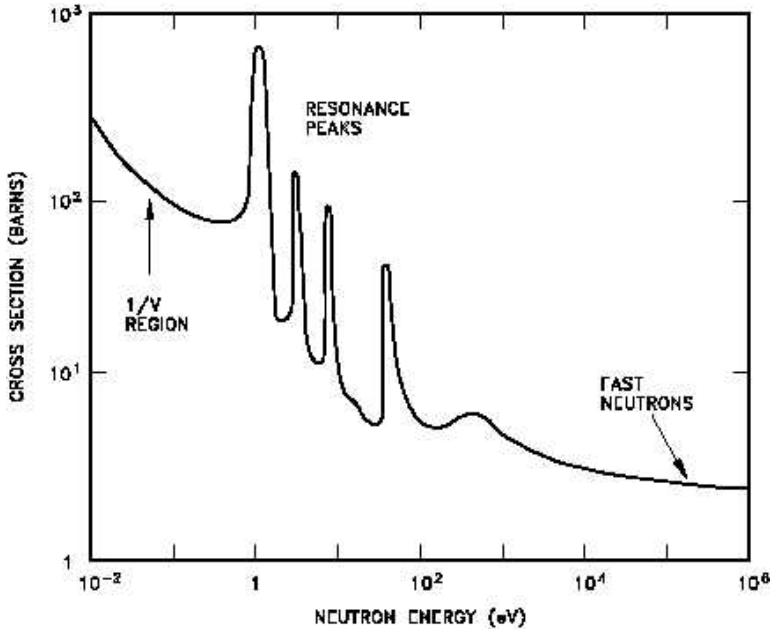

Figure 2.7: Neutron cross-section vs energy showing $\frac{1}{v}$ relationship [24]

produce displacements. The energy transferred from the neutron to the primary knock-on atom (PKA) is very large and as such can produce a significant amount of damage. From the fast spectrum, an average fuel damage is about 3000 displacements per neutron. Although not on the order of the damage produce by fission, the damage is significant.

2.2.3.3 Fission Product Flux

Thermal neutrons striking the fissile elements can cause a fission reaction. Fission releases a tremendous amount of energy, in both the kinetic release of fission fragments and high-energy photons. The fission products are a binary composition of mass that sums to the original fissioned isotope. The distribution of possible combinations is bimodal. Refer to Figure 2.8, which is a typical distribution from UO_2 fuel in a LWR [26]. Generally, there are two fission fragments and three neutrons produced for each fission event.

Since the fission products are produced at an average of 2 fragments per 3 neutrons, the

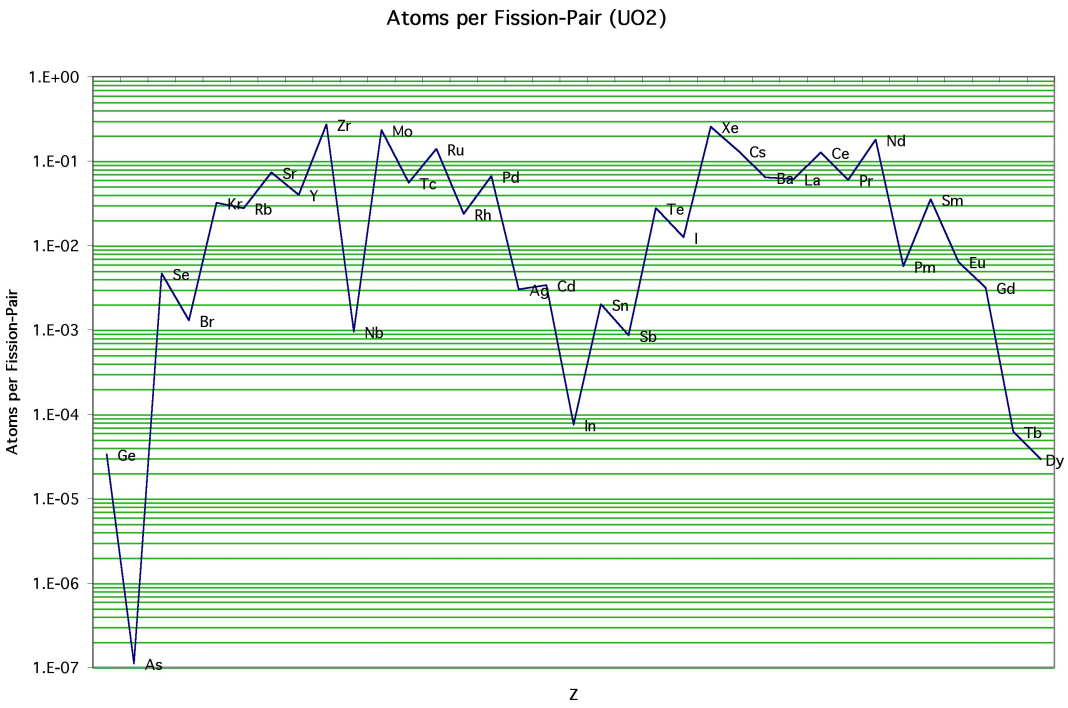

Figure 2.8: Fission product distribution (UO_2 in a LWR)

flux is then $\approx 6.6 \times 10^{12} \frac{neutrons}{cm^2 second}$ to $\approx 6.6 \times 10^{14} \frac{neutrons}{cm^2 second}$. This equates to a significant amount of fission product produced during years of service. As the number of seconds in a year is $\approx \pi \times 10^7$, the average amount of defects produced per year $\approx 10^{21}$ fission products per cm^3 for an averaged distribution. Many of these fission products do not stay in solution as they are diffused to a free surface and eventually reach the gas plenum. While many fission products are gases such as xenon or krypton, others such as iodine or cesium are very corrosive to cladding alloys. Many fragments remain in solution with the fuel. Some cause problems such as gas bubble formation or poisoning of the neutron flux, while others have little effect.

These fragments may be isotopes that are not stable, with half-lives as short as milliseconds. They can decay, by α or β processes, to form more stable isotopes. More fissile products can be produced by neutron capture such as ^{239}Pu from ^{238}U. Some isotopes pro-

duced have half-lives of hours, such as ^{135}I, which decays to ^{135}Xe.

Two of the more common elements produced from fission are the noble gases xenon and krypton. Helium is produced in large quantities from radioactive α decay. These noble gas elements are produced in a large enough quantity that there is concern that they can swell the fuel or overpressure the fuel rod. Being noble gases, they are non-reactive and thus are rejected from bonding in the crystal structure. They are then free to move throughout the structure without the energy cost of forming and breaking bonds.

The gases either sit in vacant structure sites, accumulate in defects or at grain boundaries, or diffuse to a free surface and leave the fuel. The diffusion rate is a critical design parameter due to the fact that the gases may be trapped, then accumulate, and produce bubbles that may swell and cause damage to the fuel.

Other fission products may bond and form ternary nitride forms with ZrN. Zirconium is a common fission product and thus will blend with ZrN. Many of the other common fission products are lanthanides, which all have the NaCl crystal structure and similar physical properties to those of ZrN and TRU-N. Neodymium is a common fission product that is used as a measure of fuel burn-up. Other elements form nitrides but not in the cubic form, such as cesium or molybdenum. The chemical nature of these elements provides the possibility of disruption to the crystal structure. Experience has shown, mainly with oxide fuels, that the fission gases are more critical to the fuel integrity and performance than most other elements produced. Carbide fuels have also been shown to swell from fission gases [27].

2.2.3.4 Matrix/Fuel Interface

From the fission event, high velocity particles are produced from anywhere within the fuel pellet. The impact from the accelerated particle produces a cascade of damage, depositing the displaced atoms and the accelerated ion at a depth greater than that of the

damage. Thus, with ion implantation studies, there is a discrepancy between where the displacement damage is produced and where the knock-ons and implant ions are deposited. In a reactor fuel, the fission products are produced in all directions and thus the damage will be distributed homogeneously. The fuel matrix or fuel cladding interface, however, will be more like an accelerator damage sample, in that the damage and fission product deposition will be layered by depth.

At the interface, the fuel produces fission products with a random probability outward in a spherical distribution. With enough fission events from a small area, the distribution becomes a hemisphere into the matrix for a small area of fuel. Figure 2.9 shows the fuel/matrix interface with the spherical distribution. Common depths of penetration of fission products are in the range of 10 μm with the damage range slightly less. Within this depth the fission damage and product deposition is homogeneous, but, perpendicular to the interface, there will be the separation of damage and products based upon collision and cross-section.

The magnified view of Figure 2.9 shows the layered distribution of one fission product and its damage profile. When the size of the matrix particles is twice that of the largest depth of penetration, then the matrix particle, being bombarded from all directions from the fuel, will be more damaged.

2.2.3.5 Fission Product Effects

During the fissioning process, many elements are produced. Many of these are unstable isotopes with short half lives.^{135}Xe is formed from ^{135}I as well as from fission of a ^{235}U. ^{135}I is a a decay product of ^{135}Te, a fission product with a short half-life.

As an example, ^{135}Xe is considered a neutron poison, in that it has a high capture cross-section, which reduces the overall neutron flux.^{135}Xe is normally diffused out of the

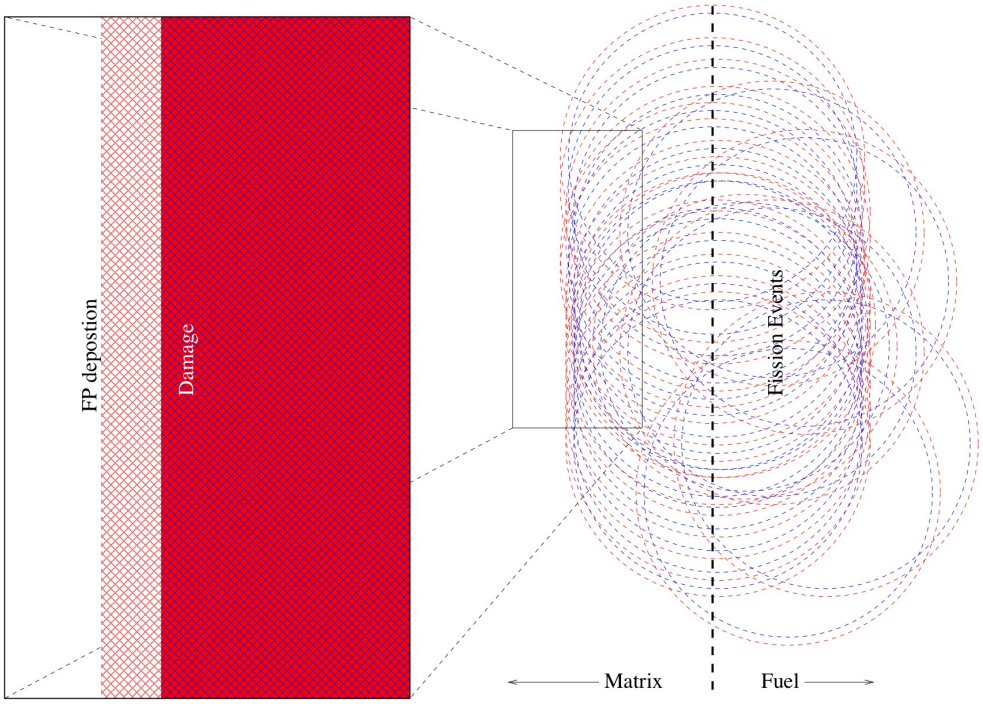

Figure 2.9: Fuel/Matrix interface

sample at a rate that limits this effect. It is known that upon shut down in a LWR, ^{135}Xe builds up over a period of hours due to ^{135}I decay. A restart is much more difficult due to the increase in ^{135}Xe, the lower temperature and diffusion, and thus the core is poisoned. Full withdrawal of the control rods is used to start the reactor in such a case. The ^{135}Xe is flushed out over a period of two days and the reactor core may then continue operation normally [12].

This not only means that the xenon build up after a core shutdown is bad for a restart, but also that it is hard on the fuel itself in a structural sense. With lowered temperature and continued production from ^{135}I decay, ^{135}Xe is produced. Since the temperature of the core is lowered, the diffusion out of the fuel is decreased, yet decay is nuclear and not temperature dependent.^{135}I decays at a constant rate and thus ^{135}Xe accumulates within the fuel.^{135}Xe has a half-life of a number of hours and thus reduces itself, but not prior to reach-

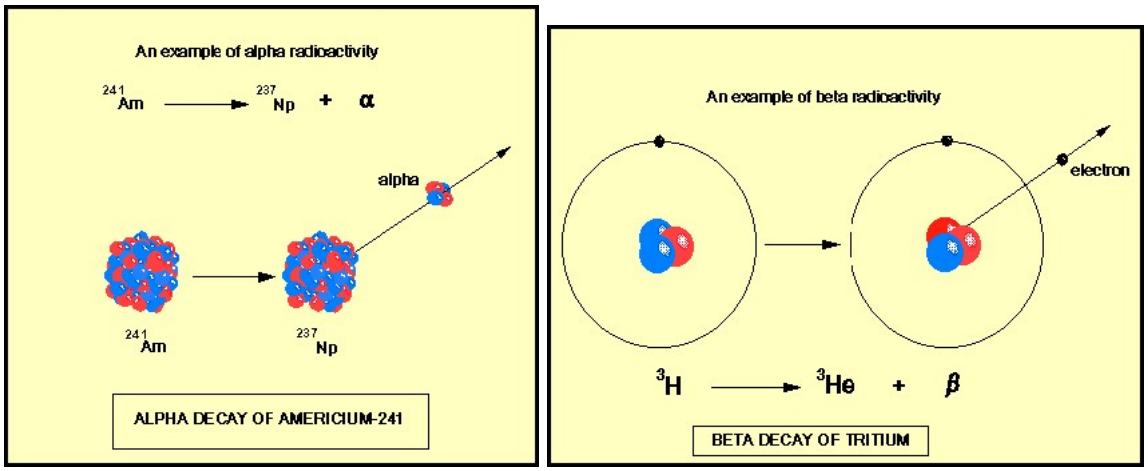

(a) Example of alpha decay (b) Example of beta decay

Figure 2.10: Radioactive decay

ing a high concentration. This peak concentration is dependent upon the ^{135}I concentration at steady state prior to core shutdown.

2.2.3.6 Decay Products

Radioactive decay, whether induced by neutron collision or by natural decay, occurs within a reactor fuel. Alpha decay produces ^{4}He while β decay produces an electron, and γ decay produces γ wavelength photons. Gamma rays are similar in energy to x-rays but are differentiated by the fact that γ rays are originated from the nuclear core. Alpha and β decay products are low in momentum and quantity and thus do not contribute a large amount of damage during the reactor operation, but, during storage, the quantity of displacements builds over a long period of time. Alpha decay produces much helium as the decay product. This in turn produces displacement damage over time, and also increases the amount of helium dissolved within the fuel. At storage temperatures, the helium is more likely to produce bubbles at traps than to diffuse through the bulk and escape.

2.2.3.7 Fuel Rod

The sintered fuel pellet is stacked into fuel rods, which are stainless steel or zircalloy tubes. Both materials are designed with radiation tolerance in mind. They must withstand damage from neutrons and fission products, the corrosive effects of some fission products that escape into the plenum, the embrittlement from both helium and hydrogen irradiation, the increased stresses imposed by a swelling fuel pellet.

These tubes, once the pellets are stacked within, are filled with either helium gas or sodium. Sodium is a liquid at elevated temperature and both medias have a high thermal conductivity. The fuel, however, must be compatible with both liquid sodium and helium.

2.2.3.8 Sintered Pellet

The TRU-N pellet design is aimed at a sintered structural ceramic with select grain size and connected porosity. The grain size is critical for diffusion and trapping effects, while the connected porosity is for gas release. The TRU-N components are dispersed within an inert matrix [28]. This composite is then pressed and sintered into a pellet.

Matrix materials must be able to handle the temperature, thermal stress, internal gas pressures, etc. Post-reactor requirements are that it must be able to be reprocessed to extract the minor actinides, and it must be compatible with the coolants used, and sodium as a thermal bonding agent [6, 29, 8, 30, 31].

Nitrides are soluble in nitric acid with time and temperature. Nitrides are also compatible with sodium, which is one of the possibilities for a coolant/bonding agent. Carbide fuels, on which there has been much more research, are reactive with sodium at temperatures exceeding 800 ° to 900 °C and thus are possibly incompatible with the AFCI process [27].

At approximately 85% dense, the pellets achieve a connected porosity while maintaining a relatively high level of thermal conductivity and fuel cross-sectional density [27]. The fuel must be able to have enough fissile and fertile material for the given neutron flux to be efficient. Conductivity is crucial to extract the heat energy, not only for energy production but also to reduce the fuel core temperature. Oxide fuels have been shown to melt in the core due to low thermal conductivity of the pellet [25]. Nitrides, however, have high conductivity allowing the reactor to run at high temperatures and increasing its thermal efficiency.

2.2.3.9 Fission Gas Escape Through Connected Porosity

Gas release is critical in this design due to the large production of fission gases, notably He, Xe, Kr, Cs and I. A certain amount of swelling is engineered into the fuel rod assembly. As the fuel pellet swells, it closes the gap between the fuel pellet and the rod inner wall. This increases direct thermal contact and allows for greater heat extraction [27, 25].

The fission product accumulation, especially the gases, must be accommodated by the structure. The crystal structure and microstructure must be able to accommodate large quantities of fission gases that accumulate over time, providing a steady-state accumulation/release at which the fuel holds its integrity and efficiency.

With a target of 85% density, the connected porosity provides a large surface-area-to-volume ratio for the gas to diffuse out of the fuel to the gas plenum. By concentration gradients, the gas is driven to this free surface. The mean free path that the gas atoms must take through the bulk to the surface or to grain boundaries should be as short as possible, to reduce the time the gas atoms should spend within the fuel. At steady-state operation, the gas should have sufficient mobility to be flushed into the cladding cavity. This must be true for sudden spikes in fission that throw this flow out of equilibrium; the flow must be

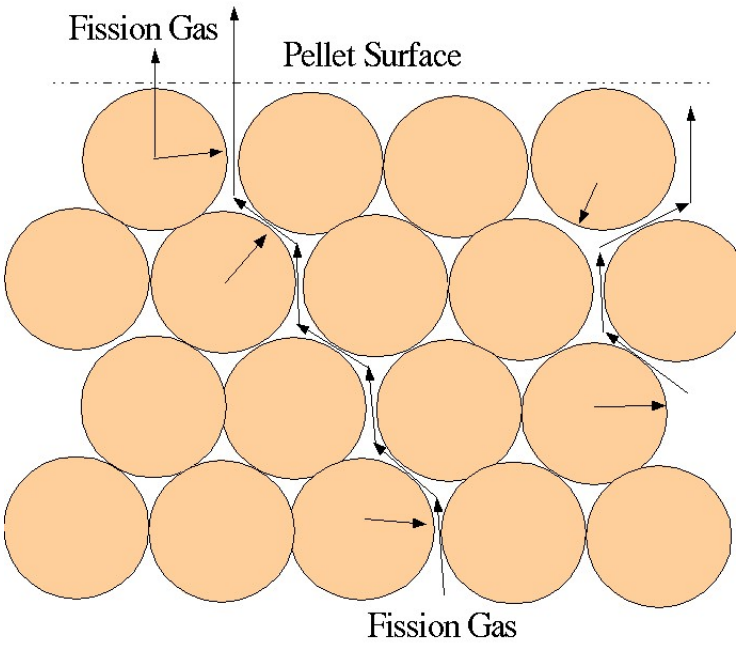

Figure 2.11: Gas escape path through connected pores

sufficient to compensate and return to equilibrium without detrimental effects to the fuel.

Due to the higher driving force, gases will diffuse to any free surface. A closed pore will become a pressure vessel as the gases move into it. Connected porosity allows the gas to escape to the volume within the fuel rod, which is designed to accept the gas pressure from the reactor (see Figure 2.11).

The grain size is important for many reasons. It has effects on the mechanical strength, but with gas diffusion it is very important due to the role of grain boundaries, both in promoting diffusion and as possible trapping sites. It has been shown that, in oxides, carbides and nitrides, grain boundaries are the main sink for dissolved gases [27, 32, 33]. As the concentration of gases builds, the gases tend to accumulate and form bubbles at the grain boundaries, which are somewhat fixed.

The pre-sintered packing distribution has a fair distribution from large to very small

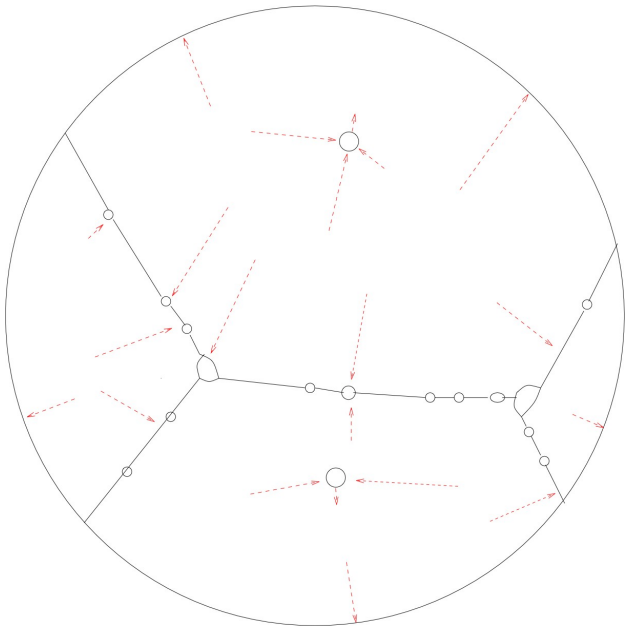

Figure 2.12: Gas movement within a grain. Gas either diffuses to the surface, or forms a bubble in the grain or at the grain boundaries. Gas, at high temperatures and with irradiation, and may also diffuse out of the bubbles

particles. Milling operations reduce the size of the particles that are produced from carbothermic reduction processing to small particles from 0.5 to 1 μm.

With irradiation defect production, the diffusion through the bulk should increase. Vacancies on both the metal and non-metal sublattices will allow for fission gases to move more easily. Dislocations will allow pipe diffusion to the grain boundaries or free surface. Yet these defects under certain conditions, may also produce traps that hinder the diffusion process. Vacancy clusters may form to produce voids,providing a free surface to the gas products. These voids can fill to nucleate bubbles. Irradiation can have effects on the voids, as thermal spikes may break them up and cause the gas to re-disperse. The heat and irradiation tend to cause bubbles to migrate [27, 25]. Figure 2.12 illustrates this effect.

2.3 Fuel Forms

Forms of fuels suggested for AFCI range from ceramic to metal. Each has its select properties that are desirable, but also undesirable properties as well.

Oxide fuels have been used for more than 50 years. There is a lot of knowledge of oxide fuels with research on UO_2, MOX, and thorium oxides. Most reactor knowledge is based upon oxide fuels and this is where there is most experience. Oxides are, by their very nature, thermally insulating, which reduces heat transport to the cooling system, and produces a large thermal gradient. This gradient, from the cooler surface to the hot core, produces some interesting long-term effects such as plutonium segregation to the periphery and pore migration to the core.

Metal fuels are different in that their melting points are very low. Plutonium melts at 640 °C, which would reduce any alloy's melting temperature significantly. By design, however, these fuels allow for a safety factor such that the fuel can melt out of the direct neutron flux if there is a thermal spike. Compatibility with sodium, and especially water, calls into question their usefulness. The environmental impact would be devastating for dissolved transuranics, especially neptunium, to escape the power plant in the event of an accident.

TRISO fuels are very different by design. Although based upon an oxide fuel kernel, the fuel design is based upon the coating. The fuel kernel, being very small (< mm), is coated with two distinct layers of pyrolitic carbon and an outer shell of SiC. The layering system has proved effective to produce a very strong pressure vessel that contains the fission products within. The volume-to-surface ratio produces a very high thermal transfer ability. HTGR's, with a helium-cooled pebble-bed design, can achieve very high temperatures (close to the melting temperature of the oxides) and are about 15% more efficient

at producing power than the conventional LWR. Fuel kernel production requires a much different process, and the coating system adds to production costs and difficulties.

Carbides and nitrides are very similar in many respects and should be discussed in detail. This allows the similarities and differences to be noted. Both have very high melting points, high thermal conductivity, and are mechanically very strong and hard. Both are difficult to fabricate, in contrast to the oxides and metal-based fuels.

2.4 Carbides for Reactor Fuel

Transition metal carbides, as well as the carbides of lanthanides and actinides, are very similar to their corresponding nitrides. The carbides have physical properties that are usually quite close to the nitrides due to the similarities in bonding within the lattice. The carbides tend to produce more covalent bonding due to their size and the low electronegativity of carbon. This produces, in general, slightly higher melting points, increased hardness and brittleness, etc. The crystal structures of the cubic carbides is NaCl, corresponding to the relative nitrides, and they are in general, very soluble within one another [34].

Carbide fuels were conceived and put into limited use in the late 1960's [27]. At LANL, the SP-100 program involved the use of carbide fuels for space-born reactors that would operate at very high temperatures. The inherent qualities were discovered to be ideal, although with some drawbacks. Mixed fuels such as (U,Pu)C, were tested, as were mixed carbo-nitrides. These data are helpful with respect to the nitride research, as the trends observed with the nitrides are generally followed.

Some of the drawbacks discovered with the carbides were the difficulty of manufacture, which also holds true for nitrides, and the poor oxidation resistance. Carbides were observed to oxidize easily and were sensitive to water. It was found that some of the car-

bides dissolved in water in a number of hours. The nitrides, on the other hand, have been observed to be resistant to water for months with no sign of degradation [27, 29, 6]. Since a water-cooled reactor uses water near the fuel, it is feared that, if there is a breach, the water will dissolve the fuel and carry it into the environment. Sodium-cooled reactors, while limiting the potential for water contact with the fuel, also have a flaw in that carbides have shown to be sensitive to liquid sodium [27, 15, 35, 29, 6].

2.5 Nitride Ceramics

The nitride ceramics cover a broad range of materials with many different crystal structures. In general they all have similar properties in that they are all hard, refractory materials [36, 34, 37]. Without moving to exotic crystal structures or phases, these materials seem to change dramatically from the base materials.

The types of nitrides are broken into groups by chemistry:

- The *s*-block elements,
- the *d*-block or transition metals,
- the *p*-block elements, and
- the *f*-block elements.

The periodic table is composed mainly of these groups based upon the electronic structure and shells filled. The lanthanides and actinides, however, have f orbitals, yet for the most part are considered to be chemically similar to *d*-block elements.

The largest group is of course the transition metals, since there are up to 10 electrons to fill the *d* orbitals. Nitrogen has $2s^2 1p^3$ electronic structure, so the *p*-orbital, or *sp* hybrid, dominates.

There are nitride ceramics that are non-traditional in the sense of use and ease of manufacture. Divalent *s*-orbital elements, such as calcium, will form a nitride with a networked structure of the base Ca_2N motif. More complex mixtures are found with the combinations with transition metals such as LiN_3, LiNiN, $BaZrN_2$, Sr,Ti,N_2, etc. These bonds are highly ionic, form layered structures, and have properties nowhere near what the transition metal cubic nitrides have [38, 39, 40, 41, 42]. They are merely a curiosity, although Sr and Cs are produced in somewhat large quantities by fission and decay, and could potentially provide a chemical reaction or interaction. Possible nucleation of these precipitates at high temperatures is unlikely.

2.5.1 Crystal Chemistry and Bonding Models

Nitrogen compounds exist with many different elements but, of commercial interest, Si_3N_4, AlN, GaN, and TiN are the most studied. Since nitrogen is next to carbon on the periodic table, nitrides and carbides have striking similarities. Carbides produce similar phase diagrams and have many similar physical properties to nitrides.

Nitrogen is a gas that has a very strong linear triple bond. It is a very thermodynamically stable molecule and requires sizable energy to break these bonds. The nitrogen atom is similarly highly reactive and readily forms bonds. Nitrogen is a highly electronegative element that has many oxidation states, both positive and negative. Although it can be brought to an oxidized state, it is usually closer to the lower oxidation states when in a crystal lattice, bonding covalently. This is balanced, of course, by the Coulombic forces that cause the ionic attraction and polarization of the covalent bonds.

The metal-like or metalloid elements Ga and Si produce nitrides, but with different crystal structures. These materials sometimes are semiconductors and are useful in the electronics industry. AlN is an electrical insulator yet thermally conductive, similar to

GaN. These are all very covalent in bonding with little *d*-orbital character. This makes these materials very hard, and, in the case of Si_3N_4, a very cheaply produced quality abrasive.

The transitional metal nitrides, as well as those in the lanthanide and actinide series, are for the most part very similar. They have mixed bonding, metallic, ionic and covalent, with more emphasis on one bond characteristic by direction. The nitrogen atoms are too far apart to bond much with each other, while they bond strongly with the transition metal. The metal atoms, on the other hand, are large enough to bond with each other. These materials are sometimes referred to as "interstitial alloys", due to the highly metallic character [43]. The thought is that the material is not so much a ceramic in the traditional sense, but a very hard, stabilized alloy like iron-carbon steel. This model sometimes fits with the thought that the zirconium metal structure is stabilized as fcc, with the addition of nitrogen to its octahedral interstices. The filled interstices provide a very hard and brittle alloy.

2.5.2 Typical Characteristics

Nitrogen-bonded ceramics all possess some similar traits. They are all physically hard and brittle and are refractory. The different crystal structures and elements produce different characteristics as well. Electrical and thermal conductivity are common traits. Chemical bonding is of various percentages of covalency, and, in some cases, metallic in character in addition to ionic.

All of the nitrides are very chemically resistant, which has made them important in the industrial setting. They all will oxidize easily, however, as the oxide is much more stable than the nitride. Depending on the structure, the oxide formed will provide either protection or a possible path for continued oxidation. An example would be AlN with a protective Al_2O_3 oxide layer, compared to ZrN oxidized to ZrO_2, which is an oxygen conductor.

The nitrogen seems to stabilize the metal structures. By contributing to the bonding, the nitrides all increase in melting temperature drastically with increasing nitrogen content. Most refractories are thought to be thermal and electronic insulators, but the cubic nitrides are all conductors or semiconductors. The electrical contribution to the heat transfer is high and thus they all conduct heat and electricity fairly well. The transition metal cubic nitrides are all superconductors, with T_C values near 10 K, with NbN at 18 K [44, 34].

Mechanical properties are similar to those of all the cubic nitrides and carbides, but, there are also many distinctions that are made. The carbides are more covalently bonded than the corresponding nitrides. This produces a bit more directionality with the bonds (*p* and *d* character). The transition metals, however, are varied in their sizes and electronegativities. Titanium is a good contrast to zirconium, having the same electronic configuration and yet quite different phase relationships. Titanium is a much smaller atom, and due to less electronic screening, is easier to oxidize to the 4^+ charge state. Even covalently bonded, the smaller size produces a much higher charge concentration, and thus the atom is "seen" to be more charged by other atoms. This produces a more ionic or "*s*" character.

Carbides are most studied with respect to mechanical properties. Toth compiled much data showing that many of the carbides slip on the $\{110\}\left\langle 1\bar{1}0\right\rangle$ system [34]. This is not on the close packed $\{111\}$ planes as expected, since NaCl-structured materials are fcc. Ionic NaCl structured materials, such as rocksalt, slip on the same system. This is explained by the movement of the planes over each other.

Figure 2.13 shows the three major slip systems for NaCl structures. Although the $\{111\}$ planes produces the ideal state, with partial dislocations, the more charged the atoms are, the more likely they will be near a like atom during half-slip. Highly polarized covalent bonds would allow atoms to be "seen" by other like atoms as having the same charge. Coulombic repulsion produces another energy barrier and, in such a case, other slip systems

are preferred. Figure 2.14 shows the half-slip systems.

The carbides exhibit a distinct ductile-to-brittle transition at relatively high temperatures in the ranges of 800 °C to 1000 °C. At these temperatures, other slip systems become active. TiC and ZrC both show this behavior, with the primary slip system being $\{110\}\left\langle 1\bar{1}0\right\rangle$. This system shows that both structures have a significant ionic character, yet, at elevated temperatures, both materials become more ductile and slip on the $\{111\}\left\langle 1\bar{1}0\right\rangle$ systems [34]. TiN has also been observed to slip on the $\{110\}\left\langle 1\bar{1}0\right\rangle$ system [45]. As such, it is somewhat expected that ZrN show $\{110\}\left\langle 1\bar{1}0\right\rangle$ as its primary slip system at room temperature.

Li and Howe, however, have demonstrated that ZrN shows $\{111\}\left\langle 1\bar{1}0\right\rangle$ as its primary slip system [46, 47]. One piece of information to take note of is that the ZrN used was intended to be low in nitrogen such that it bordered above the α phase. The lower stoichiometry of nitrogen produced many vacancies on the nitrogen sublattice, and hence, the stacking-fault energy was extremely low. This difference allowed the dislocations not only to be on the $\{111\}\left\langle 1\bar{1}0\right\rangle$ system, but also to produce large stacking faults between the two partial dislocations.

2.5.3 Transuranic Nitrides (TRU-N)

Uranium nitride has been studied extensively with respect to reactors. Plutonium nitride added in solid solution has more recently been studied as well. Moving up the periodic table through the actinides, UN shares the general properties with the transuranic nitrides while being at the cross-over point of *f* to *d*-orbital dominance. As the mass increases across the actinide series, the *f*-orbital energy is drawn inward and the energy of the *d*-orbital becomes dominant. This criss-cross point is approximately about uranium. Actinium, etc. will be dominated by the *f*-orbitals and, while the cubic set generally dominates, the overall

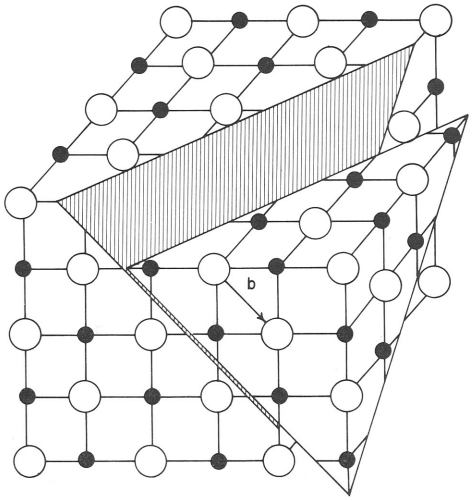

(a) $\{111\}\langle 1\bar{1}0\rangle$ slip

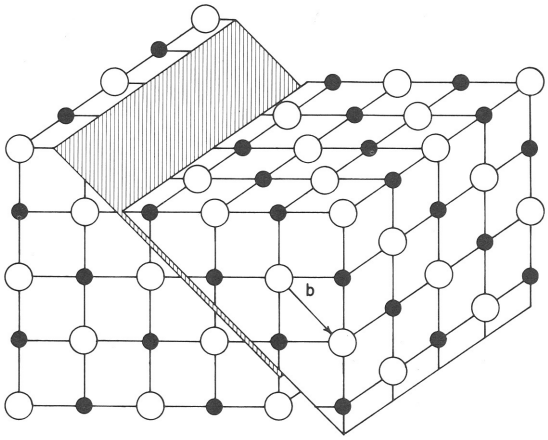

(b) $\{110\}\langle 1\bar{1}0\rangle$ slip

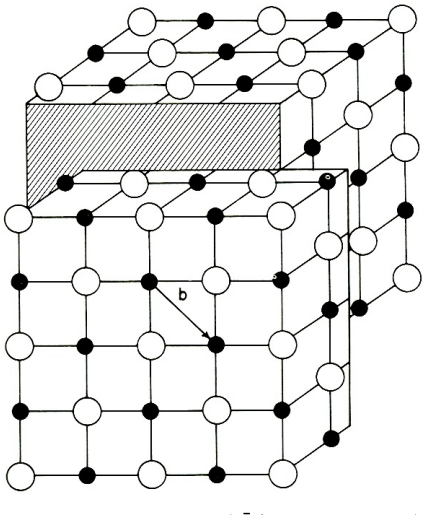

(c) $\{001\}\langle 1\bar{1}0\rangle$ slip

Figure 2.13: Major slip systems for NaCl crystal structure [34]

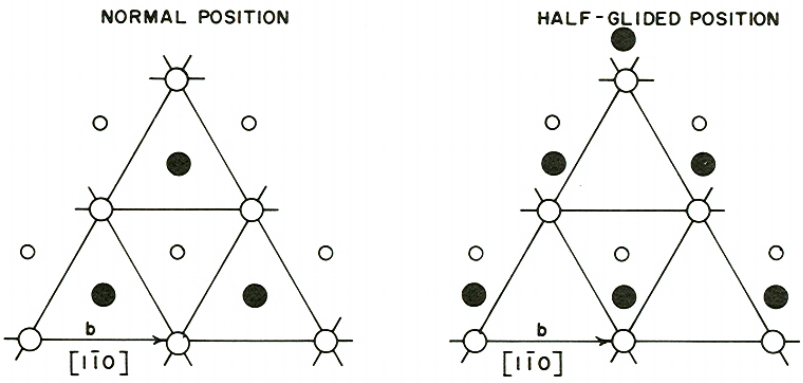

(a) The $\{111\}\langle 1\bar{1}0\rangle$ slip system

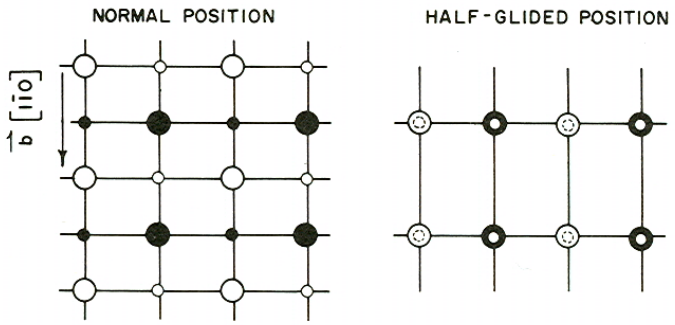

(b) The $\{110\}\langle 1\bar{1}0\rangle$ slip system

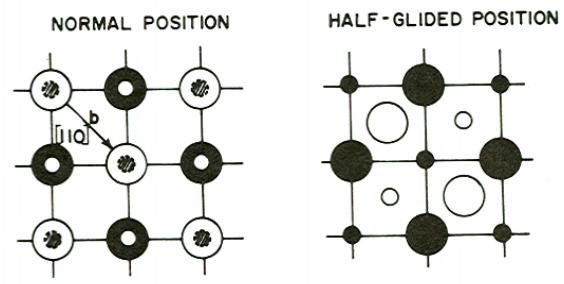

(c) The $\{001\}\langle 1\bar{1}0\rangle$ slip system

Figure 2.14: Half-slipped planes on the major slip systems for NaCl [34]

chemistry is different from that of a transition metal [48, 49, 50, 51, 5].

The transuranics are dominated by the *d*-orbitals and thus respond very similarly to the transition metals. With this in mind, many properties are very similar between the transuranics and the transition metals, including their compounds.

The transuranic nitrides are all refractory with high melting points. Like all of the cubic nitrides, they are very hard and brittle and posses a metallic shine. They are electrically and thermally conductive and theoretically are superconductors.

Much more information has been acquired on the the actinide carbides. Specifically, UC, PuC, (U,Pu)C and ThC. Some information is available on the transuranic carbides [27]. The carbides are very close in structure and physical properties to their nitride counterparts. This is useful in predicting how the nitrides will behave under stressful conditions. Carbide fuels have been used in research reactors since the 1960's. The overall performance is very good, although carbides do have a reactivity with water, which makes them somewhat undesirable from the accident/environmental standpoint [27].

2.5.3.1 Crystal Structure

The TRU-N's all have the B1 (NaCl) cubic crystal structure. The elements have the *f*-orbital energy lower than that of the *d* orbitals and thus the chemical and physical properties are more like those of a transition metal. This is due to the effect of the increased screening of the *f*-orbitals with increasing Z (atomic number), while the *d*-orbitals become more chemically active. The result is oxidation states and chemical activity that are similar to those of transition metals with the same valence electrons and ionic size. Due to the electronic screening of the *f* and *d*-electrons, there is an actinide contraction as well. The atomic and ionic sizes are very similar to those of the lanthanides and transition metals. Carbon and oxygen readily react with the metals and can be dissolved into the nitrides.

2.5.3.2 Physical Properties

Since the transuranics are difficult to work with, much of their physical properties are predicted by thermodynamics. Some work has been done on UN, PuN and (U,Pu)N. General properties follow the transition metal nitrides in mechanical properties, etc. UN has a melting point of about 2700°C, while that of PuN is a bit less at about 2550°C . The other transuranics follow to some degree with NpN at about 2750°C, and, while little is known about AmN, it is calculated to vaporize at more than 1400°C in a mixture with PuN [5, 52, 4].

2.5.3.3 Radiation Tolerance

The NILOC-II experiments with (U,Pu)N pellets produced some useful data on production with respect to the overall fuel performance and survivability in a high-temperature breeder reactor [35]. The fuel sustained very high reactor core temperatures, with spikes at over 1700°C. The pellets were produced by different means, and behaved differently with respect to grain growth and in-pile sintering. While some of the pellets showed cracking after months of abuse, one set of pellets survived quite well, even with the high temperature spike. UN, PuN, (U,Pu)N and the mixed carbo-nitrides have all been tested within a reactor core. Gas buildup, however, did cause significant cracking problems with these fuels [27].

2.5.4 Zirconium Nitride

Zirconium nitride is a very hard and brittle ceramic material with an extremely high melting point. It is electronically and thermally conductive, and is a superconductor with a $T_{\mathbb{C}}$ of 12 K [34]. It is used primarily as an abrasive, but more and more interest is being placed in it for a tool coating similar to TiN. As a tool coating, it has performed better and

out lasted TiN [53]. It has a metallic shine when polished with a gold luster, which makes it suitable for very abrasion-resistant decorative coatings.

It is relatively easy to produce coatings by either PVD with post nitriding or direct CVD. Nitriding of the metal is accomplished by heating under either nitrogen or NH_4 gas. Chemical method based on reduction of salts have been used to produce high-quality ZrN. Commonly, and most economically, ZrN is produced by the carbothermic reduction process. This reduces ZrO_2 by mixing it with carbon and running nitrogen and hydrogen across the sample at high temperatures. Oxygen is stripped away by the H and C, producing H_2O, CH_x and CO_x, while the nitrogen is taken up and nitrides the reduced metal.

2.5.4.1 Phase relationships

Zirconium nitride has three crystal structures between pure zirconium metal and the 1:1 stoichiometric ZrN. Although the β phase exists only at higher temperatures, when present it seems to play a role in accepting the nitrogen into the metal. Greater levels of nitrogen than 1:1 have been reported, yet most agree that the NaCl crystal structure cannot sustain more than a 1:1 ratio. Several forms of phase diagrams are shown in Figure 2.15 and 2.16. At a N/Zr ratio of ≥ 1.33, the Zr_3N_4 phase forms, which is grey and an insulator. N/Zr ratios of up to $\cong 2$ have been achieved by plasma sputter deposition of zirconium with nitrogen gas [54, 55]. The actual amount of dissolved nitrogen vs nitrogen bubble concentration is in question.

Zirconium metal is hcp in structure which has not been shown to dissolve nitrogen readily. At 865°C, the structure changes to the β (bcc) phase. It has been shown by experiment that nitrogen is more easily dissolved in the β phase relative to the hcp phase. The phase diagram shows that, as nitrogen is dissolved, the structure is transformed back to the α (hcp) phase with nitrogen dissolved in this structure [57]. Little information is available in

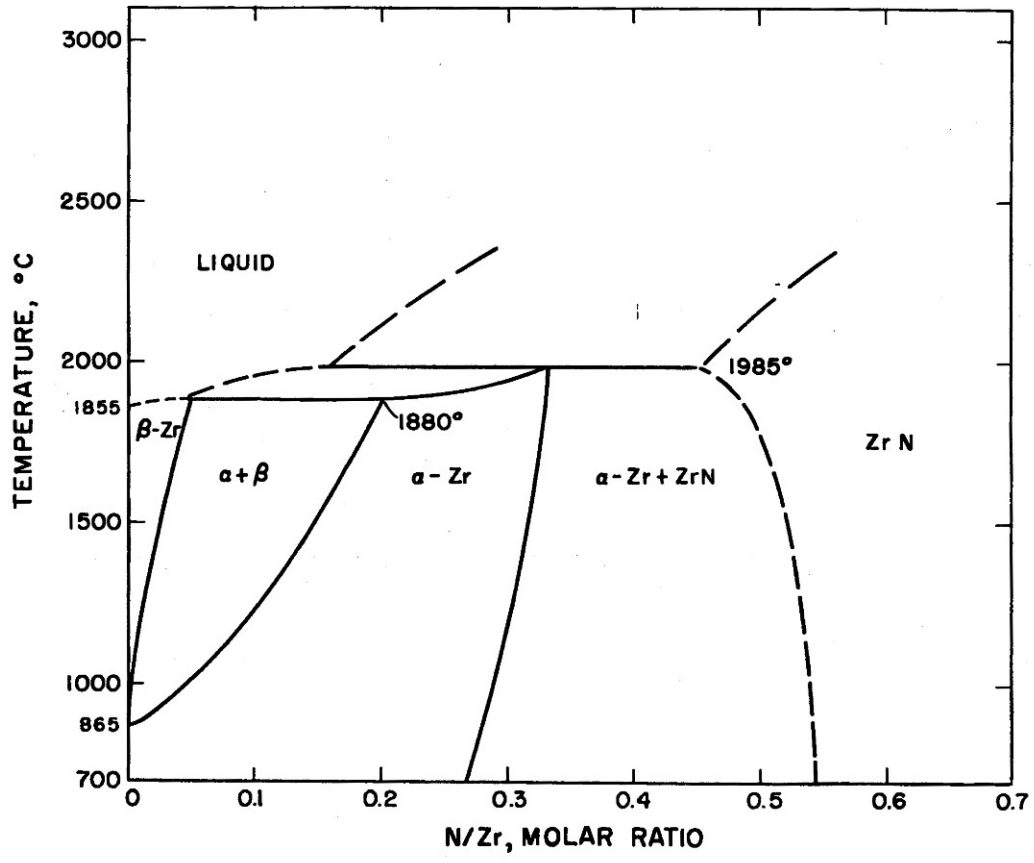

Figure 2.15: Phase diagram for the Zr-N system (N/Zr)[34]

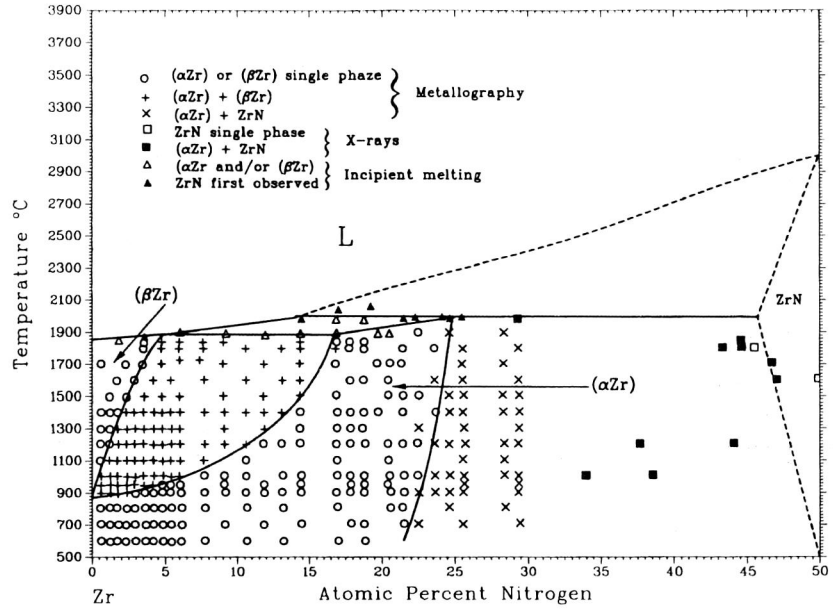

(a) Phase diagram showing relevant experiments. Note the stabilty of the α phase at higher nitrogen levels.

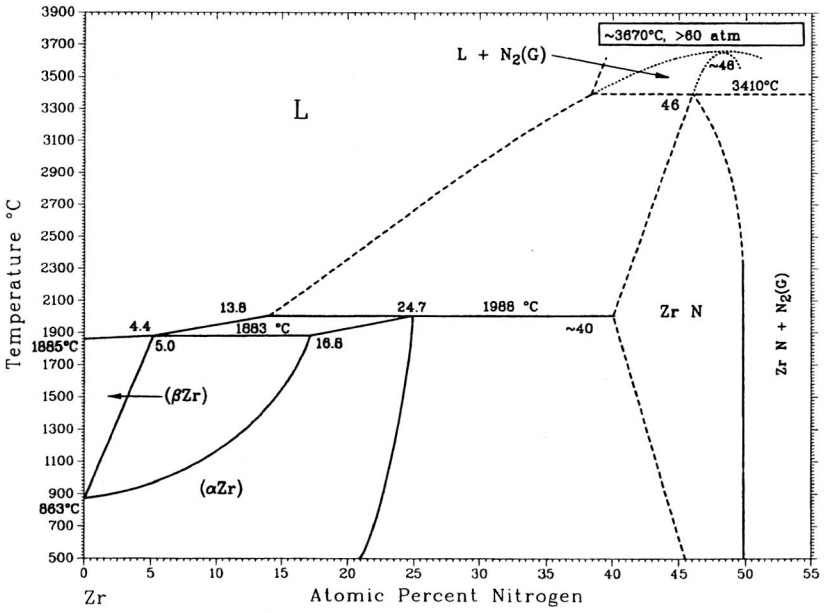

(b) Recent phase diagram showing the high 45 percent nitrogen content lower limit for the cubic phase. Note the strict upper limit for nitrogen concentration at 50 percent at which it is then contained as dissolved gas.

Figure 2.16: Phase Diagrams for the Zr-N system (atomic% nitrogen). Note the experimental and thermodynamic predictions for the α and cubic phases. [56]

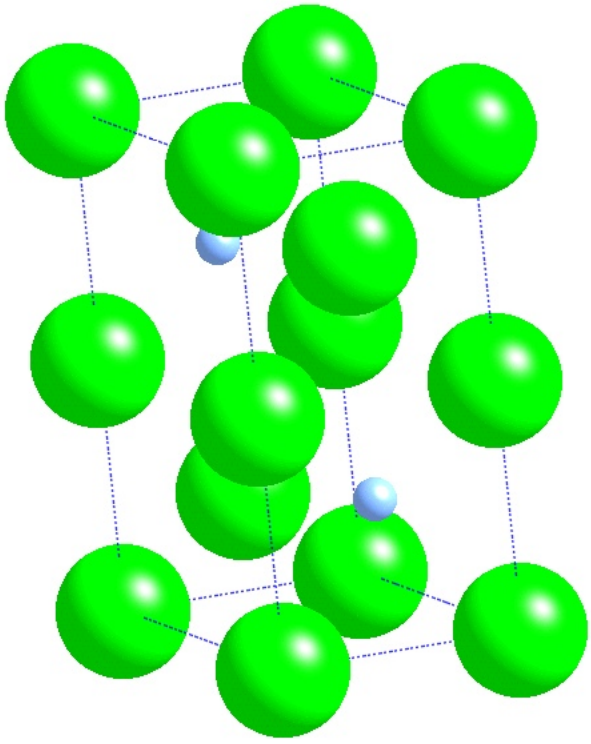

Figure 2.17: α-ZrN with dissolved nitrogen in the interstices

the literature on the nitrogen-dissolved α phase.

Following the Engel-Brewer theory on alloy phases, the nitrogen inclusion into the zirconium lattice seems to have more of an effect on the structure than a simply dissolved element. At higher temperature, ZrN moves from bcc to hcp and then fcc with increasing nitrogen, increasing symmetry up to the 1:1 Zr:N ratio. It follows the nitrogen's *s* and *p* electron orbital contributions to the transition metal's *d* orbital and thus energy is reduced with a change of symmetry [58].

It has been suggested that Zr metal and ZrN are highly catalytically active. The cubic form of ZrN has shown some catalytic activity for hydrocarbons, although other cubic nitrides have been studied more extensively [59, 60, 61, 62].

At a Zr/N atomic ratio of ≈ 0.27, or 21 atomic % nitrogen, the α phase starts to trans-

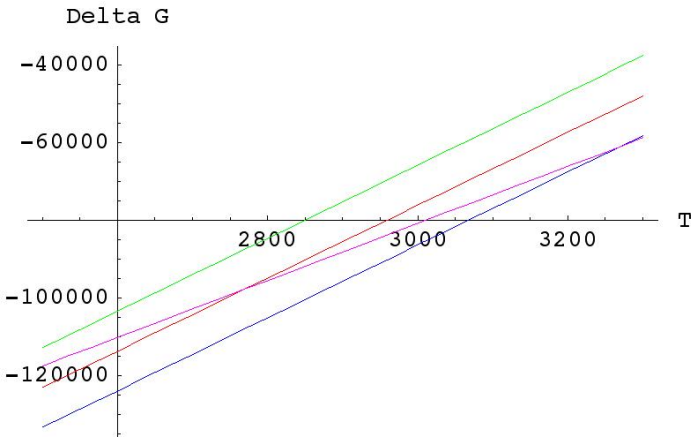

Figure 2.18: Gibb's free energy change for different phases of ZrN vs. temperature. (Red is hcp, green is bcc, blue is fcc and lavender is liquid)

form into the cubic phase. This is completed by a ratio of 0.54, which is approximately 35 to 45 atomic % nitrogen[1]. The Gibbs free energy of formation of the cubic phase is more negative than that of the hcp. (See Table 2.1 and Figure 2.18) [52, 63, 34, 6, 64].

Table 2.1: Free Energies of Formation (with respect to hcp zirconium metal) [64]

Species	$\triangle G_{\mathrm{f}}^{\circ}\,(J \cdot mol^{-1})$
hcp Zr	0
bcc Zr	3940 - 3.475T
fcc Zr	3350
Liquid Zr	24870 - 13.315T
hcp ZrN	-357443 + 93.789T
bcc ZrN	-347160 + 93.789T
fcc ZrN	-36765 + 93.789T
Liquid ZrN	-300411 + 73.222T

This cubic phase is the NaCl structure with a nitrogen-deficient sublattice. Some metal

[1]This phase transformation line has been debated, and depending on the literature, the upper α boundary may be as high as 45 atomic % nitrogen. From experience, it is expected to be at the lower value, but one has to wonder if the boundary is different due to being metastable in one direction or the other with respect to nitrogen concentration. Local domains are observed with near 33 % N that appear as short-range-ordering of the vacancies. This is common in high vacancy concentration cubic carbides and nitrides.

sublattice vacancies are observed. The nitrogen fills the sublattice easily and yet it seems to be difficult to obtain true 1:1 stoichiometry in ZrN (and other cubic nitrides) [34].

Of interest is the ordering of vacancies formed with the loss of large amounts of nitrogen. Near the α-cubic transformation line, the nitrogen vacancies have a tendency to form short-range ordered superstructures. This is a common occurrence and has been observed in many cubic carbides and nitrides [65, 66]. Recently, however, ZrN has been characterized to show this effect. TEM images show the short-range ordering producing the typical "diffuse scattering" patterns. The structure has been theorized as being a stacked set of NaCl unit cells with an ordered array of missing nitrogen atoms. The result is a possible I4/amd or $I4_1$/mmm space group lattice [65].

2.5.4.2 Cubic Nitride Crystal Structure

Stoichiometric zirconium nitride has the NaCl crystal structure (refer to Figure 2.21) with quite a large stable variability on the nitrogen sublattice. ZrN_{1-x} is a standard method of denoting the sub-stoichiometry on the nitrogen sublattice, where x=0 is considered 1:1 stoichiometric. It is a Hägg nitride, which is a classification based on a radius ratio similar to that which Pauling used. Hägg classified structures formed by carbides, nitrides, borides and hydrides according to radius ratios. Carbides and nitrides fall into a NaCl structure if the ratio of nitrogen or carbon to metal is less than 0.59.

Many lattice parameters and densities have been measured in the literature. The variability seems to stem mainly from the nitrogen loss, although oxygen and carbon content can play a role. The intrinsic vacancy concentration is high and, even at 1:1 stoichiometry, there are vacancies on both sublattices.

Zirconium has an electronegativity of 1.33, and by Pauling's method of calculating ionicity of bonds, the result is 48 % covalent (refer to Figure 2.19). Pauling did not take

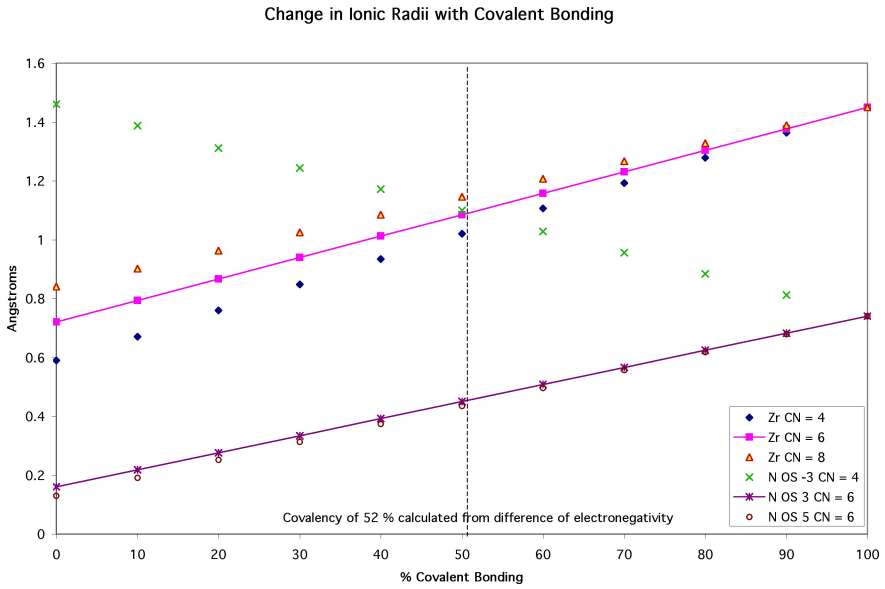

Figure 2.19: Ionic radii with differing ionic-covalent bonding

into account mixed bonding with metallic character, which does play a large role in the transition metal cubic nitrides [34, 67, 68, 69, 70, 42, 71, 72, 73, 74]. This result does help characterize, in a subjective manner, the bonding characteristics between the metal cation and the non-metal anion. The partial ionization produces Coulombic interaction, which, unlike true ionic salts, is less spherical in symmetry and is heavily directional. The covalent nature produces the directionality due to valence electron wave overlap, and the electronegativity difference produces a polarized bond, in which electrons spend more time on the more electronegative atom. This helps increase to the bond strength by not only having shared electron bonds to be broken, but also the Coulombic attraction [58, 74, 75].

The bonding models have never been truly correlated by experiment and theory so that there is universal agreement. Most individual attempts to produce a bonding model have resulted in disagreement due to a particular physical property. Thus, as of yet, there is no standard model to explain all the properties of the cubic transition metal nitrides.

The bonding model that meets the needs used in this document is the Engel-Brewer

electron counting method [58, 63, 76, 34, 77]. Although not widely acknowledged, it is a modification of the Hume-Rothery set of rules for alloys. The Hume-Rothery rules are, like the Pauling radius-ratio rules, a correlation approach to explaining certain phase relationships and properties of mixed element materials. The weaker aspect of the Hume-Rothery rules is with the early transition metals where some properties are not well correlated. The Engel-Brewer theory, on the other hand, uses a similar electron counting scheme with a different approach. The Hume-Rothery rules count all the *s*, *p* and *d* electrons and correlate them to structure predictions. The Engel-Brewer method uses only the *s* and *p* electrons.

By assuming that the *d* orbitals are lower in energy and thus contribute less to bonding than the *s* and *p*, this model has worked well. It acknowledges the *spd* hybridized orbitals, yet the *s* and *p* electrons are the ones used for conforming to a structure. In this theory, the *s* and *p* electrons are counted and shared between atoms. By correlating the *s* and *p* valence electron count to structure, Engel produced a pseudo-bonding model for transition metal alloys. The average *sp* electron count correlates to the *p* character of this bond and thus the *sp* hybridization character. The structures predicted are bcc with an averaged electron count of less than 1.5, hcp with a count of 1.5 to 2.1, and ccp with a count of 2.5 to 3. Of course these numbers are not absolute as there are many variables to consider. They do, however, give a nice predictive capability with a simple model.

For the most part, it works quite well, and, in the case of the nitride ceramics, produces fairly consistent results. An example of the cubic nitrides, specifically ZrN, is shown in Figure 2.20. Based on a total *sp* count of 2 for zirconium and 5 for nitrogen, the average electron count is plotted. It can be seen that, at pure zirconium metal, the count is 2 and thus predicts the metal being hcp. At approximately 34% nitrogen, the electron count is 2.5, which is fcc. Compare this to the ZrN phase diagram and observe the close phase correlations (Figure 2.15). Between 2.1 and 2.5 is the phase transition space which resembles

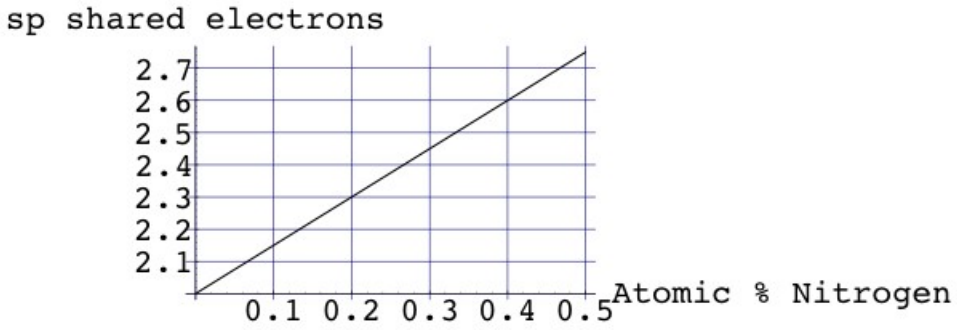

Figure 2.20: Engel-Brewer model of ZrN, from N = 0 to 50 atomic %

the phase diagram again.

This model does not fully explain all properties, nor is it considered a physical explanation, just a simple correlation of numbers. It does work well in most cases and provides insight to the real bonding. For transition metals, the approach is simplified for the first few groups due to the *spd* hybridization orbitals. Brewer notes that the d^{n-1} *sp* orbital is near the same energy as the d^{n-2} *s* orbital, (n is the total valence electrons for *s*, *p* and *d* orbitals), for the first few groups, and thus the hcp or bcc structures are stable. The right side of the transition metals are more complex, yet they are predicted well with simple electron counting rules helped by knowledge of the orbital energies.

Although the model does not prove how the bonding actually takes place, it makes assumptions that parallel some physical properties observed. It is assumed that the *s* and *p* orbitals dominate bonding due to the higher energies, while the *d* orbitals do not contribute to the structure determination. Yet, they are assumed to contribute to short-range bonding between the *d* orbitals of the adjacent metals. Metallic conductivity can be attributed to

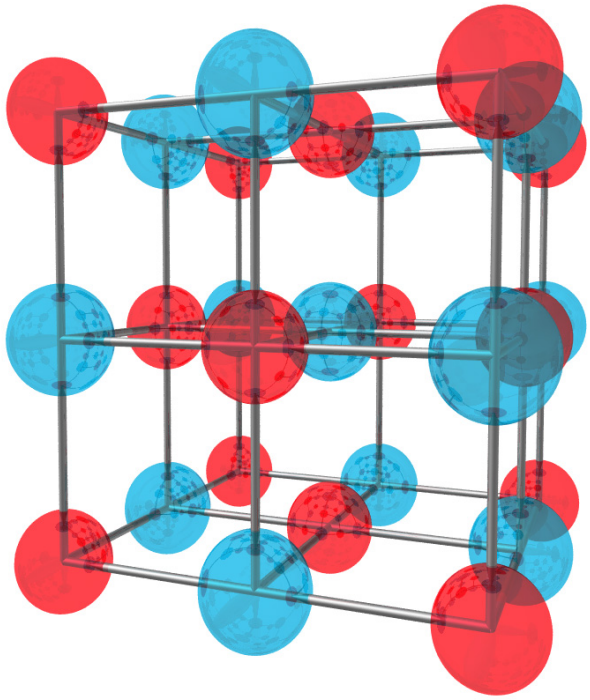

Figure 2.21: NaCl crystal structure

these inter-metal bonds.

As a simplified example, ZrN is constructed with the hard-sphere model into the NaCl structure. The coordination numbers for zirconium and nitrogen are both 12. Nitrogen sits in the octahedral interstices of the zirconium fcc lattice, which itself forms an fcc sublattice. The lattice parameter listed is approximately 4.57 Å. An ionic model is used with the ionic radius of zirconium being about 0.75 Å, while that of nitrogen is about 1.45 Å. Refer to Figure 2.19 showing the ionic radii change with increasing covalent bond characteristic. This chart, along with the Pauling ionicity calculation, indicates both ionic radii to be about the same, about 1.1 Å. The lattice parameter of the cubic structure is then the sum of twice the radii for each element. This sums to 4.4, a bit short for this structure. The first problem is that the ionic radii for nitrogen are set at the oxidation of -3, when it should be -4 to match the +4 oxidation state of zirconium. If an unlisted oxidation state of -4 is assumed

for nitrogen, this would increase the size somewhat. The second problem is that the -3 oxidation state is a 4-coordinated nitrogen whereas in this structure it is 6 coordinated. Observation of the other nitrogen oxidation states indicates, however, that the coordination number makes little difference to the size.

The third problem is the size ratio, even when the nitrogen is made slightly larger to match the lattice parameter, say 1.15 to 1.2 Å, it is still the approximate size of the metal. The radius ratio then becomes very close to one. Pauling's rules state that the radius ratio should be between 0.732 and 0.414 to form the ccp (cubic close packed) or NaCl structure. The ratio of less than 1 to 0.732 gives the bcc or CsCl structure. To add more confusion to this simple problem, the Mullikan population was calculated for ZrN to be approximately 1.4, which takes into account other factors such as metallic bonding. This lowered oxidation state of zirconium is matched by nitrogen for electronic neutrality, and thus the size of zirconium increases and of nitrogen decreases.

This information results in a hard-sphere model with zirconium larger than nitrogen. With the lattice parameter and Pauling's rules as a guide, the atomic size of zirconium is guessed at $\approx$ 1.35 Å. For the lattice parameter of 4.57 Å, a guessed size of nitrogen would be 0.94 Å and the radius ratio is then 0.69, making a 12-coordinated NaCl structure. This is somewhere near the 75% covalency according to the Pauling chart.

To pursue the atom size issue in a different way, the fcc lattice, the metal being the large atom, is the close-packed plane. Thus the radius of the zirconium is $4.57\text{Å}\frac{\sqrt{2}}{4} = 1.616\text{Å}$ (Refer to Figure 2.22). This gives the radius of nitrogen to be about 0.67 Å and a radius ratio of 0.414, which is still in the NaCl (fcc) limit. This model suggests that the nitrogen atoms are very covalent in character. The Mullikan population is considered as the probability of the electrons spending more time about one atom than the other, effectively polarizing the bond. The electrons are covalent as they are shared, but this uneven sharing gives a net

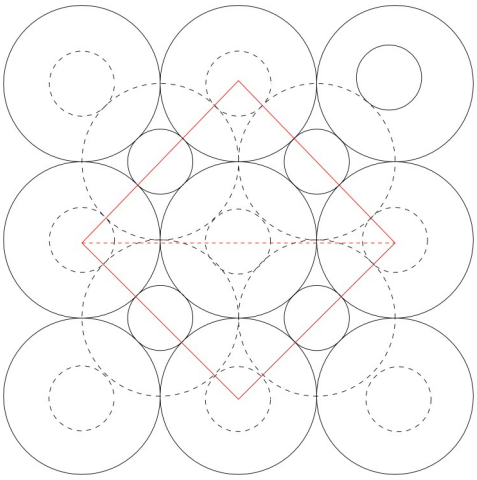

Figure 2.22: NaCl lattice 001 face. Note the red dotted line from edge to edge is connecting the large metal atoms, which is $\sqrt{2}a$.

charge to the elements involved.

The hard-sphere model based on the larger metal atom, indicates that, since the metal comprises the close-packed plane, metal-metal bonding is important. The nitrogen sublattice is not close packed due to its size, and its only bonding is to the metal. To relate to Engel-Brewer, the metal-metal bonds allow for metallic conductivity but are not strong enough to dominate the structural characteristics.

As listed above, the literature lattice parameter and density are 4.537 Å and 7.22 $\frac{g}{cm^3}$. These vary greatly, with the 73^{rd} Edition of the Chemical Rubber Companies (CRC) Handbook of Chemistry and Physics listing 4.567 and 7.09 $\frac{g}{cm^3}$ [78]. It has been found that decrease in nitrogen content actually causes the lattice to expand. Figure 2.23 shows a compilation of data that illustrates this. More recent and careful work usually includes the stoichiometry and, while a true 1:1 Zr:N ratio is very difficult to get, most quality work is accomplished on $ZrN_{0.99}$. Because of the difficulty in measuring nitrogen content, some error is involved. Direct measurements on the superconductivity provide a sensitive method to determine stoichiometry. Due to the nature of superconductivity, small decreases in

nitrogen content greatly change these properties, such as T_c [34, 79, 44].

2.5.4.3 Physical Properties

Known physical properties of ZrN have been reported for decades. The variability in these reports is astounding and due primarily to non- or mischaracterized ZrN_{1-x} stoichiometry [34]. Based on more current and better characterized reports, a list has been compiled (see Table 2.2) [20, 77, 34]. The large variability in properties has been strongly correlated to stoichiometry, being the reduction in nitrogen content and also dissolved oxygen and carbon. Oxygen and carbon are residual products from the carbothermic reduction process. ZrN readily oxidizes at elevated temperatures, and ZrO_2 is a known oxygen conductor and thus offers no protection from further oxidation.

Mechanical properties of ZrN, specifically its hardness and modulus, are explained not only by its crystal structure and bonding, but by the microstructure and defects that occur. Dislocations formed by mechanical disturbance or from lattice mismatch with a precipitate, etc., have also been observed. At room temperature and above, the stacking-fault energy is very high due to the highly covalent bonds. Recently work has been performed to show that dislocations are Shockley partials formed from the perfect $\frac{1}{2}\langle 110\rangle\{111\}$ [46]. These partials are $\frac{1}{6}\langle 112\rangle$ superjogs, and are typical for fcc materials of this nature. The material used in this study, however, was a low-nitrogen-content cubic form, such that the stacking-fault energy was reduced dramatically. Due to the low SFE, the dislocation partials spread a large distance with a stacking fault between them. From this distance, the SFE was measured to be near 5 eV. The SFE, however, has been shown to be very sensitive to the vacancy concentration, specifically within the nitrogen sublattice. The SFE for carbides and nitrides can vary from 180 eV to 5 eV within the relatively small phase field [80, 81].

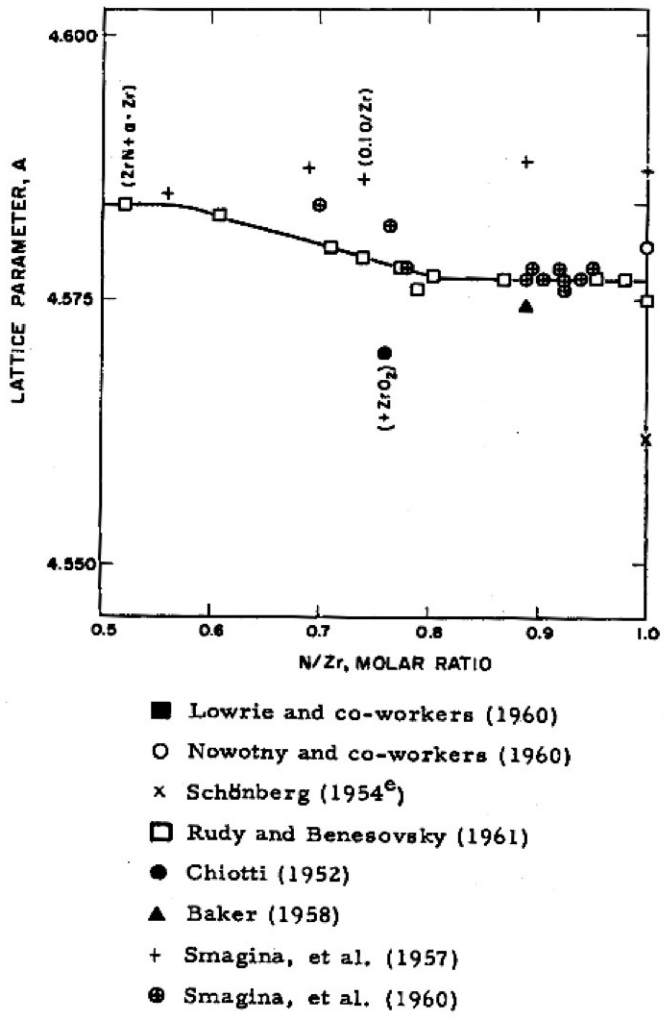

Figure 2.23: Lattice parameter change with changing nitrogen content [34]

2.5.4.4 Radiation Tolerance

Very little radiation-tolerance research is available for ZrN. High doses of argon were implanted into ZrN thin films with residual stress measurements made by GIXRD. Up to $4 \times 10^{16} \frac{Ar}{cm^2}$ at 100 keV was implanted, which produced up to 12 atomic % argon in the lattice. The result was a slight reduction in lattice parameter [53, 82].

Cobalt was implanted with a very high fluence of $1 \times 10^{17} \frac{Co}{cm^2}$ at 100 keV and at cryogenic temperature, in both AlN, and ZrN [83]. AlN will amorphize at this fluence, while ZrN remains crystalline. Annealed at 800°C for 1 hour, Co coalesced into Co clusters; Co does not form a nitride and thus will diffuse to lower its overall energy. Cartz used powders for irradiation with 3 MeV Kr with fluences up to $2 \times 10^{15} \frac{Kr}{cm^2}$, which reduced the XRD peak intensities and rounded the edges of the powders.

Neutron irradiation has been performed at moderate neutron flux densities. The only measure was a slight change in electrical resistivity [84, 85]. Compared to ZrC and NbC, ZrN had a slight decrease in resistivity, while the carbides showed a slight increase.

2.5.5 Titanium Nitride

Titanium nitride (TiN) is a common material used as an abrasive and hard tool coating. It has been used as an abrasion-resistant decorative coating that has a gold-tone appearance. Most commonly seen on coated drill bits and other hard-surface machining tools, the cost of production of this coating has made it very affordable to use for more common tasks. Titanium is plentiful in certain regions of the world, such as in Russia. As a coating, it nitrides relatively easily and is more often used this way.

TiN has been the subject of much research and is similar in many respects to ZrN, yet there are many distinct differences. TiN has a phase diagram similar to that of ZrN

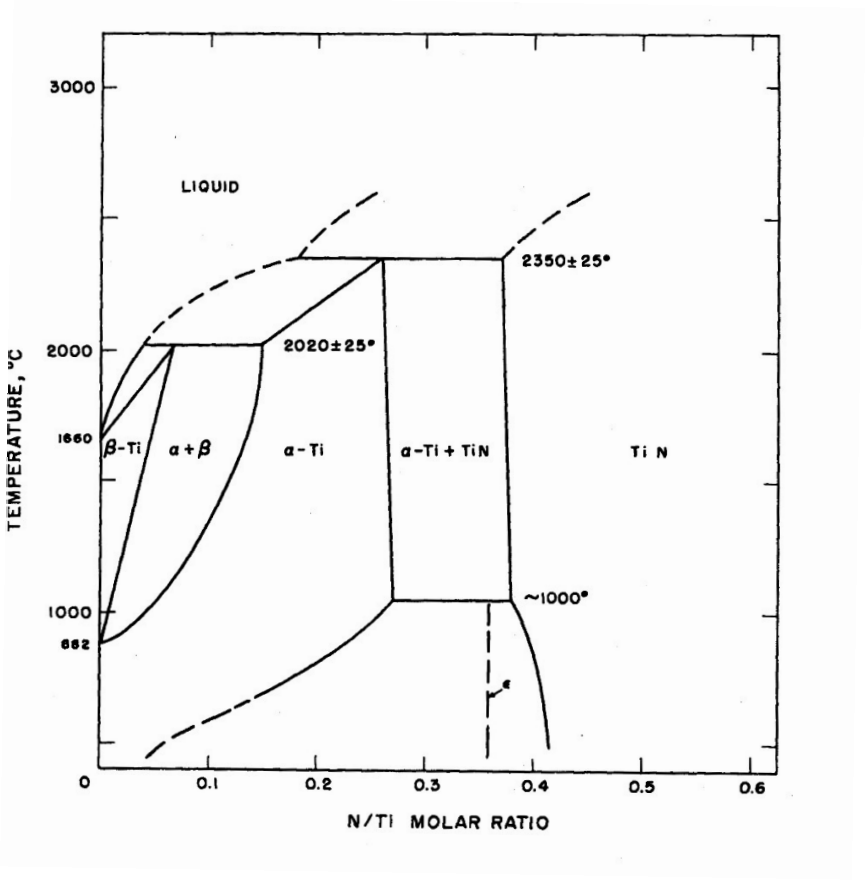

Figure 2.24: TiN phase diagram [34]

(refer to Figure 2.24). It has one major difference in that it has a line compound formed at approximately 0.36 N/Ti ratio with the ϵ crystal structure. This line compound is a constituent of the different low-temperature mixed phases, mixing with either α or the NaCl phase of TiN. There are both sub- and super-stoichiometric phases of titanium nitride, which have vastly different properties. It seems that cubic TiN can be super stoichiometric with respect to nitrogen, which is different from ZrN and HfN, which are isoelectronic.

TiN has the NaCl cubic structure, which is common for most transition metal nitrides. It is well studied due to its prominence in industry. Like the other cubic nitrides, it has intrinsic vacancies on the nitrogen lattice and is difficult to characterize. It follows Hägg's

rules for nitride structures as well as the Engel-Brewer theory.

The difference in properties between ZrN and TiN is due to the one direct difference between Zr and Ti, which is size. Titanium is a small atom with a much higher charge concentration. It is more electronegative as a result, which causes the Ti atoms to polarize the bonds between Ti and N more extensively. This shifts the ionicity of the bonds, reducing both the metallic and covalent nature. This characteristic allows titanium nitride to produce a greater variety of phases.

2.5.5.1 Physical Properties

TiN is a hard, refractory material with general nitride properties. It has a golden color, is electrically and thermally conductive, and has excellent abrasion resistance. It is a superconductor with a reasonably high T_c. It is similar in many ways to ZrN and HfN as they share the same electronic structure. Table 2.3 shows a summary of some of these properties [76].

2.5.5.2 Radiation Tolerance

The radiation tolerance for TiN has probably had the most attention of the transition metal cubic nitrides due to its heavy use in industry. Perry has shown that TiN withstands much radiation damage from argon with 100 keV implant energy and up to $4 \times 10^{16} \frac{Ar}{cm^2}$ [86]. Perry also found surface damage with lower-energy implantation of argon of the same fluence and up to $1 \times 10^{17} \frac{Au}{cm^2}$ at 20 keV [87, 82]. Transmission electron microscope investigations and grazing incidence x-ray diffraction depth profiles showed that, with the implanting of large doses of a heavy ion, the damage profile reaches far beyond the boundaries of displacement damage or implant [88, 89, 87, 86, 53, 90, 91, 92, 93, 94, 82, 95, 96]. This damage reaches up to 10 times the depth of the damage profile predicted by TRIM (an

irradiation damage/depth simulation program).

2.5.6 Silicon Nitride

Silicon nitride is a common abrasive material used in industry. It is inexpensive to produce and is extremely hard and brittle. In pure form it is transparent with a green tinge, although it is commonly seen as a black powder used for abrasion, similar in use to SiC. It melts (decomposes) at about 1850°C. $\beta-Si_3N_4$ is the standard phase for industrial use. It has a hexagonal crystal structure, with the space group $P6_3$.

Si_3N_4 has withstood 3 MeV Kr with a fluence of $2 \times 10^{15} \frac{Kr}{cm^2}$ (150 dpa) at cryogenic temperatures. At slightly higher temperatures, at or above room temperature, Si_3N_4 has been shown to amorphize easily with 1 or 7 dpa [97].

2.5.7 Aluminum Nitride

AlN is a ceramic used in the electronics industry. It is used for its high thermal conductivity while having high electrical resistivity. It has the wurtzite structure, similar to GaN. It is relatively hard and mechanically strong, which is why it its primary use is for circuit-board substrates. With high radiation tolerance, it is a candidate to be used in components of a fusion reactor.

Neutron irradiation studies were performed to determine the neutron irradiation tolerance of AlN for use near fusion reactor cores. High doses of neutrons were used, of $4 \times 10^{20} \frac{Neutron}{cm}$ at elevated temperatures [98, 99]. It has a very low swelling ratio at this fluence, and responds well to annealing. Compared with Al_2O_3, AlN is very different. Alumina swells dramatically under irradiation and thus is not considered for use near a reactor.

Irradiated with 3 MeV Kr with a fluence of $2 \times 10^{15} \frac{Kr}{cm^2}$ (150 dpa), AlN remained crystalline [100]. At very high doses of Co ($1 \times 10^{17} \frac{Co}{cm^2}$), AlN amorphized [83].

2.5.8 Gallium Nitride

Gallium nitride is of great interest to the electronics industry due to its high-frequency light output for lasers, LED's, etc. GaN is a hard, brittle material much like other nitrides. GaN has the hexagonal wurtzite structure and is a semiconductor with a band gap of 3.4 eV.

GaN has been irradiated with many ions, generally for the purpose of electronic property modification. The limit to and the understanding of these important properties and how they relate to the damage produced is strongly desired. Post-irradiation annealing studies have been performed to observe how well GaN recovers from the defects induced.

GaN shows a remarkable ability to self-heal, or "dynamically anneal" the defects while under irradiation, although loss of nitrogen from the surface has been a problem. It has been considered that the surface is a strong sink for mobile defects under irradiation. This may allow nitrogen to break free under irradiation. GaN forms a band of point defects, and, with higher doses of irradiation, forms planar defects. It is thought that the planar defects are a nucleation point for amorphization [101, 102, 103, 104].

Light-ion irradiation does not produce significant damage. With increasing energy, heavy ions, such as Au, produce more damage. With increasing temperature, damage accumulation is decreased. Irradiation-induced porosity with higher levels of damage have been observed in both the crystalline and amorphous structures. It is considered that the displaced nitrogen is the main contributer to the bubbles formed, and not the gas implanted. GaN is considered highly ion-damage resistant due to a high degree of damage build-up before amorphization. GaN amorphizes at fluences approaching $1 \times 10^{16} \frac{Au}{cm^2}$ [101] or greater

than $5 \times 10^{16} \frac{Ar}{cm^2}$ [105, 106]. Lattice parameter swelling has also been measured by x-ray diffraction up to amorphization [107].

2.6 Radiation Damage

This discussion on radiation damage has been simplified for general understanding of both the ballistic cascade and the subsequent kinetic effects. Refer to Appendix D for a mathematically based primer.

The damage in a material caused by radiation can be classed by the type of energy transfer and the resultant implantation volume effects [108, 109, 97, 100, 110, 99, 111, 112, 113, 114, 115, 116, 117]. Gamma radiation, which is not covered here, produces little damage in the materials of interest. Gamma rays are released with about 7 MeV of energy. Both α and β particles are produced in quantity by their respective decay cycles. β decay produces low momentum electrons while α decay produces energetic helium nuclei with energy of about 6 MeV [12].

Scattering of a neutron may be elastic or inelastic. Elastic scattering is scattering in which no energy is transferred from the neutron to the nucleus internals. Inelastic scattering transfers some energy and leaves the nucleus in an excited state. The excited nucleus lowers itself to the ground state by emitting subparticles and/or γ rays. Very light atoms produce elastic scattering events easily but do not produce more neutrons or particles. Momentum is conserved by the recoil of the nuclei. This interaction is purely ballistic and the neutron is reduced in energy. Light atoms, such as H, O and C are used as moderators due to this effect. They can slow the neutron enough so that the energy is near equilibrium with the nuclei of the fuel. These moderated, or thermalized, neutrons have a much higher cross-section with ^{235}U to produce fission events [24].

2.6.1 Theory

The fission of an atom produces an incredible amount of energy. Much of this energy is deposited in the expulsion of neutrons and fission products. Fission products are produced with an energy range of approximately 70 to 100 MeV each. The products are heavy, the sum of the two equaling the original fissioned element. In the case of UO_2 fuel in a typical LWR, the distribution appears like that shown in Figure 2.8 [25, 12, 27]. Fission products of the transuranics are similar in distribution although there is a slight shift in mass and energy. Transmutation with fast neutrons decreases the depth of the center well.

2.6.1.1 Fission Product Trajectory, Energy Loss, and Stopping Power

The fission product is then moving through the lattice at high velocity. The fission product element is stripped of many of its electrons and thus becomes a moving positively charged particle. This particle interacts with the lattice around it in two ways, by Coulombic force and electronic interaction force.

As an ion is moving through the lattice it encounters atoms on lattice sites. If the distance of approach is small enough, interaction will occur. The distance of interaction is an important parameter due to the electronic interaction forces. The amount of interaction is dependent upon the distance of interaction. As the velocity slows, the time spent near these electrons increases, thus interaction increases and thus there is the transfer of energy. As the velocity slows, the time spent near these electrons increases, thus stopping increases. At larger impact distances, the main interaction is dominated by the Pauli exclusion principle, whereby the electrons cannot share the same shell and spin. At closer impact distances, the interaction is Coulombic in that the nuclei repel each other strongly (refer to Figure 2.25).

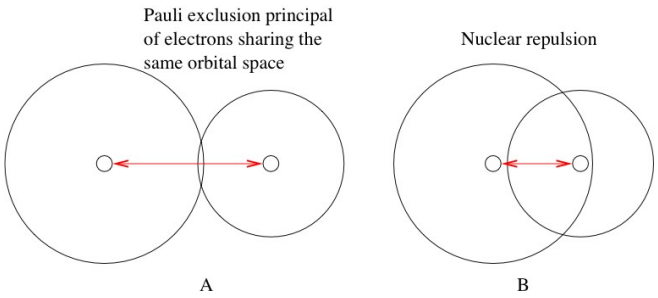

Figure 2.25: Interaction between a moving ion and a lattice atom. A represents a large distance between nuclei with electrons attempting to share orbitals, B indicates the nuclear repulsive force at smaller distances

2.6.1.1.1 Bethe-Bloch Interaction At very high velocities, the ion is stripped of all of its electrons and is a highly positively charged particle. This Bethe-Bloch stopping occurs at velocities that are greater than that of the average electrons in the lattice orbitals. The positively charged nucleus perturbs these electrons and thus there is the transfer of energy. As the velocity slows, the time spent near these electrons increases, and thus stopping increases. When the velocity slows to about the speed of the electrons, the Bohr velocity, the nucleus will obtain electrons from the lattice by ionizing passing atoms. When the nucleus pulls electrons from the atoms around it, the resultant wake of ions formed repel each other and move away in what is termed a Coulombic explosion (refer to Figure 2.26) [25, 118].

2.6.1.1.2 Electronic Interaction By gaining electrons, the ion then has electrons that can interact with atomic shells. The Pauli exclusion principle states that the electrons cannot share the same position and spin. Forced together, the passing ion's electrons and the atomic electrons strongly repel, adding energy to atomic electrons and causing them to jump to a higher state. This being an inelastic collision event, energy is only transfered to the electrons. The jump back to the ground state will produce either photons or phonons. As the ion further decelerates from the Bohr velocity, this effect is less efficient.

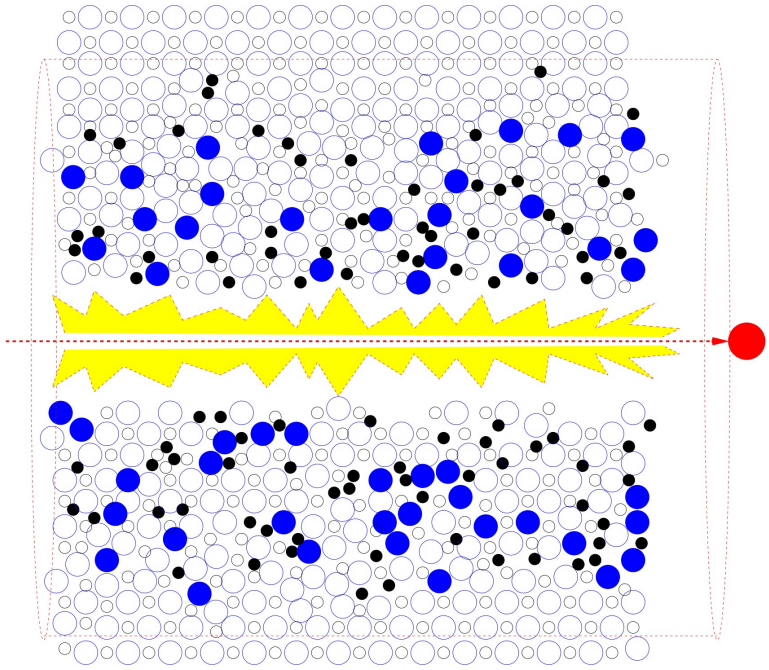

Figure 2.26: Coulombic explosion. Solid circles are displaced atoms

As a moving positive ion in a system of cations and anions, the interaction may be attractive or repulsive at larger distances, both approaching and leaving. These interactions may be inelastic in that there is no true energy transfer. The electron clouds may produce a "drag" on the moving ion, which helps decelerate it. The elastic collisions, which cause some kinetic energy transfer, help decelerate the ion more.

The entire electronic stopping regime releases much energy, proportional to the energy lost by the particle. The target atoms, either excited enough for displacement or ionized strongly to produce an instantaneous repulsion, release the extra energy through photon or phonon emission. The strong destructive forces produced during electronic interaction are found as "fission tracks" in swift ion irradiations (very high velocities).

2.6.1.1.3 Nuclear Interaction When the ion slows enough that the electronic interaction is low, the nuclei begin to approach each other without screening electrons. This

Coulombic interaction is the nuclear repulsive forces. The energy transfer is from nucleus to nucleus. Figure 2.27 shows the relation of nuclear and electronic stopping power with respect to the velocity or energy of the ion. The left-hand edge is the ion at rest. Notice the electronic stopping is much more efficient than nuclear.

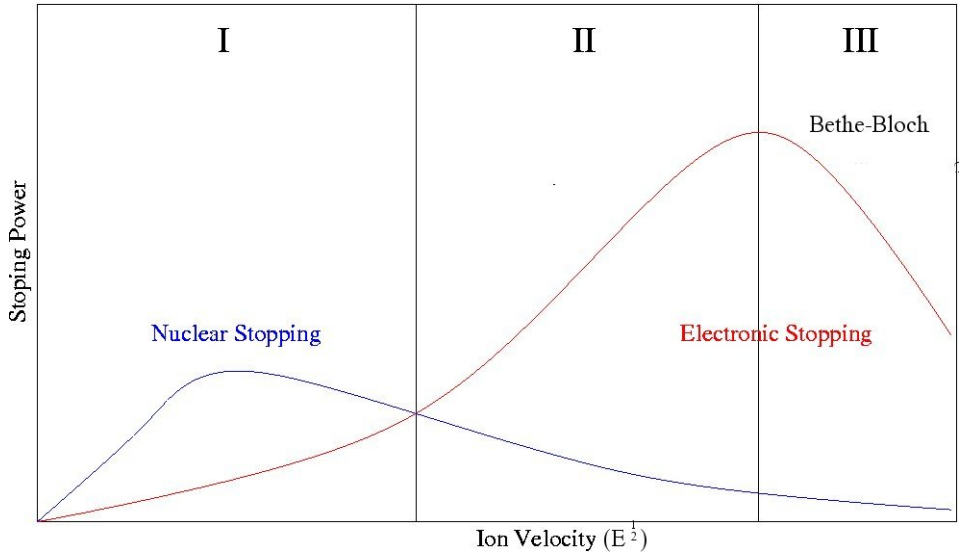

Figure 2.27: Stopping power of an high velocity ion/fission product in a lattice. Area I is nuclear stopping dominated, Area II is electronic stopping dominated, and Area III is the Bethe-Bloch region

2.6.1.1.4 Thermal Spike When the ion slows enough that it does not have the energy to displace an atom by collision, it will come to rest, either in a vacant atomic site or an interstitial position. Over the entire journey of this fission product, energy has been lost either to electrons or to atoms themselves through nuclear interaction. Each collision deflected the ion off its trajectory, while the atom of interaction, if it obtained enough energy to exceed the displacement threshold, was sent on its own trajectory. The atom displaced by the fission product is termed the primary knock-on atom, or PKA. If this atom displaces another atom, it is a secondary knock-on atom, or SKA. This cascade will continue to mul-

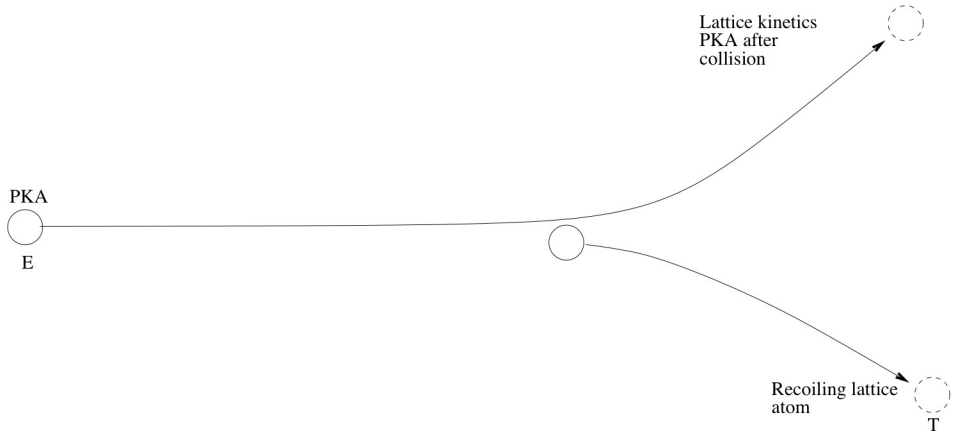

Figure 2.28: Two-particle ballistic collision

tiply, producing PKA's and SKA's until all the energy of the fission product is deposited in the lattice. As the fission product slows near its stopping point, it is near maximum nuclear stopping power and thus introduces the most PKA's and SKA's. These of course travel far less distance and deposit their energy by moving atoms until they stop. This end-of-range deposition of energy from the fission product is thus considered a thermal spike, as it produces a large amount of slow moving PKA's and SKA's that do not travel far from the end position [119]. This concentrates the thermal energy deposited by all the displaced atoms in a small area. This thermal energy is quickly quenched by the surrounding lattice.

2.6.1.2 Ballistic Collision

Elastic collisions are ballistic interactions of a two-body system. When one mass with a specific velocity strikes another mass, conservation of momentum requires that the recoil velocities of each sum to the original momentum. To take this idea further, the angle of impact promotes the angle of the recoils, as well as the energy transfer between the two masses (Figure 2.28).

On an atomic level, the masses can be imagined as hard spheres, which is commonly

done to simulate atoms in a lattice. When a fast-moving atom strikes a relatively non-moving atom, energy is shared by both and they each recoil by the conservation of angular momentum. The probability of a two-body interaction is the cross-section, or interaction probability per section of depth.

2.6.1.3 Kinchin-Pease Approximation

When the hard-sphere model for atoms is used, electronic stopping is ignored, and the same mass of each is assumed to be the same ($m_1 = m_2$), the Kinchin-Pease model provides a simplified yet fast mathematical model to predict stopping of atoms in a ballistic process. This simple model works satisfactorily for slowly moving ions with mass numbers that do not deviate much. It of course ignores high-velocity interactions with electrons.

The simple concept is such that a certain energy must be obtained by the target atom for it to be displaced (displacement threshold energy). Once this is obtained, the atom is displaced and the projectile has just enough energy to be a replacement. Twice this energy is required by the projectile to displace a second, and from there it assumes a linear relation with projectile energy $\left(\frac{1}{2E_d}\right)$ (Figure 2.29).

The Kinchin-Pease model has a tendency to overestimate the total amount of recoil-induced vacancies due to the linear nature of its assumptions. However, it does provide a fast estimation as to the extent of damage one may obtain with a certain amount of energetic particles.

2.6.1.4 Lindhard, Scharff and Schiott Theory

The Lindhard, Scharff and Schiott (LSS) theory provides for a more in-depth mathematical treatment of the irradiated collision cascade problem. Many approximations are not used, and hence the math is long and computationally intensive.

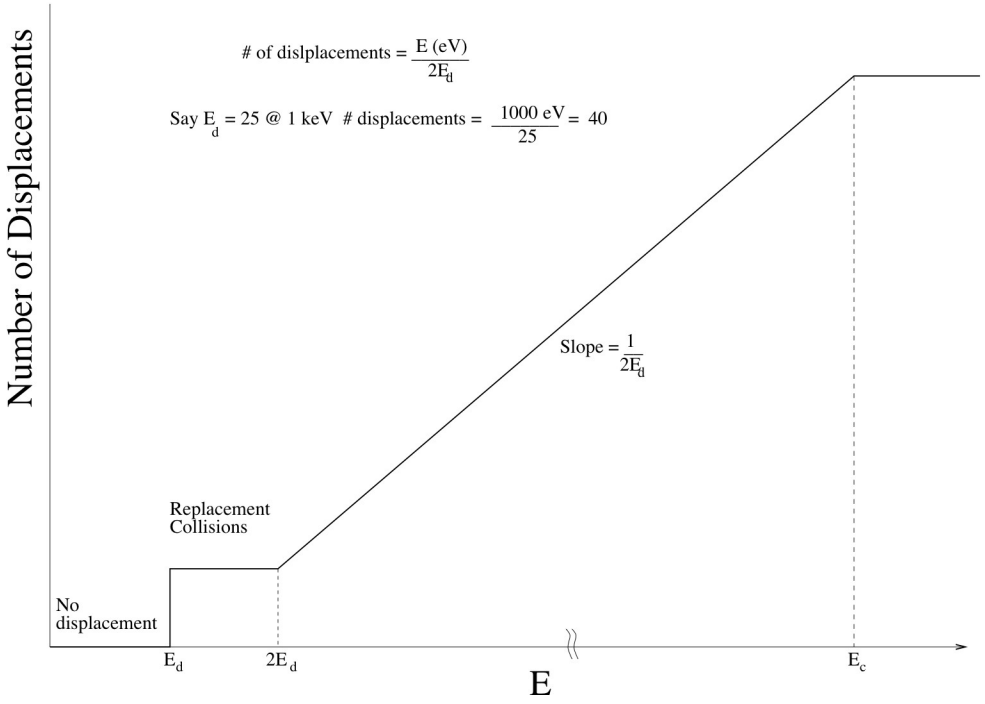

Figure 2.29: Kinchin-Pease model for displacements produced beyond the threshold energy E_d

LSS first uses the Fermi-Thompson screened potential instead of a hard-sphere approximation. This increases the complexity but also the accuracy for a wide variety of atoms and structures. LSS also includes electronic stopping potentials calculated similarly.

2.6.1.5 Ziegler, Biersack and Littmark Approximation

Ziegler and Biersack modified the LSS equations by introducing a universal potential. This is different from the screening potential used by LSS theory. Many theories have been attempted with different potential models. The ZBL modification is very common and is used with TRIM calculations [120].

2.6.1.6 Displacement Threshold Energy (E_d)

As the ion moves through the system it loses energy by exciting electrons through elastic collisions, or by inelastic collisions such as moving the electron clouds in proximity to each other in a way such that the electrons are attempting to share the same space, or by moving the nuclei close enough to each other that they repel each other by Coulombic repulsion. The velocity, the distance of interaction, the nuclear mass and the charges on each all play a role in the interactions. With any ballistic collision, energy is transfered via conservation of momentum. Displacement of an atom from its lattice site requires a specific energy.

The energy limit for momentum transfer is the displacement threshold energy, E_d, such that the target atom acquires sufficient energy from the collision to break its chemical bonds and to displace the surrounding lattice, in order to move through the lattice. Different lattice directions have different densities of atoms and as such have different E_d's. The average energy is generally reported, which is very generally considered to be near 25 eV for metals and 40 eV for ionic ceramics. These numbers vary widely, from as low as 5 eV to as high

as 90 eV [118].

2.6.2 Defects Produced by Irradiation: Initial Damage

Irradiation is a process of two-body interactions such that a projectile and a target interact. When the particle, either a neutron or an atom core, is slowed by electronic energy losses, nuclear collisions become the primary source of "stopping potential", i.e. the collision cross-section for an elastic nuclear collision. Conservation of momentum is obeyed such that momentum is transferred by mass and angle proportions to each target, which, if displaced, becomes a projectile itself. This cascade will continue until all projectiles in the cascade no longer have the energy to displace an atom and thus come to rest.

Normal irradiation-produced defects are Frenkel and anti-Frenkel defects. The Frenkel defect in this case is a vacancy/interstitial pair caused by the displacement of an atom off its lattice site. The irradiation-produced defect, however, causes a large separation between the the two complementary defects and, as a result, the system's energy is increased (Figure 2.30).

In an almost immediate sense, the displaced atoms, and their respective vacancies, will attempt to recombine. Short diffusion paths allow for most to self-annihilate almost immediately. Those that remain are prone to diffusion-limited motion, either to annihilate or to form clusters, etc. Diffusion, being induced by thermal motion, also requires sufficient activation energy.

2.6.3 Defects Produced by Irradiation: Kinetic Effects

The instant the displacement cascade occurs, a large number of vacancies and interstitials are produced and separated. The separation produces an almost hollow core, or

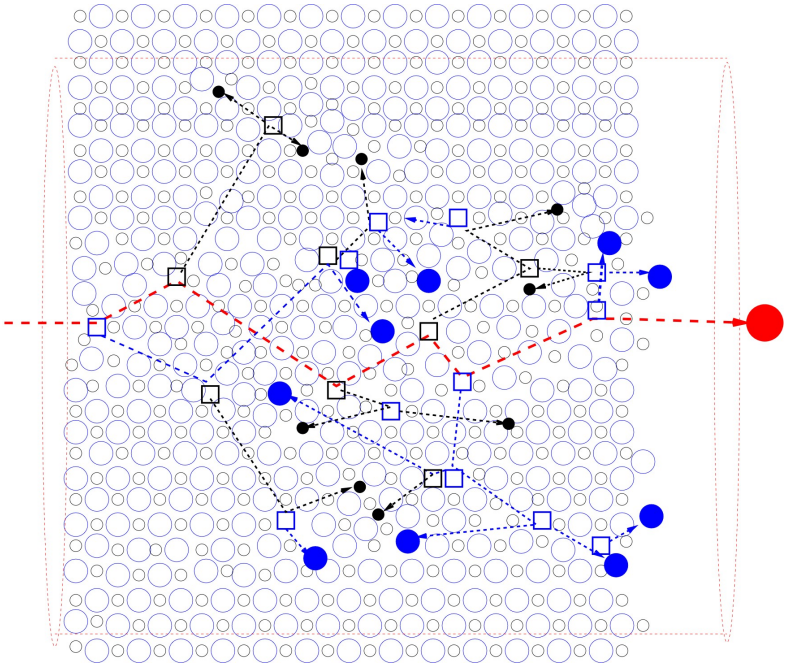

(a) Initial effects in irradiated volume showing Frenkel defects produced with the vacancies in the centerline. Blue and black squares are displacement vacancies, and solid circles are PKA's and SKA's from the cascade.

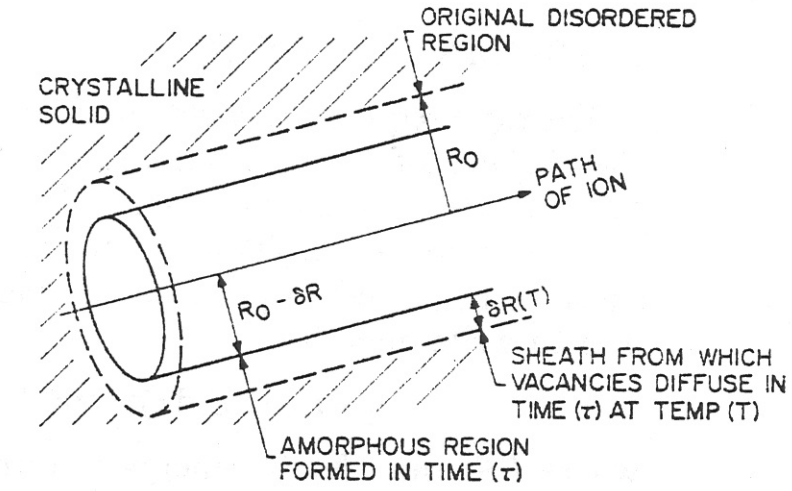

(b) Diagram showing the irradiaition-affected local volume as the central area is amorphized due to the mass movement out.

Figure 2.30: Displacement cascade from high-energy collision [118].

fission track, surrounded by the interstitial atoms that it displaced. Since both vacancies and interstitials produce a large strain energy with opposing signs, there is a large drive for the recombining of these species. The interstitials move much more freely and, in general, move to vacancies for annihilation. Even at cryogenic temperatures, this effect occurs almost instantaneously. However, as the fission track is refilled with interstitials, the drive for annihilation reduces. Depending on the material in question, there will be a substantial number of leftover defects.

As temperature increases, the vacancies can become mobile, as well as other defects such as dissolved gas atoms and defect clusters. The temperature dependence of these defect mobilities drives many types of microstructural development.

2.6.3.1 Vacancies

The vacancies produced from each displacement event will either be replaced by an implantation product or a displaced atom from the cascade, or left vacant. These vacancies are common and balanced by the numbers of interstitials formed, minus the implant replacement events. Under irradiation or annealing conditions, these vacancies can move and often find a free surface for annihilation. Often, they agglomerate into a void, producing an enlarging free surface to which vacancies can move. Alternatively, they may cluster into dislocation loops in a manner similar to interstitials.

2.6.3.2 Dislocations Loops

Dislocations formed from displacement damage occur when the residual effect of the displacement cascade is a large number of Frenkel defects with large numbers of interstitial atoms. These mobile interstitials can nucleate and grow dislocation loops, which are essentially a disk of interstitials. These then interrupt the stacking sequence of the lattice

and thus fight the stacking-fault energy (SFE) and dislocation line energy to form and grow. Dislocation loops are sessile, that is, they are immobile.

Alternatively, yet less commonly, vacancies cluster on a plane in a similar manner to interstitials. The difference is that the stress field is reversed, as is the sign of the dislocation loop that forms the periphery. Vacancy loops form stacking faults as well, and therefore are SFE limited. Since vacancies are much less mobile compared to interstitials, a vacancy loop is much less likely. Other factors such as interstitial gas stress fields are a greater driving force to cluster randomly rather than on a single plane.

2.6.3.3 Vacancy Bias

Immediately after the collision cascade, there is a lattice response to the defects produced. These defects will attempt to anneal out by vacancy-interstitial annihilation. Interstitials diffuse at much higher rate than vacancies and may either find a vacancy to annihilate or cluster with other interstitials. Interstitial clusters form on a single plane and as such are considered loops. Since by definition it is an inserted plane, it is considered a dislocation loop as the dislocation core surrounds the loop's periphery.

As dislocation loops are formed, the equivalent vacancies have no interstitials for annihilation as the interstitials are "bound", and thus a "vacancy bias" is produced. This bias is such that the total amount of vacancies is equal to the number of surviving Frenkel defects, yet, after initial interstitial-vacancy annihilation, the number is still high. But, once the interstitials are removed as dislocation loops, these vacancies are essentially "stuck" with a lower drive for interstitial-vacancy annihilation. There is a strain associated with vacancies, as well as lattice energy considerations. These extra vacancies are thus driven to reduce the total system energy once there is enough thermal energy for vacancy mobility.

At elevated temperatures, a vacancy bias promotes vacancy cluster formation. These

form either voids, bubbles, or vacancy loops. The difference between a void and a bubble here is defined by pressure. Vacancy clusters tend to nucleate on a strained lattice site, such as a gas atom interstitial. Gas atoms tend to move to the resulting free surface, thus forming a bubble, which is under great pressure. A void is a cluster that may or may not have gas atoms, but it will have so few that the pressure exerted on the cluster/lattice interface is negative.

2.6.3.4 Chemical Effects

The fission products are, for the most part, completely different isotopes from the fuel composition. As fission takes place, two isotopes are produced. These elements are ejected with much energy and through a displacement cascade, force their way through the fuel until they lose enough energy and come to rest. They deposit much heat, damage helium and during their journey, which on average is about 10 μm from the original fission event.

These fission products are distributed in bimodal distribution similar to that shown in Figure 2.8, which gives an estimate of the relative quantities of fission products at high burn-up. There are a large number of elements produced but the most important are those that affect the fuel, the cladding, or the fission process.

Xenon, krypton and helium are produced in large quantities and these are studied because of the gas swelling as well as the large amount of displacement damage produced, yet these are limited in their chemical effect. They are noble gases with filled electrons shells. Other elements produced in quantity are I, Nd, Zr, Mo, Pd, and Cs [121, 12]. Of interest are the elements that will have profoundly different chemistry from the surrounding metals and nitrogen.

Also of interest is the distribution of the released fission products. Cesium and iodine tend to form CsI gas in the plenum and have corrosive effects. Protons and α particles also

pose a deterioration risk to the cladding, as these particles produce hydrogen and helium swelling as well as embrittlement.

2.6.3.5 Gas Accumulation

As stated above, xenon and krypton are produced in large quantities, both from initial fission, and also from radioactive decay. Helium is a product of α decay product as well as inelastic neutron capture events prior to or instead of fission. Helium is produced in large quantities, and, although not a fission product, it is a nuclear-process reaction product. Helium contributes to void swelling and overall fuel swelling problems. It is a small non-reactive atom that diffuses easily at reactor temperatures. When a fuel rod is no longer fission efficient, it is pulled from the reactor for cooling. At this time the maximum amount of unstable isotopes have been produced within the fuel, but the decay chains continue to alter the total chemistry over time. Helium production will then become a significant factor for the fuel rods lifetime due to α decay. Isotopes with the shortest half-life will decay rapidly into more stable isotopes. The decay chain may produce different types of decay, but, with respect to fuel storage, α decay, and thus helium accumulation, is the most important.

With respect to AFCI and the TRU-N fuels, the predicted helium production is much greater and may be over five times the amount in the traditional UO_2 fuel from a LWR. The addition of americium as a major transuranic element is the main source of the large α decay chain. Although the energy of decay is not as high as for the fission products, and the mass of helium is very small, the damage produced is significant over time. Both the displacement damage from the collision cascades and the accumulation of helium within the lattice of the fuel and the cladding cause significant structural changes. The accumulation of helium in the cladding tends to produce both bubbles and embrittlement as helium accu-

mulates at the grain boundaries. The fuel may suffer the same effects, and as the bubbles grow, the fuel volume changes significantly and over time may rupture the cladding.

Xenon is a heavy and large atom that causes much damage when released. Krypton is produced as well and, although present in lesser quantities, its effect is very similar to that of xenon, and thus adds to the overall fission-gas problem. Both are noble gases, and both cause large displacement damage from fission. Both are too large to occupy interstices without a large lattice stress field and thus may move to a substitutional site on the lattice. Xenon, however, is different in that it has a high neutron capture cross-section. It is considered a nuclear poison, and its lowered concentration as critical for the operation of the nuclear fuel.

2.6.3.6 Defect Reactions

Defects are produced by thermal motion and are inherent in all solids. The normal Frenkel or Shottkey pair defects are system dependent, based on charge, size, and ease of defect production. Interstitial defects are normally reserved for cations of small size. This is due to the small size of the interstitial sites. Crystal structures, of course, determine the size of such interstitial sites. In any case, the sizes of interstitials sites are normally too small for normal anions, The occurrence of such would normally be paired with an anion vacancy, forming an anti-Frenkel pair (found in CaF_2) [122, 123].

For ZrN, the ionicity is based upon the electronegativity difference of the species. The bonding between the nitrogen and metal is a covalent one such that the electrons are shared. The electrons, however, will tend to spend a bit more time about the more electronegative nitrogen, and thus a partial charge occurs. A defect's charge discrepancy, however, is compensated by the local sea of electrons in the metallic bonding.

Strong oxidizers, such as oxygen and iodine, may produce a much stronger chemical

effect in the local area. Oxygen readily dissolves into ZrN and can form a couple of oxynitride forms, most notably the NaCl structure. With enough concentration, the nitride may be ionized to an oxide form, most notably the monoclinic form of zirconia.

Carbon is a common contaminant and is very soluble in the nitrides. Carbides and nitrides are isostructural and the bonding is more covalent with carbon. Carbon has one less electron to share, and thus the partial charges are less.

Both oxygen and carbon contamination have shown physical effects on cubic nitrides. Diffusion was observed to be altered by both, with carbon increasing diffusion and oxygen decreasing diffusion [27]. Both contaminants will affect the local structure in different ways, oxygen pulling electrons from the metal atoms, and carbon allowing more electronic distribution.

Reference to Figure 2.8 shows that some of the main decay products are Xe, Kr, Cs and I. Helium is produced in large quantities by α decay. Cesium and iodine are not gases but are volatile at reactor temperatures and diffuse to the surface and combine to form CsI gas [124, 125, 121]. Xenon and krypton have been shown to act identically in UO_2 fuels in the way of damage and bubble formation, and thus xenon studies are regarded to be equivalent for krypton [25].

There are many models of gas release [126, 127, 128, 129, 130, 131, 132]. The basis for each is that for each fission process, there are two fission products produced with a probability, (refer to Figure 2.8), that there will be a gas produced, either directly, or through a decay cycle. Each fission event is controlled by the number of thermal neutrons and the probability of their interacting with any of the fissile isotopes. Once a gas is produced, it must diffuse, so diffusion laws apply. The age of the fuel will determine the quantity of damage build-up from irradiation displacements and from defect interactions. Grain growth or polygonization will also effect the diffusion. Finally, neutrons themselves, as

well as thermal spikes from other fission products, enhance diffusion in non-traditional ways.

2.6.4 Irradiation Damage Measurement

Measurement of damage in a material is dependent primarily upon its purpose. For reactor environments, structural integrity is of primary concern, and thus any damage that can diminish this is what is considered. Swelling of the fuel can lead to reduced efficiency and increased fuel rod stress. Gas bubble nucleation and growth is one cause of swelling, the others being phase change or amorphization.

Before measurement, the material must be damaged by irradiation. From the nuclear fuel perspective, the 300 keV ion implantation used is a far cry from the 70 MeV energies commonly associated with fission products. Yet, as theory tells us, the nuclear stopping is in the eV range, when the fission product has slowed enough to produce a significant number of nuclear collisions. These nuclear collisions are most of the damage, and the displacements produced are similar.

TEM is one of the primary tools used to determine the tolerance of a material to radiation damage. The crystal structure and microstructure may be monitored for change at increasing doses. Diffraction patterns from very small areas on a cross-sectional sample show the depth of damage with respect to alterations or destruction of the crystal structure.

While TEM shows very small-scale details about depth, other methods can also be used to show effects. Channeling Rutherford Backscatter Spectroscopy (RBS/C) is commonly used on single crystals to provide quick and accurate analysis of the damage accumulation. Regular RBS, in most cases, can be used to track the implanted ion. GIXRD is used to measure very small depths of implantation, and can detect changes at very high resolution.

Physical changes can be tracked as well. As defects alter some physical properties,

these can be directly monitored. Nanoindentation techniques can be used to measure mechanical property change, while resistivity can show electronic property changes.

A critical tool in the measurement of radiation damage is the computer simulation. TRIM is the standard simulation tool, and, while it is simple to use and has its errors, the value of its predictions from theory cannot be overlooked [120]. The LSS theory that TRIM uses provides the information to be used in all the data comparisons. Displacements per atom and the knock-on cascade distributions are predicted. These are used as a basis for all data analysis and comparisons.

2.6.5 Diffusion Theory

Diffusion is the movement of one medium through another. In the case of fission products, they must diffuse through the fuel or matrix lattice. The crystal structure and defects play critical roles in the movement of atoms through the lattice, as do temperature, and concentration.

Fick's 1^{st} law states that matter will move to reduce concentration gradients. J is the flux through space, δC is the concentration difference at any point, and D is the diffusion coefficient. Fick's 2^{nd} law is the second derivative of the first, which gives concentration change with respect to time [133, 134].

This diffusion coefficient is a function of temperature and the activation energy required for an atom to hop from one position to the next. The positions the atom can hop from and to may be different leading to different activation energies. Since the activation energy, Q, is a thermodynamic function, it is composed in part by the enthalpy of the jump, and in part by the entropy of the jump. As with all thermodynamic processes, these parameters are in competition to dominate the reaction. Algorithm 1 shows this equation in the Arrhenius form.

Algorithm 1 General diffusion equations

$$\text{Fick's } 1^{st} \text{ law } J = -D\frac{\delta C}{\delta x}$$

$$\text{Fick's } 2^{nd} \text{ law } \frac{\delta C}{\delta t} = \frac{\delta}{\delta x}\left(D\frac{\delta C}{\delta x}\right) = D\frac{\delta^2 C}{\delta x^2}$$

$$\text{Diffusion coefficient } D = D_o e^{-\frac{Q}{kT}}$$

When the required energy of the atom is achieved, either as kinetic energy from heat, or atomic collision, the atom may hop to the available site. Vacancies and interstitials are the ideal sites for atomic diffusion. Interstitial diffusion is generally much faster than vacancy diffusion. Empty interstitial positions are generally plentiful, while the vacancy concentration is governed by damage and temperature. Atomic size is a factor, as is charge and chemical nature. Sites that are much too small will have large energy barriers, as is also the case for charged defects.

2.6.6 Irradiation-Enhanced Diffusion

Radiation gives the needed energy in the form of both heat, which is the phonon cascades, and displacement damage [97]. Since the kinetic contact of the moving ion is very large, orders of magnitude above the few eV needed for movement, diffusion is enhanced by irradiation. Even normally unattainable sites are possible for the atom due to the tremendous energy available. Of course, this energy is short lived and atoms in non-ideal sites, say a cation in an anion site surrounded by cations, will relax back into a lower-energy state as soon as such a site is available. Irradiation produces many non-ideal defects, yet most of their lifespans are limited to picoseconds. Defects produced are quickly annealed by this diffusive state until the lattice is more relaxed. Even when irradiation is performed at cryogenic temperatures, the diffusion to move the atom to a lower state dominates.

2.6.6.1 Gas Traps: Bubble Nucleation and Formation

Diffusion at lower temperatures is governed mainly by bulk diffusion. As the temperature rises, so does the mobility of defects produced by the irradiation, namely voids, vacancies and interstitials.

The vacancies may cluster and nucleate voids or bubbles. Both voids and bubbles may be broken up by irradiation if very small. Gas atoms move to free surfaces such as the voids, fill them and produce bubbles. Voids and bubbles are mobile at elevated temperatures and tend to move to grain boundaries [135, 100, 136, 137, 138, 32, 33].

Dissolved gas, diffusing through interstitial sites or vacancies, tends to move to a free surface, such as the pore surface, bubble surface, or a grain boundary. Gas tends to coalesce at grain boundaries and nucleate bubbles, or the bubbles migrate and combine. The end result is grain boundaries decorated with gas bubbles. Grain-boundary gas-bubble formation tends to be a high-temperature event, and is generally seen above 1000 °C [27].

2.6.6.2 Gas Evolution: Diffusive or Crack-Assisted

The gas must either diffuse to the surface and get washed away in the plenum gas, or move around until it gets trapped. Since the noble gases are not soluble, even at high plenum pressures the gas moves in only one direction, out of the solid [25]. As the temperature gets higher and bubbles become more mobile, much of the gas is trapped.

With enough heat and time, gas pressure builds in these bubbles and two things happen. First, the gas may re-diffuse into the solid from the bubble, which happens more in the bulk. Second, the bubbles at the grain boundaries build up enough pressure to nucleate and assist crack propagation along the grain boundary. This produces gas-release spikes, and also damages the pellet. Re-entry from the bubbles increases bulk diffusion due to the

increase in concentration. Much of this gas can then find its way to the surface [27, 126, 127, 128, 129, 130, 110, 139, 140, 141].

Table 2.2: List of Physical Properties of ZrN [20]

Property	*Quantity*
Mass	105.22 amu
Nitrogen content (1:1)	13.31 Wt. %
Structure	NaCl, B1, $fm\bar{3}m$
Lattice Parameter	4.57 Å
Heat Capacity (300 K)	$\approx 41 \frac{kJ}{mol \cdot K}$
Coefficient of Thermal Expansion (300 K)	0.004
Density (300 K)	7.25 $\frac{g}{cm^3}$
Thermal Conductivity (300 K)	400 $\frac{W}{M \cdot K}$
Young's Modulus	≈ 460GPa
Hardness	≈20 GPa
Melting Temperature (decomposition)	3253 K

Table 2.3: Physical Properties for TiN[76]

Property	
Structure	NaCl
Range of Composition	$TiN_{0.6-1.1}$
Melting Temperature	2950°C
Specific Heat	$30.7 \frac{J}{mol \cdot K}$
Thermal Conductivity	30 $\frac{Watt}{M \cdot K}$
Thermal Expansion	$\frac{9.36 \cdot 10^{-6}}{K}$
Electrical Resistivity	$20 \pm 10\ \mu\Omega \cdot cm$
Hardness (H_V)	21-24 GPa
Young's Modulus	590 GPa

CHAPTER 3

Experimental Objectives

There are many techniques used to measure radiation damage of a material. The techniques used to characterize ZrN in this study were chosen for their usefulness to the AFCI program as well as sufficient resolution of the characteristics of interest.

Transmission Electron Microscopy (TEM) was the primary tool used to observe the characteristics of the microstructure and change in the crystal structure. Scanning electron microscopy was the primary tool used to evaluate changes in surface topography and, with energy dispersive spectroscopy (EDS), to observe the implanted areas of xenon. Atomic Force Microscopy (AFM)was used to check for any swelling effects outside a masked area, and also to measure nanoindentation effects. Grazing-Incidence X-Ray Diffractometry (GIXRD) was used as a high-resolution tool to detect changes to the crystal structure near the surface. Other techniques used were Rutherford Backscatter Spectroscopy (RBS), resistivity, reflectometry, and X-ray Photo Spectroscopy (XPS). Helium release studies were performed in a specialized vacuum furnace coupled with a Residual Gas Analyzer (RGA).

The data were compiled and used not only to produce ion-irradiation damage metrics, but also to analyze the underlying reasons for the high tolerance of ZrN to the high defect concentrations produced by irradiation damage. The strange nature of the cubic nitrides with respect to this response is a puzzle, and these experiments provide some of the pieces. The data allow for some extrapolation as to why ZrN has such high tolerance for damage, and predictions for the in-pile tests.

3.1 Irradiation Damage for Experimentalists: Ion Implantation

Ion implantation is the primary tool for the fission-product radiation-damage scientist. It is used to simulate large, heavy fission products that cause damage in the lattice, place gases, change chemistry, generate defects, etc. Rate, dose and temperature are controlled by the operator. Different elements can be implanted to simulated damage from a nuclear reactor or to modify the surface structure into a thin film, alter the chemistry, or produce extrinsic defects.

Limitations of the experimental technique are varied, based upon the desired data. It is a standard technique in radiation damage studies in ceramics. The damage is generally produced at cryogenic temperatures with an inert gas such as xenon or krypton. These elements are sufficiently heavy to produce large damage cascades yet have little to no with respect to altering the chemistry of the host lattice. Although these are fission products, the real damage is produced by the cascade which may displace many orders of magnitude more lattice atoms for each implanted atom. The same effect occurs with high energy neutrons and fission products.

Although the neutrons and fission products occur at MeV levels, the collisions of interest mostly involve reduced-energy particles with keV velocities, similar to that may be produced by a conventional ion-implanted sample. One critical difference that should be addressed between an ion implanter sample and one from an in-pile experiment is that the ion irradiation is at the surface and the in-pile is bulk. The near-surface effects provide a relatively close free surface that allows defect annihilation that does not occur in the bulk. This is especially true for an *in-situ* irradiation on TEM, as the damage produced is very close to *two* free surfaces.

Cryogenic irradiation, although not a true service condition, is very useful in determining the ability of the lattice to withstand the largest amount of cascade defects. These defects, produced by the initial cascade, rush to self-annihilate but if the sample is cooled, this process is slowed such that the accumulation is faster than the decay due to annihilation. This allows for a metric from the peak calculated displacement damage such that many materials may be compared. The damage is generally increased until amorphization, at which time the damage threshold of the lattice is semi-quantitatively known.

3.2 Radiation Damage Characterization

3.2.1 GIXRD

Grazing-Incidence X-Ray Diffraction is a technique used to study thin films. It has the benefit of limited depth of penetration, hence providing diffraction data from very low depths. This is ideal for use with ion implantation due to the shallow depths reached by ions. The implanted volume is modified, and thus must be distinguished from the unimplanted "substrate" or bulk material below.

X-rays, normally Cu K-α wavelength, give very high resolution for plane spacings. Significant changes in crystal structure may be observed with this technique, and identifying contamination precipitates such as oxides and oxynitrides can be irradiated.

3.2.2 SEM

Scanning electron microscopy is used to evaluate the surface of the material. It is used in conjunction with EDS to obtain chemical information. It is also used to examine post irradiation and anneal specimens for surface blisters formed from gas pockets [142].

3.2.3 TEM

The importance of the use of transmission electron microscopy cannot be overstated. The direct observation of lattice defects, microstructure changes, amorphization, etc. is important not only to illustrate the effects of damage but also to measure effects on a microscopic scale.

3.2.4 EDS

Energy Dispersive Spectroscopy is used to collect chemical information. The excitation of electrons by the accelerated electrons causes characteristic x-ray emission. These characteristic x-rays are element specific, thus can help determine changes in chemical composition. This can be used to track and confirm the presence of heavy elements such as xenon that are implanted. .Both SEM and TEM are capable of EDS measurements.

3.2.5 Nanoindentation

Nanoindentation is a near-surface characterization technique in which an indenter tip is forced into the bulk, and the load and displacement are measured. Two types of instruments were used depending on the intended purpose. A cube-corner indenter on the *Nano* II instrument was used to measure hardness and modulus. The *Hysitron,* with a Berchavich tip, was used to produce a conventional load-displacement curve. This technique is especially useful for measuring depth-displacement events such as the critical loading for plastic-deformation. It also uses the tip as an AFM to image and measure the indentation.

Hardness is used with respect to radiation damage as a measure of the amount of residual defects. These defects, being residual Frenkel defects or clusters, will inhibit dislocation motion, thus increasing hardness. In this case, hardness is simply defined as the

resistance to plastic deformation. While dislocations are present in the material, increase in the defect concentration is measured qualitatively by hardness vs. displacement damage induced by ion irradiation. Dislocation nucleation and motion are of interest in ZrN due to the interest in defects, their production and reactions.

3.2.6 Helium Release

Gas release studies show the effects of radiation damage on the trapping of gas in and diffusion of gas out of a sample. Generally, gases chosen are either xenon, for its large impact on fission gas swelling, or helium, as a by-product of fission-product decay. Gas release rates are important to the nuclear engineers designing the fuel and cladding. Fission gas production and release must be predicted within some degree so that the fuel and cladding can take the increased gas pressure. This is also important information for the storage medium for the repositories, as helium will continue to be produced through α decay for many years.

Gas release is not a direct measurement of radiation damage but, like many physical properties, an indirect measurement of its effects. As the irradiation produces defects, these in turn interact with the lattice and each other to affect the diffusion of the fission products. Helium is of great interest for engineering reasons, as stated above, but also due to its inherent agglomeration and nucleation into gas bubbles. Helium and xenon both have a tendency to produce bubbles and voids in many materials, although the effect is variable. Bubble production swells the material, which of course is of engineering concern.

Helium is also a fast diffuser due to its size, yet its interactions with defects and their clusters, grain boundaries, etc., need to be evaluated. He release is an indirect measurement that cannot differentiate different defect effects.

Normal gas diffusion studies entail either a fixed annealing temperature, a continuous

ramp or isochronal annealing. The fixed temperature gives data at a specific temperature, while ramping or isochronal annealing gives data on multiple temperatures. The most common is the continuous ramp due to its quick results. The gas is analyzed in the vacuum while the sample is heated in a crucible. Normal release plots will show a typical "burst" at low temperatures, which is considered an artifact [143]. Then the release increases linearly with temperature, until the higher temperatures where the slope is decreased. The first slope is attributed to bulk diffusion, while the second indicates when defects are activated enough to provide traps. With a long enough time and higher temperatures, the traps produce bubbles, especially at grain boundaries, which can cause release due to intergranular fracture.

Very little is known about the gas release characteristics of ZrN, or most other cubic nitrides. Most of the known work is on carbides, although some PuN, UN, and (U,Pu)N have been studied as a fuel form [27, 25]. It has been found that an increase in carbon in the nitride, and nitrogen in the carbide, increases diffusion.

CHAPTER 4

Experimental Procedures

Analysis of ZrN for fission product retention and damage is a challenging process. The sample itself is not very forgiving with respect to preparation or expected results. Standard tools were used for characterizing and analyzing the hard, brittle and very refractory material. Much time was spent in attempting to prepare these samples. Low-density sintered pellets, nitrided foils, and epoxied powders were all attempted as samples. Each were rejected in time for various reasons. The final preferred samples were heat-treated hot isostatic pressed (HIPed) ZrN due to polishing artifacts. HIPed samples that were not heat-treated, however, showed a similar response when compared to irradiated and annealed HIPed material, and thus provide some valid data. The polishing damage on these particular samples, however, made it impossible to evaluate the damage structure in the heavily damaged region.

4.1 Samples Evaluated

Early work was done on zirconium foil that was nitrided in-house. This technique proved to be unreliable due to excess carbon and oxygen found by XPS analysis, and the non-linear nitrogen diffusion front. On one novel sample, the raw powder was mixed with epoxy. Plan-view disks from this sample were observed pre and post irradiation. Most samples used for this study were HIPed material.

Most samples were irradiated in the cryogenic range, $\approx$ 100 K (-173 °C). One sample

was implanted at room temperature, while others were implanted at 350°C, 580 °C and 800 °C. Both xenon and krypton were used almost interchangeably for irradiation experiments; however, helium was also used. Samples used for experiments are shown in Table 4.1.

The sample type was chosen for final characterization because of its high density. Hot isostatic pressed (HIPed) ZrN of 99% density, gave much better polished samples and TEM samples than previous attempts at sintered material, glued powders, or nitrided foils.

The HIPed samples could be cut and polished to a very high luster with a very high-quality and flat surface for the various experimental techniques used. The finely polished flat surface is required to produce good cross-sectional TEM samples.

4.2 Sample Characterization

Characterization of the sample is important to understand the similarities and differences with respect to the intended fuel material. The fuel form will be a sintered pellet and thus will be somewhat different from the experimental samples. The basic physical properties, however, will be the same.

4.2.1 Precursor Powder

The precursor material used was CERAC ZrN, -325/+200 mesh powder. This powder was stored under an argon atmosphere within the original container to reduce oxidation and contamination. The powder was geometrically random in shape with sharp, broken edges. The powder particles were found under TEM to be polycrystalline . Chemical analysis was performed by CERAC as well as by LUVAK.

Table 4.1: Samples and Experimental Techniques Performed on ZrN

Type	Ion	Implant keV	Fluence $\times 10^{16} \frac{ions}{cm^2}$	dpa	T	Rate	Analysis
Powder	-	-	-	0	-	-	TEM
Powder	Kr	300	1	30	LN_2	Fast	TEM
HIPed	Xe	300	1	40	LN_2	Fast	TEM
HIPed	Xe	300	2	80	LN_2	Fast	TEM
HIPed	Xe	450‡	0.01, 0.1, 1	0.4 ,4, 40	LN_2	Slow	Nano, TEM
HIPed	Xe	300	2	80	LN_2	Mod	TEM
HIPed	Xe	300	5	200	LN_2	Fast	TEM
HIPed	Xe	300	2	80	350°C	Fast	GIXRD
HIPed	Xe	300	2	80	LN_2	Fast	GIXRD
HIPed	Xe	300	4	160	LN_2	Fast	GIXRD
HIPed	Xe	300	6	240	LN_2	Fast	GIXRD,TEM
HIPed	Xe	300	0, 1	0, 40	LN_2	Fast	Reflect/Resist
HIPed	He	17	0.1	<0.1	LN_2	Fast	He release
HIPed	He, Xe	17, 300	0.1, 1	40	LN_2	Fast	He release
HIPed	Xe	300	1		580°C	Fast	TEM
HIPed & Annealed	-	-	-	-	-		TEM
HIPed & Annealed	Xe	300	0.01	0.4	LN_2	Fast	TEM
HIPed & Annealed	Xe	300	0.1	4	LN_2	Fast	TEM
HIPed & Annealed	Kr	300	2	70	800°C	Fast	TEM

‡Sample implanted with various energies to broaden displacement curve

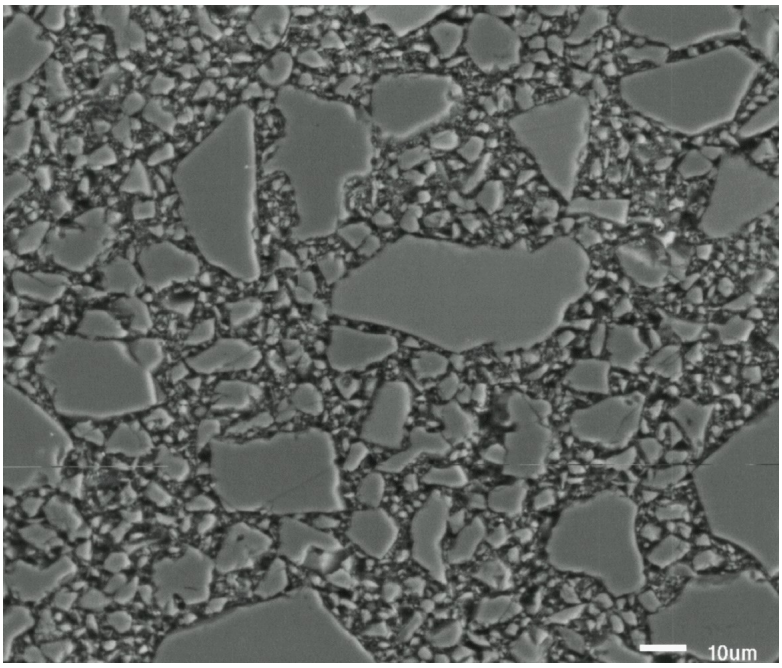

Figure 4.1: SEM of raw powder embedded in epoxy and polished

4.2.1.1 Powder Size Distribution

Distribution of powder size was measured by optical stereography. Both light and scanning electron microscopes were used to observe the powder. The average grain or particle diameter was measured with the computer software package *NIH-Image.* Many particles were measured in order to determine a statistical distribution for analysis with the statistical software *Mintab* (Figure 4.2). The size distribution showed a large amount of very small particles (less than 5 μm in diameter) along with large (40 μm) particles (Figure 4.1).

4.2.2 Hot Isostatic Pressing

Hot Isostatic Pressing (HIP) is a process in which a powdered sample is compressed with great force in a high-temperature liquid for a particular length of time. The result is the closest that one can achieve to the theoretical density of a sintered powder material.

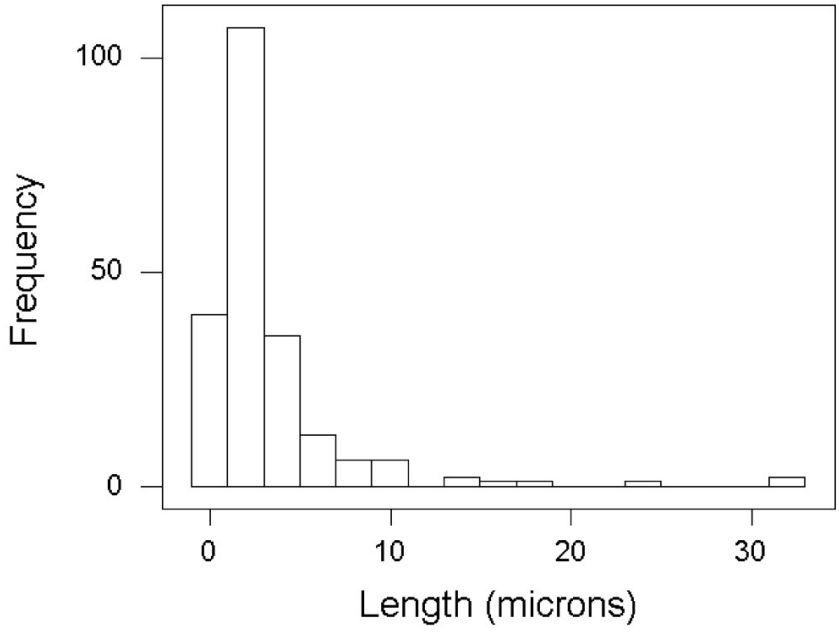

Figure 4.2: Particle size distribution

HIPing is used mainly as a research tool, due to the work and time involved in producing a sample. There is little control of the final shape, other than its being roughly a cylinder.

The precursor powder was first CIPed (cold isostatic pressed) into a rod sand then sealed into a tantalum can, (a tantalum tube that was welded shut at both ends under vacuum). The can was placed into a high-temperature hydraulic fluid. The pressure was increased to 30,000 psi and the temperature was raised to 1850°C. The can was held at this temperature for two hours and then allowed to cool slowly to ambient.

The resulting HIPed rod was cut away from the can and sliced into quarter sized samples. These “coins” were further quartered into “pie pieces.” Figure 4.3 shows the HIPed rod. The pieces have a small enough area to be polished with the force required to produce

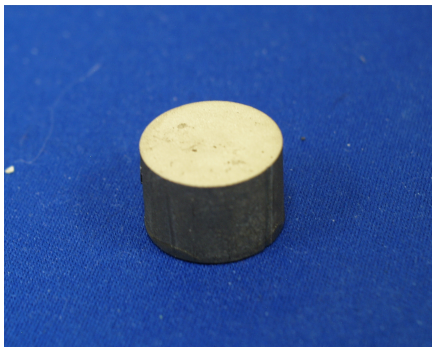

Figure 4.3: HIPed ZrN rod. Diameter is approximately 1.1 inch

the very flat, highly polished surface required for cross-sectioned TEM specimen preparation.

SEM micrographs show the high density produced. Only very small voids are observed, occurring at the grain boundaries or triple points. Analysis of the surface reveals that the sample has pull-out problems and as such the observed density may be less than actual. Careful polishing produces the least amount of pull-out and thus the observed density is perceived to be greater than 99%. Figure 4.4 shows this polish and the representative voids.

4.2.3 Glassy Phase

TEM observation of HIPed samples showed a glassy phase at the triple points that wicked into the grain/particle boundaries. This glassy phase tended to pick up metallic components preferentially during ion milling, and was first observed during TEM sample preparation.

When light passed through the sample, it was thought that a very small hole had been milled. In the TEM, no hole was observed. This glassy phase was observed with a light microscope if the sample was thin enough to be transparent with back lighting.

With further thinning to perforation, this glassy phase became very apparent. It was

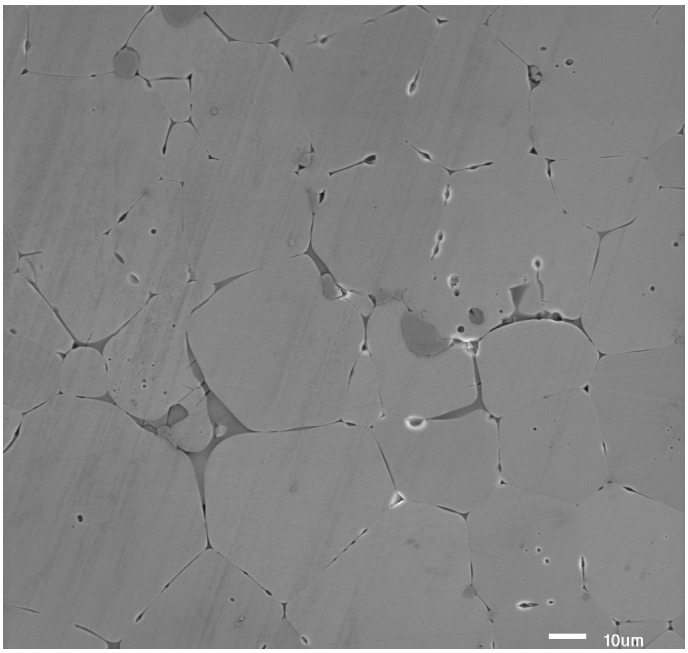

Figure 4.4: Close up of HIPed ZrN sample polished flat

electron transparent but only produced an amorphous haze with Convergent Beam Electron Diffraction (CBED) which allows microdiffraction. The lack of diffraction spots confirmed that it was an amorphous material. In EDS with a probe size of approximately 50 nm, the elements were observed as the probe was moved into the glassy phase from the obvious crystalline substrate. Care had to be taken as the surface of the glassy phase was usually covered with nano-sized particles that did diffract the electron beam (Figure 4.5).

The results indicated that the phase was higher in oxygen and seemed to be higher in hafnium as well. It appeared to be an oxide glass, rich in hafnium with respect to the substrate, that coated much of the particle boundaries. It is thought that the high pressure and temperature of the HIPing process liquefied the oxide coating that was on the surface of the particles. With the high pressure, the oxygen may have been preferentially absorbed into this phase as it was forming. The hafnium is thought to have been more soluble in this phase and to have diffused out of the surrounding area. Figure 4.6 shows an EDS spectrum

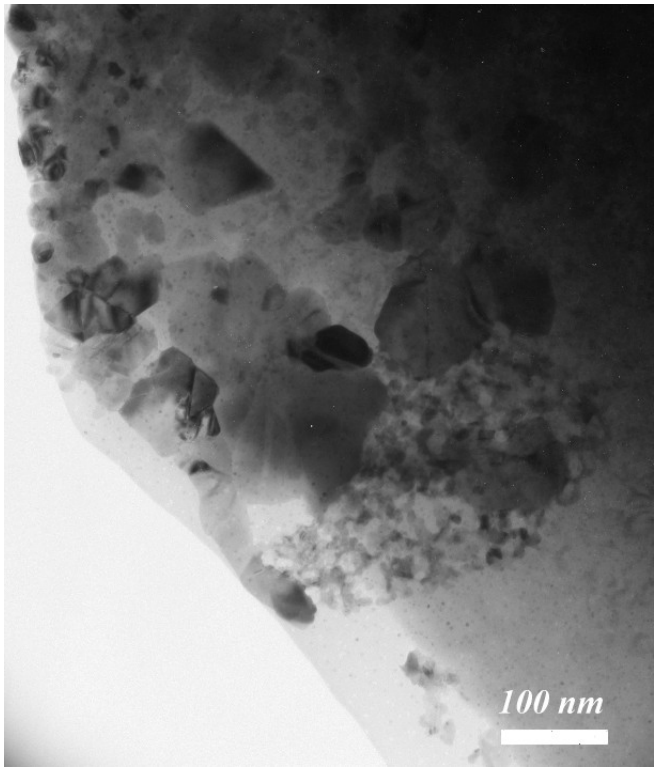

Figure 4.5: TEM micrograph of glassy phase

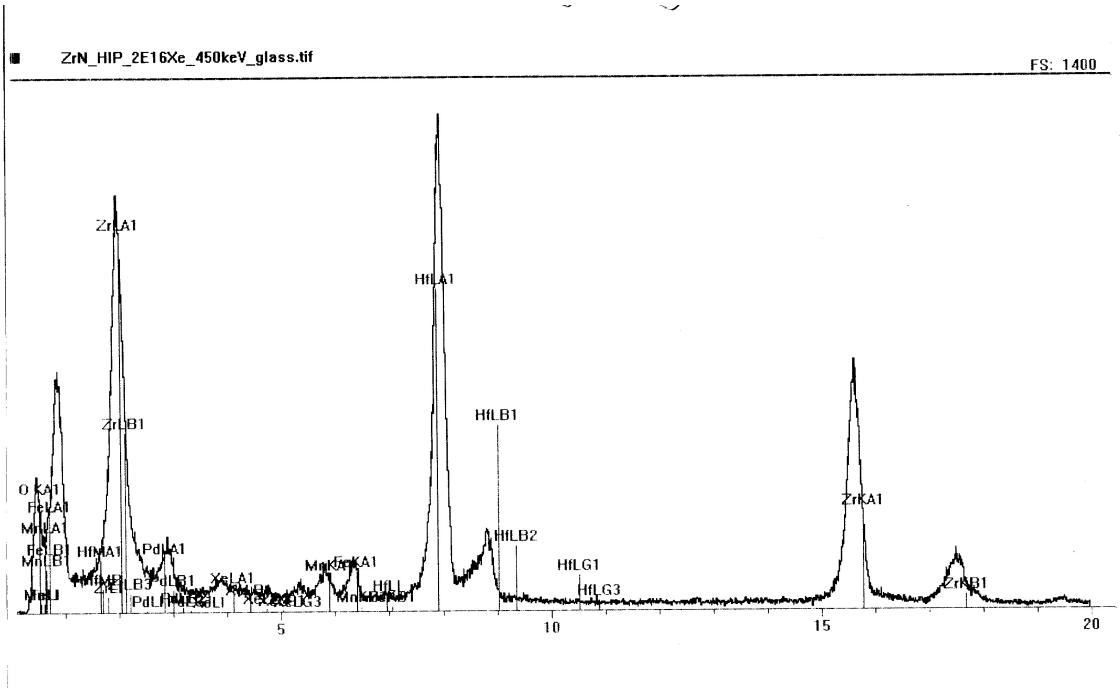

Figure 4.6: EDS of the glassy phase and ZrN substrate

of the glassy phase. Note that the EDS spectra differ depending on the particular region of glassy phase sampled indicating a variable composition. The spectra also contain Cu and Mo peaks, most likely sputtered onto the sample from the PIPS and hence e an artifact. Cu and Fe signals are also background from the column, sample holder, and grid.

The glassy phase seems to coat the particles and also occurs at triple points and in isolated pockets at grain boundaries. Sub-micron-sized particles were fused together into particles approximately the same size as the large particles. The glassy phase is more easily broken, which accounts for the ease of the particles being pulled out during polishing. Finding an area with a large particle was the key to not having to work around the glassy phase. Figure 4.5 shows a TEM image of the glassy phase with crystalline nanoparticles.

Note in Figure 4.7 the nanofibers extending from the glassy phase. These grew while images were being acquired. It is theorized that copper nanoparticles, sputtered onto the

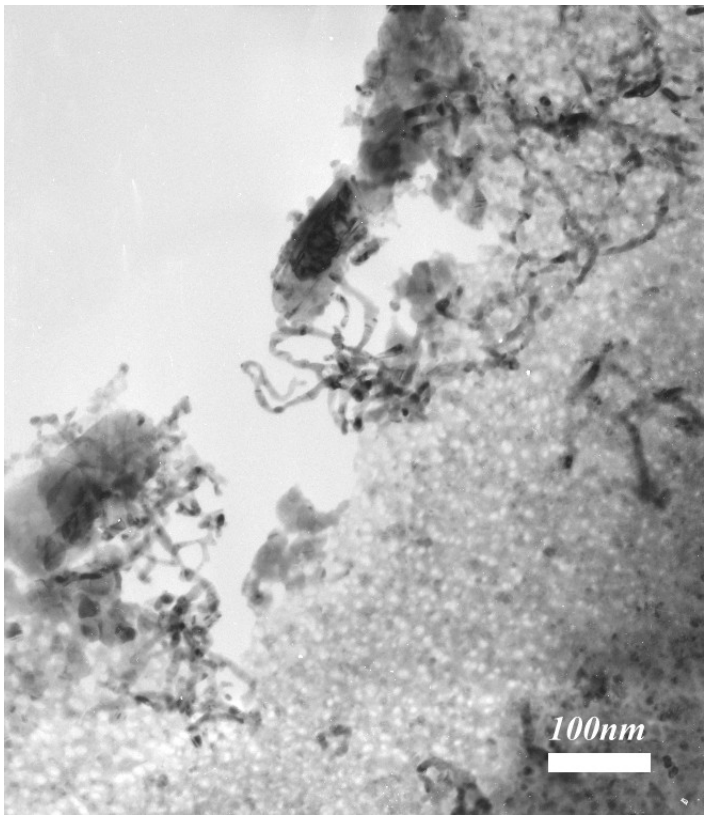

Figure 4.7: TEM of glassy phase. Note the filaments. They are most likely carbon nanofibers; *they grew in situ under electron beam irradiation*

glassy phase have a catalytic effect under the electron beam, leading to the formation of graphite plates from hydrocarbons present in the vacuum system. Suitably oriented fibers diffracted electrons, indicating that they were crystalline.

4.2.4 Ceramography

The SEM samples used for density measurements and the comparison with and without the glassy phase were etched with a modified Khol's reagent, which was a mixture of 65 % HNO_3, 34 % HCl and 1 % HF. This etchant was applied carefully with a cotton swab due to the HF and allowed to act for 1 to 5 seconds. It was immediately rinsed with

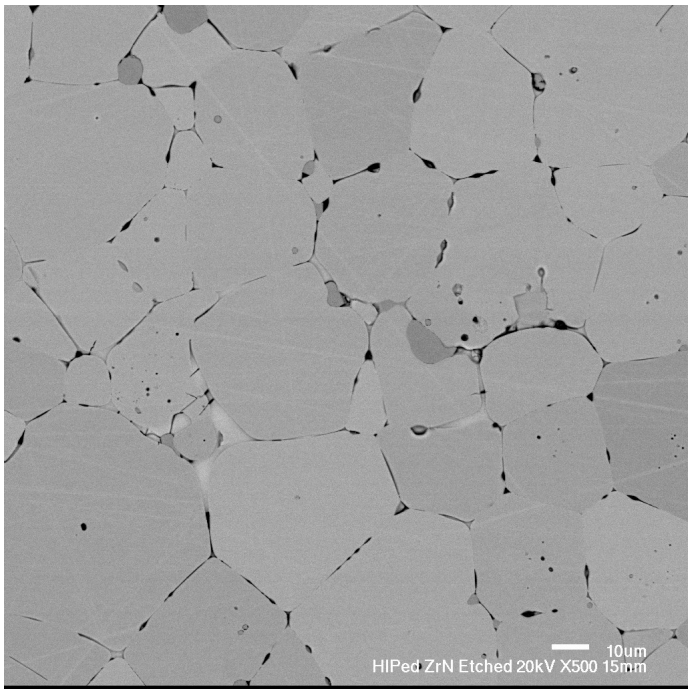

Figure 4.8: SEM of HIPed sample with glassy phase etched

water and then ethanol. Light microscopy was used to monitor the quality of the etch. This etchant and technique were also used successfully on zirconium metal, highlighting the grain structure as well as zirconium's tendency to form twins. This etchant's activity seemed to increase with age. Figure 4.8 shows the structure after etching. The etchant attacks the grain boundaries as well, but preferentially attacks the glassy phase at triple points and between particles.

4.2.5 Chemical Analysis

The precursor powder as well as HIPed samples were sent to LUVAK Inc. for chemical measurement. LUVAK use a combustion technique that has a margin of error of about ± 1 atomic %. Analysis showed that the samples all had a small amount of carbon left over from manufacture. Nitrogen content in the initial powders was nearly stoichiometric, while

the HIPed material lost some nitrogen to oxidation and decomposition (Refer to Table4.2).

Table 4.2: Atomic % Elemental Analysis from LUVAK

	Zr	N	C	O	Zr/N
Precursor Powder	48.9	49	0.5	1.4	0.999
HIPed Sample	50	45.7	0.5	5.6	0.914

Analysis did show error with respect to nitrogen content of the powder. It is assumed that the maximum amount of nitrogen that ZrN is capable of holding is 13.3 weight %, or 1:1 Zr:N stoichiometry (refer to Figure 2.16 showing the Zr-N phase diagram). The original LUVAK analysis showed 14.1 weight %, which put it to 51 atomic % nitrogen, 1 % over that which the structure is capable of holding. It was surmised that the extra nitrogen measured was from physisorbed gas on the powder surface. The high surface area of the powder and/connected porosity within the samples, could be carry along nitrogen and thus possibly produce the higher nitrogen analysis. With this in mind, the content was reduced to the maximum of 13.3 weight % for the elemental atomic % calculations.

CERAC produced their own analysis showing the trace elements. This analysis was in agreement with LUVAK with respect to experimental error. CERAC, however, did not analyze for oxygen.

4.2.6 Density Measurements

The density of the sample was shown to be critical from TEM sample preparation. Lower-density, highly porous pellets gave large peaks and valleys in cross-sectional TEM samples. HIPing the sample was the only way to achieve the high density desired. The HIPed samples showed a very high density by the optical method, once polishing procedures were optimized; (pull-out from polishing can produce anomalously low results).

4.2.6.1 Geometric Density

A common, simple technique to calculate the density from the mass and volume of the sample. By definition, the density of a material is: $\frac{mass}{volume}$. For simple geometries such as cylinders, the volume can be calculated from the height and diameter.

The drawbacks of this method are the loss of mass during handling and change in dimensions during sintering. Although the change in dimensions is the key to the density change, non-homogeneous sintering may break the symmetry of the shape and thus it may not be a perfect cylinder. Pressing a powder causes mechanical energy to be stored, which may cause cracking and delamination in certain areas, such as the corners and ends. It has also been suggested that cold pressing ZrN will produce plastic deformation such that it results in texturing of the grains.

Oxidation has proved to be another problem with the evaluation of the pellet densities. As the ZrN takes up oxygen, it loses nitrogen. A simple dissolved form of the Zr(N,O) exists when the oxygen content is very low, but, when the oxygen content increases the structure changes to other oxynitrides or the very stable monoclinic zirconia. This is observed at the surface of every sample, even raw powders. Zirconia swells the sample and alters the cylindrical shape. It has been observed that flow gas contaminated with oxygen penetrates easily throughout a pressed pellet during sintering. The addition of two oxygens with a loss of one nitrogen also alters the mass. With careful control of the atmosphere by use of sacrificial ZrN powder, the amount of oxidation is kept to a minimum.

Due to these problems, better techniques are also used to determine the density. This is, however, a very easy and quick method to assess the sintering process.

4.2.6.2 Optical Stereography

The optical stereography method uses an optical or SEM micrograph of a polished piece. *NIH Image* or *Adobe PhotoShop*, is used to render the image with a black and white color map, and the saturation was altered until a balance was achieved. The density was measured from the black-to-white ratio. Although assignment of the threshold is subjective, this method was tested with several individuals and with micrographs from the literature, and results were all within 1% of each other. By this method the HIPed ZrN samples were found to be greater than 99% dense, which satisfactory for TEM specimen preparations.

4.2.6.3 Archimedes' Method

The *de facto* method for density measurements is Archimedes' method. A large slug of the HIPed sample was submerged in *3-M* Fluorinert FC-43, a commercial low-dielectric strength fluid used for cooling electronics. Mass measurements were made with an *Ohaus Explorer* scale. The ZrN mass was measured in air and in the Fluorinert, while the Fluorinert mass was readily measured on the scale. The temperature of the room was measured for the calculation. By comparison the two mass measurements, the volume displaced, and the mass of the Fluorinert, the density was found.

The density ρ is calculated from the formula below (2). ρ_l is the density and m_l is the mass of the liquid, in this case Fluorinert, and m_{ZrN} is the mass of the ZrN sample measured submerged in the liquid.

The density measured is based upon mass, and although a HIPed sample has very little porosity, this slight amount must be taken into account. Accurate evaluation the voids and

Algorithm 2 Archimedes' method of density measurement

$$\rho = \varphi_l \frac{m_l}{m_{ZrN} - m_l}$$

Algorithm 3 Equation for the ratio of vacancies to occupied sites at equilibrium

$$\frac{n_v}{n_0} = e^{-\frac{H_f}{RT}}$$

- $n_V =$ number of lattice sites vacant
- $n_0 =$number of lattice sites occupied
- $H_f =$formation energy for a vacancy
- *R* = Universal gas constant
- *T* = temperature in Kelvin

pores allows a true density to be obtained. Using the optical technique helps evaluate the porosity effect.

4.2.6.4 Vacancy Concentration

The vacancy concentration of a material is variable and increases as temperature increases. At thermodynamic equilibrium, more vacancies are formed as temperature is increased and mass is moved to the surface, thus increasing the volume and decreasing the density. The amount of vacancies formed is obtained from an Arrhenius relation (see Algorithm 3). This equation has the energy of formation for vacancies a primary variable, and gives the equilibrium concentration for which mass must be moved to a free surface, which of course requires diffusion. The vacancy formation energy, H_f, for ZrN, is assumed to be 0.45 eV. This is assumed to be similar to H_f for TiN, which should at least be a legitimate approximation due to the similar chemical properties the two materials share.

Since diffusion is very slow in ZrN, very high temperatures are required to move atoms large distances, as required to produce the equilibrium number of vacancies. Figure 4.9 shows the equilibrium quantity of vacancies in terms of the ratio $\frac{n_v}{n_0}$ versus temperature for the ranges between 50 - 300 K and 300 - 2000 K. The ratios represent the equilibrium

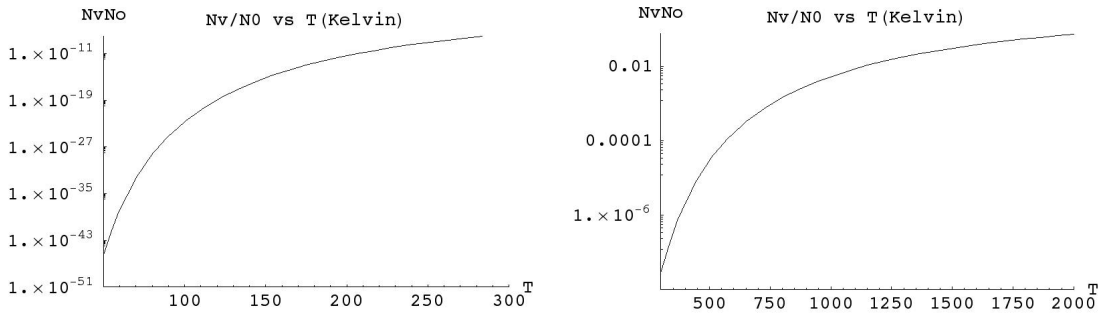

(a) Ratio of vacancies to occupied sites from 50 to 300 Kelvin. This is the range that ZrN sees during cryogenic irradiation.

(b) Ratio of vacancies to occupied sites from 300 to 2000 Kelvin. This is the range that ZrN sees during sintering and reactor operation.

Figure 4.9: Logarithmic plots for the ratios of vacancies to occupied sites on ZrN

vacancy concentrations that would be observed at infinite time, yet they also give an indication of the driving force. The cryogenic temperature range corresponds to irradiation experiments, while the higher temperature range is from room temperature, through reactor operating range, to the processing and sintering temperatures.

It should be noted that during processing and sintering, the times and temperatures used should produce vacancy concentrations closer to equilibrium. To reverse this process when the sample is cooled, the displaced mass would have to diffuse back into the sample and reside on the, vacant lattice sites. Since the temperature is reduced relatively rapidly, from the perspective diffusion rates, all these vacancies are not annihilated through diffusion. This results in a non-equilibrium vacancy concentration.

The diffusion coefficient for nitrogen is about 100 times greater than that of zirconium [144, 145]. This will have an effect during both processing and the cool-down period. Nitrogen vacancies will be produced at about 100 times the rate of zirconium vacancies. During cool-down, the nitrogen also replaces its vacancies at a higher rate, there are many more nitrogen vacancies to annihilate than zirconium vacancies. As the temperature drops below a specific point, the activation energy for diffusion cannot be obtained and the amount of

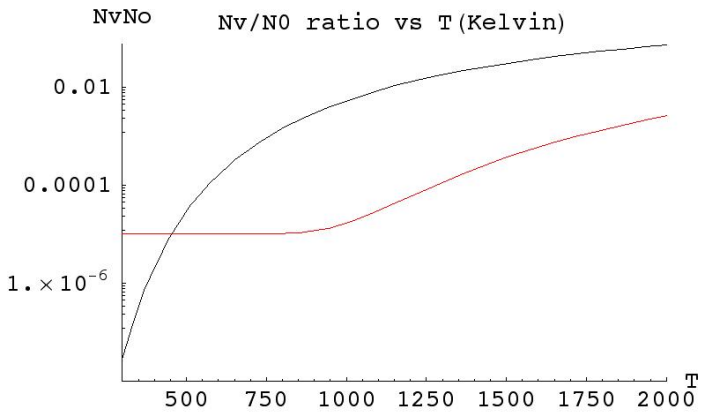

Figure 4.10: Simulated real vacancy concentration ratio vs temperature (red line) and. equilibrium vacancy concentration ratio vs. temperature (black line) in ZrN

vacancies is then relatively fixed. Figure 4.10 shows the same equilibrium vacancy concentration ratio with a symbolic, diffusion-reduced version overlaid in red. The real vacancy concentration never reaches the high-temperature equilibrium amount yet decays rapidly with temperature similar to the equilibrium plot. At lower temperatures, however, the driving force is reduced so the annealing driving force decay will be similar. At some point, this decay will be reduced and stop at a value above the equilibrium amount.

The as-processed material, either received from a manufacturer or synthesized, cannot be fully dense. The processing would have to include a very slow cooling rate under constant nitrogen and thus the expense would be too great. The density of the material is thus lower than theoretical due to this and other factors. Obtaining true 1:1 stoichiometry would be extremely difficult, expensive, and increase the risk of contamination from oxygen. Thus, none of the cubic metal nitrides will show theoretical density, even if equilibrium vacancy concentration is taken into account.

4.2.6.5 Derived Vacancy Concentration

Based on both the chemical analysis and the measured density of the samples, an approximate value of vacancy concentration was determined for both the metal and nitrogen sub-lattices. Within reason, the mass difference between theoretical and measured density is attributed to the vacancies.

In the case of ZrN, the loss of nitrogen actually increases the lattice parameter (refer to Figure 2.23). The increase in volume and loss of mass lowers the density in a nonlinear fashion. At a certain point, the structure begins to contract again. To completely analyze the system, a lattice parameter measurement should be be included in the calculation. By chemical analysis, the amount of nitrogen can be found, to within error, and the true lattice parameter estimated by using the graph (Figure 2.23).

The vacancy concentration can be found from using both methods of density calculation. Optical stereography gives a void volume %. The Archimedes' method gives the absolute density with respect to the volume displaced by a liquid. The Archimedes density is lower than actual because of the included voids. When the void volume is taken into account, a much closer approximation of the true density is achieved. This density, when compared to theoretical density, shows the total missing mass. Then, with chemical analysis, the zirconium site and nitrogen site vacancies may be calculated.

Archimedes' density measurements gave a value of 7.139 $\frac{g}{cm^3}$. Optical stereography indicated $\approx$ 1 % closed pores. The theoretical density is calculated as 7.374 $\frac{g}{cm^3}$, based on was XRD-derived d-spacings and chemical analysis. Figure 4.11 shows the XRD spectra used. The lattice parameter measured was 4.57, which agrees well with published data. The measured Archimedes density is 97 % of the theoretical density. If one takes into account the 1 % pore volume, the density increase to 98 % of the theoretical density.

If a 0.5 % density difference is assumed for the glassy phase present, the density is

calculated to be 98.2 % of the theoretical density. Although there are some assumptions and errors in measurement, this is believed to be a reasonable approximation. This leaves approximately 17 % of the nitrogen atoms missing, or around a 17 atomic % nitrogen sublattice intrinsic vacancy concentration. This assumes the nitrogen sublattice is the only vacancy-producing lattice. This of course assumes the zirconium sublattice has no vacancies, which is not so. Since nitrogen is 45.7 atomic %, the 17 % vacancy concentration would place nitrogen at 41.5 atomic %. Since the stoichiometry has been measured, with some error, it can be assumed that the nitrogen is about 1 % deficient on its sublattice, which makes up for the mass/density difference.

It has been shown that the nitrogen sublattice is much more likely to produce the vacancies, especially given the wide phase field of cubic ZrN [77, 79, 44, 34]. With some dissolved oxygen and carbon, some lattice strain is expected. Since the lattice parameter measured is close to the theoretical XRD lattice parameters, however, the high density measured is considered appropriate.

4.2.7 Nitrogen Uptake: From Zirconium Metal to the Cubic Nitride

Experiments on nitrided zirconium metal have shown that the gas diffuses through the grain boundaries first and at a much higher rate than through the bulk. At 1000°C and 15 psi nitrogen overpressure the diffusion front from the nitrogen into the bulk was ≈ 1 μm in depth after 10 minutes. The grain boundaries were not heavily transformed. Refer to the fractograph in Figure 4.12 that shows the nitrided depth and the plastic fracture through the metal. It was hoped that by doubling the nitriding time would double the nitrided depth. Figure 4.13 shows the fractograph following a 20-minute nitriding at 1000°C. Compared to Figure 4.12, one can observe that the nitrided layer did not grow significantly, yet the fracture surface became brittle and *intergranular*, indicative of heavy nitrogen transport

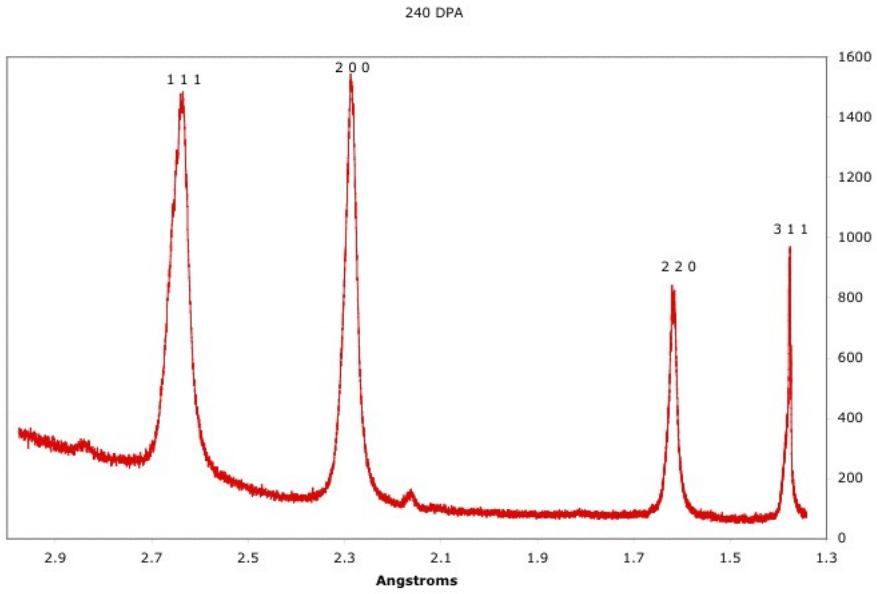

Figure 4.11: d-spacings and indexed XRD plot for virgin HIPed ZrN

and nitriding along the grain boundaries. It is considered that ten minutes does not allow enough time for nitrogen to transform the grain boundaries in zirconium from α to the brittle cubic phase, yet does allow enough time for nitrogen to penetrate the surface in sufficient concentration to produce the cubic phase at a bulk depth of about 1 μm. X-ray photo spectroscopy (XPS) measurements have shown that the surface cubic nitride has a concentration gradient indicative of a diffusion front.

In an attempt to produce a nitride sample at a temperature of 1000 K (simple to calculate thermodynamics), a zirconium metal foil was heated under pressurized nitrogen gas (15 psi) at 727°C (1000 K). General observation of nitriding at 1000°C (1273 K) showed an almost instantaneous change in color from the metallic grey to gold, which was used as a metric. With 45 minutes at 730°C, no color change was observed. The temperature was increased and the sample was observed as the temperature rose. When the temperature exceeded 865°C, the sample began to show the gold color. The significance of this temperature

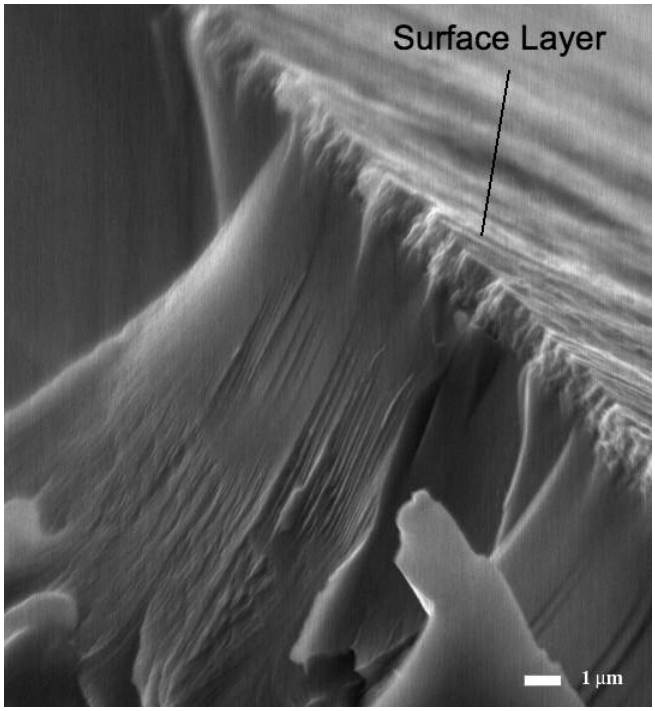

Figure 4.12: SEM fracture image of zirconium nitrided for 10 minutes at 1000°C

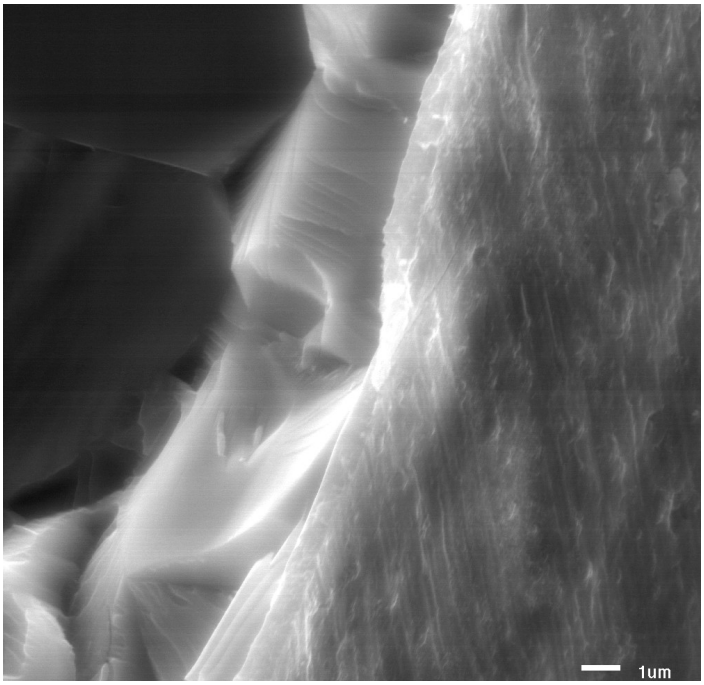

Figure 4.13: SEM micrograph of zirconium nitrided for 20 minutes at 1000°C

effect is that zirconium metal transforms from hcp to bcc (α to β) at 863 °C.

The literature provided insight into diffusion into the β rather than the α phase, . The bcc structure is less closely packed and allows the nitrogen to penetrate the surface and diffuse more easily. The bcc, versus the hcp, may also have a much higher catalytic ability. At the surface, N_2 must be broken into two nitrogen atoms before any diffusion can take place. Thus, the process is as follows:

- physisorption of the N_2 to the surface zirconium atoms,
- the surface then catalyzes the breaking of the triple bonds ($N \equiv N$),
- these atoms are then able either to re-bond and desorb, bond with the zirconium atom neighbors, or diffuse into the structure.

The surface activity of ZrN must have a catalytic effect on the strongly bound N_2 molecule. Higher rates of nitrogen uptake is reported with the use of NH_4 gas, as it is easily decomposed to NH_3 and a free nitrogen atom. Thus, the rate-limiting step appears to be the breakdown of N_2. Oyama has studied the catalytic properties of ZrN as well as other cubic nitrides with respect to hydrocarbons [59, 60, 61, 62].

The fact that the bcc structure showed nitriding immediately at its lowest stable temperature provides substantiation that the bcc structure *may* have a catalytic advantage over the hcp. Once dissolved into the bcc structure, the transformation from bcc to hcp will take place at relatively low nitrogen concentrations. This transformation is very similar to the ω phase transformation observed in titanium, or more closely to the η phase transformation in TaN. It is distinguished from the η-TaN phase by the more normalized c/a relationship to the parent bcc phase. For ZrN the relationships are $a_{hex} \approx \sqrt{2a_{bcc}}$ and $c_{hex} \approx \sqrt{\frac{3}{2}a_{bcc}}$ [63].

The ω transformation is a relationship between bcc and hcp structures in that the bcc has an atom in the octahedral interstitial. The symmetry of the hexagonal nature of the $\{111\}$ plane between two unit cells forms combined equilateral triangles. The two triangles form the base of hexagonal symmetry. The bcc structure of a transitional metal such as zirconium cannot hold an atom the size of nitrogen in its octahedral site, therefore it is theorized that it moves from ω symmetry to η form in that the bcc structure is distorted. When an atom is placed into the octahedral interstice, the cell will stretch or distort to accommodate the atom. Figures 4.14 (a) and (b) show the position of the ω and η interstices. It is simple to observe the distortions that would resolve the mismatch between the two interstitial sites. The ω interstitial atom will distort the lattice by pushing the two neighbors outward, while the η interstitial is centered in the triangle formed by the two center atoms and a corner, and will thus push these out evenly.

Nitrogen sits off-center to the octahedral site on the plane formed by the $\langle 121 \rangle$ direction. This results in lower symmetry in that the nitrogen atom becomes five-coordinated (refer to Figure 4.14 (b). The distortion elongates one direction on the bcc cube and produces a longer *a* lattice parameter. This distortion arrangement has been measured in bcc VN, and the measured lattice parameters of the bcc ZrN suggest a similar situation. Thus, the bcc phase distorts in a bcc $\rightarrow \omega \rightarrow \eta$ phase transformation that forms the hexagonal symmetry such that the α phase is formed at low nitrogen concentrations [63, 146].

It can be seen that the bcc phase must distort to have nitrogen in its interstices. This ω-like distortion can be considered as a compensation for the atomic volume, but it has been found that the overall effect is that the melting temperature is increased with nitrogen addition. This suggests that the electronic contribution of the *p* orbitals from the nitrogen is overcoming the increased strain from volume mismatch [58]. As the nitrogen *p* orbitals form covalent bonds with the metal, the lattice internal energy increases such that it takes

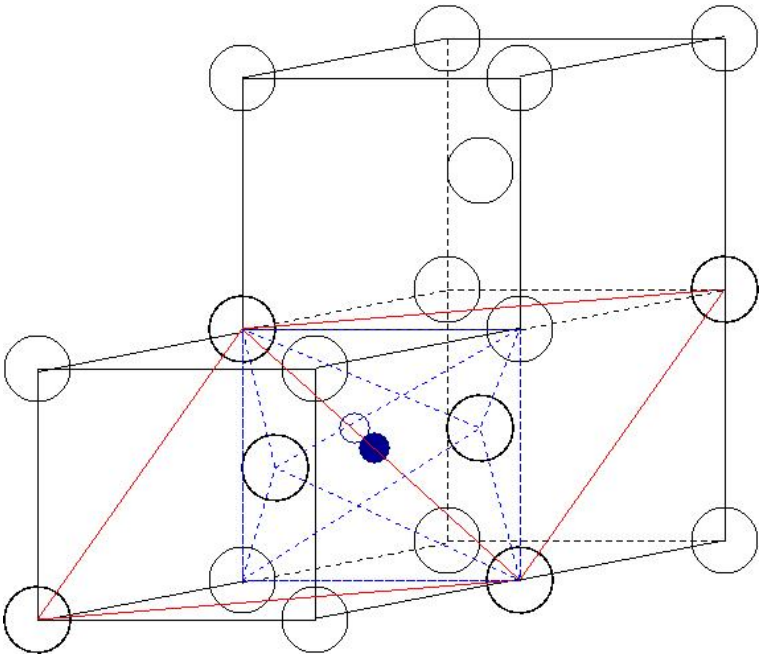

(a) ω and η phase relation to bcc. Note the solid circle in the octahedral center is ω while the off-center hollow circle is the η distortion

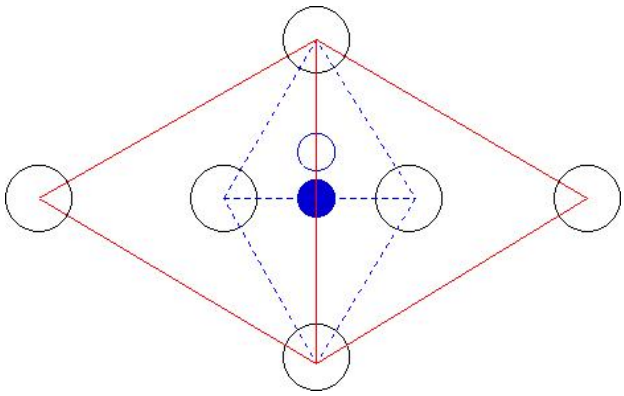

(b) ω and η phase interstice positions. Note: These are pre-relaxation conditions. The lattice relaxes differently depending on the interstitial size and position. This is not a true hexagonal system until the interstitial nitrogen moves and the structure relaxes into the α -ZrN phase

Figure 4.14: ω and η phase transition shown with respect to bcc

more thermal energy to break the nitrogen-metal bonds thus increasing the melting point.

The α phase had been shown to be stabilized by dissolved nitrogen, although, as reported above, it does not appear to dissolve nitrogen easily from the gas phase. This structure is then a stabilized form of the hcp zirconium metal structure, with nitrogen in the octahedral interstices. It has a *c* lattice parameter of 5.14 Å and an *a* lattice parameter of 3.232 Å. Alpha ZrN seems to be the zirconium metal in structure as it has much less interaction electronically from the nitrogen and, as a result, is more alloy-like than ceramic-like. Though it seems difficult to produce α ZrN at low temperatures in N_2 gas, it been shown to be formed much more easily from the β phase of Zr, moving through the ω and η transformations as stated above. The η phase shifts the symmetry from cubic towards hexagonal, similar to the hcp zirconium metal. The lattice parameter shifts as well, allowing nitrogen to fit within the interstices (refer to Figure 2.17).

4.3 Overview of Irradiation Damage Assessment

The analysis of irradiation damage is application dependent. A material may show little change with respect to one specific property and then fail with respect to another.

A reactor material, must not, within its lifetime, be damaged to the point that it cannot perform the tasks for which it was designed. For a fuel, it must not swell and cause undue stress to the fuel rod, it must be capable of holding its structure under all but the worst conditions, and it must maintain suitable reactor performance throughout its life. This means that it must not change its structural phase and any dramatic difference in physical properties.

In this study, the methods used to determine the damage were subject to the tools available. Damage was produced by implanting with ions, usually heavy inert gas ions such as

xenon.

Simulation was used to predict and calculate displacements. It is a standard tool in the electronics industry, and is well accepted in the scientific community for stopping ranges and damage. Electron microscopy was used to evaluate the damage at the microscopic level, and evaluate crystal structure for changes in square nanometer areas. GIXRD was used to show damage to the crystal structure with minute changes in the d-spacings and evolution of phase changes. Helium release studies showed how the accumulation of displacement damage altered the diffusion and trapping of helium in the structure.

4.3.1 TRIM Simulation

TRIM (Transport of Ions in Materials), or more notably SRIM-2003 (Stopping and Range of Ions in Matter), is a Monte-Carlo simulation program written by J.F. Ziegler, which predicts the range and trajectory of ions implanted into a material [120]. TRIM calculates the penetration of an ion accelerated into a material by either the LSS theory or KP theory (with ZBL modifications). It has a graphical interface and can either quickly calculate the stopping range of the ions implanted or give a detailed distribution of the ions implanted, the displaced atoms, and the displacement damage produced by each element. Multiple layers of different materials may be used with combinations of gases, liquids and solids.

TRIM is a standard program used by scientists studying implantation depth, trajectory, and irradiation effects. It is generally considered to be useful for within 10% of the actual distribution, which is quite accurate for a simulation running on a personal computer.

Main sources of errors are wrong values (discussed below) being used for the displacement threshold energy, or the density, the “Z error”, and the fact that TRIM does not use any crystallographic information. As the mass of the atoms increases, the error in predic-

tion increases. This is known as the "Z error". It is an accepted error, and is within the 10% total. Crystallographic information is especially important when the grains observed are large or textured, or there is any possibility that there may be a significant amount of ion channelling. This is when the crystal structure is aligned such that the probability of collision is at a minimum and implanted ions move further before causing a collision cascade. As defects accumulate with high displacement damage, however, the "channels" become increasingly filled and this error is greatly decreased.

4.3.1.1 Assumed Parameters

Of great interest is the displacement energy, which is unknown for many materials. The displacement energy is the amount of energy needed to displace an atom from its lattice site. Tabulated energies are available in the literature, or, if unknown, TRIM makes some guesses. 40 eV is a typical number due to its simplification of some of the calculations, although 25 eV is a common E_d for metals. E_d is a variable based on the structural changes of a material. For example, ZrN has been shown to have a nitrogen E_d of 5 eV when the lattice is full of vacancies, which in this case arrange themselves into a superstructure. The measurement of the nitrogen E_d was performed with increasing accelerating voltages during TEM observations in which a change of diffraction-based diffuse scattering, was indicative of vacancy ordering [65]. This low value is explained by the deficiency of nitrogen atoms on the sublattice, which allows a much easier displacement than with a fully occupied lattice.

The material's atomic density is also critical, though this can be calculated if not actually known. Stoichiometry is another value of concern that affects the overall probability of target interactions.

4.3.1.2 Parameters used for ZrN

ZrN was assumed to be stoichiometric and fully dense. The density predicted by is TRIM incorrect. Standard implant energies was 300 keV for Xe at 0° incidence angle, while helium was simulated at low energies of 17 keV at 60°incidence angle. Many different ions were simulated at different energies, but the parameters for ZrN, once established, were not changed. Relative damage and implanted species are reported as the peak values obtained from the plot.

A standard plot is shown in Figure 4.15 (a). This plot shows that the depth of implanted xenon spreads beyond 100 nm and peaks at 55 nm, while the damage peak is at 35 nm and asymmetrically spreads to over 100 nm. Damage taken from this plot would be about 40 dpa[1] and about 2.25 atomic % xenon, both peak numbers. Although plots such as these are used to tally damage, actual damage is much more difficult to assess. The damage simulated assumes no defect mobility for annihilation or other effects. Damage is tallied only as the amount of vacancies produced (i.e. Frenkel pairs). Under cryogenic conditions, this plot is considered to be more realistic and thus the total accumulation of damage is stated as though the actual amount of damage remains, although normally most is annihilated within the cascade event. At elevated temperature implants, the plot is used as a guideline to the total amount of damage produced.

4.3.1.3 Conversion from TRIM to DPA and Atomic %

TRIM produces a standard output in displacements per ion·Å, which is independent of the amount of ions introduced. The accumulated ion damage is statistical and not additive.

[1]Different versions of TRIM and SRIM use slightly different versions of the ZBL algorithm to calculate the vacancy population, and thus the actual simulated peak numbers may vary from 40 to over 50 dpa for $10^{16}\frac{Xe^{++}}{cm^2}$ delivered at 300 keV. Depth information is not changed. It was decided to use the conservative lower damage number rather than over estimate.

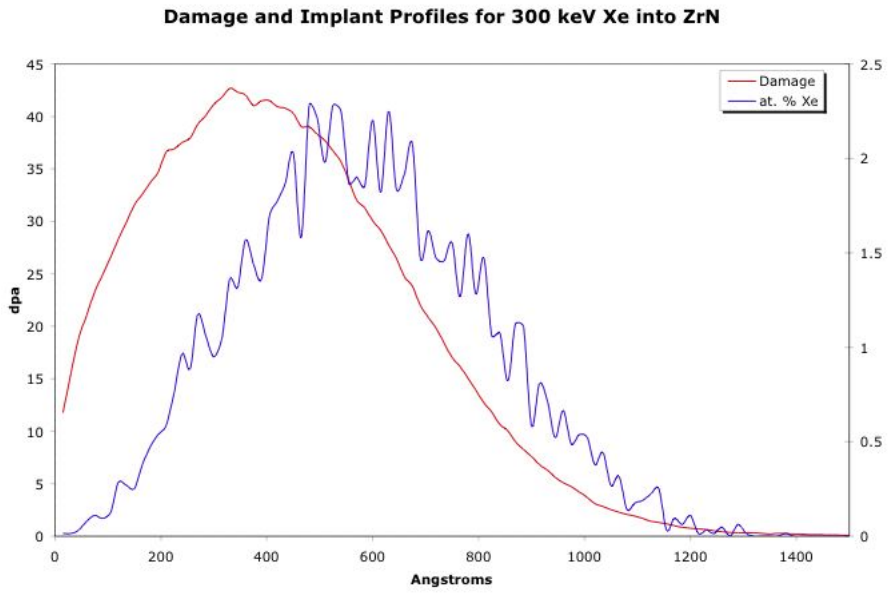

(a) Plot of 300 keV Xe implanted into ZrN showing distributions of both damage and Xe. Plot is produced for a fluence of $10^{16} \frac{Xe^{++}}{cm^2}$

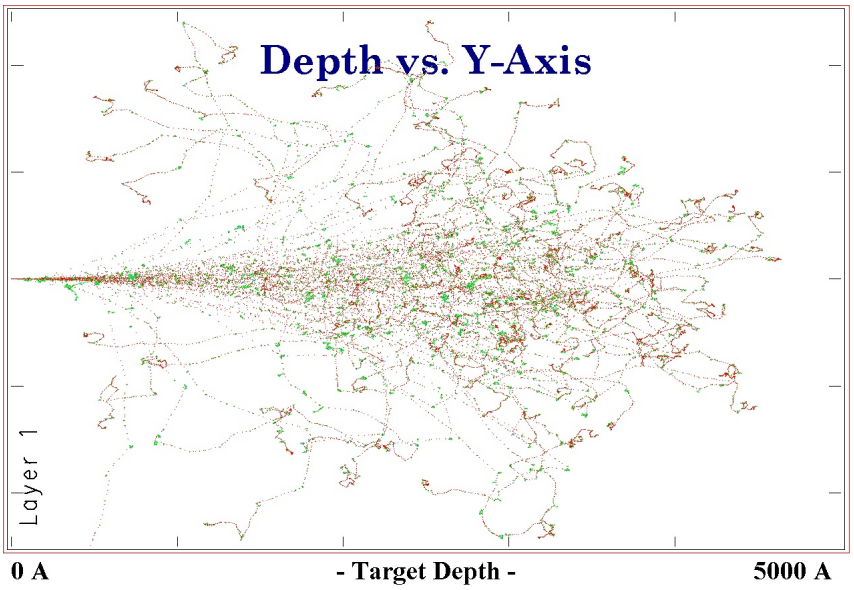

(b) Sample trajectory of He implanted into ZrN at 100 keV. Different colors show the cascades of Zr and N.

Figure 4.15: Sample TRIM simulation plots

Table 4.3: Parameters Used for TRIM Predictions with ZrN

Property	Value
Density	7.25 $\frac{g}{cm^3}$
Atomic Density	$8.3\times10^{23}\frac{atoms}{cm^3}$
ZrN_{1-x}	x≈0
Displacement energy for N	40 eV
Displacement energy for Zr	40 eV

Algorithm 4 Convert TRIM output to dpa

$\frac{displacements}{ion\times\mathring{A}}$ is multiplied by $\frac{10^8\frac{\mathring{A}}{cm}\cdot Fluence\frac{ions}{cm^2}}{8.23\times10^{22}\frac{atoms}{cm^3}}$ to produce displacements per atom at any depth, where *Fluence* is a multiple of 1×10^{16} to produce 40 dpa at peak with 300 keV Xe

A run of 10000 to 20000 ions is sufficient to produce a relatively smooth distribution. Converting this distribution from TRIM format to dpa and atomic percent requires dimensional analysis. Knowledge of the atomic density, which can be calculated by hand or found in the TRIM output files, is required.

Algorithm 4 is the formula used to convert the distribution to dpa, given a known fluence. TRIM outputs data in the form of a histogram with 20 bin sizes. Each bin is a step into the material's depth measuring total displacements, which are a sum of all vacancies formed as well as replacement collisions. The displacements are tallied as $\frac{displacements}{ion\times\mathring{A}}$, which is a generic statistical distribution. With a known fluence, the output is converted to displacements per atom (dpa).

A similar method is applied to implanted ions. The output is multiplied by 100 to produce a percentage scale. See algorithm 5.

Algorithm 5 Convert TRIM output to atomic %

$\frac{number}{ion \times \text{Å}}$ is multiplied by $\frac{10^8 \frac{\text{Å}}{cm} \cdot Fluence \frac{ions}{cm^2}}{8.23 \times 10^{22} \frac{atoms}{cm^3}} \cdot 100$ to produce atomic % at any depth, where *Fluence* is a multiple of 1×10^{16} to produce 2.5 atomic % at peak with 300 keV Xe

4.3.2 Ion Irradiation

Ion implantation is the primary tool for the fission-product radiation-damage scientist. It is used to simulate large, heavy fission products that cause damage in the lattice, place gases, change chemistry, produce defects, etc. Rate, dose and temperature are controlled by the operator. Different elements can be implanted to simulate damage from a nuclear reactor or to modify the surface structure into a thin film, alter the chemistry, or produce extrinsic defects.

Limitations of the experimental technique are varied based upon the desired data. Kilovolt-energy ion irradiation is a standard technique in radiation damage studies in ceramics. The damage is generally produced at cryogenic temperatures with an inert gas such as xenon or krypton. These elements are sufficiently heavy to produce large damage cascades, and yet have little to no effect with respect to the chemistry of the host lattice. The real damage is produced by the cascade which may displace many orders of magnitude of lattice atoms for each implanted atom. The same effect occurs with high-energy neutrons and fission products.

Although the neutrons and fission products occur at MeV levels, the collisions of interest mostly are formed by the reduced-energy particles of keV velocities, similar to those that may be produced by a conventional ion implanter. One critical difference that should be addressed between an ion-implanted sample and one from an in-pile experiment is that the irradiation damage is at the surface, while an in-pile experiment damages through the bulk. The near-surface effects do provide a relatively close free surface that allows defect

annihilation that does not occur in the bulk. This is especially true for an *in-situ* irradiation in TEM, as the damage produced is very close to *two* free surfaces.

Cryogenic irradiation, although not a true service condition, is very useful in determining the ability of the lattice to withstand the largest amount of cascade defects. These defects produced by the initial cascade rush to self-annihilate, yet, by cooling the sample, this process is slowed such that the accumulation is faster than the decay due to annihilation. This allows for a metric from the peak calculated displacement damage such that many materials may be compared. The damage is generally increased until amorphization, at which time the damage threshold of the lattice is semi-quantitatively known.

4.3.3 Ion Implantation Operation

The ion implanter used was a *Varian/Extrion* with the capability for an accelerating voltage of up to 150 keV, which can be multiplied by the ionic charge. The ions are produced in a high-temperature source chamber, and the phase of the feed material determines how it is supplied. A gas is introduced via a gas feed-tube. Liquids are heated and the then vapor is swept into the gas-feed tube by argon gas. A solid is place in the source chamber, and either melted and vaporized slowly, or a chemically active gas, such as carbon tetrachloride, is flowed over its surface. Carbon tetrachloride (CCl_4) helps reduce the enthalpy of vaporization and allows some more refractory, low-vapor-pressure materials to be vaporized.

The vaporized material is fed into a plasma arc that strips electrons off the elements. The ionized elements are attracted to the anode and accelerated out of the source. They then move past the source magnet, which is arc-shaped, while the magnetic field directs the beam through the implanter's column. The source uses accelerated ions with specific mass and charge and selects the isotope based on its magnetic moment. A doubly charged ion is

deflected twice as much as a singly charged ion, and thus its apparent mass is halved.

Each isotope is easily separated by mass and relative amounts, which produces a "fingerprint" of the given element. Xenon is observed to have five main isotope peaks with three that are relatively large in proportion to the others. Two are overlapping and are sometimes used to increase the total current. This comes at a cost of accurate lens aiming and hence also of even distribution across the sample holder.

The moving charge and chosen mass is accelerated by cathodes through a series of apertures. Rastering and steering plates alter the path of the charged elements to produce an elliptical area on the endstation of the implanter. This endstation, with different holders, holds the sample with the desired environment.

Source gases are either injected as a gas, or produced by vaporization of solids (or liquids) under heat and vacuum. Gas flow is restricted by pressure differentials in the vacuum by means of a metering valve. Measured gas addition is monitored by change in vacuum, which when the implanter is clean will run to less than 10^{-7} Torr. Normal operation with gas addition reduces the vacuum to about $2.5*10^{-5}$ Torr.

4.3.3.1 Different Sample Holders

The samples may be held with different sample holders in the endstation. The endstation has provisions for a top-loaded sample holder, or with some modifications, loaded from the sides or the very end. Within the endstation, there is a copper cylinder that surrounds the sample holders. This copper cylinder is a cold-finger, or a cooled protrusion that attempts to adsorb stray gases such as organics from diffusion pump oil, before they adsorb to the surface of the sample.

The standard sample holder has been designed for ambient- or low-temperature use. It is a hollowed-out block of stainless steel with a roller-bearing o-ring-sealed top flange. It

has one thermocouple passed through and sealed in the block. Samples are bolted, glued, or taped to the surface of the holder. Cryogenic temperatures are achieved when the cavity is filled with liquid nitrogen. Temperature is monitored by the sample-holder thermocouple and the cold-finger thermocouple.

Similar in design to the cold stage, the hot stages differ by use. They may be used for room temperature, or, with heaters, up either to 350°C or 650°C. The design is for the cavities to be filled with a thermally conducting liquid that can sustain the high temperatures desired for long periods of time. The liquid used is a MgO solution. The difference in design is the size; the large sample holder is similar to the cold stage in size, yet the thermal mass only allows the holder to reach 350°C. The higher-temperature stage is much smaller and therefore can attain the higher temperature.

A modified stage was constructed that theoretically could produce temperatures up to 1800 °C. This holder was designed with boron carbide elements with a half-inch diameter heating surface. Samples were held with tantalum wire and thermocouples could be placed directly in contact with them. With this stage, ZrN was irradiated at 800 °C for a time of six hours. The heat up and cooling time is in minutes and considered negligible. This stage not only allows higher temperature irradiations but also no lag time for a thermocycle.

4.3.3.2 Freeman Source

The standard ion source used is a Freeman based source. A Freeman source is a heated filament, in this case tungsten, that either boils the solid's surface into or uses the gas stream, which then produces a plasma at the filament. The plasma, composed of different charged fractions of the gaseous species, is then pulled into the accelerator chamber via the bias plate. The ions are accelerated and then passed through the source magnet to be separated.

The two standard sources commonly used are the gas and the solid source. The solid source differs only that the gas flows over a crucible that is near the filament. Solids are heated by the filament and, if need be, CCl_4 can be used to assist in gasification of the hot solid.

Many elements, especially those that are highly electronegative, or stable, require "assistance" in removing electrons. In such cases a carrier gas is used such as argon, which is easily ionized. The free electrons in the plasma "assist" in the removal of the electrons from elements such as helium.

Other elements were approached for irradiation studies, such as cesium and iodine. The experimental idea was to use a "set" of elements with similar masses, but with very different chemistries. From the periodic table and fission-fragment plots, typical fission products of interest are iodine, xenon and cesium. These have masses very near each other so damage would be almost the same, yet iodine would be very electronegative with a strong *p* character such that it would attempt to "steal" an electron to fulfill its octet. Cesium, on the other hand, is a one-electron *s*-block element.

An experiment was designed to try to get the gaseous form of iodine and cesium. A *Stanford Research Systems* RGA 200 was connected with a T-connection to a turbomolecular vacuum pump and a small *Swagelock* tubing and petcock system. The *Swagelock* system was terminated with a plug, which in this case served as a sample holder. The sample was heated dry and/or used with a drop of carbon tetrachloride. The CCl_4 was used to break up the surface such that it allowed some materials with low vapor pressures to release atoms to the gaseous state.

Cesium, whether cold or hot, with or without CCl_4, gave no usable gas. With a relatively high vapour pressure in the liquid stage, which occurs at 29 °C, it is considered that, being very electropositive it is attracted to and adheres to any free surface such as the stainless-

steel lines leading to the RGA. This was not considered acceptable or usable. Iodine, however, showed ease of use when under vacuum. The limiting factors were the iodine surface area and the vacuum at the surface.

Although cesium was not available for use, iodine was used with a simple in-line *Swagelock* T fitting in-line with feed gas. Argon as a gas and large iodine crystals with relatively small surface area were found to give a quite usable iodine beam for implantation. The current was lower than for say xenon, but a level of $1 \times 10^{15} \frac{I^+}{cm^2}$ was implanted and confirmed by RBS. Given the lack of a cesium beam, time and funds did not allow further experimentation into this area, and further work was not pursued.

4.3.3.3 Ion Implanter Operation

Samples are mounted and inset into the endstation. If the sample is to be cooled, LN_2 is added and the temperature monitored. The approximate temperature of the sample is 100 K. If the standard hot stage is used, a solution of MgO is added along with the heating element, and again monitored until the desired temperature is reached. Once ready and under vacuum, the filament is heated to burn off any organics and the source gas is added. Argon may be added to provide the free electrons to help form a stable plasma if needed. A small amount is added with helium, but xenon ionizes easily by itself.

By means of the source controls, the ion beam of the proper isotope is chosen. Isotopes have different energies and amounts due to charge and mass, and therefore can be identified by this "fingerprint". This is especially important if using a carrier gas such as CCl_4 is used, which has many mass and charge fragments (approximately 20) which must be weeded out. Fragments can be C^+, C^{2+}, C^{3+}, Cl^+, Cl^{2+}, Cl^{3+} , CCl_3^+, CCl_2^+, CCl^+ , etc., with many combinations of elements. By following the mass, charge and energy, these elements can be systematically eliminated.

Algorithm 6 Relation for mass/analyzer settings for the ion implantation system

$$B_x = B_{Ar}\sqrt{\frac{m_x}{m_{Ar}}}$$

B is the analyzer setting (magnetic field) and *m* is the mass for either argon or "x" element. As an example, helium is unknown, but the masses of argon and helium and the known analyzer setting for argon, allows the analyzer setting for helium to be found.

$$B_{He} = 3.7\sqrt{\tfrac{4}{4}0} = 1.17$$

Once chosen, the proper isotope is steered by a number of controls that affect the shape of the beam as well as its rastered distribution. Four Faraday cups are in place near the entry of the endstation to help monitor the charge distribution. The Faraday cups measure the charges at four corners of the beam with reference to each other and the area that they pass. The smaller the count, statistically, the more concentrated the beam. These Faraday cups are also used to count the total charge, and, by division, the total ions.

A counter is set up at a limit, connected to the Faraday cups, that measures the total electronic current. This current is converted to the ionic charge striking the sample area between the Faraday cups. The total charge is measured, and thus the total fluence of charge. A multi-charged ion is over counted by the ionic charge, so the total current is divided by this charge. In this way, the total fluence is counted. The flux can be obtained by the time for which the current was delivered, or by the direct current readout by the Faraday cups.

Charts are used to find the general analyzer/mass relation. These are calibrated with a couple of known elements such as argon and helium for a select accelerating voltage. If the element or isotope is unknown and the chart/calibration is out of date, the equation shown in Algorithm 6 allows a quick method of finding the general analyzer setting. Figure 4.16 shows an example used for low-energy implantation.

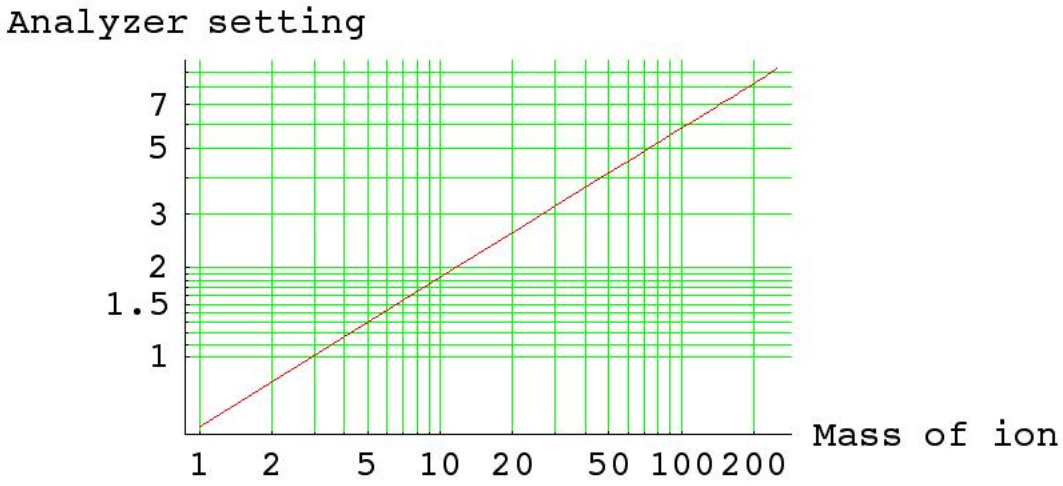

Figure 4.16: Mass-analyzer settings plot for implantation masses

4.4 SEM

Scanning electron microscopy was used to characterize the surface of the material and also to obtain chemical information. A JEOL 6300 FEG SEM with a *PGT* EDS unit was the primary microscope used. It has a field emission electron gun for high resolution. Surface topography can be observed at very high magnifications using secondary electron mode. Energy Dispersive Spectroscopy (EDS) is used either in spot mode, line scan or map mode.

Most images were taken with the secondary emission mode, but backscatter mode was used to find Z-contrasted areas. This was useful for finding areas with contaminants that would later be identified with EDS.

Backscatter SEM uses the electrons that recoil due to Coulombic interaction. The electrons are recoiled with an energy dependent on the atomic number, or Z. The heavier the material, the harder the recoil and the brighter the image. Very different amounts of a

material may be readily observed across phase boundaries, diffusion barriers, etc.

4.4.1 EDS

Electron Dispersive Spectroscopy is a useful technique to obtain chemical information on the material in question. It is based upon the principle that the electrons penetrate into a depth of the surface and are scattered. As they pass the electron clouds of the sample elements, energy transfer causes the excitation of the shell electrons. The electrons are excited to a higher energy state and then relax to the ground state, emitting a photon that is equal to the energy difference. This photon is of very high energy and has a wavelength in the x-ray region. Each element has specific shell energies and differences between them. Thus, each element will emit characteristic x-rays due to their individual shell energy distributions.

A *PGT* EDS unit attached to the SEM was used in conjunction with a *Sun Sparc* workstation. Data are collected on the Sun and printed due to the lack of any electronic transfer media. The condenser aperture was set at the second largest and the samples were either set flat or slightly tilted toward the detector. The spot size was reduced to gain the desired dead time of 20%, with an average setting of spot 3. Spot collections were collected in 100 seconds, line scans for 10 minutes, and dot maps for 30 minutes.

EDS was helpful with irradiated ZrN to try and observe where the xenon was implanted. This was used on TEM cross-sections and masked SEM samples. Implantation of a large enough amount of xenon allowed its characteristic peak to be observed. Difficulties arose due to the fact that the xenon characteristic peak lies directly on top of the ZrN sum peak. The only way to determine whether xenon is present or not is to observe a distinct change in this particular peak height.

EDS either can be used in spot mode, holding for a continuous dwell, or the spot can be moved, and the information stored and reviewed graphically. A line is slowly tracked

across the sample and a line-scan is produced. With a slow-moving rastering of the probe, a detailed map can be obtained. Each method has its pros and cons. For observing a distinct chemical change, such as dissolved xenon, the line-scan is the best choice. It tracks from the implanted to the non-implanted region so that the observation of where xenon is present can be obtained. This information is helpful, coupled with AFM to track where the xenon may cause swelling.

4.5 AFM

Atomic force microscopy is an extremely topographically sensitive technique with very high resolution. It is based upon the principal of the atomic force deflecting the stylus as it approaches contact. The instrument compensates by moving the sample and stylus to achieve a near-constant tip-to-surface distance. The stylus is slowly rastered across a chosen area of the sample and, with feedback on the stylus deflection/compensation, the topography is precisely measured.

AFM was used in conjunction with masked implantation and nanoindentation experiments. The stylus between the implanted and masked areas, and the volume change could be observed with resolution to the nanometer level. Highly polished samples were masked over part of their exposed area during implantation to produce two areas, one with and one without ion irradiation damage. With nanoindentation, the indent can be analyzed directly for volume change.

The area selected for masking is either painted over with silver paint, or masked with a metal clamp such as a screw with a washer. Masked samples used for AFM swelling studies were masked with a piece of tantalum foil held in place by screws. Tantalum is a very heavy metal so that it is much more difficult to sputter off the very edge of the mask.

This reduces the chance that the accelerated ions will impact and sputter off elements from the masking edge and push them into the ZrN sample producing an artificially large amount of implanted elements. By conservation of momentum, the tantalum atoms would have the least amount of velocity as a sputtered atom, as compared to silver and iron.

Computer correction for uneven surfaces, etc., was used in conjunction with the AFM. This allowed correction for surface irregularities, slopes from non-parallel top and bottom, etc. Direct measurement was taken from the corrected computer data.

4.6 GIXRD

Grazing Incidence X-Ray Diffractometry (GIXRD) is used to determine the effect that the ion irradiation has on the crystal structure. GIXRD requires a special configuration of an XRD in that the emitter and detector are decoupled. The x-ray emitter is set at a discrete angle and the detector is swept along an arc. The very low angles, or grazing incidence angles, produce x-ray reflections from very shallow depths. This very shallow depth of reflection can be changed by changing the incidence angle. GIXRD is used predominantly in thin-film characterization, but can also detect crystallographic changes from ion -modified surface layers.

A *Bruker* AXS x-ray diffractometer was used with the decoupled goiniometer, and fixed-angle emitter. This configuration allows the x-rays only to hit the sample at the set angle of incidence. Copper K-α x-rays are used with the incidence angle set at either 1 or 0.5 degrees. The goiniometer was normally programmed to be swept from 30° to 70°, with a 1 second dwell at 0.01° increments. The samples were highly polished and cleaned with isopropanol. Proper height and flatness were guaranteed by means of a moldable clay backing behind the sample. The clay is an amorphous synthetic material that will not cause

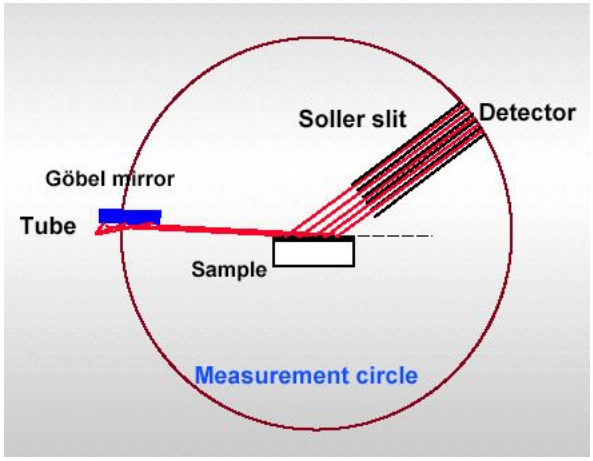

Figure 4.17: Grazing Incidence X-Ray Diffractometer geometry with Göbel mirrors for a parallel beam [147]

any contamination of the data. The sample is pressed into the sample holder with a glass slide and compression press to form the clay. Height and flatness are checked with a thick, flat, glass square that fits into the sample holder above the sample. Deviations in height are observed by fringes.

4.6.1 Increasing Irradiation Damage Measured by GIXRD

A single sample was used for a controlled experiment of increasing xenon implantation dose. The fluence chosen was $2 \times 10^{16} \frac{Xe}{cm^2}$, which equates to approximately 80 dpa at peak. The implantation was done at LN_2 temperature. A sample was cut and polished to a high luster. This virgin sample was run with the GIXRD at both 1° and 0.5°. The sample position was noted for repetition. This same sample was then implanted with xenon to produce the 80 dpa, and then run in the GIXRD at the same incidence angles. This process was repeated two more times, with the same sample achieving 160 and 240 dpa at final.

RBS was performed on the sample at its second and final implantation to observe for indications of surface loss due to sputtering effects. At 240 dpa, RBS showed signs of

sputtering, yet at 160 dpa there were no such signs. On similar samples implanted up to 200 dpa, RBS again showed no signs of sputtering losses. Sputtering means that the loss of surface atoms is at a sufficient rate to compete with the rate of xenon implantation. The sputtering reaches a limit at which the maximum amount of damage and implanted dose are achieved. Increasing the fluence has no effect on the damage accumulation.

4.7 Nanoindentation

Nanoindentation is a technique in which a very small diamond indenter tip is forced into the surface of a material. The depth to which it penetrates is very small, and thus it is very surface-sensitive. It measures the material's surface elastic constant and hardness.

The nanoindenter is targeted via computer on many areas to negate the effect of grain orientation or uneven surfaces. The indenter is pushed into the surface and a load cell measures the resistance to penetration, which measures hardness. While penetrating the material, the indenter oscillates up and down slightly, measuring the spring-back, or stiffness of the material. Both are tracked with depth.

The nanoindenter tip is a three-sided pyramidal (cube corner) diamond with a 20 $^{\circ}$ angle from the flat. This indenter is pushed into the material with a select load. The resistance of this load is measured as is the displacement. When the penetrator is first moved into the sample, the tip, which is never perfectly sharp, gives some error. As more of the indenter is moved into the sample, this error is decreased geometrically due to the increasingly near perfect pyramidal surface-to-tip area ratio.

Errors also arise from the surface never being ideally perpendicular nor flat. Other sources of near-surface error are surface effects due to chemistry, such as oxidized monolayers, and surface reorientation effects. Due to these very near-surface effects and the

non-perfect tip, the first 50 nm of penetration data are not included for analysis.

4.7.0.1 Hardness

For the tip to penetrate, the material must displace volume by either elastic or plastic deformation. The resistance to plastic deformation is the materials' hardness, and by this method is rated on a GPa scale. Plastic deformation occurs when dislocations are moved, and the resistance to this is a measure of the dislocation motion and the interference with their movement. The interference to this motion is controlled by point defects, other dislocations, and grain/phase boundary interactions.

Hardness, by its nature, is then an extrinsic property. It is controlled by outside influences, the point, line, or planar defects, and not the intrinsic chemistry of the system. Due to these extrinsically controlled defects, hardness can be manipulated through annealing, heat treating, working, etc., as ways of manipulating the factors that directly control the defect population and interaction. Dislocation motion is the main contributing factor to the plasticity of a material, and anything that interferes with this motion will increase the hardness as well as yield stress.

Hardness measurements are susceptible to error as stated above. In the raw data, the change in hardness can be observed due to these errors (Figure 4.18). The sudden increase and then decrease shows this effect. Hardness data were evaluated over the range of 50 to 100 nm and, as the tip penetrated further, the substrate below with much less or no damage could be observed.

4.7.0.2 Elastic Modulus

Modulus, or stiffness, of a material is its elastic response to applied stress. It is a function of the chemical bonds between the elements of which the lattice is composed, the

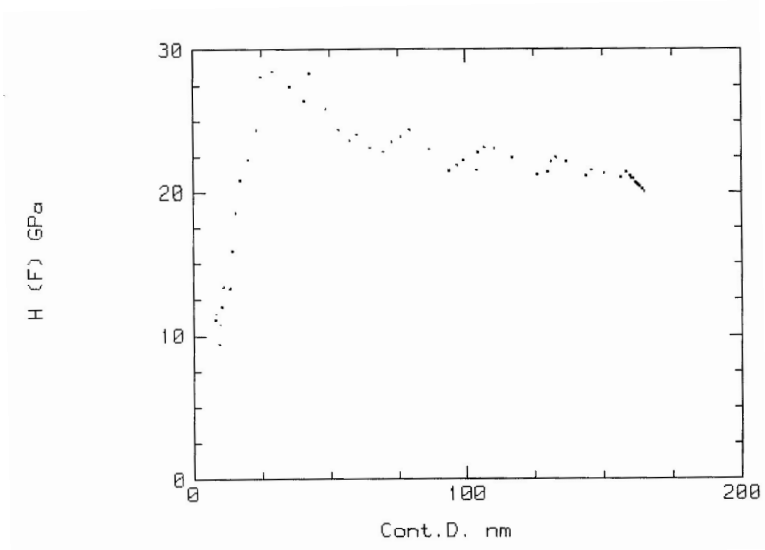

Figure 4.18: Sample hardness data (raw data plot) with x-axis shows depth while the y-axis shows hardness

strength of the bonds and the bond's response to bond length change, i.e. the "Hookien spring". The electronic interactions that form bonds do so to reduce energy of the system. The motion of atoms in a lattice is Brownian, yet are kept in relative place by these bonds. The atoms can move slightly from their ideal location by thermal vibration, but are always brought back into position. This constant pulling back has a spring-like nature, and thus is simply modeled by Hooke's law.

The chemical influence on the modulus can be explained by a Lennard-Jones plot. Figure 4.19 shows the energy interactions as one atom approaches another. The energy change is almost horizontal at long distances and barely negative. As the atoms approach each other, the energy drops to a valley, then quickly becomes very positive. This is due to volumetric interactions and, although not hard spheres, the nuclei do not want to get near each other. This plot shows a well of energy that is the equilibrium distance for ionic bonding. Motion either closer or further away even by picometers results in a gain in energy. Even though the distance of motion is very small, this would be multiplied by large magnitudes

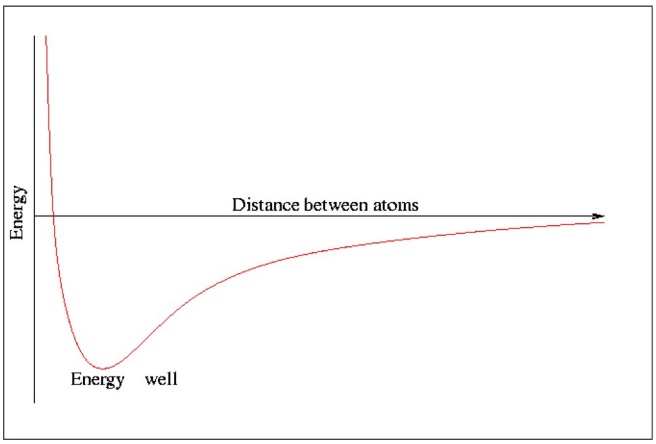

Figure 4.19: Lennard-Jones plot. As one atom approaches another, a low energy well distance found.

for each atomic movement throughout the lattice. This atomic motion, either closer to or further away from neighboring atoms, is the basis of the spring relation to Hooke's law.

Defects caused by knocking atoms off their sites do not affect the systems bonding. The spring constant from Hooke's law is not altered unless a significant amount of atomic bonds are perturbed.

The nanoindenter used at Los Alamos National Laboratory (LANL) was a *Nano II* model. At Arizona State University (ASU), it was a Triboscope^{TM}by *Hysitron.* Samples were cleaned with acetone prior to testing. It was found via TEM that there was a significant density of polishing induced-dislocations at the surface. Irradiation tests showed the effects of the point defects vs. plastic deformation, while tests at ASU explored the origin of these dislocations.

4.7.1 Irradiation Damage vs. Hardness Increase

Samples were standard "quarters" that were cut and polished, then implanted with increasing displacement damage via ion implantation. The indenter was programmed to

target specific regions with the x-y axis memorized, while being viewed on a CCD (charge-coupled device) camera. Generally, six indentations were performed and averaged for the data plotted. Data analysis was performed by Greg Swadener at LANL with statistical techniques to measure variability. The resultant data were plotted to gain a visual perspective to the change of the hardness and modulus measured, with respect to the displacement damage induced by ion implantation.

The samples were implanted over a range of energies and fluences. The goal was to produce a "flat" distribution of damage and xenon over a depth. This would produce less change with depth over this range and thus a more accurate number for hardness or modulus could be obtained.

Xenon was implanted at a low rate due to the low abundance of Xe^{3+} ions produced in the plasma. The 450 keV accelerating voltage to produced the deepest depth of implant. The next energy range was 200 keV, and the lowest was 70 keV. Due to the low depth of implant, the fluence produced a tighter distribution and therefore the damage and xenon were more concentrated. Because of the additive nature of continuous implantation, the implant fluences were reduced to produce smaller distributions with decreasing implantation energy. By combination of these three distributions, the summed distribution was flattened at the top range. Little could be done for the deep trailing edge as it gradually decreases. Figure 4.20 shows these distributions with the small dotted lines being the singular implants and the red the summed. The general formula used to produce these is:

450 keV xenon @ 2*fluence, 200 keV Xe @ 0.5 fluence, 70 keV Xe @ 0.25 fluence, where fluences used were $x = 10^x \frac{\text{Xe}}{cm^2}$

Samples were implanted with $1 \times 10^{14} \frac{Xe}{cm^2}$, $1 \times 10^{15} \frac{Xe}{cm^2}$ and $1 \times 10^{16} \frac{Xe}{cm^2}$ fluences, with the total fluence used in the above equation. This produced the broad peak distributions of 0.8, 8 and 80 dpa that were tested by the nanoindenter. The final sample, with 80 dpa,

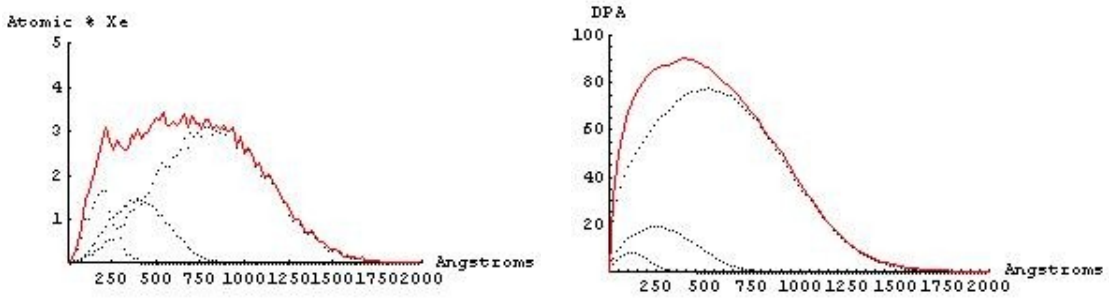

(a) Xenon implant distributions with summed total (red)

(b) Damage distributions with summed total (red)

Figure 4.20: Multiple implant of xenon. Shown is both xenon concentration and displacement profiles.

was observed with TEM as well, in order to correlate defects to the changes to mechanical properties.

4.7.2 Surface Plasticity

Nanoindentation was performed at ASU with respect to dislocation nucleation and motion. The Triboscope nanoindenter used a Berchavich tip with an approximate 100 nm radius. Tests were performed on samples that were polished with colloidal silica for a number of hours. Three distinct tests were performed:

1. 1-hour polish with colloidal silica,
2. a second-hour polish with colloidal silica,
3. a third polish to 1200 grit SiC paper, intended to induce dislocations

After each test the surface was scanned with the tip, which acts as an AFM. The indent then shows information about the plasticity of the ZrN. Plots of each run show both the AFM image and the corresponding load/displacement curves.

4.8 TEM Sample Preparation

Sample preparation for TEM is a long and involved process. The material in question is to be thinned to electron transparency, which is nanometers thick. This makes the sample very fragile, and the progression to the final thinned sample can be frustrating.

Two methods were used for processing ZrN samples for TEM:

- Cross-sectional preparation with a tripod,
- conventional plan-view technique.

Each method provided different information while starting from the same sample size, either implanted or left virgin (unimplanted). The plan-view sample provides a much faster look at the structure. Its weakness lies in the fact that there is no depth information that can be obtained as virtually all the transparent region is partially implanted, but ground and ion milled from the backside. Cross-sectional samples provide the depth information as the sample surface is observed from the edge.

4.8.1 Plan-view Sample

The sample is glued, polished side down, to a sample holder block and placed into a *Struers* 1000 automatic grinder/saw. All gluing is done with *Crystal Bond*, a low-melting-point wax. The sample is ground with a 70 μm diamond cup wheel that makes three passes and then advances at five μm intervals. The sample is ground to less than 250 μm thick in this manner. 100 μm is a reasonable thickness.

The thinned sample is then glued to a glass slide, and a *Gatan* ultrasonic cutter is used to produce 3 mm disks. The ultrasonic cutter uses a fine silicon-carbide slurry for the abrasive. A stainless-steel cutting tip is screwed onto the unit with a gas-tight copper

washer. Pre-applied pressure is placed on the sample with the cutting tip. Under the sample is a sprung base that counters this force. SiC slurry is fed onto the sample with a pipette and moved into the tip with a syringe connected internally. The ultrasonic action vibrates the SiC particles under the tip and mills the sample. The disks are cut into the glass below, allowing easy removal. These disks are then glued to a sample holder stub and placed into a *Gatan* dimple grinder.

Dimple grinding is a process of removing as much material as possible from one side of the sample. The 3 mm disk is rotated while a small wheel is set lightly perpendicular to the sample. Rotation of the sample and the wheel produces a "dimple" in the sample. The sample is thinned and polished different μm sizes of diamond, from 6 μm to 1 μm, with a glycerin lubricant, . The depth is monitored until the sample is ~20 μm thick at the center of the dimple. Final thinning is done either by PIPS or Duo-Mill.

4.8.2 Cross-Sectional Sample

Cross-sectional TEM sample preparation is much different from that for the conventional plan view. The sample is cut in half so that there are two implanted faces. These faces are glued together with *M-bond* epoxy adhesive. The faces are thoroughly cleaned with acetone and alcohol. The premixed epoxy is kept refrigerated and must be pre-warmed for at least an hour to reduce the viscosity. A horse hair-brush is used to apply the glue by first wiping on filter paper to remove as much glue as possible. This has the effect of reducing the glue line on the finished sample. The sample is then pressed face to face.

Pieces of silicon wafer are used on the opposite ends of the the ZrN sample. They are cleaned and glued by the same method. The final sandwich, being Si-ZrN-ZrN-Si, is placed into a vice and compressed with firm but gentle pressure until the *M-bond* is squeezed out from between. The vice is then placed into a curing oven set at 150°C, which activates the

epoxy. The sample is allowed to cure for two hours before cooling to room temperature.

The epoxied sample is glued to a glass slide and cut with a slow-speed diamond saw with a wafering blade to produce thin samples, about 400 - 500 μm thick, which can be cut again to produce the proper size of $\approx$3 mm in length. The thin slices are now laid down to show the edge-on view. The sample is then flattened on both sides by hand with 30 μm diamond film. The diamond film used was *Struers* polycrystalline-diamond-impregnated mylar lubricated with water.

A tripod polisher was used with a silica stub, which forms the third leg. The polisher was leveled and the stub flattened with 30 μm diamond film. A zero measurement was taken with a micrometer for the thickness of the stub. The sample was glued to the stub and measured again. The sample was then polished by hand using 30, 15, 9, 6, 3, and finally 1 μm diamond film on a glass platen. Measurements were be taken during the polishing to observe the sample thickness.

The sample was moved carefully in a "figure-eight" pattern with approximately even pressure even on all three legs of the tripod. Then, before polishing with a lower μm size, the sample was moved in a back-and-forth motion several times to produce parallel scratches. These were used to view the extent of surface removal during polishing with the next film. Rotating of the sample by 45°or 90° between each film, facilitated observation of the scratches from the previous film under a low-power stereo microscope with top, side and bottom lighting.

On a power wheel, a felt paper was used with a small amount of *Syton* with a colloidal silica solution. *Syton* is slightly basic and produces a mild chemical etching effect as well as sub-micron polishing. With flowing water, the *Syton* is pipetted from a secondary container onto the felt wheel at intervals. Care must be taken to check for and clean any *Syton* agglomerations. With slow-to-moderate wheel speed, the tripod is moved in a circular

motion so as to not produce any parallel scratches.

The sample was thinned, generally to less than 200 μm, and unglued and re-glued on the other face. The sample was glued so that the face-to-face glue line faced forward from the tripod. It was again polished with 30, 15, 9, 6, 3, and 1 μm diamond film. This time, the sample was wedge thinned, where the back adjustable tripod legs were lowered or raised 50 μm. The sample was thinned carefully to near 10 μm, where the silicon became transparent to the bottom light on the stereoscope. The transparency was evident due to the red color produced. Silicon goes from red at 10 μm to yellow at about 5 μm. The sample was then polished as evenly as possible where both sides of the silicon were red. The silica stub was removed, and, the sample was gently removed by dissolution of the *Crystal Bond* with acetone. The sample was then ion milled to perforation.

4.8.3 Ion Milling

The final thinning is produced by an ion mill, either a *Gatan* Duo-Mill or PIPS (Precision Ion Polishing System). The Duo-Mill is set at a minimum of 16° angle with 4.5 keV argon beam. It has a wider dispersion and a more "gentle" removal of material and hence removes material at a very slow rate, requiring approximately 24 to 48 hours of milling for a ZrN sample described above, It is also used as a cleaner after the PIPS, which sometimes leaves sputtered material adhered to the surface that the Duo-Mill removes in 10-15 minutes.

The PIPS has a much lower angle of attack, from 4° to 8°, and a much tighter beam. The beam is 4.5 keV argon which produces a very aggressive milling on the surface but at such a light angle that it should produce more thin area. The PIPS has two advantages over the Duo-Mill; it has a very low angle, and it reduces milling time to two hours. Its main disadvantages are that it can sputter material onto the sample and that it can be too

aggressive, such that it overmills the glassy phase between grains preferentially. Reducing the voltage for the last 10 minutes or so reduces this effect.

The sample is thinned until perforation, and then checked by light microscopy for its quality. When light microscopy shows sufficient quality, the sample is ready for TEM evaluation.

The ion damage from milling has been assessed from the TRIM code. The argon atoms are used at a low angle to sputter the sample atoms off the surface. Statistically, some argon atoms will be deflected into the sample with penetrating energy. They can cause displacement damage and deposit argon at a certain depth. Due to the low angles and energies, this depth is very shallow. At the steepest angle used, 16° on the Duo-Mill, the maximum penetration of 4.5 keV argon is 14 Å. This is almost two orders of magnitude less than for 300 keV xenon. Therefore, the damage from ion milling is not an issue when radiation damage is assessed.

Ion milling is no different from other types of sputtering operations. Material is sputtered and tends to coat any cooler surface, including the back side of the sample. Two artifacts caused by ion implantation should be noted: a very thin layer of the material is redeposited onto the surface, and ion tracks are produced.

The sputtered coating can, under the right conditions, produce very small moiré fringes across the entire transparent region. With a cross-section that has been glued, the glue tends to act as a very good sink for sputtered material. Small crystals are normally found in the glue. These crystals can produce a significant amount of diffraction. These are also found in the glassy phase. Typical methods of cleaning the surface post-mill are to use a very low-energy beam for a few minutes (PIPS) or the *Gatan* Duo-Mill (the beam is much more spread and “gentle”) or to use a plasma cleaner. Cleaning does not eliminate the artifacts, but it does reduce the final concentration.

Ion tracks can appear to "chip away" the material. These can show up as surface artifacts and dislocations. A low-voltage cleaning operation helps to smooth some of the ion tracks.

4.9 TEM

Transmission electron microscopy is a direct method of observing the effects of displacement damage to the crystal structure and microstructure. A combination of techniques, such as bright field, dark field, diffraction and EDS analysis, provides thorough sample characterization.

A Philips/FEI CM-30 was used primarily for TEM analysis. The CM-30 uses a 300 keV electron beam from a LaB_6 filament allowing for good resolution at greater than 100,000 magnification. Bright-field imaging and convergent beam electron diffraction (CBED) microdiffraction were used extensively to determine the extent of damage to the crystal structure and microstructure. A *Kevex* EDS unit was used for chemical composition analysis.

Alternatively, an FEI Technai microscope was used at University of Nevada Las Vegas (UNLV) for some analysis, including Scanning TEM (STEM). This particular microscope was equipped with a field-emission gun for the brightest images.

4.9.1 Bright-Field

Bright-field was used as a primary mode of operation. Bright-field were obtained with objective and condenser apertures set at 2, the second largest, and the condenser spot size set at 2. This gave the brightest electron beam with good resolution.

Micrographs were taken by evaluating the screen image by gray scale, and then using the binocular close-up screen, measure the current to exposure time evaluated by the CM-

30's computer. The spot size was then adjusted so that the shortest amount of exposure time was used, with a maximum being 3 seconds. Manual control was used and exposures were taken at increments below and above the selected setting. This ensured that the best exposure would be obtained by this subjective method.

4.9.2 Dark Field

Centered-dark-field images were obtained on the Phillips CM-30. Images were acquired for long time periods, due to the low intensity. Times used were 30 to 90 seconds. Weak-beam dark-field images are obtained from the opposing g vector such that the diffraction is very weak. This sharpens the contrast and is helpful in obtaining good resolution of dislocations, etc.

4.9.3 CBED

Convergent Beam Electron Diffraction (CBED) was used to sample a very small spot in a particular area. By this method, microdiffraction images were obtained. The standard technique in obtaining quality microdiffraction is to reduce the objective aperture to the second smallest, then reduce the spot size to a setting of 9 (12 nm probe diameter). This is the smallest probe size before moving to "nano-probe" mode, which takes special configuration.

The small probe size allows very distinct areas to diffract without interference from other areas. The spot can be focused on a particular area, such as the implanted region.

Tilting of the stage in the x and y directions allows CBED patterns to be aligned on a specific pole. Of interest are the low-index {001}, {011} and {111} poles, as the patterns from these are more easily indexed. Kikuchi patterns, found when the sample is thick but

Algorithm 7 fcc selection rules

$\frac{1}{d^2} = \frac{h^2+k^2+l^2}{a^2} = \frac{N}{a^2}$ where N = 3, 4, 8, 11, 12 $\cdots$ or h, k and l are all odd or all even

still electron transparent, are very useful to find poles.

Patterns were collected at a camera length of 900 mm. Common acquisition times were 15 or 30 seconds, depending on the brightness. Times as long as 3 minutes were used for obtaining inter-spot resolution of diffuse scattering.

4.9.3.1 Diffraction Pattern Indexing

Since ZrN has the NaCl structure, which is a fcc metal sublattice with the octahedral interstices occupied by nitrogen forming another fcc sublattice, the resultant selection rules are the same as for simple fcc. The peaks intensities are modified, but the reflections are the same. Algorithm 7 shows the relation to the *hkl* distances and the selection rules [148, 149]. Table 4.4 shows the bcc indices. The Weiss zone law provides a way to check the correctness of the indexed spots. The zone vector is orthogonal to the *hkl* vectors, and thus the dot product is 0 (Algorithm 8).

Algorithm 8 Weiss zone law

$hU + kV + lW = 0$ where [*UVW*] is the zone. Alternately, the dot product

$$\begin{pmatrix} h \\ k \\ l \end{pmatrix} \bullet \begin{pmatrix} U \\ V \\ W \end{pmatrix} = 0$$

Table 4.4: bcc and fcc selection table

bcc		fcc	
$h^2 + k^2 + l^2$	*hkl*	$h^2 + k^2 + l^2$	*hkl*
2	110		
		3	111
4	200	4	200
6	211		
8	220	8	220
10	310		
		11	311
12	222	12	222
14	321		
16	400	16	400

d spacings may be determined from the distances from the center spot to the diffracted spots. The equation used is the standard diffraction relationship, (Algorithm 9), where *R* is the measured distance (radius) from the center spot, *d* is the interplanar spacing, λ is the wavelength of the electron beam (dependent upon accelerating voltage) and *L* is the camera length. Since λ and *L* are constants, for the given camera length of 900 mm, the equation reduces to $d = \frac{16.57}{R}$ at 300 keV.

Algorithm 9 Spot/distance relationship in diffraction patterns

$Rd = \lambda L$ where $R_1 d_1 = R_2 d_2 = R_3 d_3 = \cdots$ resulting in $d = \frac{16.57}{R}$ for camera length of 900 mm at 300 keV

4.9.4 Analysis of Dislocations

Burgers vectors are determined from $g \cdot b$ analysis. The Burgers vector, $\overrightarrow{b}$, is useful to indicate active slip planes in the system and the type of dislocations present. For ease of notation, the vector symbols are generally ignored yet understood.

The simple steps to take for analysis are to obtain images of the selected area for at least three different diffraction conditions, in each case for a selected g vector such that a two-beam condition is achieved. The image and corresponding diffraction patterns are recorded showing the selected g and the image to which it corresponds.

The most useful condition is that in which the dislocation image fades to near invisibility. Although not truly invisible, the contrast is greatly reduced so that the invisibility criteria, or $g \cdot b = 0$ (or actually $\overrightarrow{g} \cdot \overrightarrow{b} \times \overrightarrow{U}$) is achieved. From the images with the known g vectors, especially with $g \cdot b = 0$, the Burgers vector can be found.

4.9.5 EDS

A *Kevex* energy-dispersive spectrometer was used in conjunction with the 300 keV electron beam. The EDS unit is similar in operating principals to the *PGT* unit connected to the SEM.

A small spot size and focused condenser lens are used to produce a small focused spot that can be placed at different points on a cross-sectional specimen such as the very edge, exciting only the implanted region. In this way, elemental analysis can be obtained from a a very small yet distinct area.

For analysis, the condenser spot size was reduced to 5 to adjust the dead time to 20%. Spectrograms were collected for 100 seconds. The specimen was tilted 25° toward the detector for maximum resolution. The tilt angle is critical for EDS on the TEM.

4.10 Helium Release Studies

Implantation for helium release was performed at the Ion Beam Materials Lab at LANL. Standard implantation techniques were used to implant xenon, but helium required a low accelerating voltage and a special specimen stage. Xe^{2+} was implanted at fluences of 0, $1\times10^{15}\frac{\text{Xe}}{cm^2}$ or $1\times10^{16}\frac{\text{Xe}}{cm^2}$ at 300 keV and at LN_2 temperature. These three samples, had damage produced at 0, 4 and 40 dpa, and at a depth of 35 nm. They were then implanted at room temperature with helium at a fluence of $1\times10^{15}\frac{\text{He}}{cm^2}$. The helium was implanted at the same depth by a 17 keV accelerating voltage while the sample was mounted on a special 60° angle fixture on the sample stage. Implantation at 60° incidence reduces the depth of implantation by simple geometry. 60° was the maximum angle that could be obtained before sputtering became a dominant feature. 17 keV was the minimum voltage obtainable by the ion accelerator. These parameters placed the helium at a depth of 35 nm, the same depth as the xenon-produced damage. Both distributions were predicted by TRIM (refer to Figure 4.21).

Helium was implanted after the xenon implantation so that the xenon implantation would not affect the helium mobility during implantation. The low energy of implantation used with helium did not require a cooled specimen due to the lack of significant beam heating.

Helium release studies were performed at Pacific Northwest National Laboratory by Brian Oliver. The studies were performed with a custom-built vacuum furnace with a residual gas analyzer (RGA) attached. (Refer to Figure 4.22). A small silicon-carbide crucible wrapped with nickel-chrome heating elements is used within. Samples must be less than a $\frac{1}{4}$ inch to fit into the small crucible. The small crucible is designed for a small thermal mass of a highly refractory and thermally conductive material. This eliminates

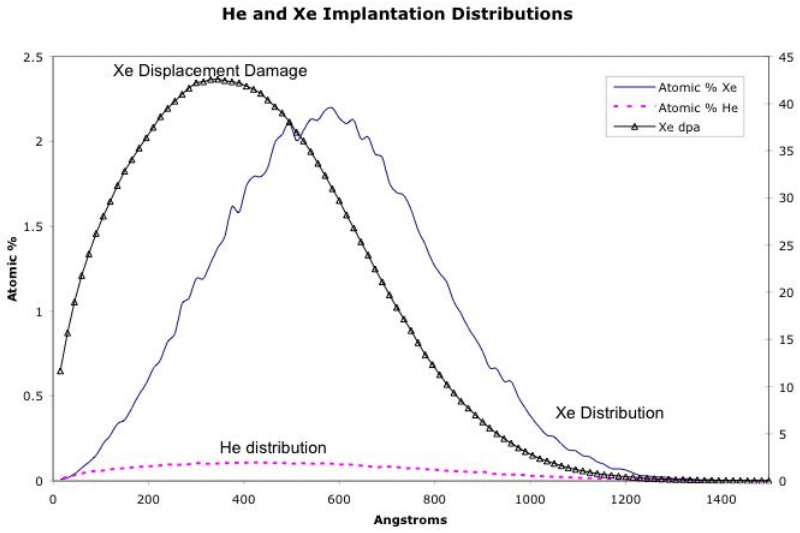

Figure 4.21: Xenon damage with xenon and helium implant distributions

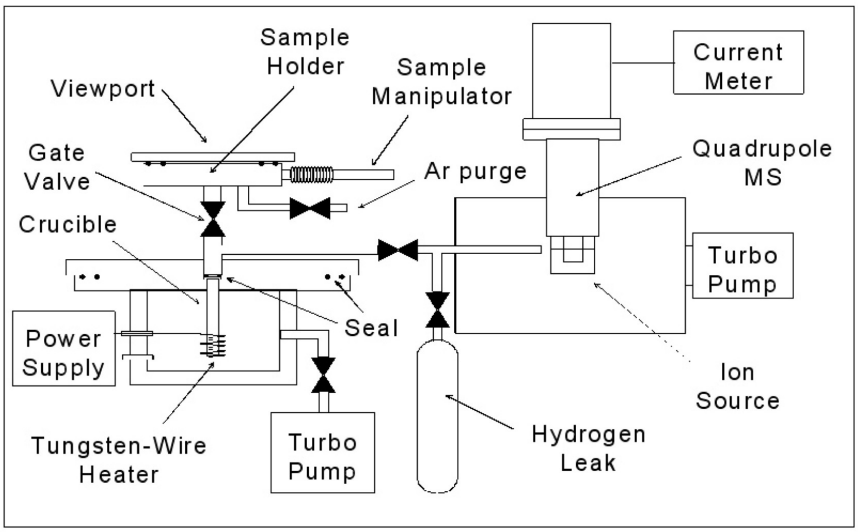

Figure 4.22: Gas release measuring system

much of the thermal lag at the actual sample.

The instrument is heated at a set heating rate and the RGA measures the evolution of gases trapped in the solid. The heating rate used was 25 ° per minute. A Stanford Research Instruments RGA-100 was used along with a personal computer to collect the data. The maximum temperature for which the furnace is rated is 1200°C.

Data collected were corrected for temperature measured vs. the true temperature due to the thermal lag of the crucible. Data was plotted as $\frac{He}{cm^2 s}$ vs. either time or temperature, when corrected. Plots were smoothed for comparison by means of the computer software *Datathief*.

CHAPTER 5

Results and Discussion

The samples used for the experiments changed as time progressed. As some problems were solved, others developed. The experiments evolved as the desired data became elusive. As the tools available were used, either at LANL, UNLV, PNNL or ASU, data were compiled to address the results observed from other experiments. In this way, a puzzle was slowly being solved as pieces were put together such that predictions could be made. Although not a complete survey of every possible physical property, data are presented to give a predictive picture as to the radiation tolerance of ZrN.

5.1 Artifacts and Effects of Experimental Techniques

Certain artifacts were observed with consistency via TEM. Early irradiation experiments showed a significant amount of microstructural change that was not common in irradiated materials. These changes were grain refinement and micro-twinning, both of which were explained via rapid amorphization and recrystallization events due to irradiation. It was observed, however, that no matter what the dose, implanted species, or damage level, these effects were consistent. It was assumed early on that this was an effect due to the damage and not the experiment.

These grain refinement effects were directly observed in a novel experiment in that a sample of epoxy-impregnated powder was cut into a disk and dimpled to produce a plan-view TEM specimen. The result showed large polycrystalline (at times) particles with large

Table 5.1: Samples and Experimental Techniques Performed on ZrN

Type	Ion	Implant keV	Fluence $\times 10^{16} \frac{ions}{cm^2}$	dpa	T	Rate	Analysis
Powder	-	-	-	0	-	-	TEM
Powder	Kr	300	1	30	LN_2	Fast	TEM
HIPed	Xe	300	1	40	LN_2	Fast	TEM
HIPed	Xe	300	2	80	LN_2	Fast	TEM
HIPed	Xe	450‡	0.01, 0.1, 1	0.4 ,4, 40	LN_2	Slow	Nano, TEM
HIPed	Xe	300	2	80	LN_2	Mod	TEM
HIPed	Xe	300	5	200	LN_2	Fast	TEM
HIPed	Xe	300	2	80	350°C	Fast	GIXRD
HIPed	Xe	300	2	80	LN_2	Fast	GIXRD
HIPed	Xe	300	4	160	LN_2	Fast	GIXRD
HIPed	Xe	300	6	240	LN_2	Fast	GIXRD,TEM
HIPed	Xe	300	0, 1	0, 40	LN_2	Fast	Reflect/Resist
HIPed	He	17	0.1	<0.1	LN_2	Fast	He release
HIPed	He, Xe	17, 300	0.1, 1	40	LN_2	Fast	He release
HIPed	Xe	300	1		580°C	Fast	TEM
HIPed & Annealed	-	-	-	-	-		TEM
HIPed & Annealed	Xe	300	0.01	0.4	LN_2	Fast	TEM
HIPed & Annealed	Xe	300	0.1	4	LN_2	Fast	TEM
HIPed & Annealed	Kr	300	2	70	800°C	Fast	TEM

‡Sample implanted with various energies to broaden displacement curve

grain sizes (on the micron scale). The sample was then taken and implanted with krypton to approximately 30 dpa. The electron-transparent region was of course destroyed during this process, yet the irradiated surface was maintained. The sample was again back-thinned with the ion mill and observed post-irradiation with TEM. The results were startling and proof of the irradiation effects on the crystal structure of ZrN. TEM showed both grain refinement and micro-twins, which could be directly attributed to the irradiation.

One experiment provided information to suggest either a rate and/or a thermal cycle effect that would cause these changes. The sample was implanted with Xe^{3+} such that the energy would be 450 keV, providing additional depth. Subsequent implants on the same sample were at lower energies. The Xe^{3+} ion was about 10% the yield in the plasma for the Freeman source in the implanter and thus, the rate of implant was very slow. The resultant TEM, in this particular sample, showed no micro-twins or grain refinement from the irradiation, but the damage layer common to irradiated materials. This suggested that the material showed a rate dependence for defect annealing or recrystallization.

As a confirmation experiment, a half-way rate was used on a sample. The resultant TEM showed a significant effect. No grain refinement was observed and there was a damage layer similar to the low-rate sample. Twinned grains, however, observed. This seemed to confirm the argument of the rate effect.

A separate experiment showed a different result and complicated the assumptions. A sample was implanted with xenon several different times at the standard high rate. A dose of 80 dpa was produced each time and, after the third time, the sample was evaluated by TEM [1]. The sample, although implanted at a high rate, showed the same effect as the very-low-rate implant. No grain refinement or micro-twins were observed, only a damage layer

[1] RBS measurements showed that after approximately 200 dpa the surface damage would become approximately equal to that of the rate of implant. This limits the maximum dpa to approximately 200 dpa, although TRIM predicts 240 dpa. For this reason, the damage is stated as “over 200 dpa” or “approximately 240 dpa”.

due to implantation. This suggested that, even with a high rate of implantation and much damage, multiple thermal cycles produced a stronger effect and the grain refinement and twins were not formed.

Many experiments were performed and repeated with superior samples. As the sample quality increased, so did the data that were acquired. Table 5.1 shows the main experiments that were performed and the samples types that were used.

5.1.1 Oxidation During Implantation

Currently, every single sample produced for TEM since that time has shown no grain refinement or twinning. This produced a conundrum; HIPed samples were produced at a more recent date, and although it was not considered too significant, the samples were different from both the nitride foils and the epoxy powder. The powder was the precursor to the HIPed samples and thus it was assumed that these would show the same results.

The last set of experiments provided some insight as to the origin of the grain refinement and micro-twins. These experiments were conducted with annealed samples that, although heavily shielded, showed that ZrN would oxidize readily with extremely low amounts of oxygen. It was found that the oxygen dissolved in the system would grow oxide crystals of significant size. The oxide crystals sometimes grew from small 20 nm diameter crystals to micron sizes, depending on the annealing time and oxygen available. Figure 5.1 shows a sample of these crystals.

Monoclinic ZrO_2, identified easily in *every* GIXRD spectrum taken at $2\Theta < 30°$, also transforms to its tetragonal structure at a temperatures over 1100 °C. This transformation produces such a large stress due to the volume change that the crystal twins readily. Many of the oxide crystals observed in the annealed ZrN showed significant twinning.

Although not proved, it is suggested that the early grain refinement and twins observed

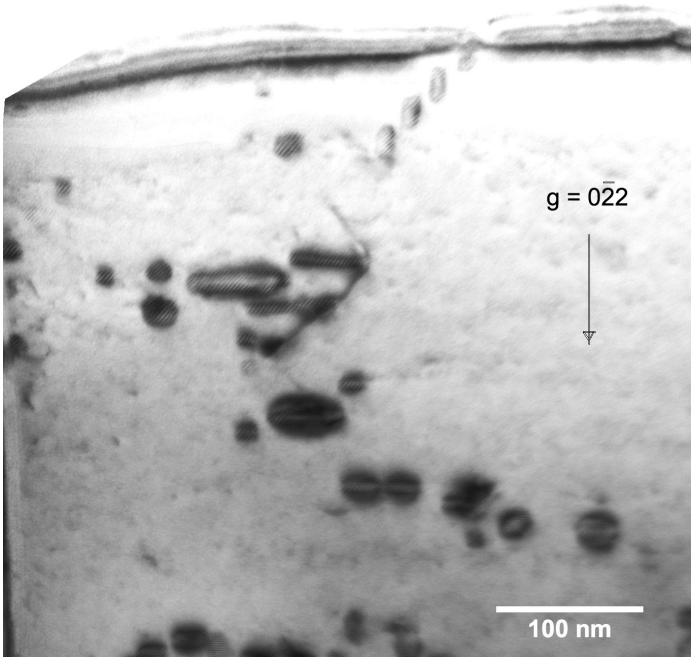

(a) TEM Micrograph of ZrN annealed at 800 °C. Note the planar orientation of the precipitates. Also note the fringes.

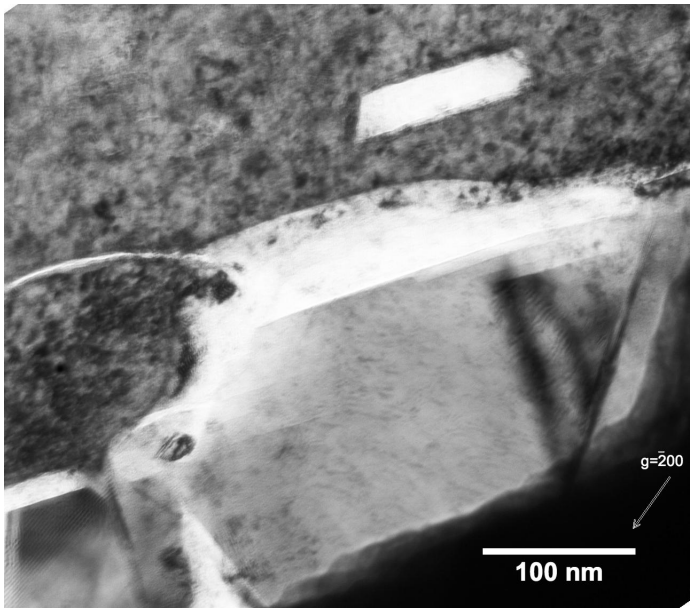

(b) Large oxide formed during 1400 °C heat-treatment. Sample irradiated to 70 dpa with Kr.

Figure 5.1: TEM micrographs of oxide crystals produced near the surface during heat-treatment of ZrN

were all produced from oxidation of the surface during the implantation process. The process, although cryogenically cooled, has a thermal effect within the very small volume that is being implanted. Although the kinetic energy being dumped into this volume is quickly quenched, it produces a very high temperature for a very short amount of time.

It was during the time period when the grain refinement and micro-twins were no longer observed that the ion implanter was heavily serviced with respect to its vacuum system. It is suggested that leaking vacuum allowed oxygen to enter the chamber and oxidize the surface when under irradiation. Subsequently, with a better vacuum, grain refinement and twins were no longer observed. It is thus my feeling that the results previous to these changes were in heavily oxidized material, and showed not the effects of irradiation on ZrN but rather oxidation during irradiation. It is interesting to note that the oxidation took place at cryogenic temperatures under irradiation at quite low doses.

5.2 High Rate with Three Thermal Cycles

Rate experiments were performed early on to address the change of microstructure from twinning/grain refinement to a solid defect band. It was theorized at the time that the rate of implant had a strong effect due to the rate of accumulation versus annihilation of defects. It was also suggested that thermal cycles had an effect due to the mechanical strains introduced. It was found, however, that the rate and thermal cycling had little to do with the change in microstructure.

A high rate is defined as essentially the highest rate of implant one can obtain. This is near 2 to 4 μA which relates to about 40 dpa per hour. Low is about 10% this rate, while medium is about half this rate.

For a sequential damage accumulation GIXRD experiment, the sample was implanted

with $2 \times 10^{16} \frac{Xe}{cm^2}$ three consecutive times. It was implanted at a high rate and lowered to LN_2 temperature each time during implantation. The samples were warmed to room temperature for each GIXRD experiment, producing a thermal cycle. After the third implant and GIXRD analysis, a cross-sectional TEM sample was made. The sample was implanted with over $6 \times 10^{16} \frac{Xe}{cm^2}$ for a total of $\approx$ 240 dpa. The surface started to sputter as was observed by RBS. This tended to spread the damage distribution out so the peak might not be 240, yet it is over 200 dpa. The total amount of xenon implanted was approximately 15 atomic $\%$.

Figure 5.2 shows the results. The high-rate, thermal-cycled sample shows no polygonization, only the dense defect band that is similar to the much lower dose samples at lower implant rates. Microdiffraction shows no amorphization and no change between the defect layer and the substrate below.

At the very edge of the of the defect layer adjacent to the vacuum, there was an observed change. With long film exposures, extra spots and patterns began to show. Both CBED and SAD showed this effect. It very much resembled the diffuse scattering produced by short-range ordering. Since this has been observed in the literature, it is conceived that this is happening at the very surface of the sample with very high fluence [65, 66, 150, 149]. Since the nitrides show short-range ordering from vacancy superstructures, it might show the preferential loss of nitrogen from sputtering. Figure 5.3 shows such a CBED microdiffraction pattern.

5.2.1 GIXRD

To address changes in microstructure with increasing dose, the same sample was implanted with xenon at LN_2 temperature with a fluence of $2 \times 10^{16} \frac{Xe}{cm^2}$, producing 80 dpa at peak. Three consecutive implantations were performed with GIXRD measurements done

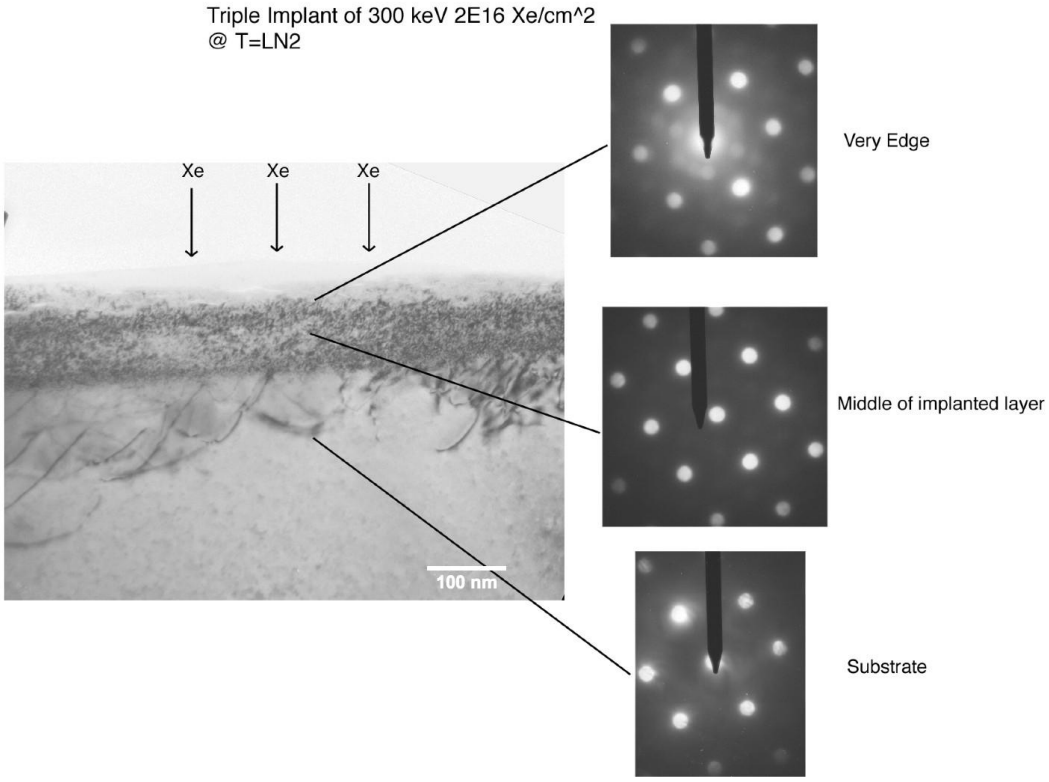

Figure 5.2: 240 dpa implant, thermal cycled 3 times. Note denuded zone at surface.

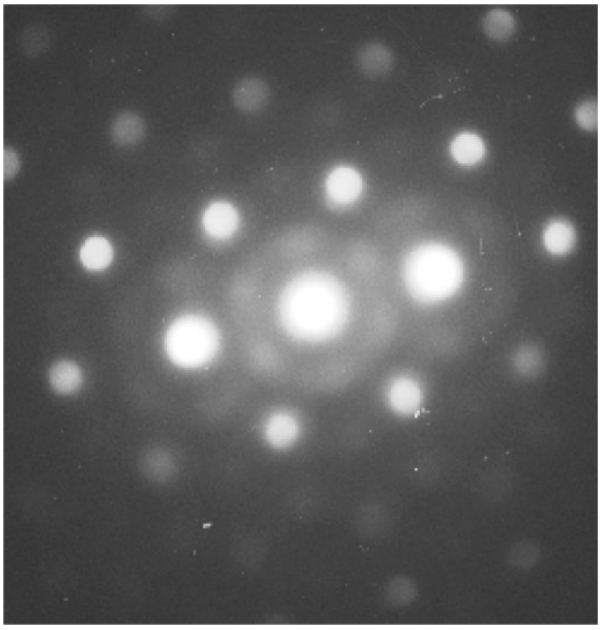

Figure 5.3: CBED microdiffraction pattern of the very edge of the high dose, triple thermal cycled sample. Possible short-range-ordering of the nitrogen vacancies produce diffuse scattering structures such as these. (500 mm CL)

after each. The sample was run before implantation for a virgin ZrN baseline. GIXRD was performed at both 1° and 0.5°. The 0.5° measurement seemed to provide the most data relative to the substrate.

Figures 5.4 shows the virgin material compared with the 80, 160 and 240 dpa runs. Figure 5.4 shows the sample pattern from 30° to 70° 2θ. As can be observed, there is little difference between the spectra. Closer observation of some of the peaks shows a significant amount of splitting. The spectra of these peaks are shown in Figure 5.4 (b). Two observations can be made. As the dpa increases, the lattice parameter increases and the peaks spread. Both are expected due to the implantation [151, 53]. Upon further implantation, at 160 dpa, the lattice parameter seems to relax, yet the peaks split from one to three.

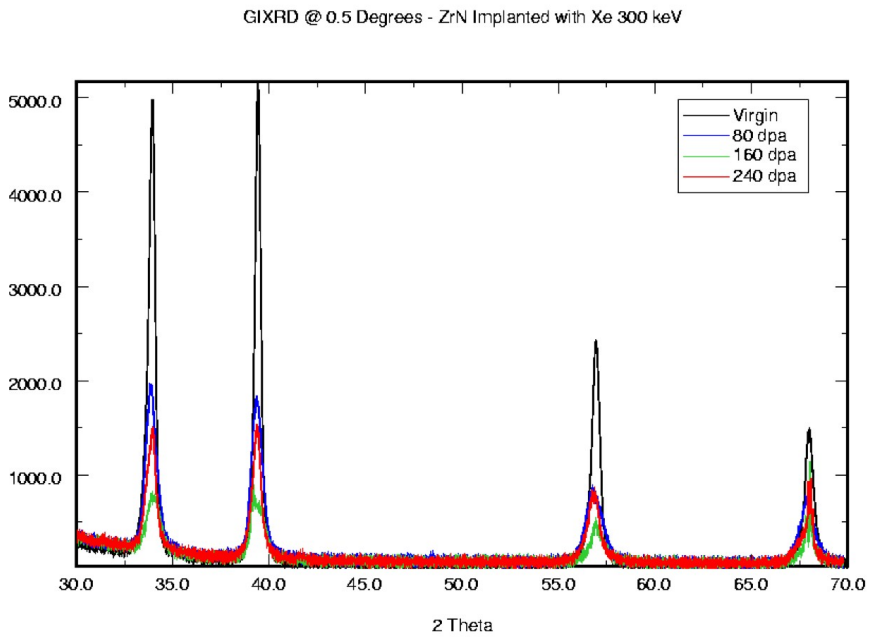

(a) Wide spectra showing the effects of increasing dislplacement damage on ZrN.

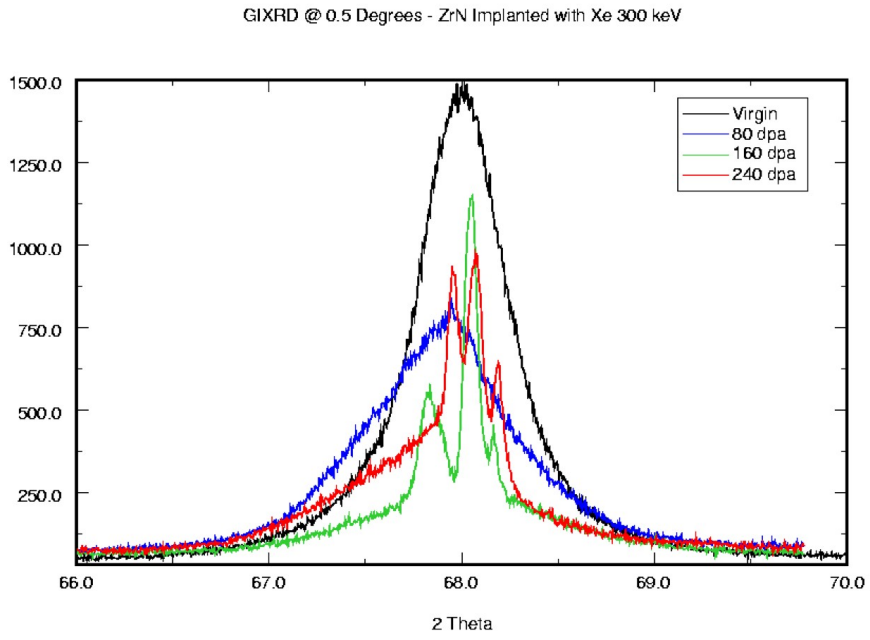

(b) Close up view of the tetragonal distortion causing peak splitting with increasing displacement damage.

Figure 5.4: GIXRD @ 0.5° incidence angle of ZrN implanted with 80 dpa multiple times

5.2.1.1 Tetragonal splitting

This observation gives more credibility to the ordering found in the TEM results. A model based upon the works of Li and Howe, together with the software *Crystal Maker* and *Crystal Diffract,* was used for ZrN to produce some of the splitting [65, 150]. The model used the I4/mmm space group as the base. When the lattice parameters were adjusted slightly, the spectra produced similar splitting at the same peaks observed on the GIXRD spectra. This model is essentially two NaCl cells stacked with a substructure of vacancies on the nitrogen sublattice. Figure 5.5 shows the modeled vacancy superstructure for both theoretical space groups. The vacancies arrange themselves into this motif on the nitrogen sublattice, producing a tetragonal supercell. These supercells might form enough to diffract the x-rays and produce two of the peaks while the third and middle peak could be the non-ordered NaCl structure. The atomic scattering factor of nitrogen is quite low, and thus observing the nitrogen sublattice requires that there must be many supercells [152]. Electron diffraction is much more sensitive to nitrogen and thus can produce images as seen in Figure 5.3.

5.3 Higher-Temperature Implants

Radiation damage within an active reactor core provides a very different set of environments. Diffusion of atoms and defects is faster, so the defects can self-anneal or cluster faster. Elevated-temperature implants were observed with either GIXRD and/or TEM. Temperatures used during implantation were:

- Room temperature over two hours, 80 dpa,
- 350 °C over six hours, 80 dpa,

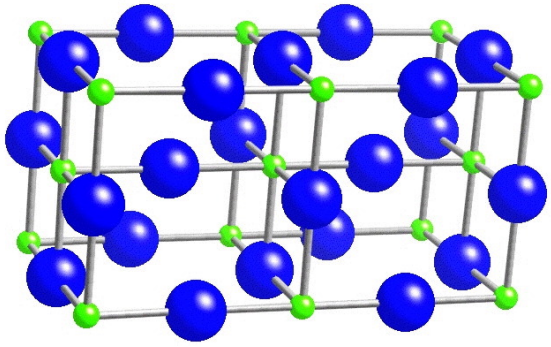

(a) Structure from ordered vacancies producing the I4/mmm space group.

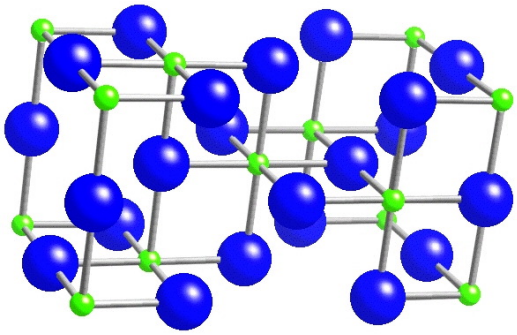

(b) Structure from ordered vacancies producing the I41/amd space group.

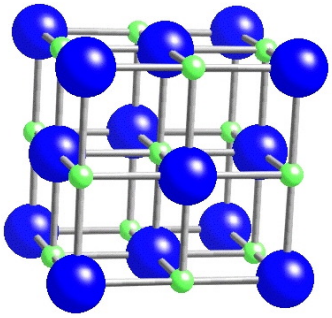

(c) ZrN with the NaCl structure for comparison.

Figure 5.5: Possible vacancy superstructures when nitrogen is reduced to the approximate ratio of Zr4:N3. Note the subtle differences between the vacancy superlattices (green = nitrogen) and also very close resemblance to the full NaCl structure.

- 580 °C over six hours, 40 dpa,
- and 800 °C over 4 hours, 70 dpa.

5.3.1 Room Temperature

The room temperature sample showed no difference in the GIXRD spectra from that of the virgin. During sample preparation for TEM, the entire sample was destroyed. It was decided not to pursue experimentation with this temperature. Since the higher-temperatures results were not dissimilar to those for cryogenic irradiations.

5.3.2 350 °C

A sample was irradiated at 350°C with $2 \times 10^{16} \frac{Xe}{cm^2}$ to about 80 dpa. GIXRD was performed on this sample (Figure 5.6), showing some slight differences from cryogenic implants. The plot shows these differences between the virgin material and the effect of implanting at higher temperatures (note the extra peaks). It is surmised that the peaks are a developing α ZrN structure from nitrogen loss at the surface due to the irradiation-induced sputtering. A structural model of the hcp nitride was proposed and put together with *Crystal Diffract*. When hcp zirconium was used as a base and the lattice was expanded to fit the nitrogen atoms, the peaks appeared to fit the experimental data. It was figured that near the surface, the nitrogen is lost forcing a precipitation of the α phase which is nitrogen poor.

Nitrogen loss has been observed in GaN irradiated at high doses [102, 103, 101]. At the depth of implant, along with irradiation-enhanced diffusion, nitrogen could be displaced and would have a much easier time to degas from the structure. Nitrogen diffusion is slow at 350°C yet, with some irradiation enhancement, it could likely diffuse through the bulk to the surface [135].

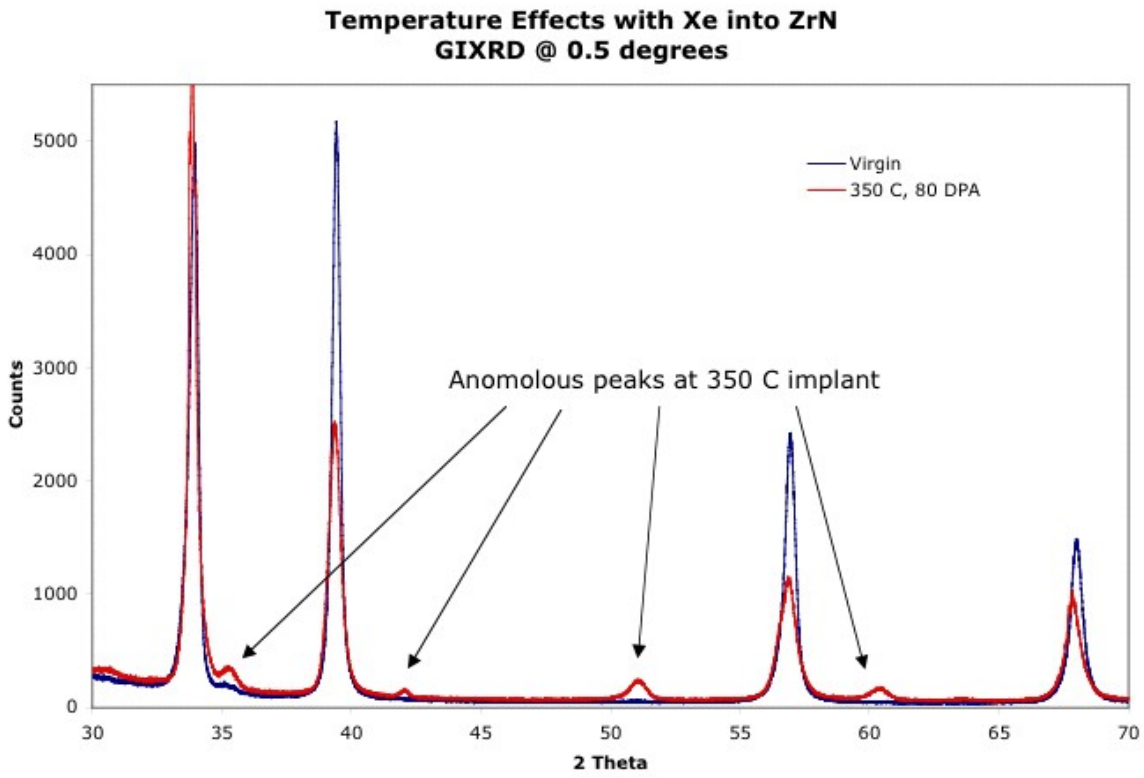

Figure 5.6: GIXRD of higher temperature xenon implant.

TEM showed that there was little distinction between the 350 °C implant and a cryogenic implant. Two effects were noted; the dislocations and point defects appeared to have moved deeper into the sample, and the denuded zone was larger. Figure 5.7 shows these effects.

5.3.3 580 °C

At 580 °C, the sample showed some increase in oxidation with GIXRD. The peaks observed, however, showed little change. There were some differences from the 350 °C sample such that the hexagonal ZrN peaks did not appear. There were other peaks, however, and these were confirmed by Reitvelt refinement (performed by Thomas Hartman at

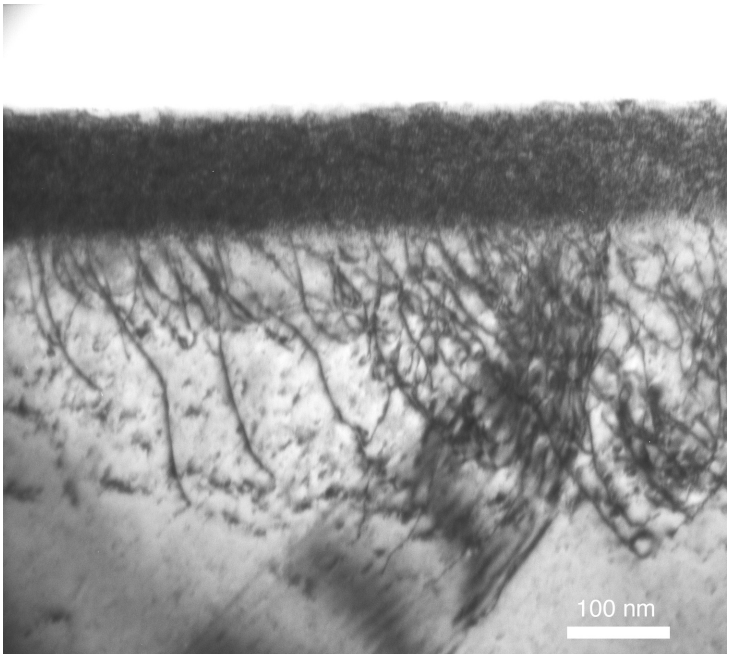

Figure 5.7: TEM micrograph of 350 °C Xe implant into ZrN. Note the depth of the dislocations and defects beyond the 100 nm implantation region. Note denuded zone at surface.

UNLV) to be a mix of ZrO_2 forms and an oxynitride. The quantity was quite low and, while the refinement attempts to provide a quantitative phase analysis, the GIXRD tends to accent certain phases due to the extremely low angle. As such, the phase quantities are assumed to be qualitative only.

It was expected that TEM would reveal the amount of defects to be reduced from annealing and pre-existing dislocations, form clusters, dislocation loops, and gas bubbles formed due to the high implant load (almost 4.5 atomic % xenon at peak). What was actually observed was virtually identical to the results for similarly damaged cryogenic and 350 °C samples. It appeared that the defects are mobile at higher temperatures, yet do not anneal with any significance. Figure 5.8 shows the TEM cross-section micrograph results, (note the large denuded zone at the surface).

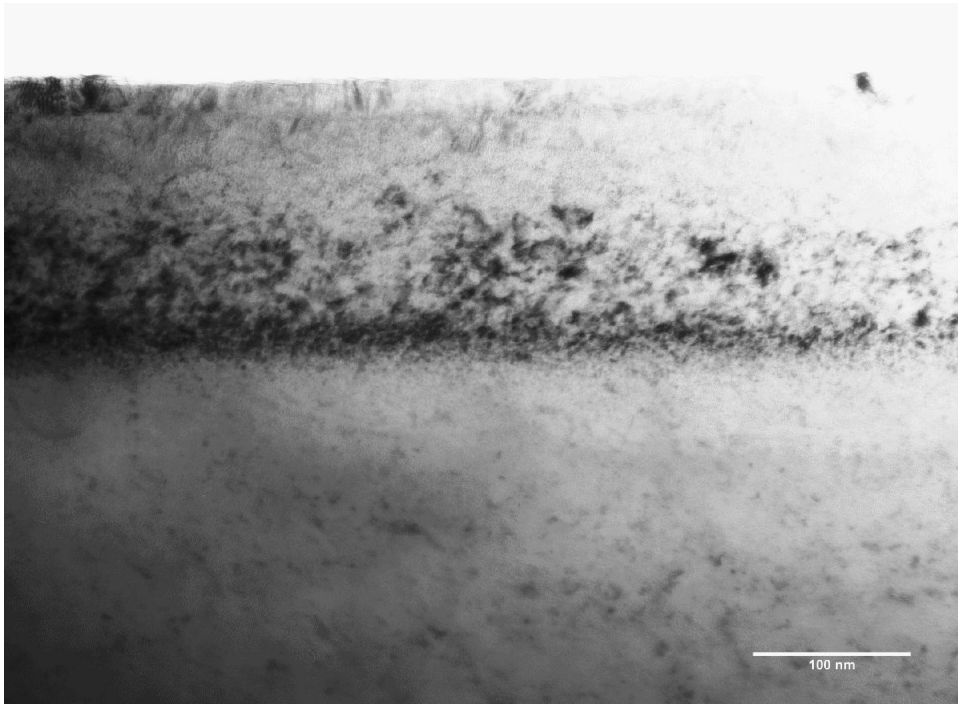

Figure 5.8: TEM micrograph of 580 °C Xe implant into ZrN. Note denuded zone at surface.

5.3.4 800 °C

The previous elevated-temperature implants showed evidence of defect mobility, however the defects did not anneal. They also showed virtually no change in lattice parameter with respect to the virgin sample. They did not show any bubble formation or distinct dislocation loops. The previous samples, however, had significant dislocation concentration at their surfaces. It was feared that, since dislocations can act as point-defect sinks, the defect accumulation during irradiation was much lower than in a corresponding material without surface damage.

Experiments at INEEL (now INL) and Argonne East showed major differences in results [153, 154]. These researchers used higher-energy implants and higher temperatures. They produced plan-view samples, however, and so performed had no damage/depth analysis. They did show results that appeared to be similar to those observed during the present

study at LANL. They observed many moiré-fringed domains yet had no explanation for these. Their results, in contrast, showed bubble formation, a lattice expansion of nearly 9% by electron diffraction spot analysis, and precipitates. They produced an analysis that stated that "the fcc structure of ZrN began to order into an $L1_2$ ordered structure", and assumed that these were the precipitates they were observing. Their results showed that ZrN would not make a proper fuel diluent/matrix material.

To address these results, an experiment was designed to mirror as closely as possible INEEL's implantation process. They used krypton and implanted to 80 dpa over a number of hours. At LANL, the implanter was equipped with a newly designed and constructed hot stage that could reach 800 °C within minutes. The sample was implanted with a fluence of $2 \times 10^{16} \frac{Kr}{cm^2}$ at a slightly reduced rate to approximately 70 dpa. The sample used was a heat-treated sample that had a much-reduced surface dislocation concentration.

GIXRD analysis showed virtually no change in lattice parameter with respect to the virgin sample. Oxidation was kept to a minimum but was present on the GIXRD spectra. As with any high-dose sample, the GIXRD spectra show peak broadening in relation to residual stress. This makes sense due to the large amount of Frenkel defects produced. If the left edge of the full-width, half-max of the 200 peak is used as a point of reference for lattice-parameter measurement, then it is observed that there could be a maximum 0.3 % increase.

Cross-sectional TEM analysis showed virtually no change with respect to that of other samples observed at LANL. The defect band was present, however, it was also observed that the defects were mobile and that there did appear to be some defect clustering. The clusters were noticed as a much more mottled appearance and also appeared much deeper into the bulk. No bubbles were observed and the defect clusters all appeared to be <10 nm in diameter.

To contrast the INEEL results, the heat-treated samples had significant oxides formed within the structure. It was considered that the dissolved oxygen coalesced, nucleated, and grew these oxide crystals. These are artifacts of the processing and considered only because of their possible misrepresentation of the ZrN. When the oxides are observed with SAD, the diffraction pattern appears to be cubic with double-diffraction satellites and/or superstructure reflection. This directly corresponds to the diffraction results that INEEL observed. The oxide is a mix of monoclinic, tetragonal and cubic phases (observed with GIXRD). Most of the TEM observations of the oxides show the twinned structure that is the monoclinic/tetragonal phases. The twinned structure gives the "superlattice" effect, (refer to Figure 5.9). The diffraction patterns also, if measured for lattice spacing, show a lattice parameter of 5.05 Å.

The results of observing the oxides, I believe, can be construed as a reflection of the results observed at INEEL. The lattice parameter of 5.05 versus 4.57 Å produces about a 10 % difference, close to their observations. The superlattice observed, the precipitates, etc., all seem to correlate with their results, and thus it is believed that the implantation at INEEL produced a large amount of oxidation, and that this was erroneously analyzed as irradiation damage.

5.3.4.1 Defect Clusters

The defect clustering observed is one distinction from all other experiments observed with TEM at LANL. The clusters appeared to be mobile, as some were up to 160 nm deeper into the bulk than the normal 100 nm. The relatively short time under irradiation and temperature allowed for some significant diffusion of defects.

Under high magnification it was observed that some of these defect clusters had the appearance of dislocation loops. Figure 5.10 shows a sample TEM micrograph of the

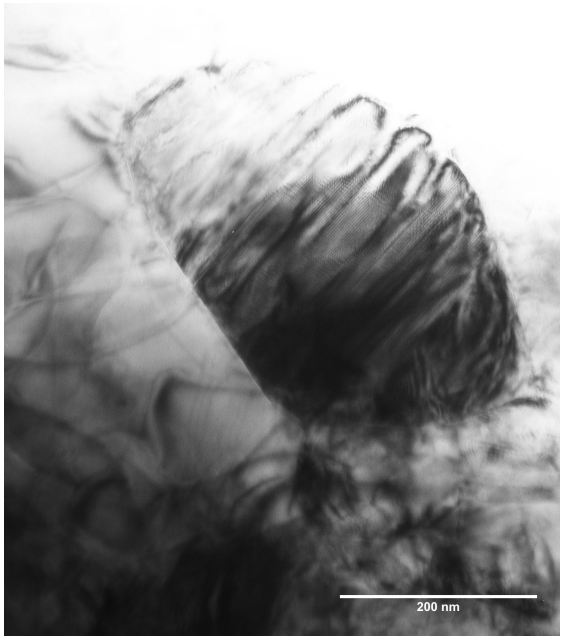

(a) Twinned oxide precipitate in ZrN from annealing treatment.

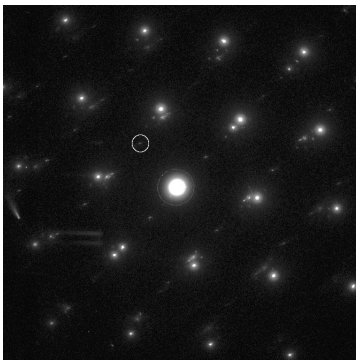

(b) SAD of oxidized area showing extra spots.

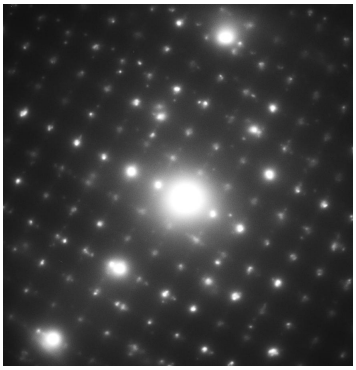

(c) SAD of oxidized area showing superlattice spots. This oxide was heavily twinned.

Figure 5.9: Oxides observed under TEM showing twinning, extra spot formation and superlattice diffraction effects. Results are similar to those reported by INEEL.

possible loops. The strain fields about a loop tend to produce the halo effect with a darker and lighter side [155, 156]. Attempts at analysis failed to identify whether the loop was either vacancy or interstitial, or even possibly an oxide nucleation.

Dark field analysis, however, did show that, when on a 001 zone axis, the 220 spots produced strong diffraction while the 200 spots produced weak diffraction (refer to Figure 5.11). This suggests that the {110} is the preferred clustering orientation for defects. Referring to Figure 5.1 (a), the oxide particles appear to produce Guinnier-Preston like precipitation along the same plane systems.

The dislocation loops and clusters did appear to be mobile, or otherwise formed after significant mobility of the point defects. It is considered that the defect mobility is enhanced by the implanted gas atoms, which diffused into the bulk until either they began to cluster or vacancies clustered about them. At 800 °C, the amount of mobility seems high while defect annealing seems low.

5.3.5 Low-Dose Cryogenic Implantations

With the successful removal of much of the surface dislocation concentration, it was possible to analyze the defects from the low-concentration implantations. ZrN had proved to be highly tolerant to heavy-ion irradiation damage and had exceeded 200 dpa at cryogenic temperatures. The density of the defect band from these high-dose irradiations, however, made it impossible to distinguish a single defect. Low-dose irradiations prior to the annealed ZrN samples showed such a density of dislocations, and again it was impossible to distinguish the point defects.

The annealed samples allowed low-dose defect observations. The fluences used were 10^{15} and $10^{14} \frac{Xe}{cm^2}$, which correlate to 4 and 0.4 dpa. These samples were implanted at cryogenic temperatures to preserve as much damage accumulation as possible.

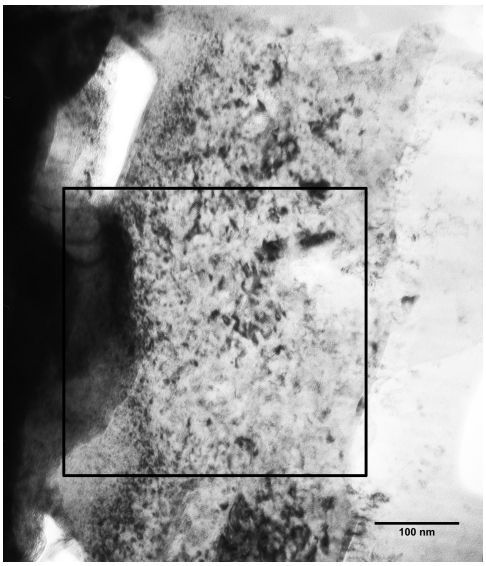

(a) Cross-sectional TEM micrograph showing damage depth. The right side shows the glue/ZrN interface.

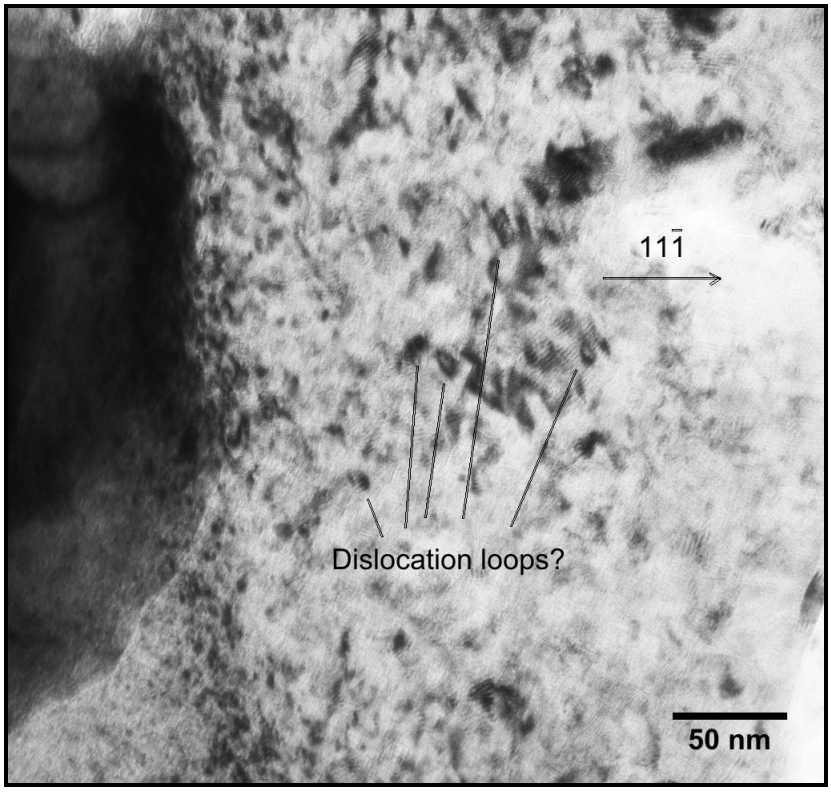

(b) Close-up view of the left showing what resembles dislocation loops.

Figure 5.10: Possible dislocation loops observed with 70 dpa implant of Kr at 800 °C

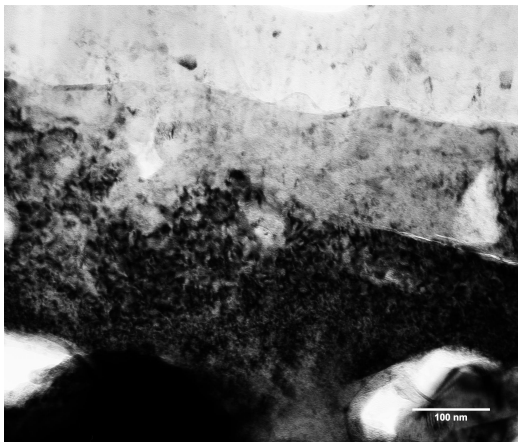

(a) Bright field image showing defects and clusters from surface.

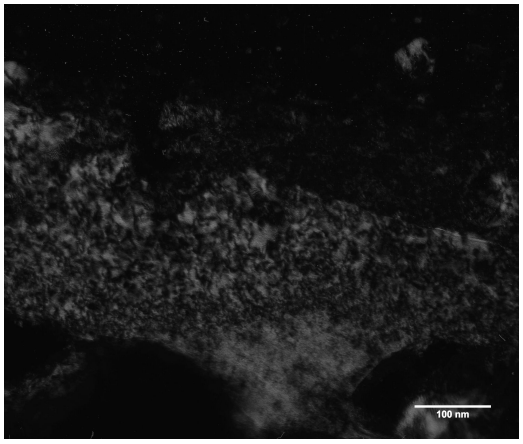

(b) Dark field image on the 001 zone axis with a selected 220 spot. Note the high contrast.

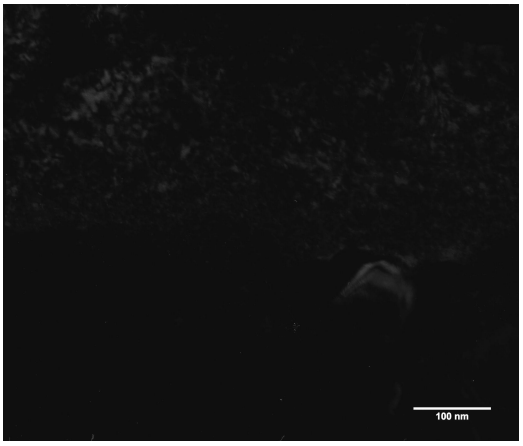

(c) Dark field image on the 001 zone axis with a selected 200 spot. Note the lack of contrast.

Figure 5.11: Bright and dark field TEM of defect clusters formed at 800 °C from 70 dpa Kr. 001 zone axis with all 200 and 220 spots observed. Respective dark field images are representative of all respective reflections.

Although little dislocation damage was observed, the defects showed little of interest. The amount of defects retained produced a dense band, even at 0.4 dpa. Of interest, however, is the defect strain effects (high contrast) that were observed with TEM. Between the two low-dose samples, there is a significant difference in implant depth. This cannot be the case due to the similar parameters used. The one difference is the amount of xenon implanted. If the displacement damage profile and implanted xenon profile are observed, the damage peaks at a lower depth of 35 nm, while the implanted xenon peaks at 55 nm. Both distributions terminate near 110 nm, yet the damage is skewed toward the surface while the implanted xenon is skewed toward the termination.

Since the implanted xenon produced the same damage and implantation depth profiles between the 4 and 0.4 dpa experiments, the difference must be in the amount of xenon implanted. The damage on both is in the same region and *appears* to be similar in concentration; however, the implanted xenon region appears to be very dark in the 4 dpa sample while the 0.4 dpa sample appears not to show this contrast. The order-of-magnitude greater amount of xenon implanted, whether in interstitial or substitutional sites, appears to produce enough strain at the higher implant dose ($\approx$0.225 atomic %) to produce distinctly dark contrast (lattice strain). This allows it to be observed with TEM diffraction contrast due to the lattice strains. The 0.4 dpa sample does not show this strain effect due to the much smaller amount. It does give some insight to the depth of damage from the implantation.

The evidence that the end-of-range xenon (or krypton) produces strong contrast is interesting with respect to the mobility of defects at elevated temperatures. Many of these mobile defects are quite possibly the implanted gas atoms diffusing into the bulk. It appears that these defects have a high contrast such as those observed at the end-of -range. Figure 5.13 shows the 0.4, 4 and 70 dpa implants on annealed ZrN samples for comparison of the defects and relative depths.

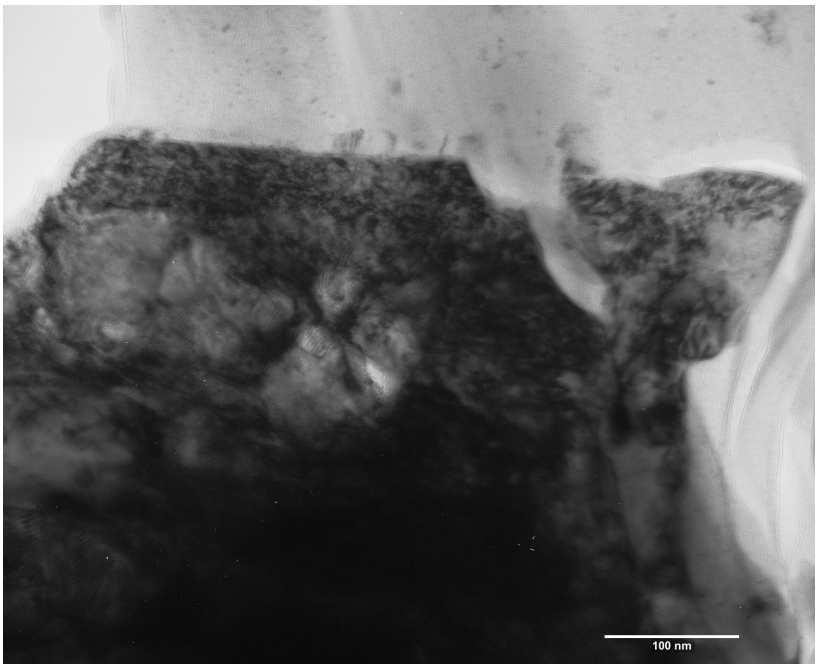

(a) 0.4 dpa damage from xenon implant. Note the low depth of damage.

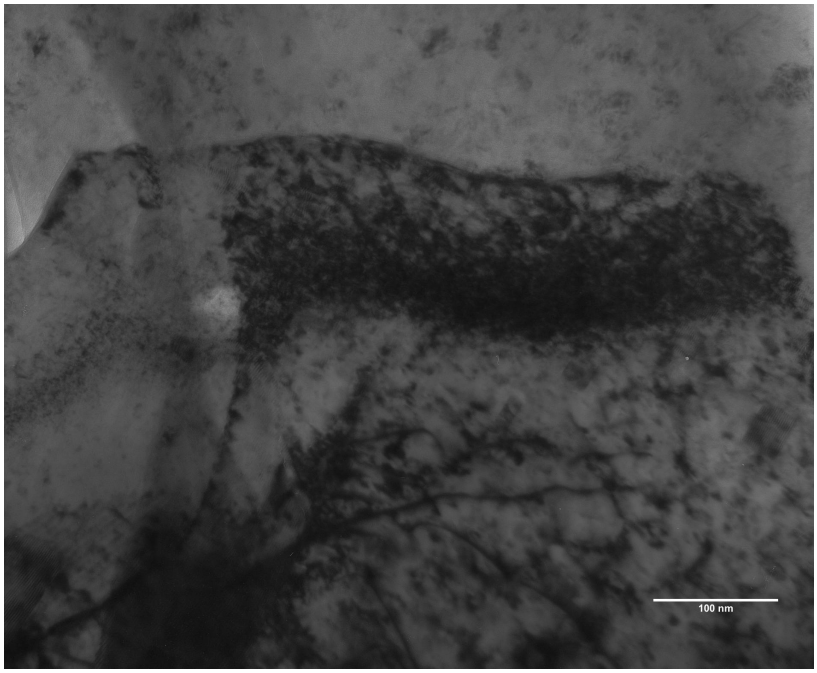

(b) 4 dpa damage from xenon implant. Note the end-of-range damage that has higher contrast.

Figure 5.12: Low-dose implantation of xenon into ZrN at cryogenic temperatures

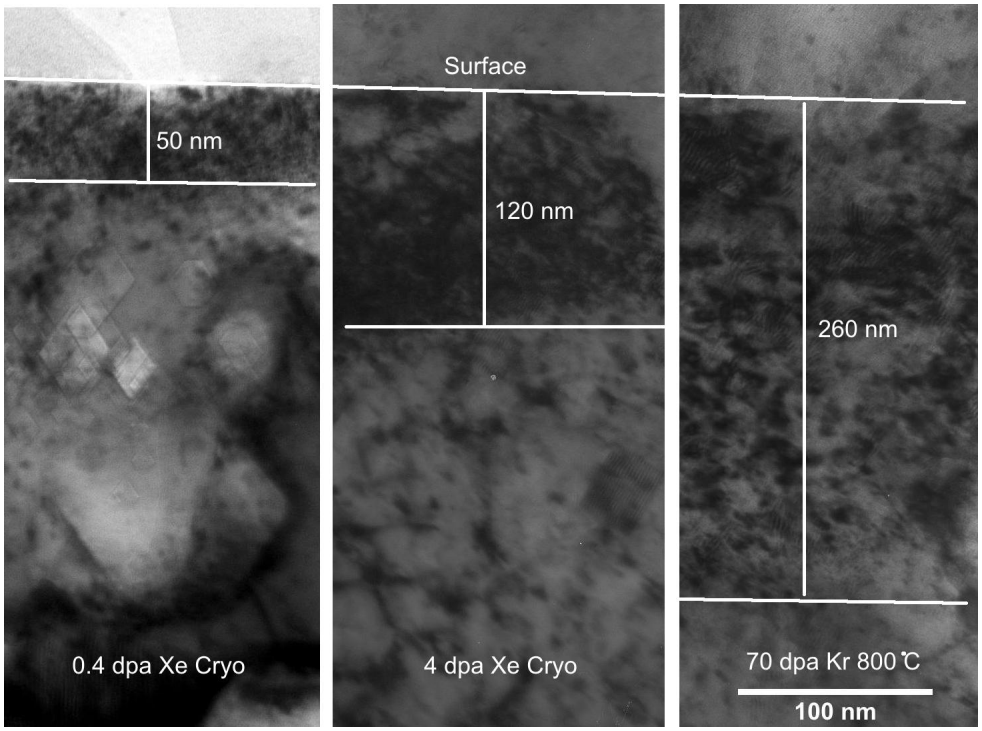

Figure 5.13: Comparative cross-sectional TEM micrographs showing relative depth from surface

5.4 Physical Property Changes

Various physical properties are important for AFCI as well as an understanding of the inherent structure of ZrN. A wide selection of techniques has been used to study many important factors.

5.4.1 Volume Change

Polished samples were implanted with up to a fluence of $5 \times 10^{16} \frac{Xe}{cm^2}$, which equates to about 12.5 atomic % xenon at the distribution peak. This peak depth is about 55 nm and is a slightly skewed Gaussian curve with a maximum depth of about 110 nm. The sample was masked over an area to eliminate implantation. The volume change can be determined from the depth change across the line separating the implanted and unimplanted regions.

First, SEM was used to target and confirm the presence of xenon by EDS. Figure 5.14 shows such a plot. EDS measurements are difficult due to the overlap of the zirconium sum peak and the xenon primary peak. Samples were cut and viewed from the side with SEM to observe the volume change step. No step was observed with SEM.

With AFM, which has a much higher resolution, the samples were again tested across the separation line. The only observation was a slight increase in volume at the interface, but it was on the unimplanted side. This was confirmed with EDS. It was determined that, with the resolution of AFM, at $5 \times 10^{16} \frac{Xe}{cm^2}$ fluence, approximately 200 dpa and 12.5 atomic % xenon, gas swelling was not observed. These samples were implanted at cryogenic temperatures and not annealed.

Due to the lack of bubbles or amorphization observed with TEM, the lack of detectable volume change is not surprising. Some ceramics, such as Al_2O_3, amorphize very readily under irradiation. It has been observed that Al_2O_3 swells approximately 30 % when it

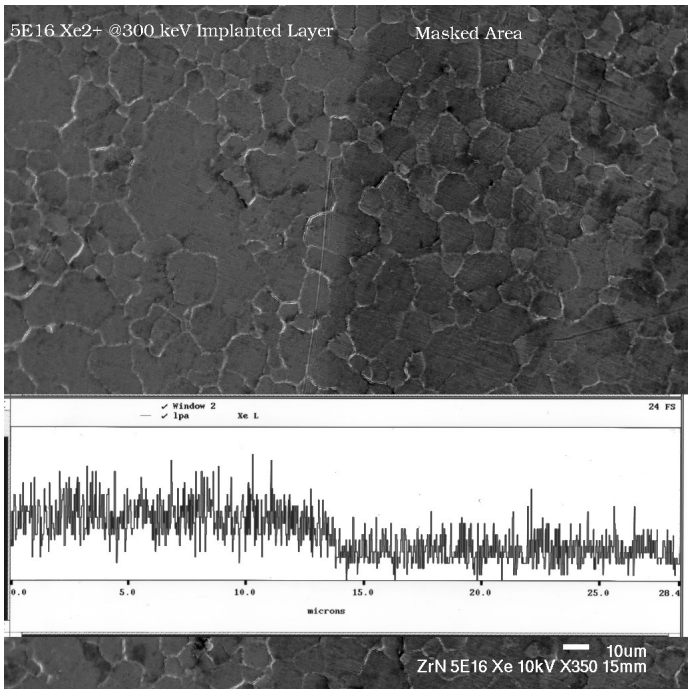

Figure 5.14: EDS xenon line-scan of ZrN sample surface

amorphizes [157, 158, 159, 160]. Swelling with bubbles is also very large in metals and significant effects are found within conventional nuclear fuels [155, 27, 25].

5.4.2 Mechanical Properties

An understanding of the intrinsic mechanical properties of ZrN before and after irradiation damage is important. Understanding the observed dislocation production in a very hard material seems prudent, while moving these dislocations with increasing resistance brought on by the introduction of irradiation-induced defects gives a metric of defect density.

5.4.2.1 Texture

It has been observed that there is a texturing effect from the pressing and sintering process that differs from that of the HIPing process. It has been suggested that these are

the result of plastic deformation. Samples observed with OIM (Orientation Imaging Microscopy) and x-ray pole figures from diffraction show distinct differences between green, sintered, HIPed, and a sample that was CIPed and then highly annealed in a xenon float-zone furnace (temperature $\approx$ 3000 °C)[2] that caused significant grain growth [161]. The results correlate with the observation of polishing dislocations such that there is significant plastic deformation in ZrN.

5.4.2.2 Hardness and Modulus with Increasing Irradiation Damage

The nanoindentation technique provided the mechanical information as to the microstructural development and the defect interactions. The technique penetrates only a few hundred nanometers into the surface. This provides some depth information, but it is mostly averaged. Damage was assessed with xenon implanted at 300 keV with fluences to give 0.4, 4 and 40 dpa. An unimplanted sample was used as well to give 0 dpa.

The hardness shows a dramatic increase resulting from the implantation damage. The increase in very large from 0.4 to 40 dpa, but less from 4 to 40 dpa.

Irradiation damage causes many defects that tend to inhibit dislocation motion. The dissolved gas will strain the lattice, and the displacement interstitials tend either to form dislocation loops or to become a movement inhibitor. Dislocations can be produced with sufficient number that the dislocations will tangle. These defects, produced by the irradiation, will then harden the material [162, 163, 164, 165, 166, 167]. Yet, as can be seen in Figure 5.15, the hardness does not increase linearly. It tapers off as the damage increases. This shows that the displacement-produced defects are becoming saturated. Frenkel defects are produced in sufficient quantities that they have are significantly close and can join them

[2]Cold-pressed and sintered pellet, HIPed, and float-zone sintered sample produced at LANL. Green pellet produced at ASU. All texture analysis performed at ASU.

and annihilate. This has been observed in metals as well as ceramics such as monoclinic ZrO_2 [168, 169].

The modulus data show no statistical change from the unimplanted sample. This makes sense as the structural bonding characteristics are not changed. Amorphization would alter the bonding, was confirmed not to occur with this level of displacement damage. Since xenon, krypton and helium are noble gases, no chemical activity is expected. Large amounts of vacancies will disturb the electronic character, as observed by SQUID detectors on the superconductors. It is also thought that large amounts of nitrogen vacancies would decrease the modulus by altering the electron density about the atoms [80, 170, 171, 81]. If this is true, it would show that the vacancy concentration produced by irradiation is not stable and recombines quickly.

5.4.2.3 Surface Plasticity

TEM investigations showed dislocations in every cross-sectional sample, and these were at first thought to be produced by the damage-induced strain. This seemed likely given that oxide ceramics with similar mechanical properties showed no such surface defects. However, it was shown in several unirradiated virgin samples that dislocations were produced during the specimen preparation stage.

One such experiment used a sample polished conventionally to 1 μm diamond. The sample was sectioned in half and then one half was polished with a much coarser 6 μm diamond. The two halves were then glued face-to-face and processed as a cross-sectional TEM foil. The result showed a distinct correlation between the diamond size used for polishing and the depth that the dislocations protruded (Figure 5.16).

This result prompted a long process to attempt to remove these dislocations. The origin of these dislocations, however, is interesting in its own right. A *Triboscope* nanoindenter at

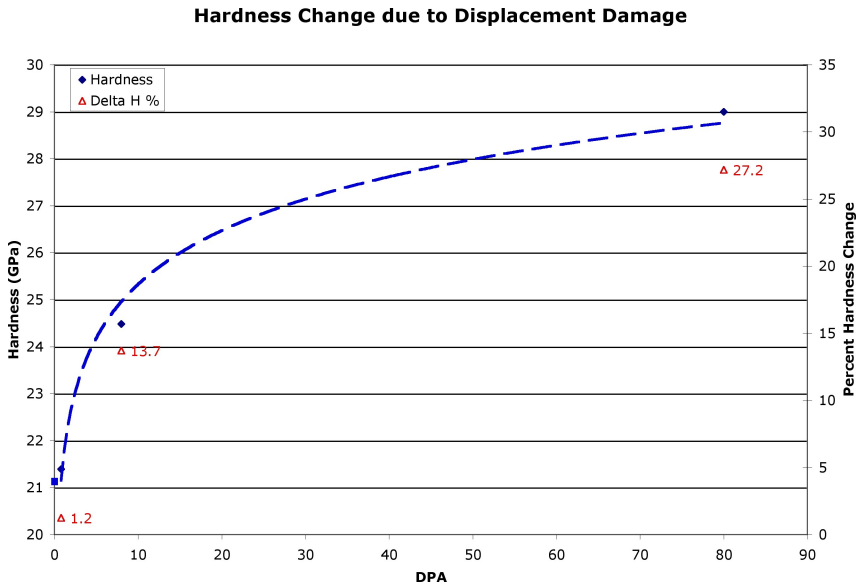

(a) Hardness change with increasing displacement damage

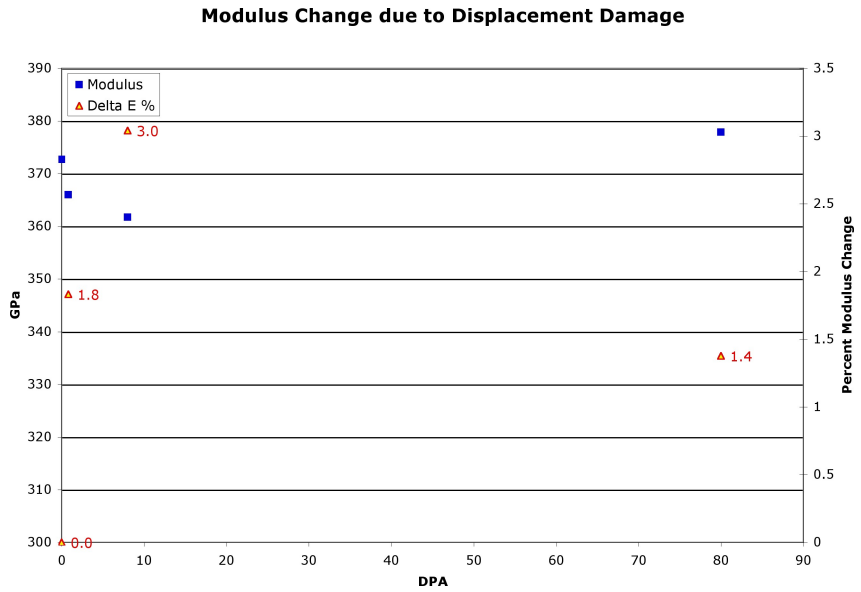

(b) Modulus change with increasing displacement damage

Figure 5.15: Nanoindentation measurements of hardness and modulus vs. dpa. Note the % change on the right y-axis of each graph

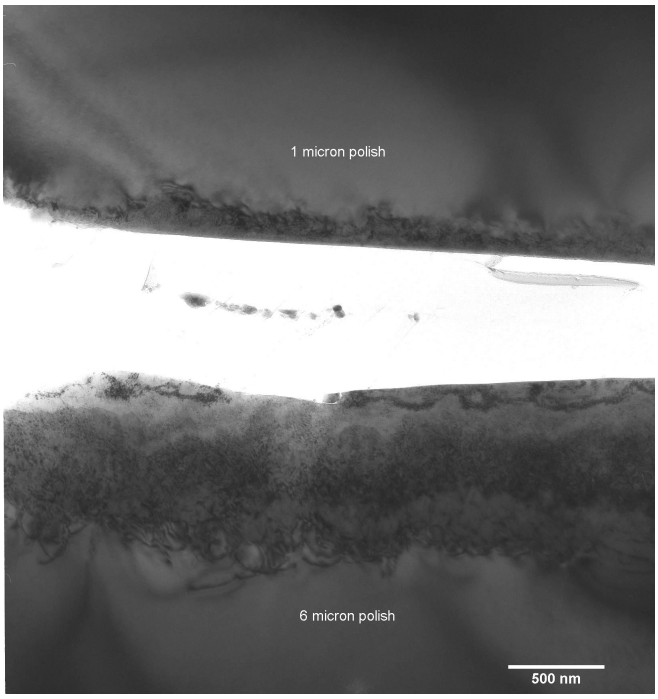

(a) Dislocations produced by 1 and 6 μm polishing. The depth shows a near 100 nm to micron media relation.

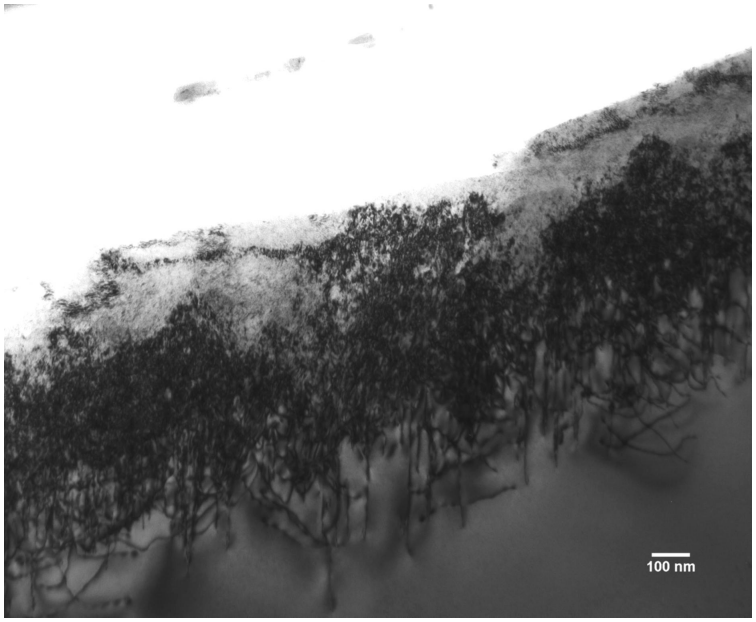

(b) Closer view of the dislocations produced to near 600 nm by the 6 μm polish.

Figure 5.16: Cross-sectional TEM of 1 and 6 micron diamond polishing effects on a virgin ZrN sample

ASU was used to study the effects of continued submicron polishing with colloidal silica[3]. The nanoindenter has a diamond tip that doubles as an AFM such that the area indented can then be scanned for plastic deformation effects.

The experiments showed three distinct relations with the load on the tip. First, there was a distinct and sudden onset of plastic flow, or the "avalanche effect," as dislocations are suddenly nucleated and/or multiplied. With continued polishing with colloidal silica it was shown that this critical load was increased from 900 to 1600 μN. Secondly, if the load to below this critical value, the result was almost perfectly elastic, and AFM showed a surface that is extremely flat and featureless. Thirdly, the highly polished sample was again polished with 800 grit SiC paper to induce a mass of dislocations via the relation shown in Figure 5.16. The resultant load/displacement curve shows a virtually plastic response. The AFM image shows a significant "push-out" signifying distinct plastic deformation.

These results taken together signify that dislocation presence in large numbers allows much plastic deformation with minimal critical load, while with continued polishing this dislocation density decreases and thus the critical load is increases. Gerberich noted that an oxide layer has a distinct relation of thickness to dislocation nucleation [172]. There results appeared to show some merit as, from using the equations listed in the reference, a predictive energy graph was produced, and this plot appeared to match the data yet predicted a growing oxide layer.

Since no oxide layer had ever been observed on ZrN with XTEM, this did not seem to fit the model. Gerberich noted in a paper by Kramer that "oxide effects" for producing dislocations showed up in pure oxides such as Fe_2O_3 or in a precious metal such as gold [173]. As such, the model was modified to include surface and sub-surface defects.

The small sub-surface defect theory may play well with oxide crystallites observed near

[3]Nanoindentation/polishing experiments performed by Kirk Wheeler and Pedro Peralta at ASU.

the surface by XTEM. Although invisible under bright field, these "crystallites" are observed very near the surface as random spot reflections under CBED. The reflections show crystallinity even while the precipitates are too small to observe. Very small domains were observed with samples that were not heated during preparation. These domains showed the moiré fringe effect, suggesting a lattice-parameter mismatch. It was feared that these were artifacts of ion milling; however, on these specimens, they appeared only in the damaged region (near surface). With annealing experiments, oxide precipitation showed up more strong with precipitates growing to 20 nm or larger. These oxide precipitates all produced this moiré fringing, and thus it was suggested that the oxides were growing from the dissolved oxygen in the lattice. For a diffusion front of oxygen, however, it is also suggested that some of the dissolved oxygen is high enough in concentration to produce homogeneous nucleation near the surface.

It is suggested that, in all ZrN surfaces, there are oxides formed on the sub-nanometer scale. From CBED, these were observed for the first 10 - 20 nm from the surface. With the ZrN sample that was implanted at 580 °C, it was observed with CBED that these random spots appeared as deep as 50 nm from the surface. This suggests that oxygen diffused at the higher temperature. GIXRD also shows oxides on every sample of ZrN observed. The monoclinic ZrO_2 phase is the largest amount, while the tetragonal phase was also observed. When the glancing angle was reduced, the proportions of oxide phases were shown to be very near surface (<25 nm by the *Bruker* AXIS software).

In the sub-surface oxide crystallite theory, the near surface then appears as a separate material - a composite of ZrN with ZrO_2 particles. The depth of this "composite" is approximately 20 nm; however, this has been shown to be different with surface age and thermal history. The elastic moduli of each material are sufficiently different that, when the nanoindenter tip is pressed against the surface, the ZrN/ZrO_2 lattice interface is strained.

With this model, the oxide particles will, if enough stress is applied, nucleate dislocations. Since these particles are in close proximity to each other, multiplication may occur via the Frank-Reed source process. At this "critical stress", dislocation nucleation and multiplication happens almost instantly providing plastic flow and thus producing the "avalanche effect."

From the nanoindentation experiments at ASU, polishing with colloidal silica showed an increasing amount of applied force before the critical load was obtained. This suggests that the polishing removed pre-existing dislocations and oxides, further increasing the stress needed to nucleate and move dislocations. Figure 5.17 shows the effect of a one-hour polish. Note the sudden increase in strain, or the "avalanche" of dislocation activity. Figure 5.18 shows the effect on the same sample if the indenter is not allowed to reach the critical load of about 900 μN. This shows virtually no plastic deformation with no residual indentation. The load-displacement curve also shows almost perfect hysteresis. Figure 5.19 shows the effect of a second one-hour polish on the same sample surface. The avalanche effect is still apparent; however, it is at nearly 1600 μN before the dislocations are nucleated, multiplied and moved. It is expected that the polishing removed the oxides and/or dislocations at the surface such that the critical stress was increased.

Dislocations were put into the surface deliberately by polishing with 1200 grit SiC paper. This near-surface dislocation density negated the need for a critical nucleation stress, and thus the indentation was virtually plastic. Figures 5.20 and 5.21 show these effects, contrasted to the Figure 5.17, with "push-out" of material around the indentation. The load-displacement curve shows no avalanche effect but almost immediate plastic deformation.

The plasticity observed at the surface is unusual for a ceramic of such hardness values; however, carbides have been known to show some plasticity, especially at elevated temperatures [34, 45]. TiC and ZrC have both been shown to be plasticly deformable at

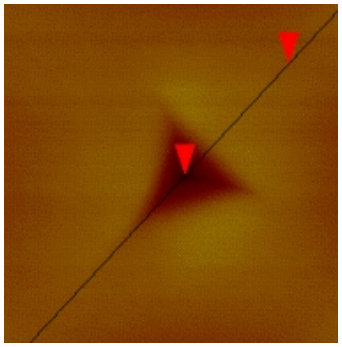

(a) AFM surface detail

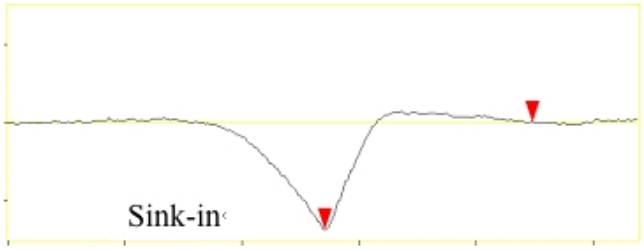

(b) Line -hieght profile of indentation

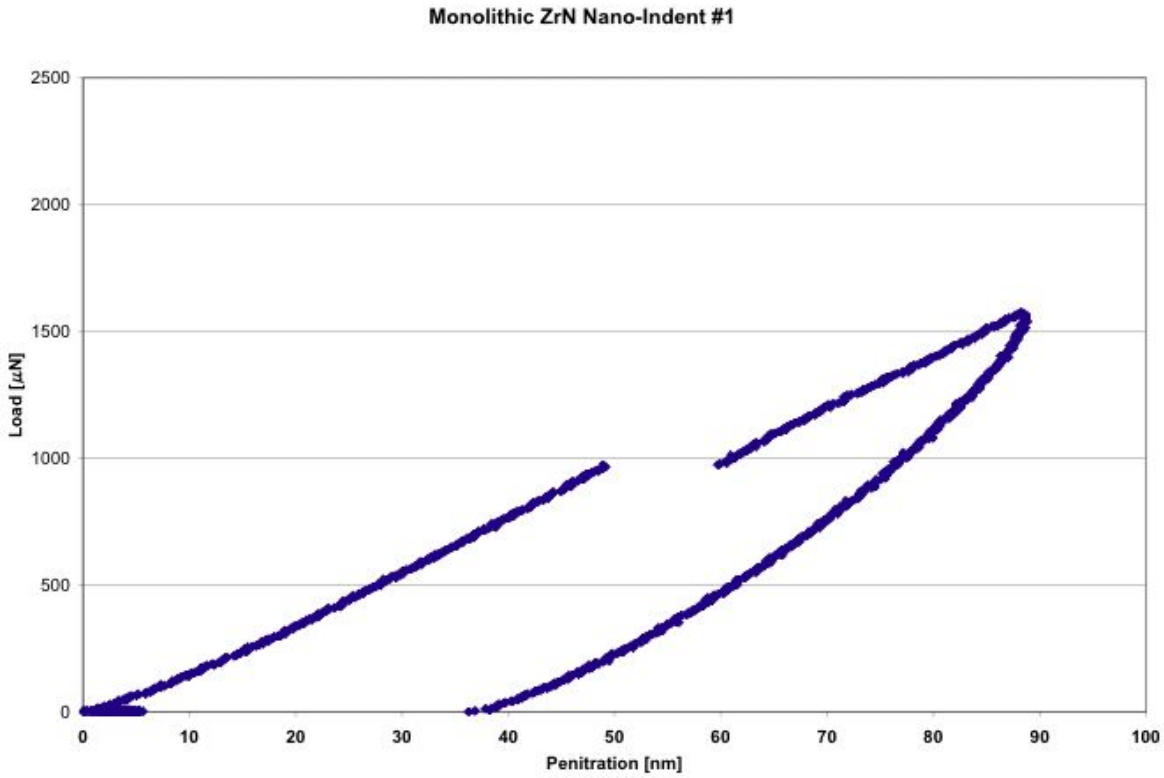

(c) Load-displacement plot showing a sudden "avelanche" effect at aobut 900 μN.

Figure 5.17: Nanoindentation of ZrN with 1 hour polishing with colloidal silica

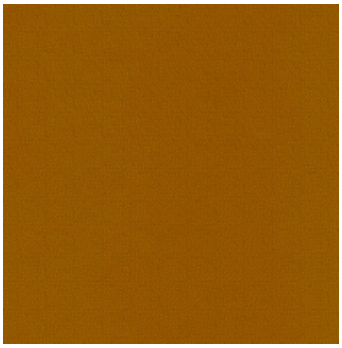

(a) Subcritical loading produces perfectly elastic responce. Note the lack of any indenter detail.

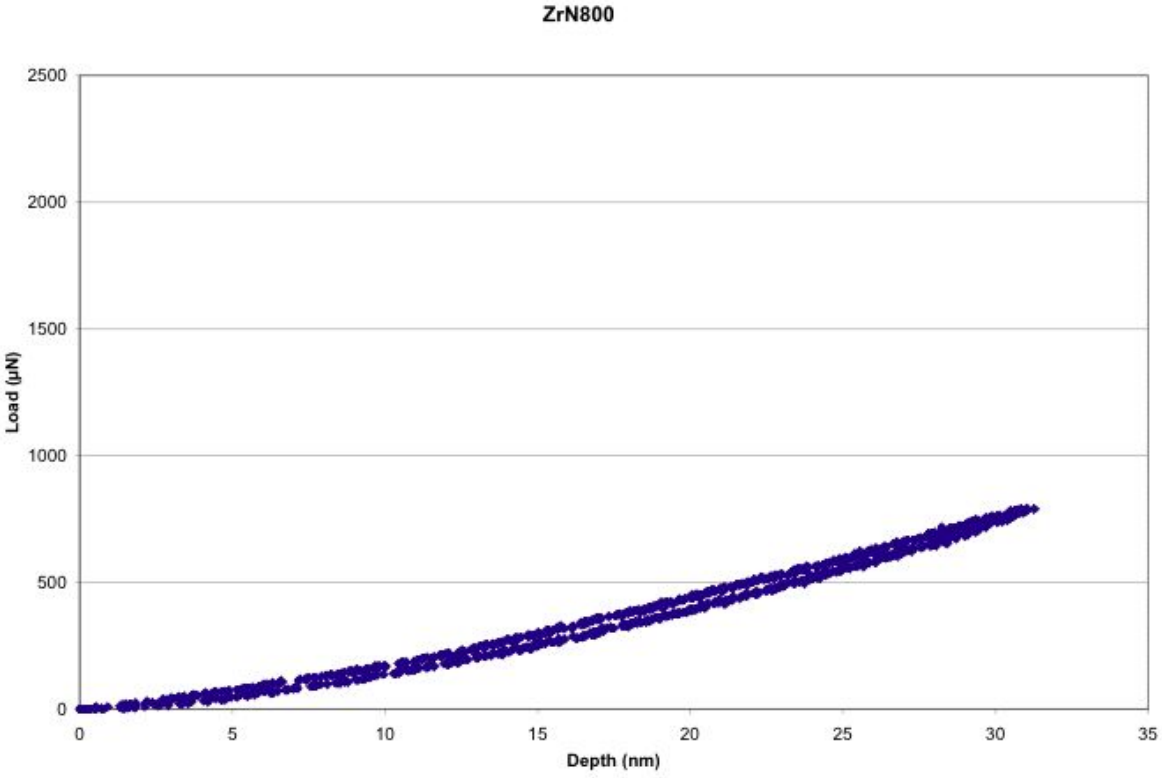

(b) Load-displacement showing elastic responce.

Figure 5.18: Sub-critical nanoindenter loading

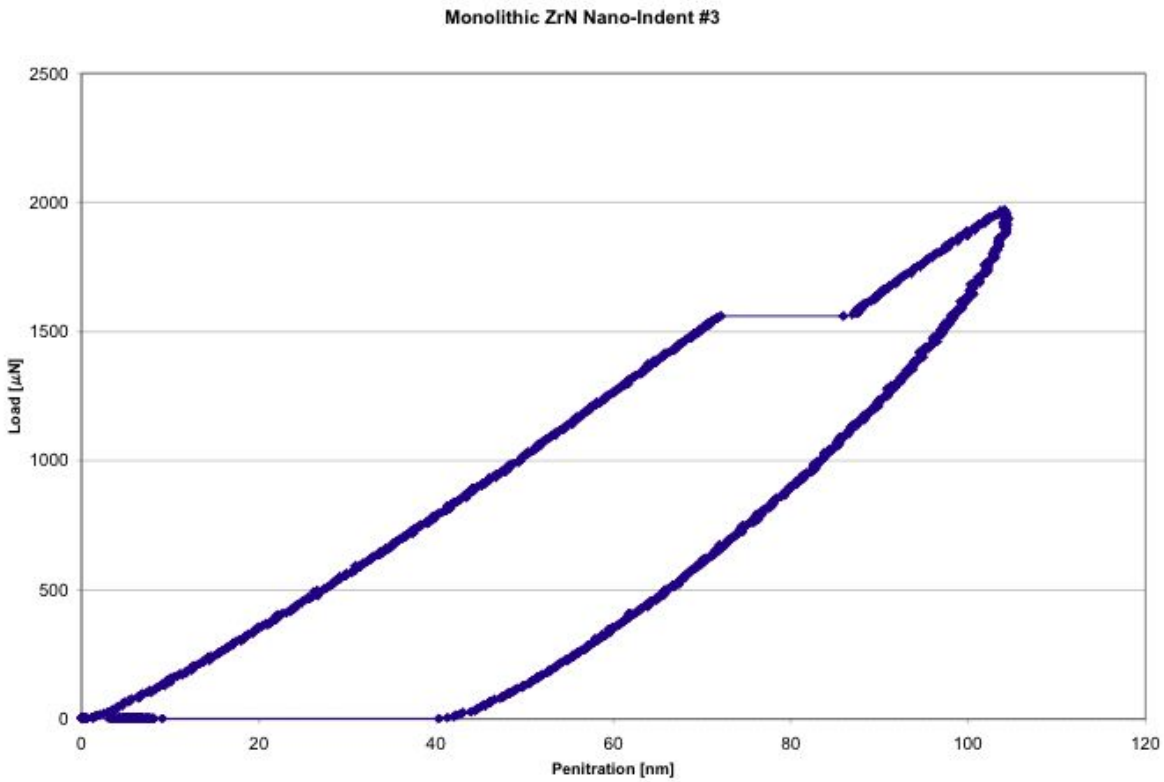

Figure 5.19: Load-displacement curve for continued polishing with colloidal silica (2 hours total)

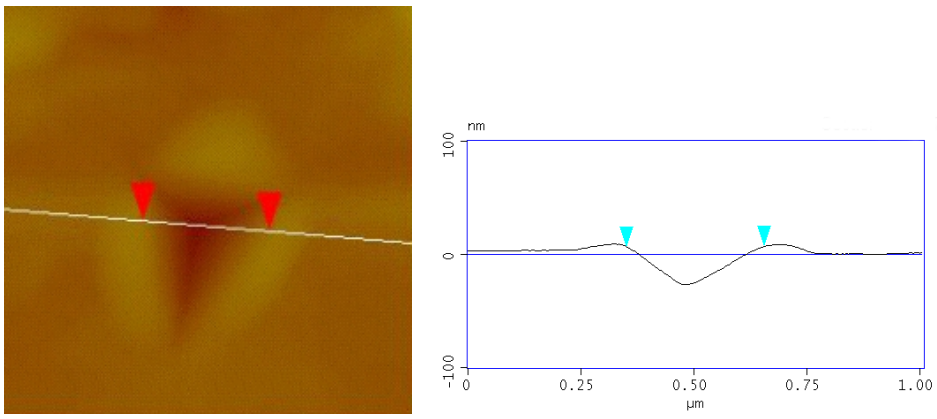

(a) Surface detail showing area used for height profile.

(b) Height profile of nanindetation. Note the "push-out".

Figure 5.20: AFM data from ZrN surface polished with 1200 grit SiC paper to induce surface dislocations. Note the push-out from plastic deformation

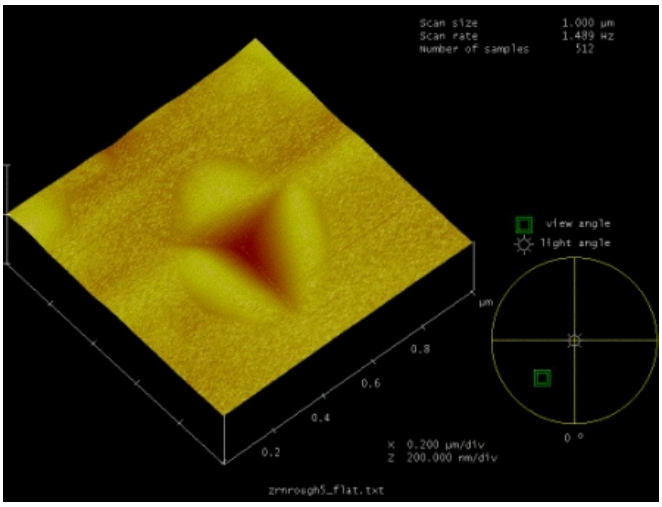

(a) Surface topography from plastic deformation due to nanoindenation.

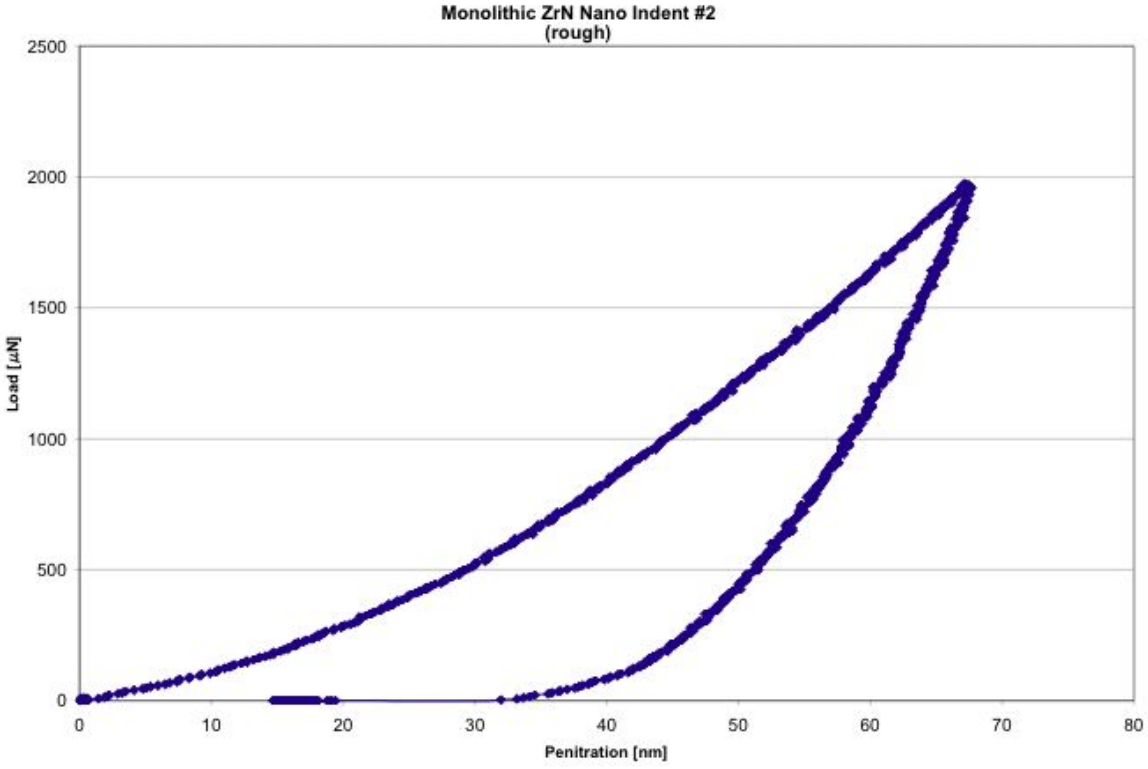

(b) Load-displacement curve showing no "avelanche" effect but plastic flow.

Figure 5.21: AFM data from ZrN surface polished with 1200 grit SiC paper to induce surface dislocations. Note the load-displacement plot showing heavy plastic deformation with little loading

temperatures over 1000 °C. It was shown that in TiN, similar to TiC and ZrC, the primary slip system is the $\{110\}\langle 1\bar{1}0\rangle$ [45]. This is similar to strictly ionic crystals such as sodium chloride. However, at elevated temperatures other slip systems become available through a brittle-to-ductile transition, allowing much more plasticity. It is expected that ZrN would have similar properties.

5.4.2.4 Dislocation Analysis

Dislocations were observed in virgin material produced by polishing. Three different zone axes were tilted while the same area of dislocations was observed. The dislocations appeared to be jogged and in motion from flow. Figure 5.22 shows some different tilts with dislocations from the same area. Bright-field TEM showed the dislocations that looked to almost be two close partials. By using weak-beam dark-field TEM, it was shown that the dislocations are sharp single cores (Figure 5.23).

Tilting to the 100 zone axis showed dislocations with different contrast. As it happened, this zone axis produced a $g \cdot b = 0$ contrast while the opposing g vector showed the dislocations as highly contrasted straight lines (Figure 5.24). These dislocations were lying on a plane parallel to the zone axis, shown to match the $g = 220$. $g \cdot b = 0$ shows that either $b = \langle\bar{1}10\rangle$ or $\langle 1\bar{1}0\rangle$. Since only one $g \cdot b = 0$ or invisibility criterion was met, the Burger's vector cannot be determined with certainty. The plane in which the dislocations lie is, from the diffraction pattern, the $\{110\}$set of planes, i.e. those that bisect the cube from corner to corner. This indicates the dislocation slip system to be the $\{110\}\langle 1\bar{1}0\rangle$, which is similar to that of the carbides and TiN [34, 45].

The dislocations that move along the slip system $\{110\}\langle 1\bar{1}0\rangle$ shows some effect of atom charge, similar to ionic crystals. Moving the atoms atop each other during glide on the $\{111\}\langle 1\bar{1}0\rangle$ system will put like atoms near each other, and as such, Coulombic

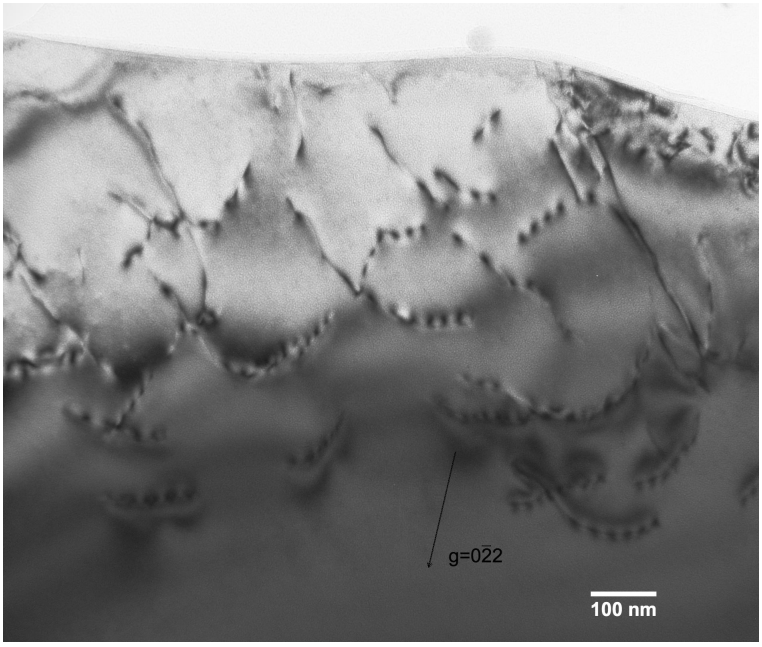

(a) Disolocations from 2-beam condtion

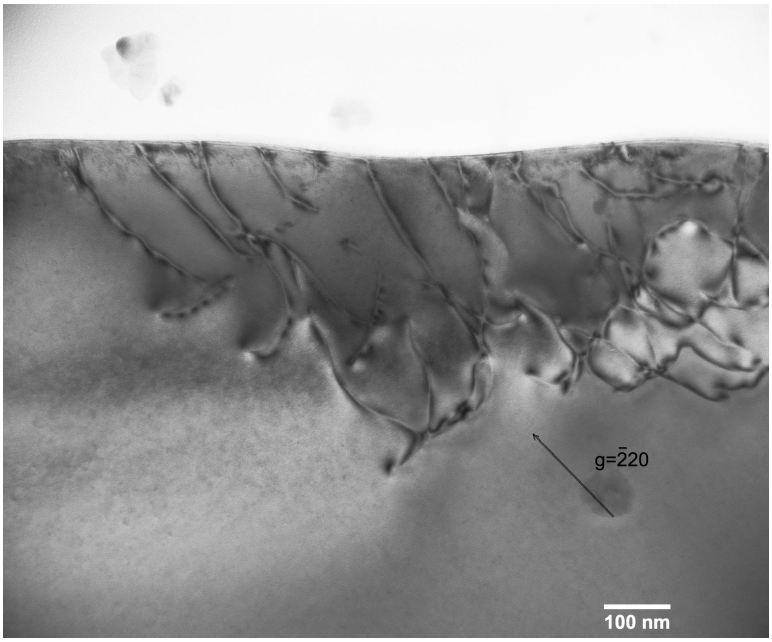

(b) Disolocations from 2-beam condtion

Figure 5.22: TEM micrographs showing dislocations at the surface of ZrN from polishing

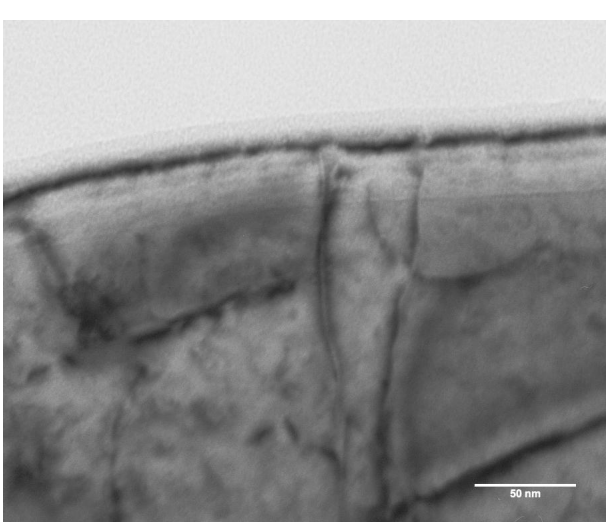

(a) Near-surface view of dislocations.

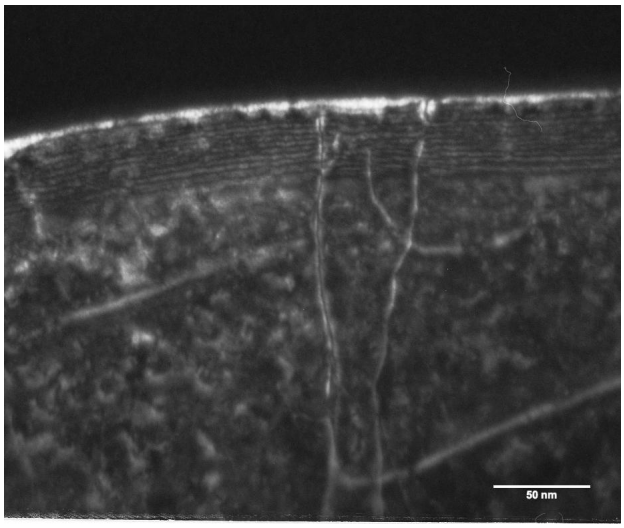

(b) Weak-beam dark-field view of dislocations. Note the sharp resolution of the dislocation core.

Figure 5.23: TEM micrographs showing dislocations at the surface of ZrN from polishing

repulsion will add an energy that is high enough to force the primary slip system to be $\{110\}\langle 1\bar{1}0\rangle$. Figures 2.13 and 2.14 show a lattice overlay of the glide systems and half-slip is shown with the nearest-neighbor atoms. From this analysis, it appears that ZrN has significant partial charges on the zirconium and nitrogen atoms.

5.4.2.5 High-Rate Deformation/Fracture on ZrN Powders

Dislocations at the surface formed by polishing are of concern for the validity of the experimental results. The fuel pellets in question, however, undergo processing procedures such as milling and grinding. It is expected, therefore that the final fuel product will have a significant concentration of dislocations while in service.

To understand the nucleation and multiplication process, a simple experiment was devised. Powders were observed with TEM for their response to high-rate deformation/fracture. This high-rate fracture was based on the use of a hammer and anvil to “smash” and break

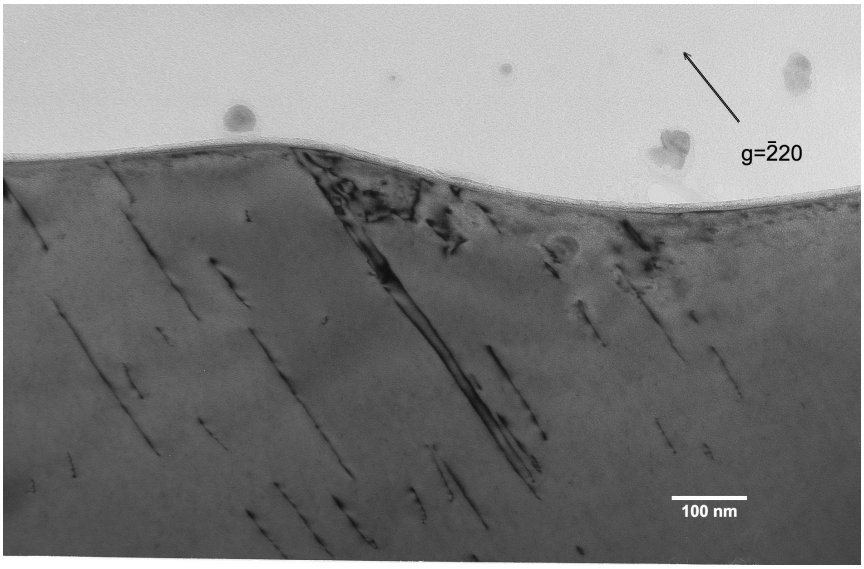

(a) 100 zone axis showing dislocations along the 220 planes. In this case $g \cdot b = 2$

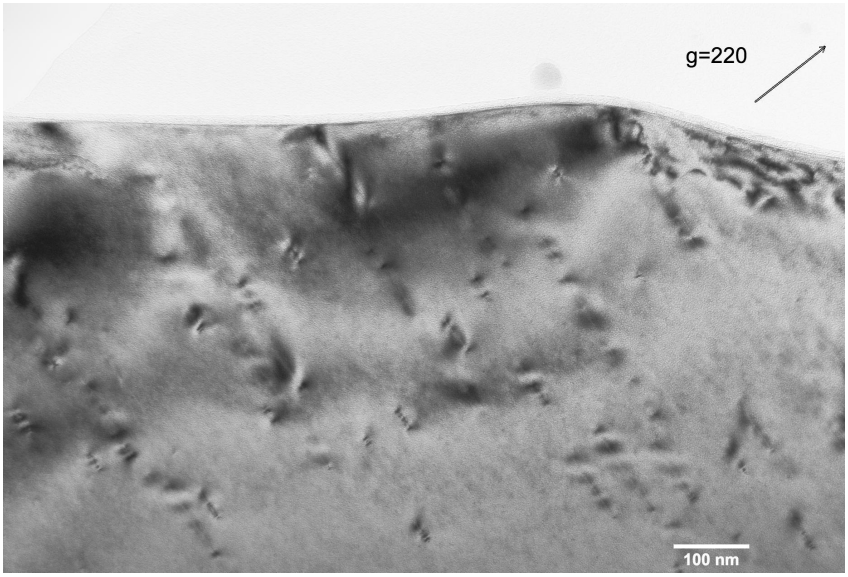

(b) Dislocations shown with no contrast so that $g \cdot b = 0$

Figure 5.24: TEM micrographs showing dislocations on the 100 zone axis

the powder quickly. Powders from different stages of processing were analyzed with and without hammering to show their susceptibility of the dislocation nucleation.

Five samples were analyzed:

- CERAC raw powder,
- Raw powder that was hammered,
- CERAC powder Spex-milled for 45 minutes,
- Cold pressed and sintered into a pellet (CPS) then hammered,
- HIPed sample hammered.

These samples were then placed onto a lacey grid and observed under TEM. A simple grading system allowed for quick but subjective measurements of the dislocation density. Dislocation concentration was assumed to be low with few to none, medium with a noticeable amount, and high with a large concentration. Numerical values were then assigned as shown below. 30 different powders were analyzed for each sample type. The data were tallied and mean values produced (Table 5.2).

Dislocation Grading:

Low	1
Medium	2
High	3

The results are somewhat surprising in that the dislocation density range is well covered. The raw powder showed the lowest concentration of dislocations, yet they were not absent. Hammering the raw powder increased the density somewhat but not as much predicted.

Table 5.2: High-Rate Fracture Sample Dislocation Density Analysis

Sample	Raw Powder	Raw Hammered	Spex Milled	CPS Hammered	HIPed Hammered
Mean	1.300	1.733	1.600	2.300	2.500

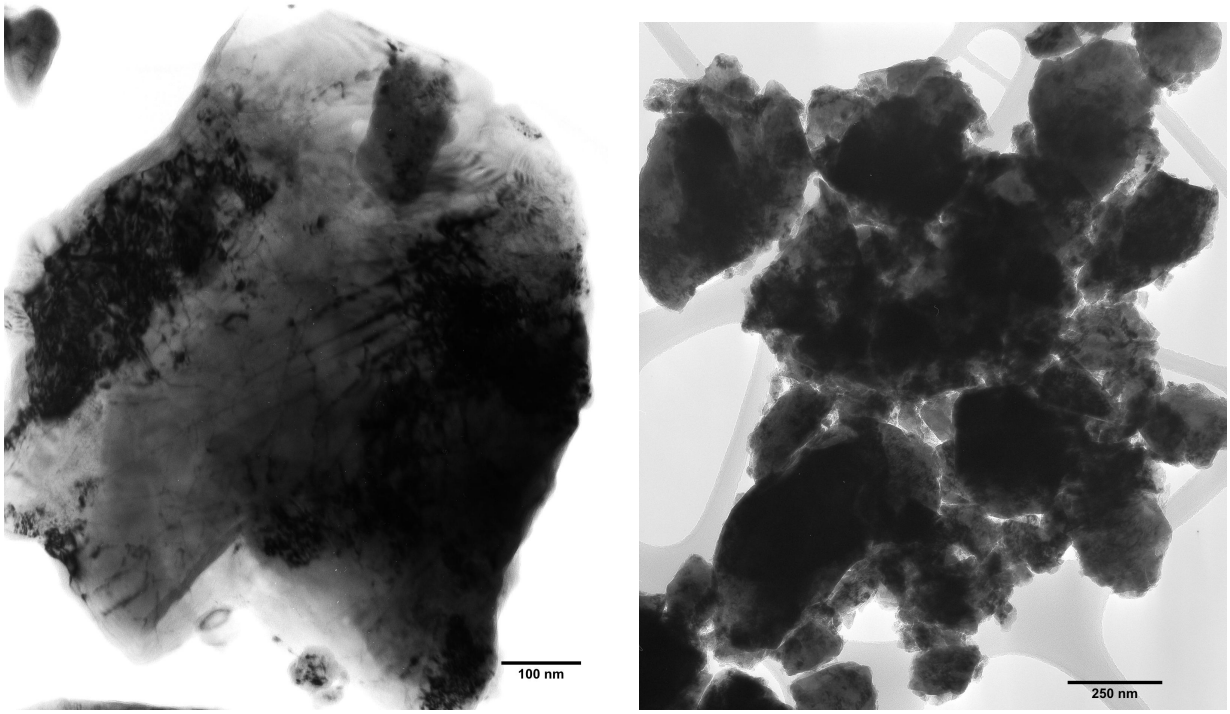

(a) Hammered raw powder showing medium dislocation density

(b) Spex-milled sample showing high dislocation density

Figure 5.25: TEM micrographs showing medium and high dislocation densities

The Spex-milled sample showed somewhat lower dislocation density than that of the raw hammered. Both the highly processed samples, the CPS and HIPed, showed a high density of dislocations from hammering.

High deformation rates lead to fracture by producing too much stress for dislocations to reduce by moving. The high-strain rate fractured samples appeared to be virtually free of dislocations. They almost appeared like “shards of glass” under TEM, showing the ragged fracture surface, yet virtually no defects or dislocations.

Samples that had a lower strain rate, such as with general processing, showed a much

higher dislocation density. These samples were processed by cold pressing and either sintering or hot isostatic pressing. Although both processing procedures use high temperatures, they both apply much mechanical stress to the system.

Spex-milled samples showed near a dislocation density close to that of the raw powder that was hammered. Spex milling is a process in which the powder is shaken violently in a ceramic jar with a steel or ceramic ball placed within. The ball essentially bangs the powder against the side of the jar and breaks it down to smaller and smaller particle sizes. This is performed for up to 45 minutes, while, in contrast, the hammering took two or three blows.

The range shown by the hammering of the specified powders shows the relation of the powder processing to the subsequent effect of high deformation rates. HIPed samples, of course, have been shown before hammering to contain relatively few dislocations. The Spex-milled samples have also been shown to have a medium to low dislocation density, yet they are the most fractured and milled of all the samples. The cold-pressed and sintered pellets were not observed before hammering, but some of these powders were used as sacrificial coverings for the heat-treated HIPed samples. Some of these powders sintered to each other and to the surface of the HIPed sample. Figure 5.26 shows an example. Note the low dislocation density.

These results show two interesting factors: that processing the material at high pressures and temperatures increases the ease of dislocation loading, and that dislocations will be of significant density in the as -manufactured fuel pellet. It is not understood how the dislocation production may be enhanced by processing other than the possibility of oxygen contamination effects.

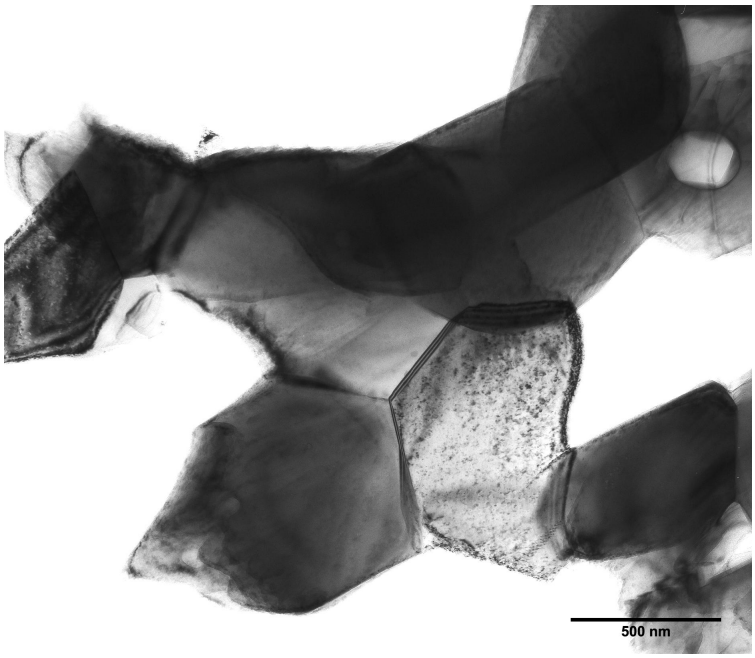

Figure 5.26: Powder sintered onto the surface of HIPed sample during heat treatment

5.5 Helium Release

Samples of ZrN were implanted with fluences of xenon of either 0, $1\times10^{15}\frac{Xe}{cm^2}$ or $1\times10^{16}\frac{Xe}{cm^2}$. In each of these samples, helium was implanted at $1\times10^{15}\frac{He}{cm^2}$ and at the same depth as the xenon damage peak. The peak xenon damage depth, as well as the peak helium implant depth, was about 35 nm. The peak damage was approximately 4 and 40 dpa for the implanted specimens.

5.5.1 RGA Analysis

A pristine, non-implanted sample was sent to PNNL for calibration, as well as with the helium-implanted samples. The results are shown in Figure 5.27.The first sample run was implanted with helium only. This low-energy implantation produced very low displacement damage on the order of 0.01 dpa. This is considered noise with ZrN. The results showed

very little helium loss at the lower temperatures, with a sudden onset of release near 950°C and again at 1150°C. The total integrated amount is near 20% of the total implanted helium.

The 4 and 40 dpa samples showed similar features to each other, with three distinct results. The 4 dpa sample had a release peak near 350°C, which was not present on the virgin sample. The 40 dpa had this peak as well.

At the higher temperatures, the 950°C peak is still present on both, but the 1150°C peak is reduced into the noise on the 40 dpa sample. It can still be observed on the 4 dpa sample.

The total helium release on the implanted samples was reduced to near 5% of the total implanted helium. It would seem that, with increasing damage, helium release is reduced and almost eliminated at 1150°C.

Without high-temperature TEM, or at least post-annealed samples, it can only be theorized as to the mechanisms for the helium release. From the low-temperature implantation, with frozen-in defects, it can be imagined that, with the increased density, of dislocations and vacancies, the rate of helium diffusion would increase. The non-damaged sample showed little helium release at temperatures below 900°C. The damage seemed to decrease the total release while adding a lowered barrier for diffusion activation. The addition of vacancies could allow a higher jump frequency for helium.

The lowered overall release with irradiation damage suggests that the helium is being trapped by irradiation-induced defects. Vacancy mobility activated by increased temperature may form agglomerated voids that can trap helium as bubbles. Grain boundaries can be a sink for vacancies and gases. If the helium agglomerations produce a stable bubble, then it will grow at the expense of helium diffusion to the surface.

Although the xenon implanted is only approximately 2.5 atomic %, this value can be relatively large with respect to predicted metal/nitrogen radii. Xenon has an atomic radii of about 1.3Å, which is near the metal cation predicted radius. If it produced a replace-

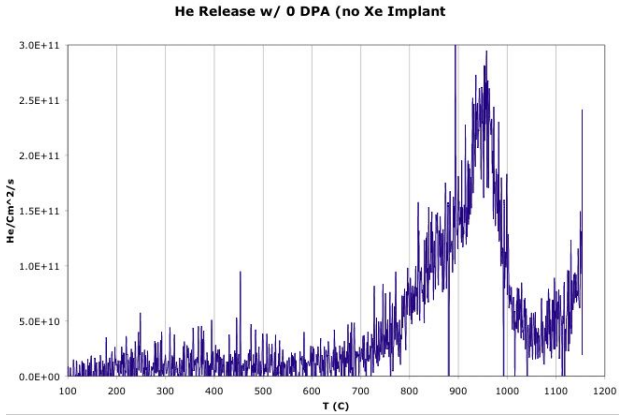

(a) Virgin ZrN with He implantation. Displacement damage is extremely low and considered 0.

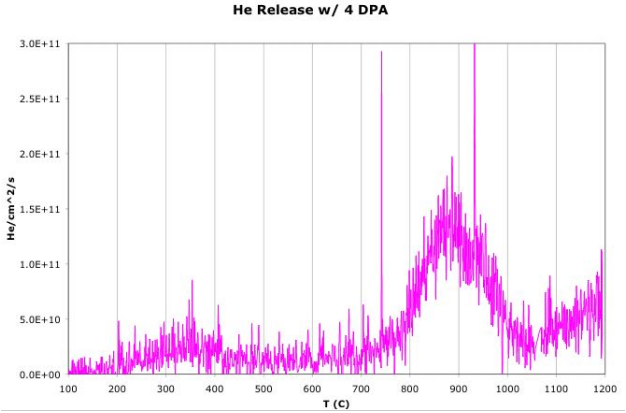

(b) 4 dpa dislplacement damage from Xe implant.

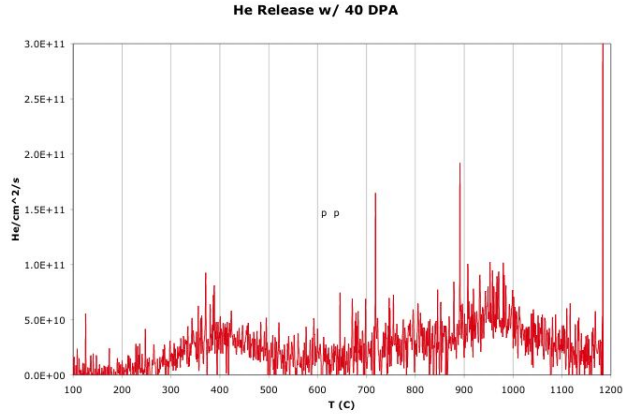

(c) 40 dpa dislplacement damage from Xe implant.

Figure 5.27: Helium release vs temperature with increasing damage from xenon implantation. $1 \times 10^{15} \frac{He^+}{cm^2}$ was implanted in each sample. (a) 0 dpa from xenon (b) 4 dpa (c) 40 dpa. Note the distinct changes at 350 °, 950 ° and 1150 ° C

ment collision with the nitrogen, however, the predicted radius is below 0.9Å, so the lattice stress would be large. The calculated Zr/N interstitial size is about $\approx$ 0.36Å; thus it is very unlikely that xenon, zirconium or nitrogen would fit, yet helium with an atomic radius of 0.31Å might squeeze in. This might allow helium to diffuse by interstitial movement, although a hop to a vacancy would relieve much stress on the lattice. With the introduction of xenon, the intrinsic vacancies are filled more, and thus this might reduce vacancy diffusion. The vacancies produced from displacement events may form stable clusters and thus further this effect.

Since only part of the helium implant curve is immersed by the xenon, it is possible to explain the increase in low-temperature diffusion by the increased vacancies for these close-to-the-surface helium atoms [9]. There is an activation energy barrier for helium diffusion that is lowered by the xenon implant. The part of the curve that is deeper and sharing lattice space with xenon atoms, helium could be blocked by simple volume stress and a decreased number of vacancy/interstitial positions into which to hop. Higher temperatures increase the mobility and agglomeration of vacancies, divacancies, etc., that can form traps. Since these traps, in the bulk and the grain boundaries, are more active at higher temperatures, it is expected that there would be less release with this damage [143, 9].

CHAPTER 6

Why is ZrN Radiation Damage Tolerant?

The predominant experimental evidence is that ZrN shows substantial resistance to irradiation-induced amorphization. As the primary metric used to assess irradiation damage by experiment, ZrN has withstood as much as 200 dpa or more without amorphizing, while achieving the sputtering limit imposed by the experimental equipment. The standard rule of thumb with respect to radiation tolerance is that the more ionic a compound is, the more resistant it is. Highly covalent materials, such as diamond, have been shown to be very easily damaged while ionic compounds such as zirconia (fluorite structure) are very radiation tolerant.

How then, being very covalent in character, can ZrN have such high tolerance for displacement damage and high implant atom loading? Using the experimental results obtained, the answer, I believe, lies with the structural bonding characteristics. The bonding of ZrN is the crux of its physical characteristics, from its electrical and thermal conductivity, to its very high melting point and strength. From the atomic bonding, the structure is produced with intrinsic defects and a specific resistance or acceptance to certain defects. From the lattice and defects the microstructure and thus macroscopic physical properties are derived.

Irradiation produces many damage effects, from initial displacements to defect dynamics. Displacement damage theory is fairly well established, and predictions of said damage is relatively accurate [120, 118]. With the amount of displacements per depth predicted

by tools such as TRIM being accepted, the question to answer is "what happens to all the damage from the time of implant to the time of observation?" Significant alterations of the structure can be considered somewhat irreversible, such as amorphization, phase transformation, or defect cluster formation. With the assumption that such changes are observable post-experiment, then ZrN has shown virtually no change in structure. What has been observed has been by different experiments, showing within each experiment's resolution, specific changes. Each experiment is a piece of the entire puzzle, of which there are not all the pieces. They are clues as to what is the intrinsic basis of ZrN's high irradiation tolerance.

Of the post-irradiation experiments that are of particular interest in providing such clues, TEM is probably the most important in that it shows pictorial assessments of the damage. GIXRD is the most sensitive to crystallographic changes such as significant phase change. Nanoindentation shows the response of the lattice to plastic deformation, which is altered by the amount and types of defects. Helium release also shows the effect of damage on helium diffusion trapping. Diffusion is altered by the types of defects and their dynamics. These basic clues lead to a theory that tries to explain the substantial irradiation tolerance of ZrN. Other cubic nitrides show similar traits with some differences.

The NaCl structure does not lend itself to displacement defects in that the available interstitial sites are very small. From first principles of radiation damage, the structure should should succumb to small amounts of displacements due to the interstitial-in strain. Even at small displacements, the strain loading would exceed the lattice theoretical yield stress. If the lattice is to yield, significant changes must be made. The most familiar change is the formation and movement of dislocations. For this to happen in the lattice, however, the strain must be localized such that a plane of atoms is displaced. Clustering of atoms can achieve this effect with the interstitial dislocation loop.

6.0.2 Intrinsic Vacancies

The theoretical density of ZrN is approximately 7.35 $\frac{g}{cm^3}$. The CRC places the density at 7.09 $\frac{g}{cm^3}$ while the accepted XRD-derived density is approximately 7.25 $\frac{g}{cm^3}$ [78, 20]. Even with the slow diffusion explanation, the vacancy concentration appears to be significantly high (measured by density). Toth has observed that the cubic nitrides and carbides of the transition metals show intrinsic vacancies on the non-metal sublattice [34]. It is also known and has been observed that, for many cubic nitrides and carbides, at the low end of the wide phase field with respect to nitrogen content there is an ordering of the vacancies on the non-metal sublattice [34, 66]. The wide phase field with respect to nitrogen shows the relative ease with which the metal sublattice can accommodate the loss of nitrogen. There has been shown to be some slight loss of metal from its sublattice, but the proportion is skewed heavily with respect to the non-metal.

The question remains as to why there is such an easy of loss of nitrogen, and such difficulty to achieve the true stoichiometric nitride? An answer in terms of the bonding properties is proposed here. In the most simplistic model, the nitrogen is bonded covalently to the zirconium, both of which are octahedrally coordinated and bonded to six of the opposing atoms. Zirconium is bound to six nitrogen atoms, and in turn each of these nitrogen atoms are bound to five other zirconium atoms. This provides the basis for the NaCl structure.

The bonding orbitals of the nitrogen are the *p* orbitals, which are oriented in the octahedral directions. The only other orbital nitrogen possesses is the *s* orbital, which is not available for bonding unless highly ionized, e.g. N^{3+}. The zirconium, however, has both *p* and *d* orbitals available for bonding. The use of the *d* orbitals is appropriate and in this case the octahedral alignment produces a split of *d* orbital energies. The high-energy *d* orbitals can be used for octahedral bonding, while the low-energy orbitals are oriented in the wrong

directions.

To understand the complex bonding within ZrN, the types of bonds should first be understood separately. The bonding orbitals are also important to understand the underlying thesis that the bonding structure of the cubic nitrides leads to a larger-than-predicted number of intrinsic vacancies.

6.0.2.1 Crystal Bonding: Nitrogen-Zirconium

Bonding can be described in three ways; ionic, covalent and metallic. Each produces its characteristic physical properties such as electric conduction, thermal insulation, or strong directionality. The bonds between different atoms in a crystal, however, are more complex and as such a mix of bond type is a more realistic model. Although most oxide ceramics are considered ionic, the actual amount of ionicity of the bonds may be roughly calculated from Pauling's electronegativity equation. This produces a "percent ionicity" of the bond, the remainder being assumed covalent. It is unusual to mix metallic bonding in with covalent and ionic, yet in some cases this factor makes a large contribution to the overall properties. As it turns out, a combination of all three bond types is present in ZrN, which makes it difficult to understand many of its properties. This also discredits, in this case, the calculated values of "percent ionicity".

6.0.2.2 Ionic Bonding

Ionic bonding is very common between atoms of different positions on the periodic table. Ionic solids are produced from the ionization of each atom into its stable excited form. The driving force for ionization in the solids is the electronegativity of each atom, which allows the "donation" or "capture" of an electron from the other atom. The amount of electronegativity between two atoms may be used to obtain the total "percent ionicity".

Pauling summed this up in a popular equation (Algorithm 10). This equation allows an approximate quantification of the ionic and covalent contributions to a bond between two atoms.

The fundamental aspect of ionic bonding is electrostatic attraction and repulsion. The Coulombic attraction to charge concentrations (oppositely charged ions) produces a strong bond, while concurrently the next nearest neighbor would have the same charge and produce a repulsive force. The electrostatic attraction decays exponentially as the inverse of the distance between charge centers squared ($\propto \frac{1}{d^2}$). The structure is compounded by the summation of these attractive and repulsive forces by geometric distance, which is summed up by the Madelung constant. As such, the ionic bond is neither directional nor allows free electrons, which are bound to the negative ions or negative vacancies. Typical physical properties of ionic solids are a wide array of strengths, from mild to extremely strong, and they that they are brittle, and electrically (and thermally) insulating.

Ionic solids have oriented atoms in ways so that strict electrical neutrality is maintained. Defects produced intrinsically or extrinsically are both countered by other defects to obtain local electronic neutrality. All oxides are ionic in character, which is 95% of all industrial ceramics. Oxides are easily produced, being stable mineral forms of most elements that can be manipulated for various physical characteristics. Most ceramic science is largely based on the study of oxide ceramics. Note that "oxide" does not necessarily mean containing oxygen. It is referring to the oxidation/reduction reaction of the ionization that takes place. Sulfur, for example, makes ceramic oxides such as FeS.

Atoms tend to try and achieve the "complete octet" of electrons in the valence shell,

Algorithm 10 Pauling's electronegativity equation for percent ionicity

$Ionicity = \left(1 - e^{-\left(\frac{1}{4}\right)(\chi_A - \chi_B)}\right) 100$ where $\chi_{A,B}$ are the respective electronegativities from atoms *A* and *B*

such as the filled shells of the noble gases. One effect is that the character of the atom becomes more like a point charge, or at least approaches spherical symmetry with respect to the electrostatic attraction/ repulsion of other ions. The smaller the ion, the more highly charged it appears to other atoms (charge held constant). Charge concentration allows for such small ions, such as Ti^{4+}, to be very reactive. Since the high symmetry of the ionic bond is spherical, it is sometimes referred as having *"s* character", referring to the *s* shell which has no directionality.

6.0.2.3 Metallic Bonding

Metallic bonds occur when atoms release external electrons into an overall "sea of electrons" in which the electrons are free to flow. From band theory, the metallic conduction is from either a half-filled valance band, or in which the conduction band overlaps into the valence band. In either case, the electrons are able to move thermally into a higher state and move freely. The overall nature of the loose "electron sea" holds the atoms together.

Metal atoms show symmetric bonding characteristics, or *s* character, such that the bond direction is not important to the strength of the bond. The distance between atoms is the most important factor in metallic bond strength.

The physical properties commonly produced by metallic bonding are of course electrical conductivity, from which thermal conductivity is derived, as well as a host of mechanical properties, etc. The free electrons allow for a reflective nature to the surface due to the interaction of free electrons with incoming photons. Metals and alloys are typically shiny, conductive, and malleable when compared to ceramics. There is no "strong" bonding between the atoms themselves, hence the relative ease of breaking these bonds for dislocation motion.

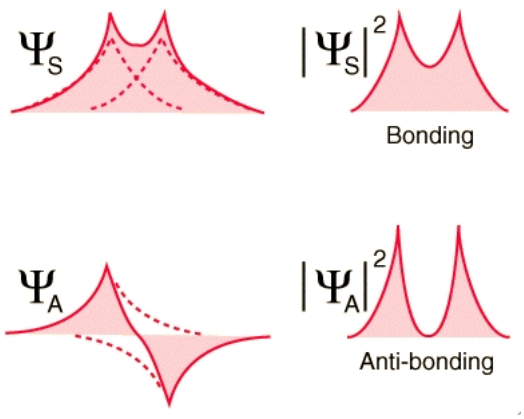

Figure 6.1: Bonding and anti-bonding wave overlap electron density calculations

6.0.2.4 Covalent Bonding

Covalent bonding is simply described as "sharing of electrons between two atoms." While this is true, a more appropriate definition is the linear combination of the electron wave equations Ψ. These equations make use of the particle-wave duality of an electron, and as such the overlap of the electron orbital space will allow an electron to spend time between both atoms. This is only allowed when the wave equations are of the same "sign," which is an arbitrary designation not having anything to do with electric charge but "fermion spin." This makes reference to Fermi statistics and the $\pm$ electron spin. The sign of each wave equation is assigned to a portion of the atomic orbital, and is represented by a color in the images represented below.

The importance of the sign of Ψ is that the linear combination with the approach of the two atoms will produce a bonding or anti-bonding interaction. The combination of the "asymmetric" wave functions (Ψ_A) produces the anti-bonding orbital. This places the electron density probability away from any overlap or sharing between the atoms, hence causing "anti-bonding". The importance of anti-bonding will be more apparent with the discussion of the possible ways to construct a ZrN lattice with the NaCl structure.

The bonding orbitals will then figuratively share electrons. The electron density can then be shown to be between the atoms in a way that satisfies the linear combination of the wave equations. In a perfect covalent bond, the electrons are shared between the two atom's specific orbitals. H_2 is a common example, yet is a diatomic molecule. The diamond structure of carbon or silicon is completely covalent. The orbitals are sp^3 hybrids, and each specific orbital shares with one other orbital of the adjacent atom. The pair coupling of the atoms and electron shells accounts for the non-conductive nature of purely covalent materials. However, these materials, such as silicon, are not total insulators. The band gap produced from the hybrid orbital combinations lowers the overall band energy to less than 3 eV, resulting in a semi-conductor. Defects can also place energy domains between the band gap, allowing for smaller excitation energies into and from these energy domains.

Covalent bonding between different atoms, especially when the electronegativity is significantly different, produces a polarized-covalent bond. This is essentially the "percent ionicity" produced from Algorithm 10. The higher electronegativity of one atom with respect to the other causes the electron to spend more time around its nucleus than the other atoms. Figure 6.2 illustrates this from electronic density calculations. This non-symmetric electron density in turn produces a net partial charge on each atom that in turn produces an electronic dipole. The result is an enhanced ionic character with respect to the local area.

Covalent bonds, because of the strict electron sharing between two atom's direct overlapping orbitals, have a strong tendency for directional strength. The bonds in diamond are a good example. Ionic character produces a more spherical bond character, which reduces the overall directionality of the covalent bond. The directionality is due to the symmetry character of the bond orbitals, either *s*, *p*, *d*, or even *f*. The *s* orbital is spherical with a constant wave function sign at the surface, and thus it is not directional in bonding. The other orbitals are more complex and discussed below; however, the wave function, by sign,

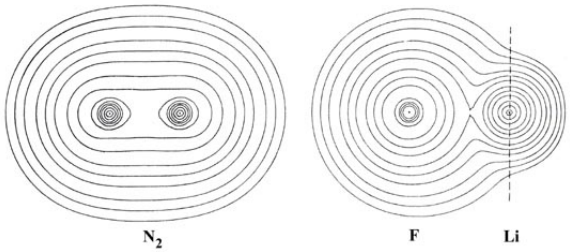

Figure 6.2: Polar-covalent bond electron distribution

does not allow for electron sharing from only but a limited set of the other atoms orbitals.

6.0.2.5 Atomic Orbitals

The atomic orbitals are pivotal in the understanding of bonding. They hold the valence electrons and allow for ionization, the linear combination, hybridization and integral splitting of spin states such that a "band" is formed throughout the lattice.

The *s* orbital is spherical in symmetry and as such has no preferred direction of bonding. It has only one available orbital and sign for bonding, and thus is only available to bond with the respective sign of another atom. This is easily accomplished in molecules as most *s* orbital atoms tend to be terminal rather than in chains. This is not the rule, however, it is more a concept of "filling the octet" or achieving the most stable electronic structure for all bonded atoms. The sharing of electrons allows for a more stable electron spin couple and to fill in a way to lower overall energy by Hund's rule. The *s* orbital has only two electrons at most to donate or receive, and as such is not typically available for a covalent crystal. It can, however, combine with the *p* orbital and produce a *sp* hybrid. Hybridization of the *s* and *p* orbitals is very common and allows for many types of structures such as graphite (sp^2) or diamond (sp^3). Hybridization is the linear combination of two orbitals to produce a "hybrid" which in turn produces a more stable bond to other atoms.

The *p* orbitals are directional, as are the *d* and *f* orbitals. The shape of these orbitals are

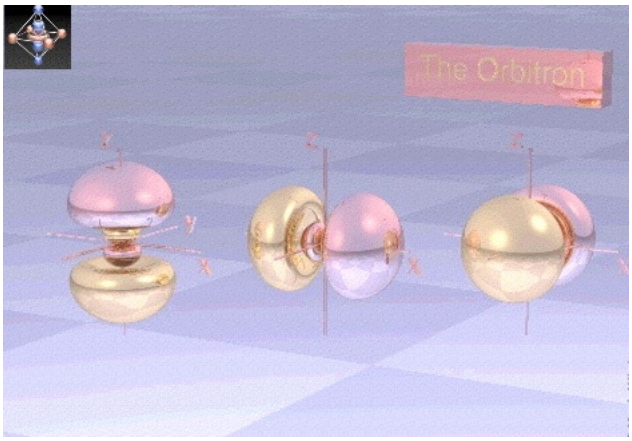

Figure 6.3: Illustration of the *p* orbital [174]

usually termed as "dumbell shaped" with each opposing end an opposite sign. There are three *p* orbitals oriented in the octahedral directions, being along the x, y and z axis. Figure 6.3 illustrates the *p* orbitals. Note the opposing ends of each "dumbell" are different colors, which represent the opposing signs of the wave function.

The *d* orbitals are more complex, having five different orientations. They are similar to the *p* orbitals in having the "dumbell shape" with the exception that four out of five *d* orbitals are a combination of two "dumbells". There are five *d* orbitals, which can be divided into two classes, the tetrahedral and octahedral. The tetrahedral are all "dumbell shaped" with opposing signs on each axis. These may be imagined as "plus signs" in orientation of the "dumbells", each oriented at 90° to each other. The tetrahedral orbitals are designated as d_{xy}, d_{xz} and d_{yz} with respect to the orientation of the planes in which they reside. As such, they tend to point towards cube corners and can bond in the tetrahedral manner. These are observed as the three bottom images in Figure 6.4.

The octahedral *d* orbitals, referred as the $d_{x^2-y^2}$ and the d_{z^2} are the top two images in Figure 6.4. $d_{x^2-y^2}$ has orbitals pointed along the x and y axes, while d_{z^2} is pointed along the z axis. These are the orbitals oriented in the octahedral directions.

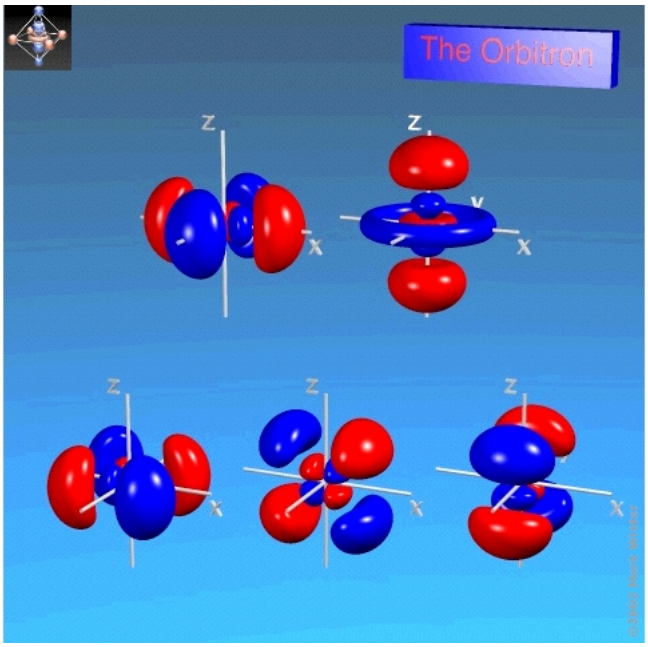

Figure 6.4: Illustration of the *d* orbital [174]

In a structure such as NaCl, the metal's octahedral *d* orbitals are along the x, y and z axes, which are lined up with the *non-metal's p* orbitals. This lines up well with the octahedral bonding arrangement required for the NaCl structure (covalent bonding). What to take note of is that the d_{z^2} orbital is shaped differently from the other four. It is a single "dumbell" with both ends the same sign. It is encircled at its node by a "donut" or toroid, which is the wave function of the opposite sign. This is the dilemma: how to combine the *p* orbitals from the nitrogen, with their opposing signed ends with the two *d* orbitals.

Most bonding theory is centered on either semiconductors or chemistry. Semiconductors are not composed of such oddly bound structures, and molecules are easily terminated. The issue is how to combine a *d* block element, or transition metal, with a *p* block element, such as nitrogen. As stated before, oxygen, sulfur, etc, normally ionize and the structure is not covalently bound. Nitrogen, however, shows the odd behavior of producing semi-covalent bonds with the cubic orientation in the transition metal nitrides.

The permutations of the possible arrangements show that no matter what directional mix, for every nine Zr-N bond pairs there is a d_{z^2} of the opposing sign to a nitrogen's *p* orbital, which produces the asymmetric wave overlap and, as such, an *anti-bond*. The effect that this anti-bond actually has is debatable. The two atoms are still bonded on five other sides, yet the energy to condense into a solid structure, H_f, should be higher for every atom pair with anti-bonding. As such, it is suggested that the structure may be able to hold a vacancy instead. This is not to say that *every* ninth atom pair is a vacancy, but it is to suggest that the formation energy may not favor bonding nitrogen in such a position every time.

It was suggested that *spd* hybrid orbitals may solve this wave function sign problem of the d_{z^2} orbital. Very little literature is available to describe in detail the *spd* hybrids. Figure 6.5 illustrates the octahedral oriented hybrid, the d^2sp^3 hybrid orbital. What to note, more carefully with the second image, is that there are six orbitals aligned with the x, y and z axes. Each orbital is a "mushroom" shape with a small "donut" at its node. These, when all combined at a nuclear center, only have one sign of a wave function with which to bond. This, of course, is a much less energetically feasible situation for bonding than the octahedral *d* orbitals. It would seemingly produce an anti-bond every other metal atom. The *spd* hybrid produces very good bonding for *s* block elements into molecules that have no other way to achieve an octahedral arrangement. This, however, is a very unlikely situation for the octahedral bonding into a NaCl lattice.

It has been suggested by Brewer that the bonds are formed by the metal *p*'s to the non-metal *p*'s [58]. There is no physical evidence as such, and if there was strict *p*-*p* bonding, the high intrinsic quantity of vacancies would not be explained.

The model followed currently is that there is metal *d* orbital bonding to the nitrogen *p* orbital. However, this does not explain the metallic conduction observed in this set of

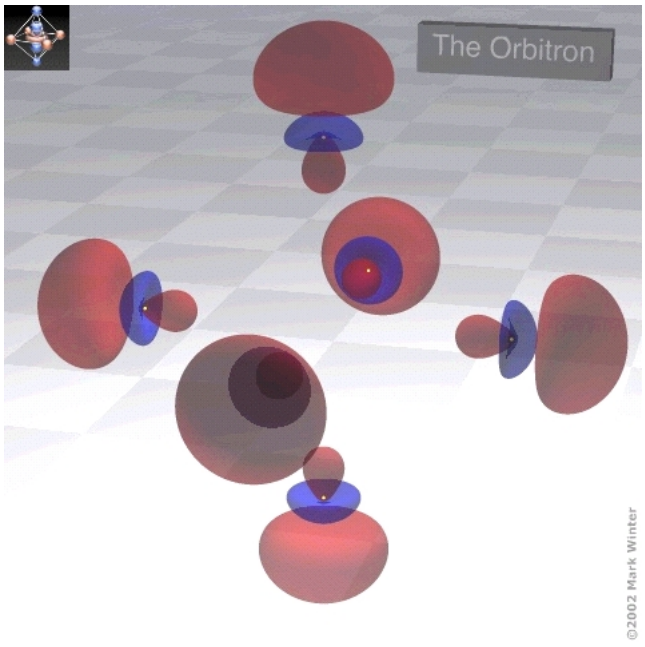

(a) Exploded view of the spd hybrid orbital showing octahedral orientation of the lobes. Note that the nucleus is shown centered in each as a small yellow sphere.

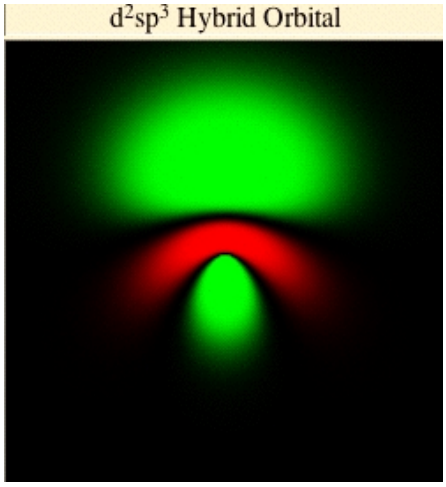

(b) Cross-section of the spd hybrid orbital. Note the wave function sign is constant on the outer (large) lobe.

Figure 6.5: Illustration of the d^2sp^3 hybrid orbital [174, 175]

materials (cubic nitrides and carbides of the transition metals, lanthanides and actinides). Metallic bonding is suggested, in addition to the effective polarized covalent bond. The addition of metallic bonding increases the spherical symmetry of the bonding ability such that the strict directionality is reduced. It is unlikely to have metallic conduction across a polarized covalent bond, yet the metal atoms are situated in a manner such that the tetrahedral *d* orbitals (d_{xy},$d_{xz}$and d_{yz}) are pointed at each other along the {111} set of planes in <110> directions. It is assumed that metallic bonding in these orbitals can occur from thermally excited electrons, being true metallic bonds.

Metallic bonding explains the "shiny" luster the nitrides and carbides have, as well as their electrical and thermal conductivity. This may also allow for less vacancies due to relaxing the strict bond/anti-bond requirements.

6.0.3 Anti-bond Effects

The *d-p* bonding conundrum will have physical effects on the properties of the carbides and nitrides. The amount of vacancies has been calculated to be about 1 atomic %, and, while this number seems high, it is not beyond question from the thermal vacancy or thermodynamic standpoint. These bonds and anti-bonds may yet explain some chemical effects observed.

6.0.3.1 Effects on Sintering

The structural composition of cubic ZrN, starting from about 35 to 50 atomic % nitrogen shows interesting chemical properties. The self-diffusion of the nitrogen has been observed to be 100 times faster than that of the zirconium, and zirconium diffusion is considered negligible [144, 145]. The nitrogen sublattice can accommodate 15% loss of nitrogen before complete loss of cubic structure. The melting point of ZrN is extremely high, and is considered more of a decomposition than melting [34]. During sintering, it has been observed that argon, not nitrogen gas, must be used as otherwise the grain/particle boundaries are weakened and sintering is highly reduced. It has also been observed that, during nitriding of a bare metal surface, the nitrogen moves into the grain boundaries and then through the bulk. The diffusion front was measured with XPS and observed with SEM.

These properties are based on lattice geometry and bonding. Although very strong and directional covalent bonding allows for such a high melting temperature, hardness, etc., it is obvious that the N-Zr bond can be broken easily enough to allow nitrogen to diffuse through the lattice. The Zr-Zr, however, seems to be more stable. It would seem that the anti-bond Zr-N would be the easiest to break (five instead of six bonds) and thus nitrogen

is free, while the metal is still held by the metallic bonding component.

During sintering, in which the surface must break up and both zirconium and nitrogen must diffuse across the surface, it has been found that high temperatures and time are needed to gain sufficient bonding. HIPing has also been used, yet seems to form a glassy oxide phase that glues the particles.

From the vapour pressure/diffusion point of view, it would seem that discharge of nitrogen from the surface gains the chance of a N-N combination and loss, although more than likely it would be re-catalyzed and absorbed back into the structure. The temperatures used are relatively low with respect to the standard ceramic rule of thumb: of $\frac{2}{3}$ the melting point in Kelvin. Typical temperatures used are 1500°C, or 1873 K. This is with respect to the M_P of 3000°C or 3273 K, with the ratio of 57% M_P. By the rule of thumb (which is for oxides that sinter relatively easily), the required temperature needs to be approximately 1900°C.

Although the lower temperatures are used, some sintering has been accomplished. It would be one's first impression that a higher partial pressure of nitrogen would stabilize and enhance, not hinder sintering. Ultra-high-purity (UHP) nitrogen gas sintering showed a large negative effect in the sintered pellet's strength and ability to achieve sintering. The use of argon has no negative effects. It may be theorized that the nitrogen gas is trying to move into the ZrN by breaking into two nitrogen atoms and saturating the grain and particle boundaries being formed. Since a boundary is a mis-match of lattice planes, they are held together much more by weakened chemical bonds and Van der Waals bonds than the bulk. If the nitrogen atoms saturate these boundaries yet are not really allowed to diffuse into the bulk, it would seem that they might have a screening effect and weaken both chemical and Van der Waals bonds.

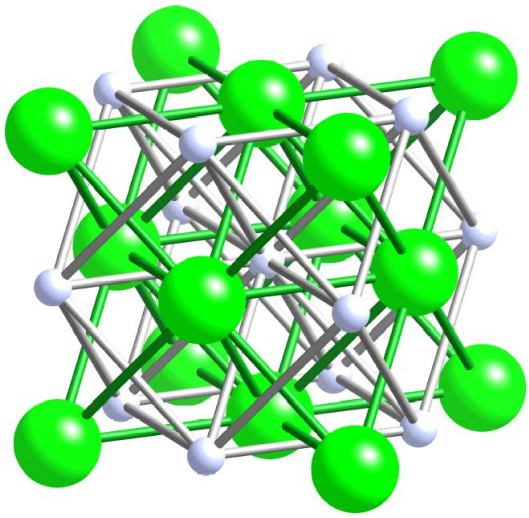

Figure 6.6: NaCl lattice showing tetrahedron formed

6.0.4 Interstitial Size

The sizes of the interstitial sites within the NaCl lattice are tied to the radii of the two constituents. The NaCl lattice is, by definition, an fcc lattice with all of its octahedral interstices filled by the opposing atom. The fcc lattice has eight octahedral sites and eight tetrahedral sites. The NaCl lattice has only the eight tetrahedral sites available. There are 16 distorted tetrahedral sites formed by the sides of the octahedral sites, yet these are smaller than any other and thus less likely to be considered. A vacancy, however, may be considered an octahedral interstice on one of the fcc sublattices. Figure E.1 shows an illustration of the NaCl lattice. Atom connections serve to illustrate the octahedral and tetrahedral interstices. Note the eight tetrahedral interstices adjacent to the corners.

The octahedral interstices are filled with a true 1:1 ratio of elements. Figure E.2 shows both an open tetrahedral interstice and a filled octahedral interstice. Figure E.7 (b) shows the interpenetrating tetrahedron formed by the two elements with full-sized atoms.

The size of the interstices is dependent upon the geometry of the system, which is

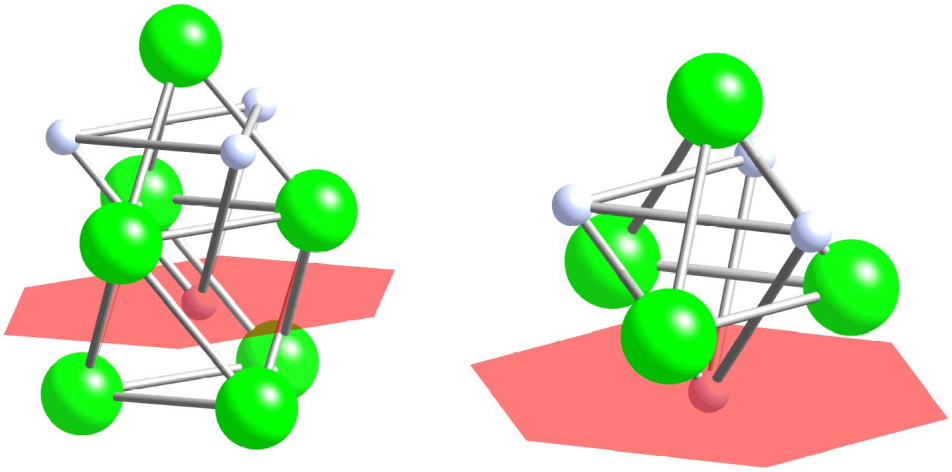

(a) Octahedral interstice filled by light blue sphere. Note this forms the tip of one tetrahedron while the sides of the octahedron form part of the other. 111 plane shown in shaded red.

(b) Interpenetrating tetrahedra shown with respect to the 111 plane.

Figure 6.7: Octahedral and tetrahedral interstices

dependent upon the radii of the atoms forming the lattice. It has been considered and explained elsewhere that the zirconium atom is considered the large atom and thus produces the "hard-sphere packing" that leads to the lattice. As such, the zirconium dominates the geometry of the interstices and forms the basis for the interstitial size.

The solutions for the interstitial radii for both octahedral and tetrahedral interstices is based on the logic that;

- the interstice is the center of the geometry formed by the close-packed and bonded atoms,
- the maximum radius is from the center of the interstice to the closest atom that it may touch.

In this basis, the center is found for the two geometries.

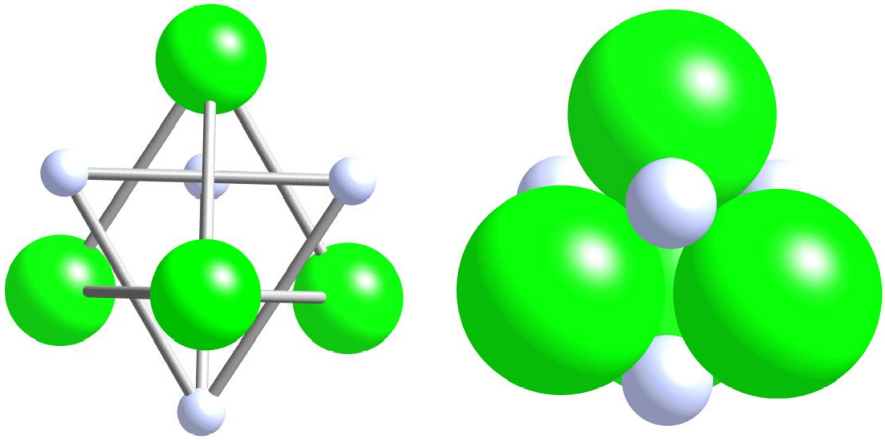

(a) Ball-and-stick model of the ZrN tetrahedral interstial site. This is located at the center of both interpenetrating tetrahedra.

(b) Space-filled view. Note for perspective that the nitrogen atoms have no part in determining the interstitial size.

Figure 6.8: Interpenetrating tetrahedra of Zr and N (green and grey respectively)

The solution to the geometric relations between atom sizes and the interstitial size produced can be found in Appendix E. The octahedral arrangement fits well for the size of the nitrogen within the zirconium's metal lattice. The tetrahedral interstice between the two, as illustrated in Figure E.7, shows the relative size of the atoms in the interpenetrating tetrahedra. Since the nitrogen atoms are too small to touch, the zirconium atoms produce the critical geometry (which is identical to the nitrogen's). The interstice is thus shared between the two sublattices.

Given the solutions for the atomic sizes of nitrogen and zirconium, the radial size of the tetrahedral interstice is found to be 0.363Å. This number is nearly half that of nitrogen's radius, while zirconium is almost five times the size.

6.0.4.1 Lattice Strain from Interstitial Atoms

The stress imposed by an atom that is placed into this interstitial site is relative to the difference in size. Imagine an atom larger than the interstitial size that is forced into it with a large activation energy. The interstitial cannot hold this atom unless the atom shrinks or the interstitial grows. Simplifying to hard-sphere mechanics, the interstitial site must enlarge to fit the atom inserted. For the tetrahedral interstice, the growth is from the center outward toward the four corner atoms. These are along the $\{111\}$ directions in the cubic lattice. As such, the difference in radii may be considered Δr, which is the distance the four atoms are displaced along the $\{111\}$ directions. Thus, for each interstitial site occupied, there is a strain produced in four directions of Δr.

The strain to the lattice is then $\frac{4\Delta r}{\sqrt{3}}$, correlating to the directions the tetrahedral atoms move as the lattice "swells". Each interstitial defect produces a different strain based on the size of the element placed within. The radii of the elements is a complex issue, based on the local bonding, coordination and oxidizing/reducing properties of the neighbors. As a simplification, the radii used for the elements are near their atomic radii, specifically the VFI atomic radii empirically calculated from the structure of the elemental structures [176]. Zirconium and nitrogen radii used are the same as those used to build the structure, $\approx$1.6 Å and 0.69 Å. Helium is assumed to be small and to have a radius $\approx$0.31Å. Xenon had the largest range of any calculated or measured radius, measured from 1.08 to 2.16 Å. The discrepancy is due to the compounds measured, either xenon solid or xenon in a compound, or from using the calculation for the radius (See Algorithm 11). From this calculation, the radius was placed at 1.31 Å, and is a good compromise for such a wide range of measurements. Since xenon is an inert element, local reactions with zirconium or nitrogen would not be likely. It has its valence shell completely filled and is considered a relatively "hard" element, and thus would fit will with a hard-sphere model. Neither

Algorithm 11 Calculation of atomic radius (based mostly on metals) [177]

$$radius = \frac{h^2}{8Ae^2mZ^{\frac{1}{3}}}$$

Variable	Definition	Value
h	Plank's constant	6.626068×10^{-34}J·s
A	Madelung constant	1.74756 (NaCl)
e	Charge of electron	$1.6022 \times 10^{-19}C$
m	Mass of electron	$9.10938188 \times 10^{-31}Kg$
Z	Valence	1

nitrogen nor zirconium is expected to ionize enough to change its respective radii within an interstitial, so they are assumed to be hard spheres with constant radii as well.

The other half of the Frenkel defect (or anti-Frenkel defect) produced during displacement damage is a vacancy. The strain produced by a vacancy is complex due to the lack of shielding from other charged species. In simple terms, the Madelung relation of distance between like and unlike charged particles can be used to produce an estimate of the lattice relaxation. Like charges will be repelled, while unlike charges will be attracted. Add to this the lack of structure, which allows the lattice to contract, and the system becomes much more complex. As an estimation, the vacancy-induced relaxations used are ≈3% decrease for a zirconium vacancy and ≈11% increase for a nitrogen vacancy (-0.06Å and + 0.075Å respectively). The lattice strain produced by the vacancies is very small with respect to strain caused by the interstitial defects. These numbers are a calculated value from ZrO_2 with highly charged species [178].

With these assumed hard-sphere lattice strain values, the local stress for each defect is produced. A maximum, assuming no defect annihilation, can be calculated from TRIM for a given fluence of an energetic ion implanted (Table 6.1). It can be shown by these calculations that the maximum strain is produced not by the extra implanted species, but by the displaced lattice atoms. The amount of nitrogen and zirconium displacements is sub-

Table 6.1: Stress and Strain Calculated for Displacement Damage in ZrN - Theoretical Maximum

Element/defect size	Radii (Å)
ZrN Interstitial	0.363
Zirconium	1.61
Nitrogen	0.675
Xenon	1.31
Helium	0.31
V_{Zr}	1.55
V_N	0.75

Calculations based on hard-sphere strain effects. The strain values are used as an estimate for hardness increase due to the interaction of this strain with a moving dislocation.

Xe into:	Δr (Å)	Local volume strain (MPa)	Local lattice stress (GPa)
Interstitial	0.947	13.7	5.206
Zr site	-0.3	-0.4	-0.166
N Site	0.6355	4.1	1.57
Zr into:	Δr (Å)	Local volume strain (MPa)	Local lattice stress (GPa)
Interstitial	1.247	31.3	11.886
N site	0.935	13.2	5.01
N into:	Δr (Å)	Local volume strain (MPa)	Local lattice stress (GPa)
Interstitial	0.312	0.5	0.186
Zr site	0.947	13.7	5.206
He into:	Δr (Å)	Local volume strain (MPa)	Local lattice stress (GPa)
Interstitial	-0.053	-0.002	-0.001
Zr site	-1.3	-35.44	-13.467
N site	0.075	0.007	0.003

Vacancy	Δr (Å)	Local volume strain (MPa)	Local lattice stress (GPa)
V_{Zr}	-0.06	-0.0003	-0.001
V_N	0.075	0.007	0.003

Assuming the lattice will attempt to rearrange the local implanted atomic arrangement for a xenon atom implanted into an interstitial

	Δr (Å)	Local volume strain (MPa)	Local lattice stress (GPa)
Xe_{Zr}, Zr_N, N_i	-0.3, 0.935, 0.312	13.2	5.031
Xe_i	0.947	13.7	5.206

stantial. The displacement graph also shows areas of maximum strain from these defects. This is theoretical, of course, and does not show the events that actually happen within the crystal during and after displacement damage.

Defects do move, even at cryogenic temperatures. The distance to which they can move is determined by their relative diffusivity, which is a function of the lattice and temperature. The more Frenkel defects that are produced, the greater the saturation of the lattice by these defects. This then decreases the mean distance required for interstitial-vacancy annihilation, and thus at a given temperature and time scale, decreases the residual defect density. At a specific temperature, a defect may have a radial probability of movement. With an opposing defect inserted within this radius, not only is there a probability of random walk collision but the local strain will produce a directionality. This prejudices the movement and hence, the probability of annihilation is much greater, becoming unity if given enough time will become unity.

The radius at which there is a substantial probability for annihilation is complicated by the fact that both defects can move, and with very different diffusivities. There are the reaction possibilities that also complicate matters, such as cluster effects, repulsion effects, etc. To a degree, however, the interstitial will annihilate with a vacancy at close proximity, as this results in the lowest overall energy state. If in close proximity to free surfaces, these act as sinks for both. Bubbles, voids, grain boundaries, dislocations, clusters such divacancies, etc, and interstitial loops, are all defect sinks.

Most defects produced are almost immediately annihilated. Those that remain reveal the strain tolerance of the material and its ability to accept these defects.

6.0.5 Dislocation effects

The dislocations observed have been shown to be on the $\{110\}\left\langle 1\bar{1}0\right\rangle$ system. While the standard fcc structure should show glide on the$\{111\}$ close-packed plane, dislocations in ionic crystals are more likely to move on the $\{110\}$ planes or $\{100\}$ planes. The main argument is that charged atoms will move close to like neighbors during slip on the $\{111\}\left\langle 1\bar{1}0\right\rangle$ system. Other slip systems reduce this Coulombic repulsion. Although ZrN is not considered ionic, it does show charging on the atoms. This is not unexpected due to the electronegativity difference that will polarize the covalent bonds. This will then produce "partial charges" on the atoms. These partial charges have enough Coulombic effect to inhibit slip on the $\{111\}$ plane.

As an interesting aside, a reduction in nitrogen has a large effect on the SFE [81]. This is shown by the large stacking faults between partial dislocations in low-nitrogen ZrN . These dislocations are in the $\{111\}\left\langle 1\bar{1}0\right\rangle$system, but produce Shockley partials by the reaction: $\frac{1}{2}\left[0\bar{1}1\right]0\rightarrow\frac{1}{6}\left[1\bar{2}1\right]+\frac{1}{6}\left[\bar{1}\bar{1}2\right]$ [179, 46, 47, 65]. The reduction of nitrogen appeared to change the partial charging enough to allow for slip across the $\{111\}$, i.e. allowing like atoms to move closer to each other. This shows a dramatic shift toward metallic bonding.

6.1 Summary

The bonding structure of ZrN is complex, which allows for interesting physical properties. While the anti-bonding effects allow for ease of nitrogen vacancy formation, the interstitial size is too small to allow for the insertion of Frenkel defects from either lattice. During the collision cascade, however, Frenkel defects are produced with tremendous energy. With the high strain produced by irradiation produced interstitials, the structure appears to reconstruct itself very rapidly.

Hardness measurements show the effect of dislocation movement with residual Frenkel defects increasing the hardness. The number of residual Frenkel defects increases non-linearly such that it appeared that, as more irradiation occurred, more annihilation took place. The ZrN lattice appears to respond rapidly to the additional stresses, not by amorphizing, but by forcing the diffusion of the interstitials to a less strained state. High-temperature irradiation, however, showed that the structure did not need to reduce the strain in the lattice much beyond what happens at the time of the initial displacement cascade.

It has been considered that, with the intrinsic vacancies present, the addition of Frenkel defects would only redistribute these vacancies. There would be more vacancies available for interstitial annihilation, however, and the vacancy bias would be redistributed. The possible dislocation loops observed could well be the result of the vacancies being more highly concentrated. The stacking-fault energy, however, is far too high to allow loop growth beyond the very small.

The dislocations produced during polishing show some insight into physical properties. The partial-charged atoms from the polarized covalent bonds act like ions. These atoms, however, are not charged as interstitials as they are no longer bound. These interstitial atoms may help shield both the repulsive like atoms and attractive opposing atoms and allow for altered physical properties, such as increased diffusion. Every atom displaced reduces partial charging of its vacant lattice site.

Thus, the effects observed from the high level of damage show that ZrN can absorb a large amount of energy from heavy-ion irradiation. The defects produced appear to be accepted up to a certain amount, at which point the lattice appears to self-heal rather than amorphize. With over 200 dpa implanted at cryogenic temperatures, the ZrN lattice has been shown to accept the defects presented. At temperatures of up to 800 °C, with 70 dpa, the defects do not appear to cause a large enough driving force for annihilation. Cluster

formation may account for some of this effect; however, cluster size did not grow significantly. With defect mobility observed at high temperatures, it is then accepted that the lattice will accept many defects, yet remain intact. This is a radiation and fission tolerance goal that has been met.

CHAPTER 7

Conclusion and Postulated Model

The AFCI program requires a fuel form to address the needs of reducing the nuclear waste stream. A possible solution is to use a transuranic nitride-based fuel that is diluted or held together with a compatible matrix. A candidate for this matrix is zirconium nitride which is a material with many similar properties to that of the transuranic-nitrides. Two important factors that are addressed in this study are the tolerance of ZrN to radiation damage and fission products. These factors are important for the overall fuel performance for AFCI.

These concerns have been addressed by observation of the effects via heavy and light ion implantation. Ion implantations were performed at both cryogenic and elevated temperatures to assess the damage accumulation tolerance and defect mobility effects. Crystallographic changes were observed with TEM and GIXRD. Post-irradiation defect concentration was tracked with nanohardness measurements. These methods showed that ZrN can accept a tremendous amount of damage, does not amorphize, and does not form bubbles or defect clusters with ease. These observations show a high tolerance for radiation damage, both at cryogenic temperatures and up to 800 °C (reactor temperatures).

Helium implantation and release studies showed the effect of irradiation-produced defects. Helium was shown to have increased mobility at lower temperatures with increasing xenon damage, while possible gas traps formed at temperatures approaching 1000 °C. TEM analysis showed helium to be mobile even at cryogenic temperatures.

Based on the study of the defects and their dynamics, a model of the bond structure has been postulated. The defects appear to cluster at high temperatures, but, these clusters are very small. The high SFE reduces the growth potential of clusters such as dislocation loops. Gas bubbles were not observed, and, although the defects were shown to be mobile, they did not appear to be driven to annihilation. Dislocations were observed to be common. Analysis of the slip system shows a strong charged component to the bonding. Literature shows that with a high vacancy content, the high SFE is reduced and the dislocations change primary slip systems. The change in SFE allows large stacking faults between the dislocations, while the change in slip system shows a distinct change in bonding.

Since tolerance to radiation damage and fission products is believed to be related to bonding, the ease of vacancy formation on the nitrogen sublattice and the effects these have on the bonding will have effects on the overall defect acceptance. As the bonding becomes more metallic, defects are less likely to be discriminated against with respect to mobility.

The overall effect is that zirconium nitride shows a very high tolerance to radiation damage as well as to fission-product implantation. These results, of course, are subject to the limitations of the experiments. However, it is expected that ZrN, as well as all the cubic nitrides, will show substantial radiation tolerance within the reactor core. As such, the goal for AFCI may be met.

CHAPTER 8

Future Work

Zirconium nitride, as all the cubic nitrides, has some very interesting properties. Continued research is suggested both for AFCI as well as for basic science.

8.1 Helium Quantity and Depth Profile

Attempts were unsuccessfully made to address the quantity question with the helium release results. These results show only about a fifth of the helium released during the experiment. The question arose as to whether the helium is residing within the lattice and very slowly being released, or whether it is trapped, or whether it was quickly lost before the sample was tested. Helium is such a light, small and electrically minor element that it is very difficult to detect by most methods. Attempts have been made with EDS, although it is known that the low Z of helium would reduce the sensitivity. Electron Energy Loss Spectroscopy is a method that increases sensitivity with lower-Z elements, however, this method failed as well.

Elastic Recoil Analysis (ERA) is a method that uses a low-angle, high-energy carbon beam to penetrate and scatter light elements out from the surface. The loss in energy from depth and recoil produces a depth profile. This technique has been used recently to obtain helium distributions in Cu/Nb nanolayers with surprisingly good agreement with TRIM calculations. The amount of helium required, however, is an implant of over $10^{17} \frac{He}{cm^2}$. The successful use of this technique may allow the question to be answered: Where does the

helium go during the gas release experiments?

8.2 In-situ TEM Irradiation

The damage produced during irradiation is increasingly interesting in that there are conflicting arguments as to the source of the high damage tolerance. The initial cascade produces a large amount of damage, but, this damage has mostly annealed by the time the sample is prepared and observed with TEM. It is possible that the sample undergoes localized amorphization yet heals such that the recrystallization produces perfect epitaxy. The lattice may also be able to accept the large damage and heal when the level of damage becomes to high.

In-situ TEM studies might allow for the direct observation of this damage cascade. The cascade could be observed at liquid-helium temperature to slow or essentially stop diffusion. At warmer temperatures, the self-annealing of the cascades may be observed. Temperatures could be raised to 800 °C and highly dynamic effects observed, such as clustering. These types of observations would be helpful in understanding the radiation damage tolerance, fission product retention, and defect dynamics.

8.3 Greater than 1000 °C Irradiations

The helium-release experiments showed an increase of helium evolution at lower temperatures with increasing displacement damage. At higher temperatures, however, the effect was reversed. Temperatures of 950 °C and beyond showed the main release of helium during the experiments with the undamaged sample. With temperatures over 1000 °C, this release was greatly reduced.

This is significant in that the defect dynamics may have been altered by attaining the activation energy for trap formation. These traps capture gas atoms and form bubbles. Usually at grain boundaries, bubble formation is a competing activity with respect to helium release.

With TEM evaluation of >1000°C irradiations, these effects may be properly analyzed. Questions remain as to the xenon damage effect in nucleating these traps and where they occur. Grain-boundary bubbles can lead to brittle fracture if the fuel is suddenly stressed, such as with a thermal spike in the reactor.

8.4 Mechanical Properties and Their Relation to Atomic Bonding

It has been observed that many carbides and nitrides assume the same slip system as that found with ZrN in this study. However, many of these carbides have exhibited a brittle-to-ductile transition temperature near 1000 °C. The effect is that other slip systems become active. With respect to ZrN, the effect may help explain some differences observed with grain texture versus optical float-zone samples, cold-pressed and sintered samples, and hot-pressed samples. A better understanding of this phenomenon may help to develop a more efficient production technique.

The high hardness and brittle nature of ZrN is known, yet the amount of dislocations produced by simple polishing is interesting. Due to the nature of the surface, it is suggested that oxide particles are assisting in nucleating and multiplying dislocations. While some characterization has been accomplished, there is more work to be done. Obviously, the effect of temperature is one area of study. Possibly a cross-sectional sample across a nanoindent would provide much information. The stoichiometry effect has been shown via

the extremes, although the transition from one slip system to another might be important.

Resonant Ultrasound Spectroscopy (RUS) is a method used with single crystals to obtain elastic moduli from the different crystallographic directions. An important feature of these data beyond knowledge of stiffness/compliance would be to use this technique to understand the bonding structure. If the model proposed is correct, the covalently bonded directions, $\langle 100 \rangle$, will have very different stiffness characteristics from those of say the metallic bonded directions, $\langle 110 \rangle$. One may also be able to use this to obtain stoichiometry effects, possibly with correlation to the change in slip system .

8.5 Vacancy Measurements

It has been indicated that vacancies are an intrinsic defect on the nitrogen sublattice. It has also been suggested that obtaining a fully dense nitrogen substructure is not very likely due to both the anti-bonding effects as well as thermodynamics. The vacancy concentration and its effects on the physical properties are important, yet only a rough estimation could be performed. With positron annihilation, however, a quantification of vacancies could be obtained. This, again, would be useful for correlations with slip and other properties.

Appendix A

Glossary of Useful Symbols, Terms, and Scientific Information

Madelung Constants

Table A.1: Madelung constants for various crystal structures

Compound	Lattice	Constant
NaCl	NaCl	1.74756
CsCl	CsCl	1.76267
CaF_2	Cubic	2.51639
$CdCl_2$	Hexagonal	2.244
MgF_2	Tetragonal	2.381
TiO_2(Rutile)	Tetragonal	2.408
ZnS (Wurzite)	Hexagonal	1.64132
Al_2O_3	Rhombohedral	4.1719

Useful Constants

Table A.2: Physical constants used in various calculations

Symbol	Title	Value
N_A	Avogadro's number	$6.022\times10^{23}\frac{molecules}{mole}$
k	Boltzmann's Constant	$1.38066\times10^{-23}\frac{J}{K}$
h	Planck's Constant	$6.6260777\times10^{-34} J\cdot s$
amu	Atomic Mass Unit	$1.66054\times10^{-27} kg$
e or q	charge on electron	$1.602177\times10^{-19} C$
eV	Electron Volt	$1.602\times10^{-19} J$
λ	Electron wavelength at 300 keV	0.0197Å
$Cu_{k\alpha}$	X-ray radiation wavelength from Cu source	1.54Å

Appendix B

Periodic Tables with Useful Information with Respect to Nitrides

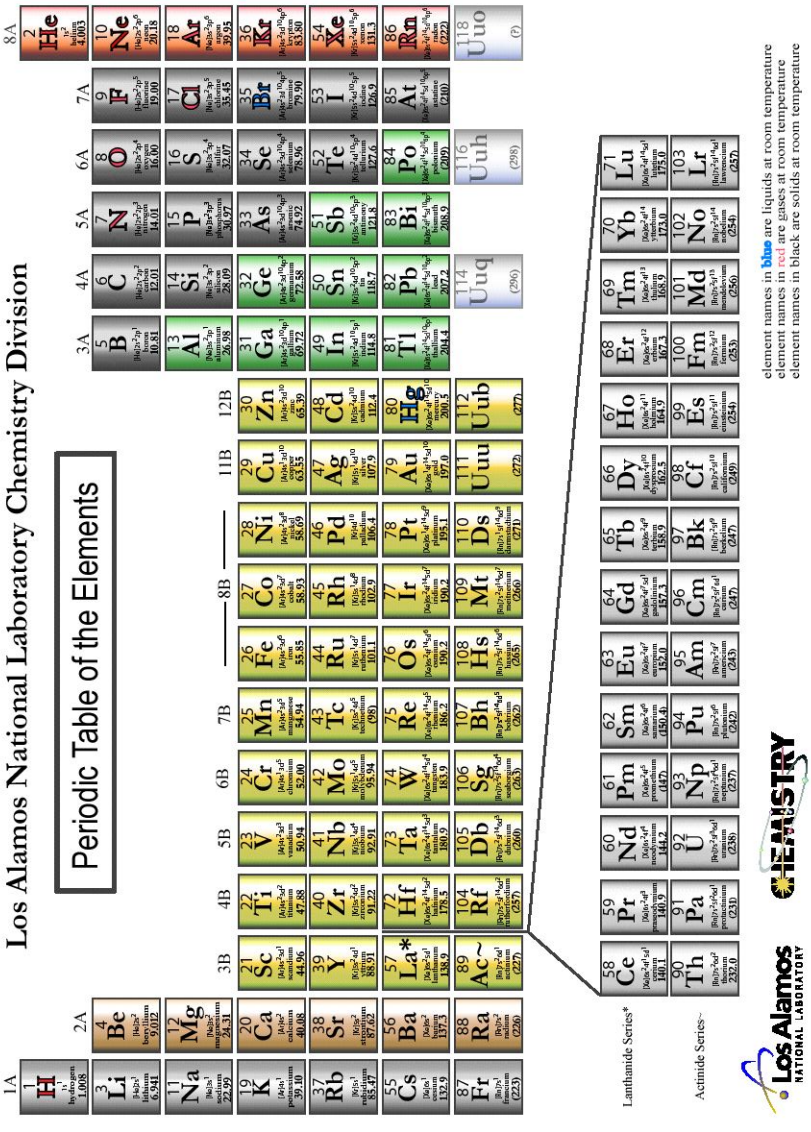

Figure B.1: Periodic Table of the Elements

Figure B.2: Periodic Table of the Elements with respect to nitride ionicity

Figure B.3: Periodic Table of the Elements with respect to nitride lattice parameter

Figure B.4: Periodic Table of the Elements with respect to nitride melting points

Appendix C

Possible Artifacts

Experimental Artifacts

During any experiment, artifacts may be observed as evidence of nonexistent results. Many times this is due to inherent defects with the experimental procedure, while other times it is due to mistakes made during the experiment. The experiment here is described from birth of the sample until final observation.

The samples used were prepared and characterized well to describe possible artifacts. While the commercial ZrN is assumed to be pure, it is found to have traces of oxygen and carbon in an as received state. This is taken into account as a standard to work from. Carbon presence is from the manufacturing of ZrN through carbothermic reduction.

HIPing Contamination

The HIPing introduced more oxygen, and backscatter SEM and EDS showed that part of the tantalum can diffused into the particle boundaries. It was found that the infusion moved approximately 1 mm from the outside surface. This area is avoided during sample preparation to avoid problems. HIPing produces a glassy phase between the particles that provides the bonding or "glue". Using EDS, the glassy phase was found to be a mixed oxide of various constituents with a heavy concentration of hafnium. The hafnium is assumed to be extracted from the ZrN, which will always have a small percentage. This glassy phase can appear similar to the epoxy used at the surface interface. It is amorphous and thus

has the same diffraction haze that the glue has. The true test is to follow the "glue line" a significant distance. The particle boundaries tend to end in a triple point that breaks off into two lines at ≈60° and -60° forming typical dihedral angles.

Polishing Damage

The HIPed sample is cut and polished in a manner typical to hard ceramic materials using fixed diamond media. Samples are polished to 1 μm and then finished with *Syton* colloidal silica. It is assumed that from this final polish will remove virtually all the residual damage produced by the diamond media. In very hard ceramics the normal residual damage from polishing is considered to be approximately the first 10 nm from the surface. In metals, being much easier to produce and move dislocations, the rule of thumb for damage is approximately three times the depth of the final polish grit size. Observed in ZrN is damage at a depth much greater than anticipated. It is shown that the heavy damage depth is approximately 100 nm with another 100 nm of random dislocations.

Implantation Artifacts

Implantation has its own artifacts that may show up. First, there is an assumed error in the reading of the current from the Faraday cups. The error is accepted to be 10% of the fluence, yet in practice what has been measured by RBS has been closer to 5% error.

The sputtering limit of the material limits the total damage one can implant into a material. It has been shown that as a material is implanted its surface is sputtered at a specific rate. As the fluence increases, the surface is removed until the actual rate of damage accumulation is equal to the sputtering rate. This produces a damage and implant profile in which the distributions are peaked from the surface and are constant until the depth reached in which it decays normally. More implantation only pushes this depth further

but removes the surface at the same rate such that the total peak damage never increases. Afanasyev-Charkin calculated that in ZrO_2 the actual sputtering limit was 200 dpa. This result countered previous published data that showed the damage up to 600 dpa [180]. For ZrN, the effect was measured with RBS and found to be about $5\times10^{16}\frac{Xe}{cm^2}$ or 200 dpa, the same as ZrO_2.

The beam is scanned across the sample stage in forming a circular pattern approximately 4 inches in diameter. Again, the deflection causes some error in the implanted quantity. Annually, carbon samples are placed on the corners and implanted with a select amount of a species. This is then checked with RBS to observe for any discrepancy. While there is some, it is minor and most samples mounted are placed near the center.

The temperature of the material can have a distinct impact on the accumulation of defects and implanted species. At high temperatures the defects can much more easily diffuse to each other and annihilate. The implanted species can diffuse to the surface and escape into the vacuum or diffuse into the sample. While under irradiation, the sample undergoes much greater diffusion due to the local "shake up" of the atoms. While most of the irradiations are controlled with respect to temperature, it was observed that during one implant the effect on the sample was profound.

The sample is mounted to a large mass stainless steel block with silver paint. The silver paint gives maximum thermal transfer to keep the sample near the temperature of LN_2. Irradiation, however, is effectively a transfer of kinetic energy from an ionized and accelerated gas into a small volume of the material. The flux or current is measured, the mass of the gas is known, the displacements are calculated as well as non-displacive momentum transfer. In essence, the total energy of each 300 keV, 131 amu xenon atom is transfered into an volume of 1 $cm^2\times100$ nm. By using the rate of thermal transfer, the temperature of this area can be calculated assuming a steady state. While in actuality, the local displace-

ments create localized “thermal spikes”, the system temperature does not rise significantly. It is approximated to be 3 °C increase in the 100 nm depth. The low temperature is due to the very high thermal conductivity of ZrN.

In the case of the anomalous experiment, it was observed that during an implantation of neon, the sample glowed orange. It was at first thought that the ZrN was scintillating or producing ionoluminescence, but this is not considered possible due to the nature of ZrN. It is metallic and thus could not have the typical “f-centers” that captures electrons and allows irradiation to excite photon production. While removing the sample it was observed that it had all but decoupled with the mounting block and was held on by a very small amount of silver paint at two edges. RBS was used to measure the neon profile, but it was found that the neon was spread thin and deep. This is what would be expected from a sample that was irradiated at high temperatures. It was then considered that the sample, not being coupled well to the cooling block, increased in temperature until it began to “glow”.

During the implantation, the sample is in a vacuum, yet the vacuum is not considered “good” by any means. There is may gases in the system; hydrocarbons from various oils, alcohols, residual acetone, with water vapor, N_2 and O_2 from the air. While most larger molecules are condensed using the cold finger cooled by LN_2 the nitrogen, oxygen are still in the vacuum. During the implantation the accelerated gas beam may strike and “sweep” O_2 molecules into the beam and implant it into the sample. The quantity and energies would be small, but there is the possibility. Any gases physisorbed to the surface would be in effect a target for implantation mixing. Of course, any substance left on the surface such as silver paint or finger prints are mixing targets as well.

If the sample is heated in the implanter, then not only can the sample be slightly implanted with elements in the vacuum, it becomes more chemically active. In the case of ZrN, over 400 °C it becomes an oxygen scrubber. It will essentially clean much of the free

oxygen in the vacuum. ZrN will also dissolve carbon, but it has a very high affinity for oxygen, and any oxide the forms at the surface at high temperatures is a very poor passivation layer. ZrO_2 is an ionic conductor of oxygen.

Appendix D

Radiation Damage Theory - An In Depth Primer[1]

The basis of radiation effects is the interaction of a particle with another particle, in this case neutrons or fission products with lattice atoms. understanding this effect one must first define various subsets of the interaction. First, the cross-section of interaction, then the two-body collision and its mathematical development into a practice theory, and then the defects produced and their interactions.

Damage comes from the two-body interaction of a fast moving particle, either a neutron, fission product or even electron. Fission produces two heavy fission products with energies near 70 MeV. The displacement of an atom off its lattice site only requires 5 to 80 eV, depending on structure and bonding. Once the fission event has occurred, the fission products and/or transmuted isotopes may continue to decay at a significant rate. The rate at which an isotope decays is described as a half-life.

D.0.1 Radioactive Decay

x decays to y

Decay of x is exponential with time (refer to Figure D.1). C_x° is the initial concentration of x at $t = 0$. $t_{\frac{1}{2}}$ is the half-life, or when $C_x = \frac{1}{2}C_x^\circ$. t_e is the time when when $C_x = \frac{1}{e}C_x^\circ = 0.36788C_x^\circ$. $t_e > t_{\frac{1}{2}}$.

[1]The bulk of the radiation damage theory was transcribed from class notes. The class, "Radiation Damage in Materials" was taught by Dr. Kurt Sickafus and extraction and use of his notes was under his approval. Scanned plots taken from [181, 182].

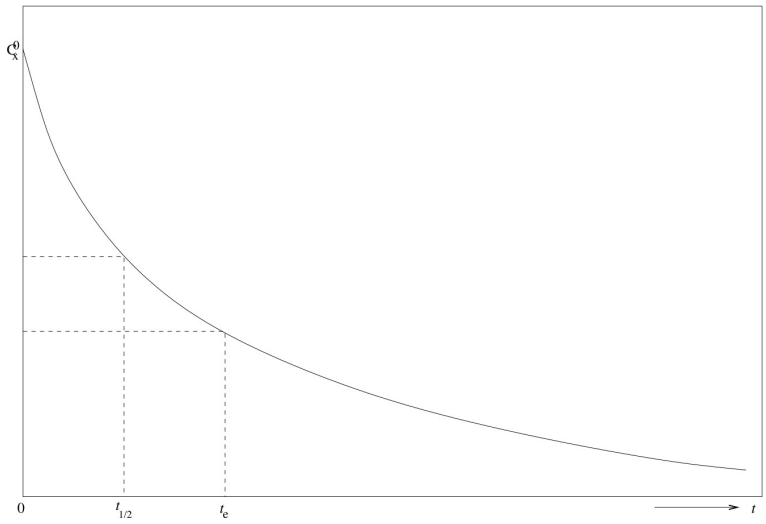

Figure D.1: Radioactive decay

$t_{\frac{1}{2}} = ln(2)t_e = 0.69315t_e$. $t_{\frac{1}{2}} \simeq 70\%$ of t_e

Differential equations for the decay in concentration of x and the growth in concentration of y:

Equation 1:

$\frac{dC_x}{dt} = -\frac{1}{t_e}C_x$

Time rate of change of C_x is proportional to C_x; proportionality constant is the reciprocal of the characteristic decay time, -$\frac{1}{t_e}$.

Equation 2:

$\frac{dC_y}{dt} = +\frac{1}{t_e}C_x$

Time rate of change of C_y is proportional to C_x; proportionality constant is the reciprocal of the characteristic decay time, $+\frac{1}{t_e}$.

Simultaneous linear differential equations:

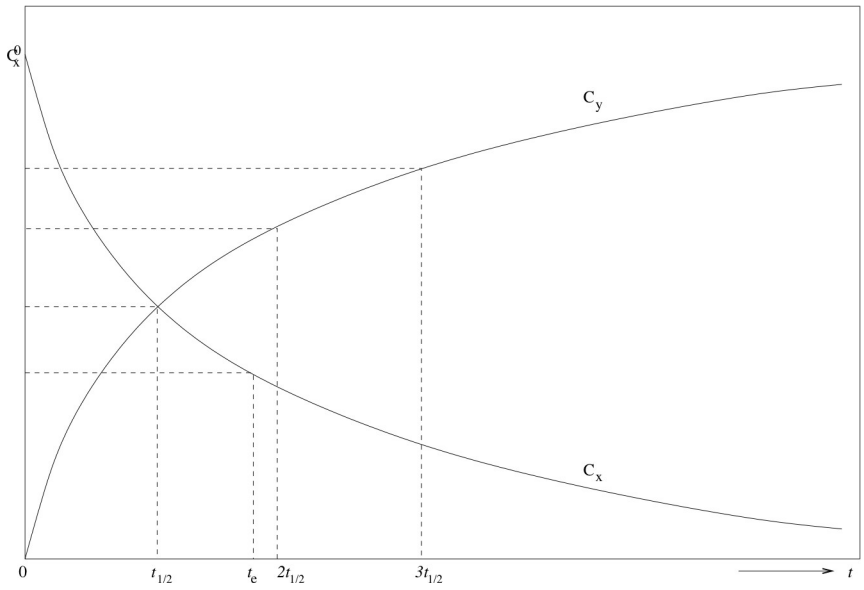

Figure D.2: Combined decay and production plot

- $\frac{dC_x}{dt} = -\frac{1}{t_e}C_x$
- $\frac{dC_y}{dt} = +\frac{1}{t_e}C_x$

Solve equation 1 first because it depends only on C_x (no C_y dependency). Then substitute the solution for C_x into equation 2

- $C_x(t) = C_x^\circ e^{-\frac{t}{t_e}}$
- $C_y\left(t\right) = C_x^\circ\left(1 - e^{-\frac{t}{t_e}}\right)$ Note that $C_y\left(t = 0\right) = 0$.

The equations show the decay of one product and the rise of another. Figure D.2 shows the relative quantities with time.

- $C_x\left(t\right)$ and $C_y\left(t\right)$ are equal at $t = t_{\frac{1}{2}}$
- $C_x\left(t\right)$ and $C_y\left(t\right)$ = 1 for all *t*

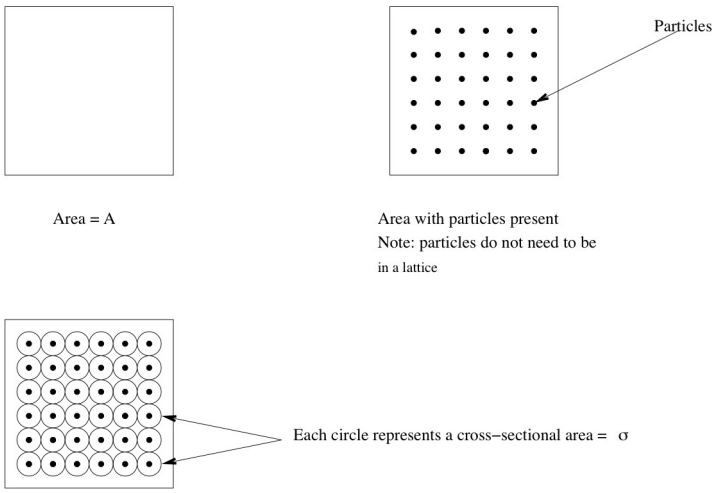

Figure D.3: Plane of atoms and σ representation

D.0.2 Cross-Section (σ)

A fundamental basis for radiation damage, or any two-body interaction, is the cross-section. This is essentially defined as the probability of interaction between two particles.

Imagine a plane of atoms such that they form a 2-D lattice with a spacing (Figure D.3). Each atom has a defined area that represents the cross-section or probability of interaction. The cross-section, σ, is the area that one atom presents to a beam of incoming particles for initiating a specified "interaction." In this case, cross-section has units of area.

As a particle penetrates the area of atoms, the probability of an interaction is then σ. If an incoming particle hits inside area σ, "interaction" occurs. Alternatively, if an incoming particle hits outside areaσ, no "interaction" occurs.

The surface density of atoms is defined as $\rho_s \left[\frac{atoms}{area}\right]$ and $\rho_s A$ =total # of atoms inside area *A*. $\left[\frac{toms}{area}\right]$ $[area]$= [dimensionless].

Thus, when a particle is shot into area *A*:

Probability of "interaction" = $\frac{(total\ area\ presented\ by\ atoms\ of\ cross\ section\ \sigma)}{(total\ area\ A)}$

$\frac{\rho_s A[dimensionless]\sigma[area]}{A[area]} = [dimensionless]$

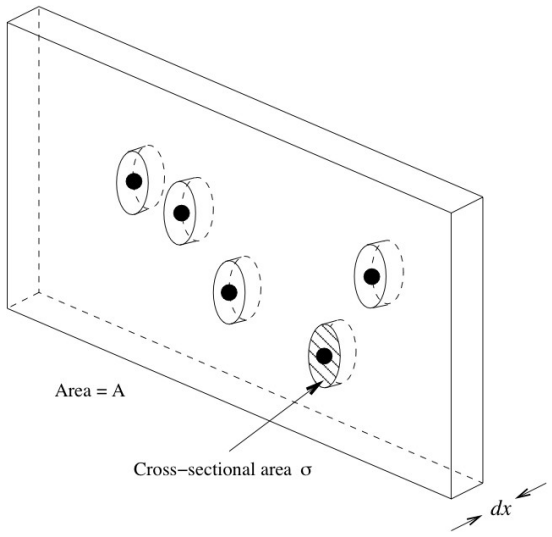

Figure D.4: Adding depth to σ

$\rho_s\sigma\,[dimensionless]$ =Probability of interaction

So, if you shoot $N_\circ$ at area *A,* the number, *N*, that "interact" with atoms is: $N = N_\circ\rho_s\sigma$. The fraction of particles that "interact" is: $\frac{N}{N_\circ} = \rho_s\sigma$. The fraction of particles that "interact $\equiv$ PROBABILITY. [dimensionless] = [dimensionless]

D.0.3 Probability of Cross-section

Cross-section idea is extended to 3-dimensions: imagine a slab of atoms of area *A* and thickness *dx.* Assume incoming particles impinge normal to slab. Each atom again present as an area, σ, $\equiv$ cross-section, to the incoming particles for initiating a specified "interaction". σ[area], the same as the 2-D model. If incoming, normal incidence, particle hits inside areaσ, "interaction" occurs, otherwise no "interaction" (Figure D.4).

D.0.4 Atomic Density

The atomic density is required to define the probability for particle interaction. Atomic density is simply the number of atoms per volume, $\rho_a \left[\frac{atoms}{volume}\right]$.

$\rho_a dx \equiv (\text{"}AREAL\text{"}\, atomic\, density)$

$\left[\frac{atoms}{volume}\right][length] = \left[\frac{atoms}{area}\right]$

$\rho_a Adx$ = total number of atoms inside volume *Adx*

$\left[\frac{atoms}{volume}\right][area][length]$ = [dimensionless]

Shoot a particle into slab, volume *Adx*

Probability of "interaction" = $\frac{(total\, volume\, presented\, by\, atoms\, of\, cross\, section - \sigma)}{(total\, volume\, Adx)}$

$\frac{\rho_a Adx[total\, number\, of\, atoms\, in\, volume\, Adx]\sigma dx\left[\frac{cross\, sectional volume}{atom}\right]}{Adx[total\, volume]}$

$\frac{\rho_a Adx[dimensionless]\sigma dx[volume]}{Adx[volume]}$

$\rho_a dx\sigma\,[dimenesionless] =$ probability of interaction

Probability of "interaction" = "Areal" atomic density$\times$cross-section

So, if you shoot $N_\circ$ particles into volume *Adx*, the number, *N*, that "interact" with atoms is $N = N_\circ \underbrace{\rho_a dx}_{\rho_s} \sigma$ where ρ_s is the "areal" density $\left[\frac{atoms}{area}\right]$. The fraction of particles that "interact" is $\frac{N}{N_\circ} = \rho_a dx\sigma$. This fraction $\equiv$ *PROBABILITY*, with both being dimensionless.

PROBABILITY$\propto$*CROSS-SECTION*

The probability constant $= \rho_a dx$= "areal density of atoms.

Definitions of Flux and Fluence

Imagine a flux, $\varphi_\circ$, of incident particles impinging on a slab of material, with a volume *Adx* (Figure D.5). The flux, φ, that "interacts" with the atoms in the target (the slab) is: $\varphi = \varphi_\circ \rho_a dx\sigma$. The probability of "interaction" as the fraction: $\frac{\varphi}{\varphi_\circ} = \rho_a dx\sigma$, both being dimensionless.

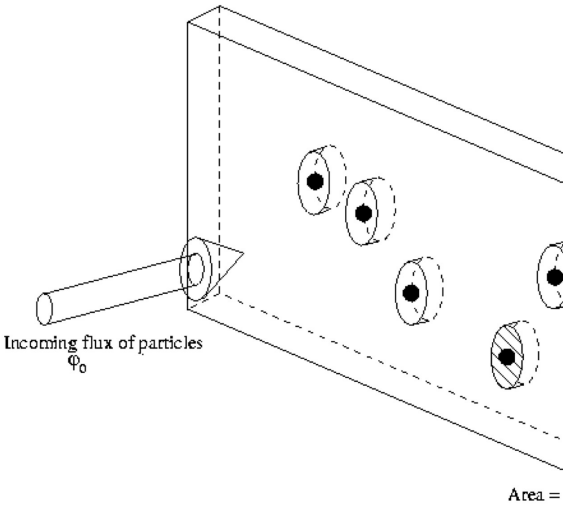

Figure D.5: Incoming flux of particles

Now, suppose an irradiation experiment is run for some period of time *t*. If the incident particles flux is $\varphi_\circ$, then the total incident fluence is $\Phi_\circ$where: $\Phi_\circ = \varphi_\circ t$ with units $\left[\frac{\#particles}{area}\right] = \left[\frac{\#particles}{area \times time}\right] [time]$

Fluence=Flux$\times$time.

Then, the fluence, Φ, that "interacts" with the target atoms (the slab) is:

$\Phi = \Phi_\circ \rho_a dx \sigma$ with units $\left[\frac{\#particles}{area}\right] = \left[\frac{\#particles}{area \times time}\right] \underbrace{\left[\frac{\#atoms}{volume}\right] [length] [area]}_{dimensionless}$

$\frac{\Phi}{\Phi_\circ} = \rho dx \sigma \equiv$ Probability of "Interaction", both dimensionless.

D.0.5 2-Body Collision

Two bodies, a projectile and a target, are collided in space. In this example, the projectile, with mass $m_1$and initial velocity $\vec{v}_{10}$ is projected towards the target with mass m_2 and initial velocity of $\vec{v}_{20} = 0$, because in this case, the target is at rest. Fig shows the projectile and target with a separation of b, the impact parameter. This is considered *laboratory* coordinates, with the final velocities of $\vec{v}_{1f}$ and $\vec{v}_{2f}$, and angles deviating from original trajectory of θ and ρ, for the projectile and target respectively (Figure D.6).

Since energy is $\frac{1}{2}mv^2$, the energies can be calculated. Initial energy of the projectile is $E_\circ$ and the final is E_f. The target is at rest thus only the final energy is T_f, with *T* being the traditional symbol for target energy.

D.0.5.1 Center of mass coordinates

Typically a 2-body collision is calculated by using center of mass coordinates (CM), transformed from laboratory coordinates, and then back to laboratory coordinates. Center of mass coordinates is the mass-weighted average of the position vectors (Figure D.7). The

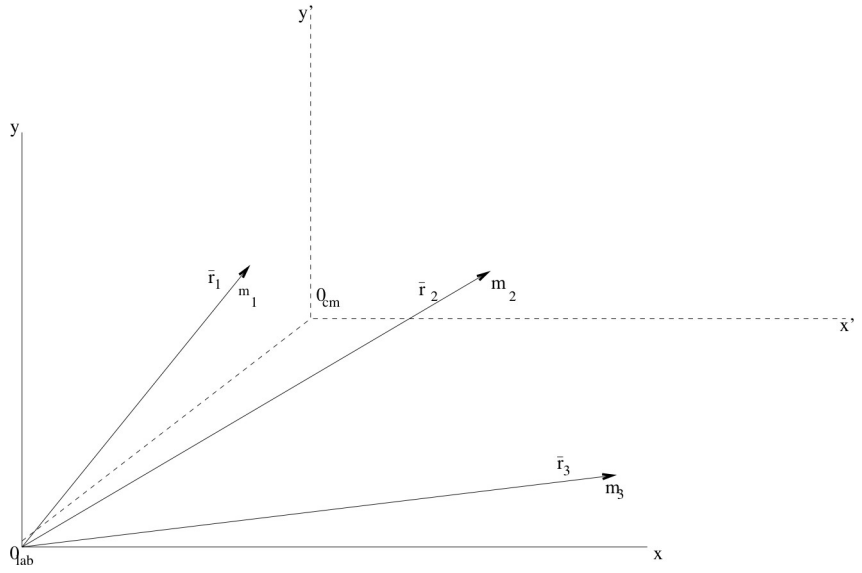

Figure D.6: Two-Body Interaction

simple method is to transform from lab to CM, interact mathematically, then transform back from CM to lab. The key is that the center of mass velocity never changes. $\vec{u}_{cm}$ is the center of mass velocity.

$$\vec{u}_{cm} = \frac{\sum_{i=1}^{n} m\dot{\vec{r}}_i}{\sum_{i=1}^{n} m_i}$$ for time derived. $\vec{u}_{cm} = \frac{m_1}{m_1+m_2}\vec{v}_{10} + \frac{m_2}{m_1+m_2}\vec{v}_{20}$, but since the target is at rest, $\vec{v}_{20} = 0$, so $\vec{u}_{cm} = \frac{m_1}{m_1+m_2}\vec{v}_{10}$.

D.0.5.2 Interaction math

D.0.5.2.1 Properties of CM coordinates for a 2-body collision:

1. $\vec{v_1^{cm}}$ is always anti-parallel to $\vec{v_2^{cm}}$.

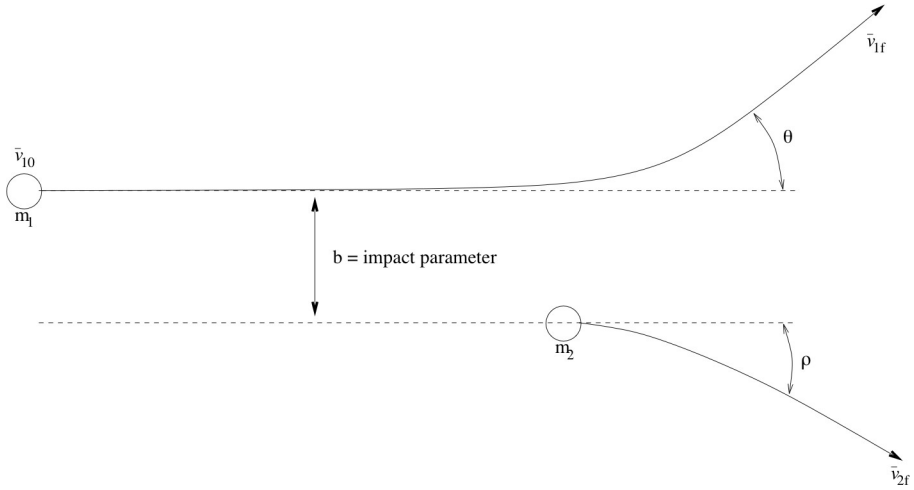

Figure D.7: Center of mass coordinate system

2. Magnitudes of velocities are unchanged by scattering interaction. $v_{10}^{cm} = v_{1f}^{cm}$, $v_{20}^{cm} = v_{2f}^{cm}$

3. Velocity of CM unchanged through out interaction. $\vec{u}_{cm}$= constant

D.0.5.2.2 Steps Figure D.8 illustrates these steps.

1. Draw the vectors in lab space. For this example, as in radiation damage, the target atom, m_2, is at rest.

2. Calculate $\vec{u}_{cm}$ and subtract from both $\vec{v}_{10}$ and $\vec{v}_{20}$. This can be observed graphically. The velocity vectors in center of mass coordinates, $\overrightarrow{v}_{1f}^{cm}$ and $\overrightarrow{v}_{2f}^{cm}$, point at each other and connect tip to tip.

3. Rotate an image of these vectors so that each produces an angle of deflection in center of mass coordinates, θ_{cm}. θ_{cm} is determined by the impact parameter b, and the details of the interaction potential.

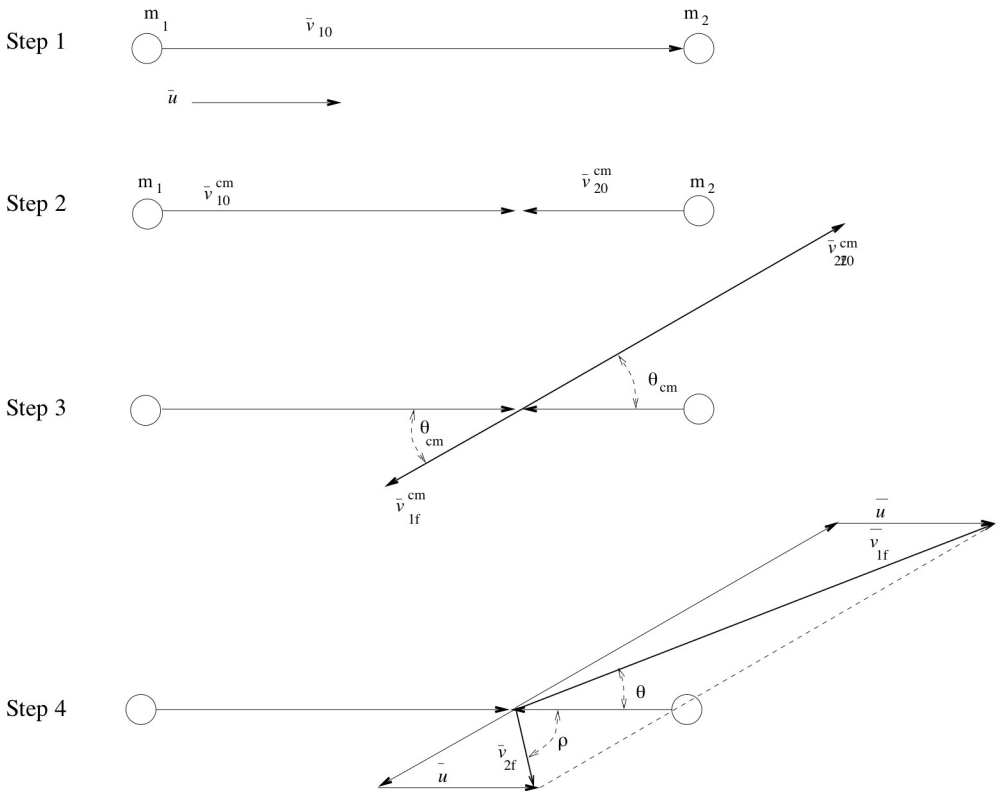

Figure D.8: Steps to convert from laboratory to center of mass coordinates

4. Add $\overrightarrow{u}$ back to each side. This creates a parallelogram if one connects the $\overrightarrow{u}$ added to each other. From the intersection point, draw a line to the tips of the added $\overrightarrow{u}$'s. These are the transformed vectors from center of mass to laboratory coordinates. The angles formed between these new vectors are different, θ being the deflection angle for the projectile and ϕ for the knock-on.

D.0.5.2.3 Find θ_{cm} Using the law of cosines, one can find θ_{cm} and thus θ and ϕ. Using the fact that the velocities in center of mass coordinates does not change and the law of cosines,:

$v_{2f}^2 = \left(v_{2f}^{cm}\right)^2 + u^2 - 2v_{2f}^{cm}u \cdot Cos\left(\theta_{cm}\right)$ and vector magnitudes do not change in cm, thus $v_{2f}^{cm} = v_{20}^{cm} \therefore v_{2f} = u$

$v_{2f}^2 = u^2 + u^2 - 2u^2 \cdot Cos\left(\theta_{cm}\right) = 2u^2\left(1 - Cos\left(\theta_{cm}\right)\right)$

$\Rightarrow \vec{u_{cm}} = \frac{m_1}{m_1+m_2}\vec{v}_{10}$ but $u = \frac{m_1}{m_1+m_2}v_{10} = 2\left(\frac{{m_1}^2}{(m_1+m_2)^2}v_{10}\left(1 - Cos\left(\theta_{cm}\right)\right)\right)$

Kinetic energy is: $KE = \frac{1}{2}mv^2$ so $\frac{1}{2}m_2v_{2f}^2$=$\frac{1}{2}\left[2\frac{m_1}{m_1+m_2}v_{10}^2m_2\left(1 - Cos\left(\theta_{cm}\right)\right)\right]$

Here we define variables for energy. T = the kinetic energy of the target

$E_{10} = \frac{1}{2}m_1v_{10}^2$

$T = \frac{2m_1m_2}{(m_1+m_2)^2}\frac{1}{2}m_1v_{10}^2\left(1 - Cos\left(\theta_{cm}\right)\right)$, so max T = head on collision, and $\theta_{cm} = \pi$, and $Cos\left(\pi\right) = -1$

$\therefore T_{Max} = \underbrace{4\frac{m_1m_2}{(m_1+m_2)}}_{\Lambda}E_{10}$ and Λ = kinematic efficiency factor.

So $T_{Max} = \Lambda E_{10}$ with the impact parameter b being the minimum so that $\theta = \pi$

$T_{2f} = \frac{1}{2}T_{2f}^{max}\left(1 - Cos\left(\theta_{cm}\right)\right)$ So that T_{2f} maps out θ_{cm}

D.0.5.3 Kinematic Efficiency Factor

The kinematic efficiency factor, Λ, is at a maximum at $m_1 = m_2$, or when the masses are equal. An alternative way to write the kinematic efficiency factor is: $\Lambda = \frac{4\frac{m_1}{m_2}}{\left(1+\frac{m_1}{m_2}\right)^2}$

D.0.6 2-body collision: The Kinchin-Pease Approximation

Maximum efficiency of energy transfer occurs for $m_1 = m_2$

What about high mass disparities? Electrons hitting an atom or atom hitting electrons. For a head-on collision:

- $m_e \approx$ 5E-4 amu
- $m_{atom} =$ 1 amu to 250 amu (from periodic table)
- $\frac{m_e}{m_{atom}} =$ 5E-4 to 2E-7 (from Periodic table)

- $\frac{T_{max}}{E_{10}} =$ 2E-3 to 8E-7 (Periodic table)

Consider e^- head-on collision: Ca atom with e^-(5E-4 amu) $\Rightarrow$ Ca (40 amu).

$\frac{T_{max}}{E_{10}} \approx 4 \cdot \frac{5E-4}{40} \approx 4 \cdot 1.2E - 5 = 5E - 5.$

So for a 1MeV e^-, $E_{10} = 1$ MeV. T_{max} ≈5E-5 MeV = 50 eV = maximum energy transfer to Ca atom.

Equivalently, if a 1 MeV Ca atom slammed head-on into an e^-, it would impart 50 eV to the electron. (Symmetry of the kinetic efficiency). Now that the threshold for displacement of atoms in most material rates are as follows:

10 eV $\leq E_d \leq$ 100eV

So, 50 eV imparted to a Ca atom is of the order of what is necessary to displaced it from it's lattice site. But if the e^- started with energy E_{10} =100 keV, then the energy imparted to the Ca atom is only 5 eV, not enough for atomic displacement. e^- induced atomic displacement begins at energies of the order of 100 keV (transmission electron microscopes (TEM) voltages are enough; scanning electron microscopes (SEM) voltages are not enough).

What about atom-atom collisions? Consider Ne $\Rightarrow$ Ca.

Ne (20 amu) $\Rightarrow$ Ca(40 amu) $\frac{m_1}{m_2} = \frac{1}{2}$

$\frac{T_{max}}{E} = \frac{4\frac{1}{2}}{\left(1+\frac{1}{2}\right)^2} = \frac{2}{(1.5)^2} = 0.888$ This is a highly efficient kinetic energy transfer.

Now, a Ne atom with only 56 eV of kinetic energy is sufficient to impart 50 eV to a Ca atom. So, atomic collisions are much more efficient than e^-s at displacing atoms in a solid. Now, note that T_{max} scales linearly with E_{max}.

Maximum energy transfers:

- A 56 eV Ne atom imparts 50 eV to a Ca atom

- A 560 eV Ne atom imparts 500 eV to a Ca atom. This is MUCH more than needed to overcome the displacement threshold E_d.

- A 5600 eV Ne atom imparts 5000 eV to a Ca atom. This energy goes on to displace many more atoms in the solid.

For atoms with $\approx$ 1 keV of energy or greater, they induce a displacement cascade.

How big is a displacement cascade? The earliest and most often quoted work on this subject was Kinchin and Pease [183].

Kinchin-Pease Theory (KP)

A simple KP model of the energy threshold effects on atomic displacement (Figure D.9).

1. The number of atoms displaced in a cascade scales with incident energy, E, of the primary knock-on atom (PKA).

2. The scaling actor is $\frac{1}{2}E_d$

3. Below a PKA energy of $2E_d$, only one or non atoms are displaced

4. Additional atoms are no longer displaced above a PKA energy of $E_c \equiv$ critical energy. (electronic stopping dominates at high energies).

- No displacements below E_d

- One displacement (net) between E_d and $2E_d$

- $E_c \approx$ mass of target in keV, i.e. Ca target at 40 amu would have $E_c \approx$ 40 keV

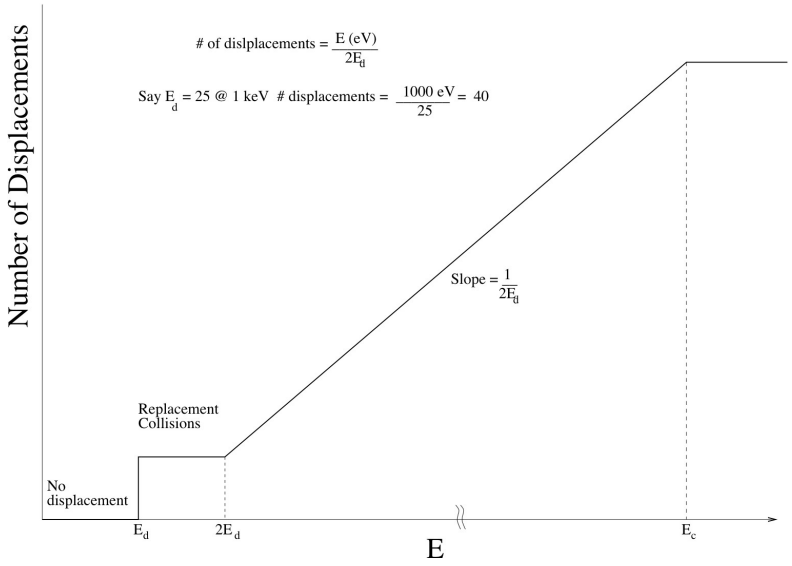

Figure D.9: Kinchin-Pease displacement plot

- Assume E_d =25 keV
- $E = \begin{cases} 0 - 25eV & 0\,displacements \\ 25 - 50eV & 1\,displacement \\ > 50eV\ (< E_c) & \frac{E(eV)}{2(25eV)} displacements \end{cases}$

D.0.7 Interaction Potentials

Example: Ionic bonding

$V_{attarctive} = -\frac{constant}{r}$ $V_{repulstive} = +\frac{constant}{r}$

$V_{total} = \frac{-A}{r} + \frac{B}{r^m} + \triangle E$ $\triangle E =$ the energy required to form two ions from neutral atoms

The first derivative, $\frac{dV}{dr} = 0$ gives $d_\circ$ The second derivative, $\frac{dV^2}{d^2r} =$ modulus.

Potential energy minimum occurs at a distance $r = d_\circ$ where the attractive and repulsive forces just balance. Departure from this equilibrium spacing $d_\circ$ increases the potential energy and thus produces a restoring force. The part of the interatomic potential that plays a role in "ballistic" (nuclear displacements) radiation damage is the repulsive part of the

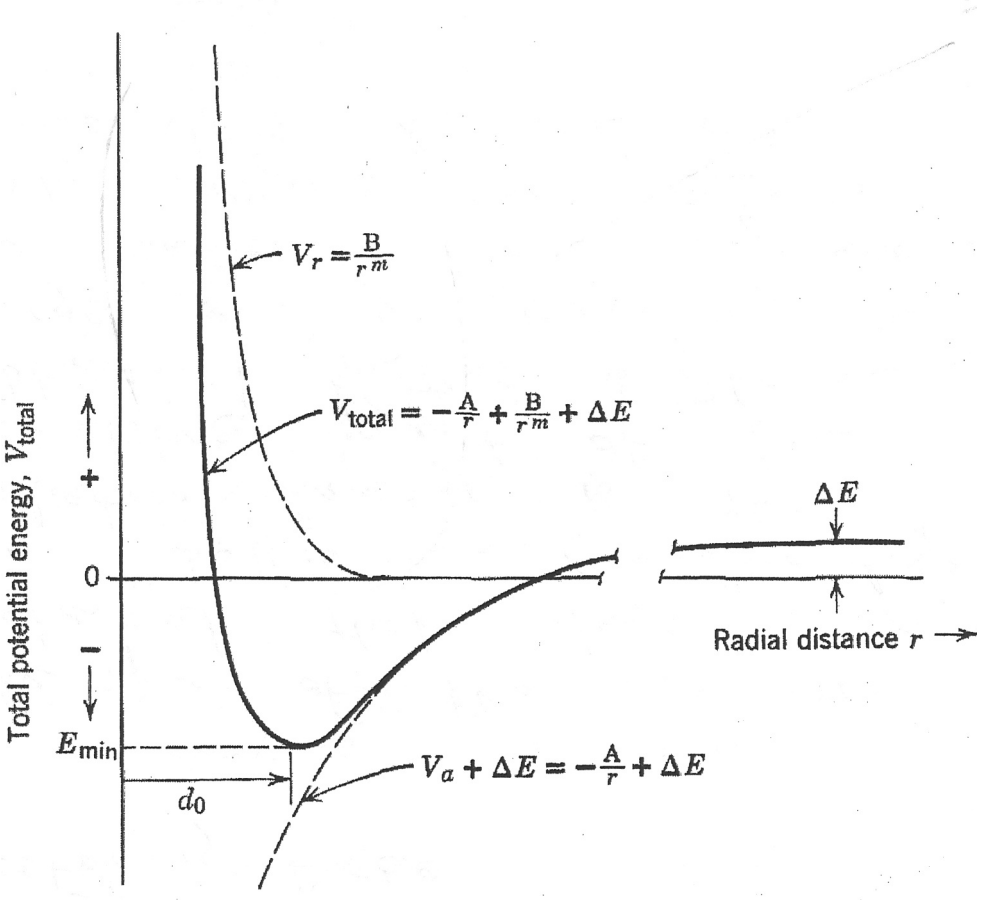

Figure D.10: Potential energy diagram for atoms at a distanc r

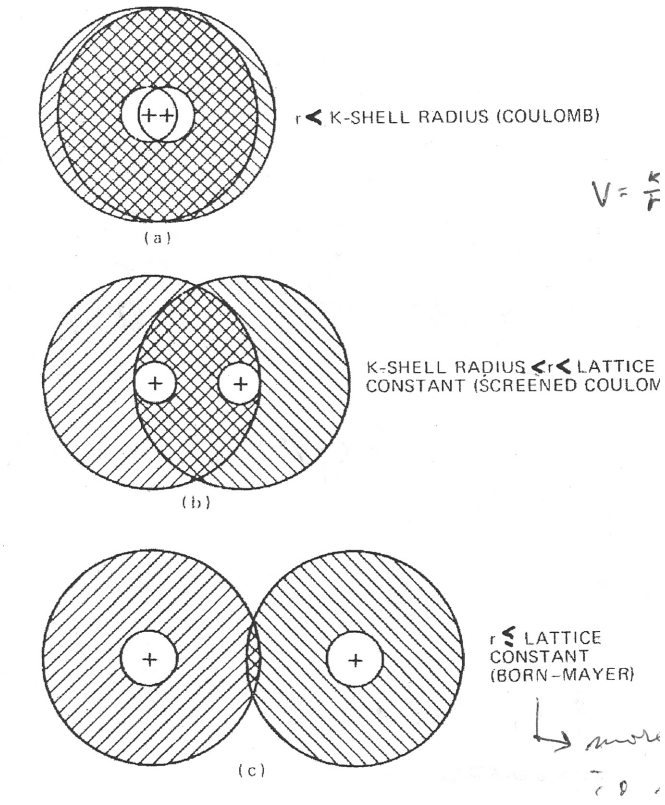

Figure D.11: Threee regimes of interaction

potential. This is because large energy transfer, sufficient to cause atomic displacement, only occurs for *close* encounters (small r). Fgure D.11 shows 3 regimes for repulsive interactions when $r < d_\circ$.

- The closest encounter (a) is described by a bare Coulomb interaction.
- A medium distance (b) encounter is described by a "screened" Coulomb interaction.
- An interaction at distances near $d_\circ$ (c) is described by a Born-Mayer potential.

D.0.7.1 Coulomb Potential

$V(r) = \frac{Z_1 Z_2 e^2}{r}$ $F(r) = \frac{Z_1 Z_2 e^2}{r^2}$

D.0.7.2 Screened Coulomb Potential

$V(r) = \frac{Z_1 Z_2 e^2}{r} e^{\frac{-r}{a}}$ a is the screening radius.

D.0.7.3 Born-Mayer Potential

$V(r) = Be^{\frac{-r}{\rho}}$ B and ρ are determined from equilibrium properties of the solid.

D.0.7.4 Bare Coulomb Interactions

These occur for close encounters of a fraction of an Angstrom $\left[\text{Å}\right]$. Less than a K-shell (1s) radius. For H-H , this would be $\approx$ 0.5 . The radius of an electron's orbit is Bohr's theory of the Hydrogen atom:

$r = n^2 a_\circ$ First Bohr radius, n=1

$r = a_\circ$

$a_\circ = \frac{h^2}{4\pi m_e e^2} = 0.529\text{Å}$

D.0.7.5 Bare Coulomb Interaction

$V(r) = +\frac{Z_1 Z_2 e^2}{r}$ + = repulsive

Here, the constant is equal to 1. This equation is in esu units (electrostatic units) In esu units: $e^2 = 14.4eV \cdot$ Å.

Two protons $(Z_{1,} = 1, Z_2 = 1)$ spaced 1 Å apart have a potential of interaction of 14.4 eV.

For a Coulombic potential of interaction, we showed that the cross-section for kinetic energy transfer T to a target atom m_2 from a projectile m_1 with kinetic energy E (not during class):

M$d\sigma = \frac{\pi K^2 \frac{m_1}{m_2}}{E} \frac{dT}{T^2}$ where K is the Coulomb force constant = $Z_1 Z_2 e^2$(esu units)

Integrate this equation to derive the total cross-section for Coulombic scattering.

$d\sigma = c\frac{dT}{dT^2}$ where $c = \frac{\pi K^2 \frac{m_1}{m_2}}{E}$

$\sigma_{total} = \int_{T_{min}}^{T_{max}} d\sigma$ $T_{min} = 0$ (glancing incidence) $T_{max} = \Lambda E = \frac{4m_1 m_2}{(m_1+m_2)^2} E$ (head-on collision)

$\sigma_{total} = c\int_0^{\Lambda E} \frac{dT}{T^2} = -c\frac{1}{T} \mid_{T=0}^{T=\Lambda E} = -c\left(\frac{1}{\Lambda E} - \frac{1}{0}\right)$ But $\sigma_{total} \Rightarrow \infty$ from $\frac{1}{0}$!!

The Coulomb potential is *too* long-range. $V(r) = \frac{K}{r}$ is finite even at infinite separation. Bare Coulomb potentials are valid for very short range interactions. But need to use screened Coulomb potentials for longer range interactions.

Figure D.12 from Olander shows the bridging of interaction potential description. Note that bare Coulomb is only valid at r≈ 0.01Å.

D.0.7.6 Screened Coulomb Potential

- $V(r) = \frac{Z_1 Z_2 e^2}{r} e^{\frac{-r}{a}}$ with a= screening length

Original Lindhard, Scharff, and Schiott (LSS) [184], tried to develop a "universal"

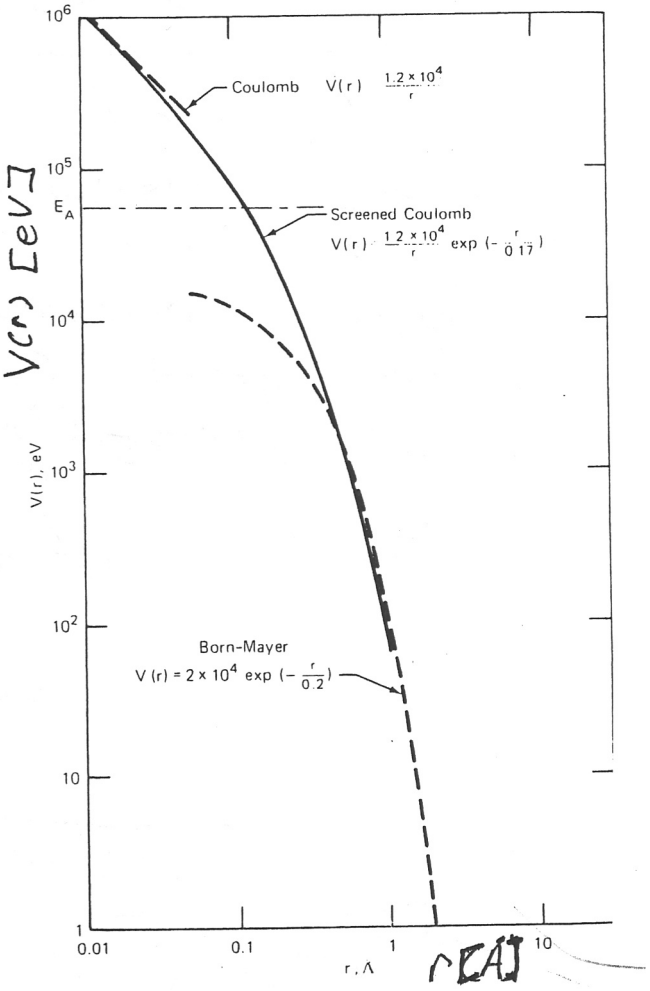

Figure D.12: Bridging interaction

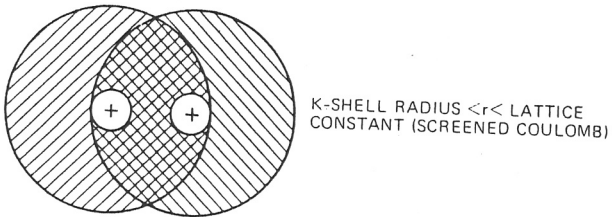

Figure D.13: Screened Coulomb potential

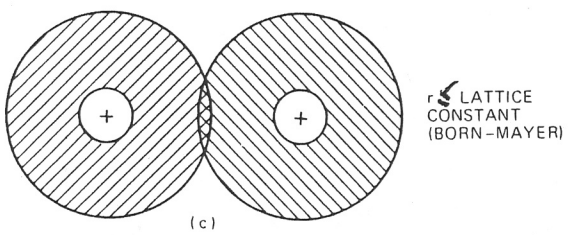

Figure D.14: Born-Mayer interaction potential

potential. of interaction, using a version of the Thomas-Fermi-Firsov (TFF) screening length given by:

- $a_{LSS} = \frac{0.8853 a_\circ}{\sqrt{Z_1^{\frac{2}{3}} + Z_2^{\frac{2}{3}}}}$ where $a_\circ$ is the Bohr radius of the hydrogen $a_\circ = 0.529177\text{Å}$.

Ziegler, Bierzack, and Littmark (ZBL) improved upon the LSS "universal" potential, and developed their own screening length:

- $a_{ZBL} = \frac{0.8856 a_\circ}{Z_1^{0.23} + Z_2^{0.23}}$

and with this derives the ZBL "universal" potential. This is the potential described in the book "*The Stopping Range of Ions in Solids*" [120], and the potential of interaction used in TRIM.

For $r \ll a_{LSS}$ or $r \ll a_{ZBL}$, the screened Coulomb potentially reduces smoothly to the Coulomb potential function. Screened Coulomb accounts for the diminution of the pure Coulomb repulsion between nuclei due to electrostatic screening of the positive charges by the intervening inner-shell electrons.

D.0.7.7 Borne-Mayer Interaction Potential

Valid near a lattice constant separation.

- $V(r) = Ae^{\frac{r}{\rho}}$

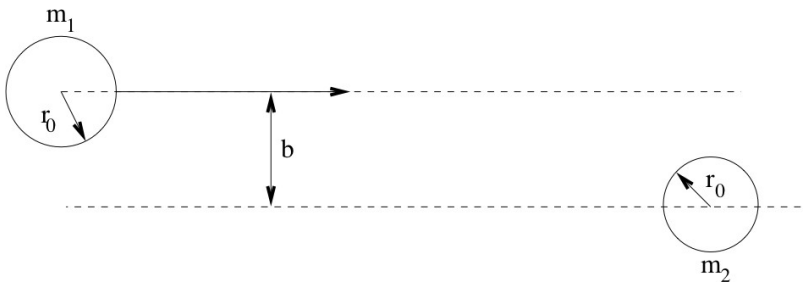

Figure D.15: Two-body collision showing the impact parameter b

Born-Mayer and Screened Coulomb do not bridge smoothly. Use power law to bridge smoothly.

- $V(r) = \frac{A}{r^s}$ (s = 2,3)

Vary constants A and s to fit to Screened Coulomb at small r or Born-Mayer at large r.

D.0.7.8 Hard-Sphere Potential

An often used but unrealistic interaction potential function.

- $V(r) = \begin{cases} 0 & ; r > 2r_\circ \\ \infty & ; r < 2r_\circ \end{cases}$

$r_\circ$ is the radius of the colliding hard spheres.

b = impact parameter

- b > $2r_\circ$ $\Rightarrow$no interaction
- b < $2r_\circ$ $\Rightarrow$ interaction

Look at the interaction in projection along an aΓaxis parallel to the motion of projectile m_1 (Figure D.15):

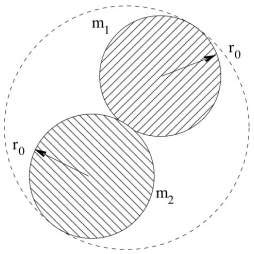

Figure D.16: Glancing collision interaction

D.0.7.9 Glancing Collision

Figure D.16 shows the glancing collision interaction. The diameter of the dotted sphere is $4r_\circ$; radius = $2r_\circ$. The sphere represents the *total* cross-section for the hard-sphere scattering (remember cross-section = area).

$\sigma_{total}^{hard-sphere} = \pi\left(2r_\circ\right)^2 = 4\pi r_\circ^2$

In the center-of-mass (CM) system, scattering is "isotropic" into all space. All space solid angle = 4π. $\therefore \frac{d\sigma}{d\Omega} = \frac{\sigma_{total}}{4\pi} = \frac{4\pi r_\circ^2}{4\pi}$

$\frac{d\sigma}{d\Omega}$ is the differential scattering cross-section for scattering into a differential solid angle.

$d\Omega = 2\pi Sin\left(\theta\right) d\theta$ where θhere is θ_{cm}

If we transform $\frac{d\sigma(E,\theta)}{d\Omega} \Rightarrow \frac{d\sigma(E,T)}{dT}$ we find for hard-sphere collisions.

$\frac{d\sigma(E,T)}{dT} = \frac{4\pi r_\circ^2}{\Lambda E} = \frac{\sigma(E)_{total}}{\Lambda E}$

Useful cross-section $\Rightarrow$ no T-dependence. This potential is assumed in the Kinchin-Pease (K-P) theory.

D.0.8 The LSS Energy-Partitioning Theory

We consider a primary knock-on atom (PKA) born with an energy grater than E_d, the *displacement threshold energy.* This PKA can interact with a lattice atom with a 2-body interaction kinetics shown in Figure D.17.

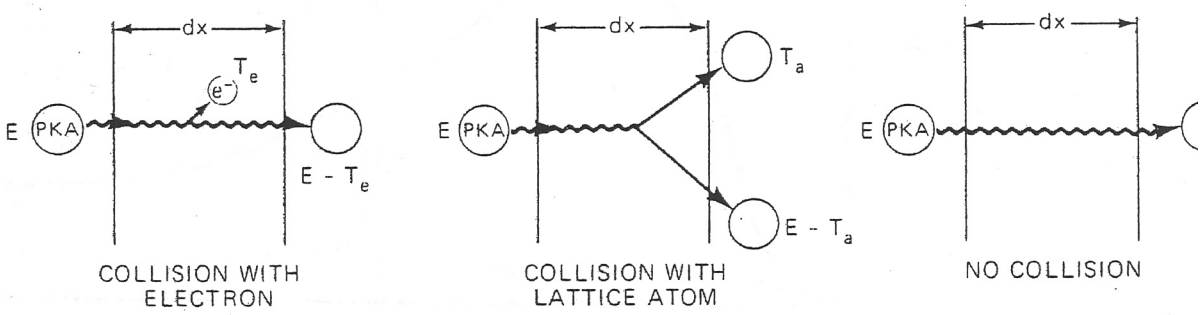

Figure D.17: Two-body collision with PKA and recoiling atom

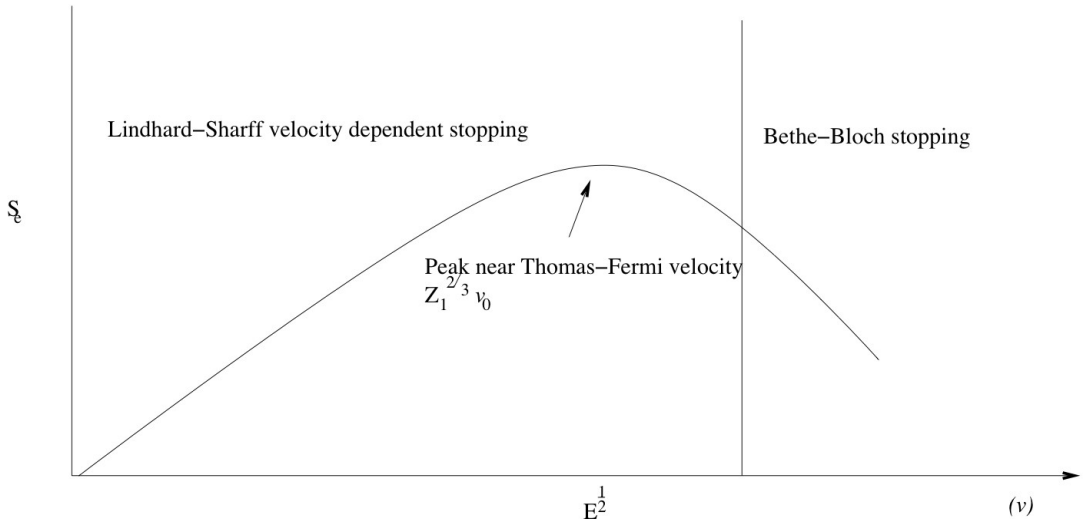

Figure D.18: Stopping Power

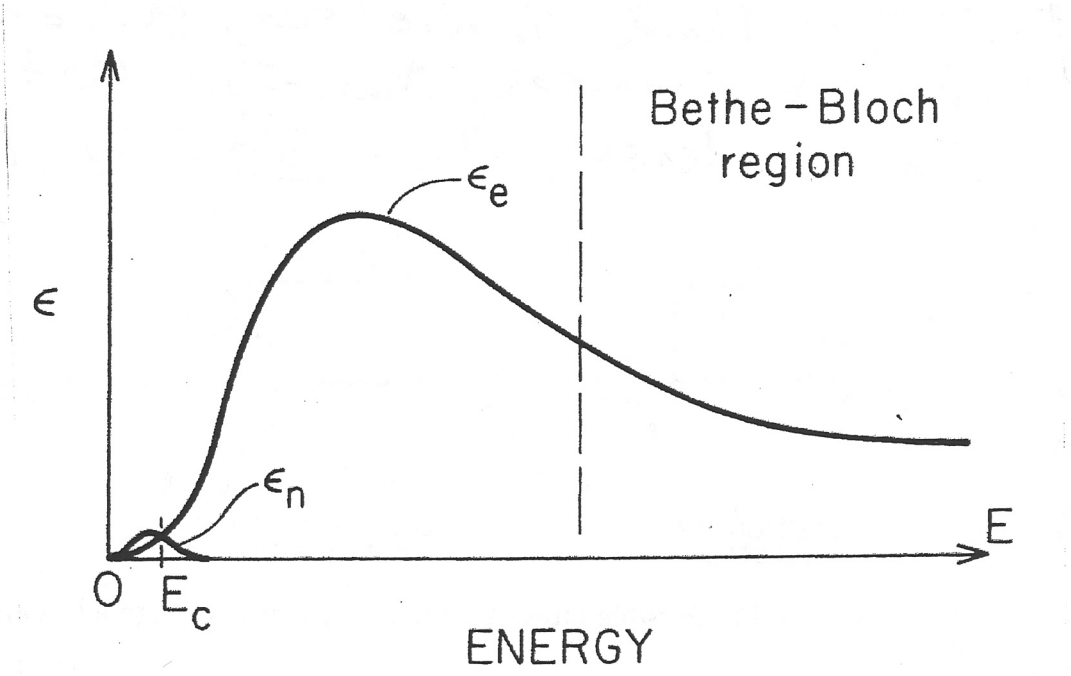

Figure D.19: Electronic Stopping vs. Projectile Energy E. Three ranges are shown being I, nuclear stopping dominated, II, electronic stopping dominated, and III Bethe-Bloche region

But the PKA can also interact with target electrons. Collision of the PKA with electrons compete with atomic collision with lattice atoms. The two processes can be treated independently and each can be represented by separate energy-transfer cross-sections.

At high projectile energies, electronic stopping, $\varepsilon_e\,(E)$ or $S_e\,(E)$, dominates nuclear stopping, $\varepsilon_n\,(E)$ or $S_n\,(E)$. Electronic stopping $\Uparrow$ as E $\Downarrow$(Bethe-Bloch regime). At lower projectile energies, electronic stopping becomes less efficient and electronic stopping $\Downarrow$ as E $\Downarrow$. Al low projectile energies, nuclear stopping predominates over electronic stopping $(\varepsilon_n > \varepsilon_e)$.

This plot sequence shows how the "range" of an energetic ion in a solid depends first on electronic stopping and then, at the "end-of-range", on nuclear stopping (Figure D.19). At low projectile energies, electronic stopping is proportional to $\sqrt{E}$. This is a classic LSS plot of electronic and nuclear stopping in reduced coordinates. Energy is plotted as ε, a

reduced [dimensionless] energy. Range is plotted as ρ, a reduced [dimensionless] distance. $\therefore$ Stopping power, $\frac{d\varepsilon}{d\rho}$, is reduced and [dimensionless].

Electronic stopping scales as $\varepsilon^{\frac{1}{2}}$. Nuclear stopping is either independent of ε; $\frac{1}{r^2}$ potential, or "universal"; Thomas-Fermi potential.

D.0.8.1 Energy loss to Electrons (Ionization)

I= binding energy of an e^- to an atom of the solid (ionization energy).

Projectile ion must transfer at least I to an e^- for ionization.

$$\begin{array}{ccccc} T_{max} & = & \Lambda & E_I \\ \Downarrow & & & \Downarrow \\ I & & & E_c \end{array}$$

- $E_c = \frac{I}{\Lambda} = \frac{(m_1+m_e)^2}{4m_1m_e} I$

When $m_e \ll m_1$, $E_c = \frac{m_1}{4m_e} I$

- $I_{semiconducter/insulater} \approx$ 1 to 6 eV. This is the energy needed to bridge the forbidden zone.
- $I_{metal} \approx$ 2eV. (half the Fermi energy).

D.0.9 Fermi-Dirac Statistics

The density of states $N(\varepsilon)$ vs. electron kinetic energy εpotential

$$N(\varepsilon) = \frac{3N_\circ \varepsilon_F^{-\frac{3}{2}} \varepsilon^{\frac{1}{2}}}{2\left(e^{\left(\frac{\varepsilon-\varepsilon_F}{kT}\right)}+1\right)}$$

In a typical metal, each atom contributes *one* electron to the "free-electron-gas". In metals, electrons very near the top of the "Fermi sea" can be excited by any amount of

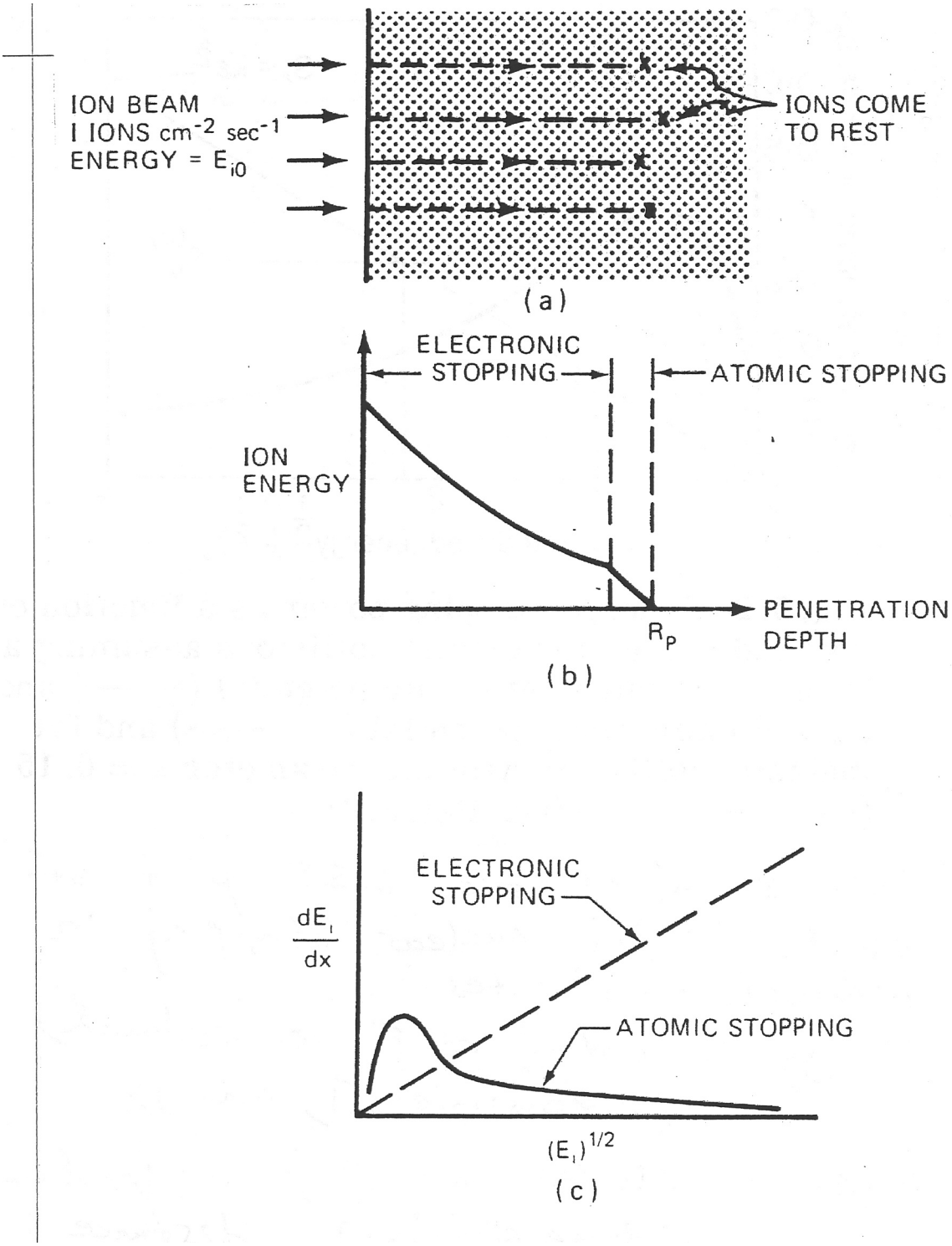

Figure D.20: Paths and energy losses of ions penetrating solids

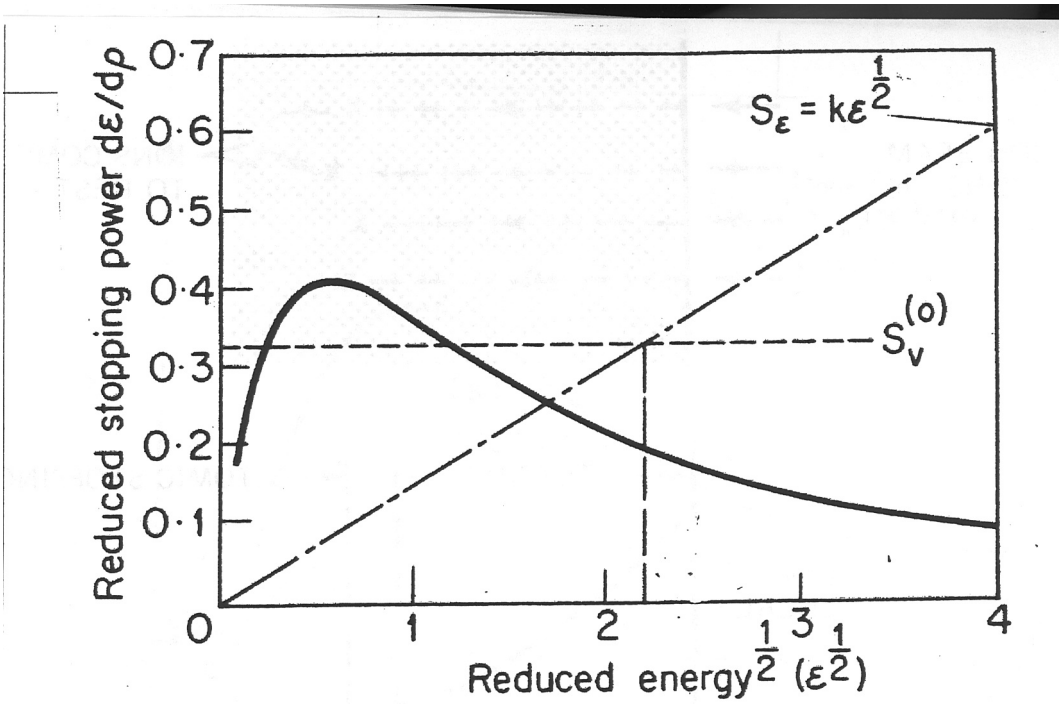

Figure D.21: Reduced stopping power

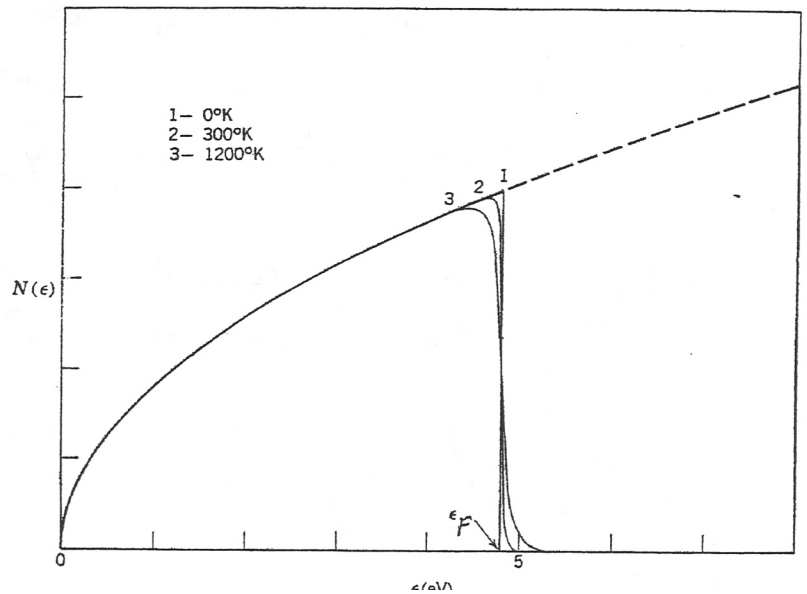

Figure D.22: Densioty of states vs. electron kinetic energy

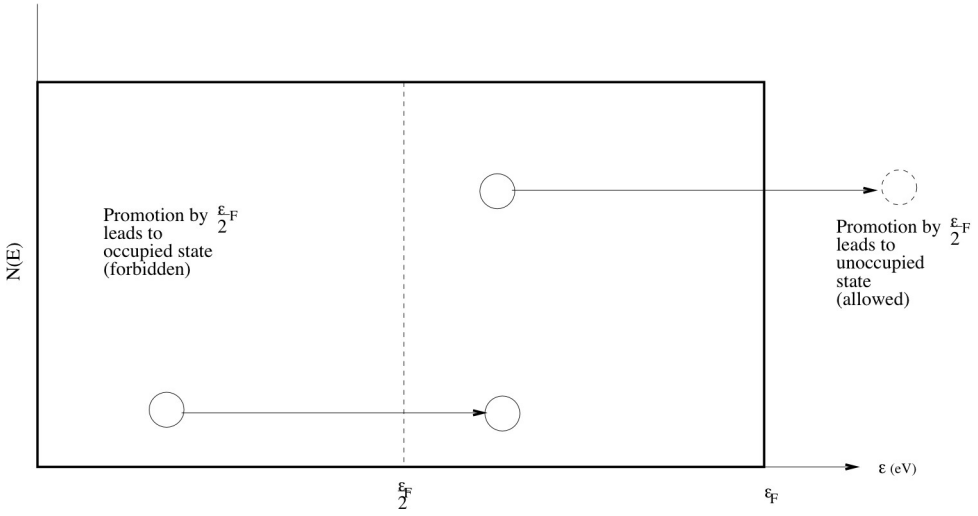

Figure D.23: Simple model of electron promotion

energy. But most conduction electrons lie well below the Fermi level. higher energy levels are *occupied!* This precludes arbitrarily small additions of kinetic energy. Very crudely, the average conduction electron in a metal needs to receive about one-half the Fermi energy in order to become excited and thereby remove energy from the moving atom (Figure D.23).

Even at $0°K$, the average kinetic energy of a conduction electron in a metal is quite large. For mono-valent metals, the electron density $\rho_e = \frac{N}{V}$ is between 10^{22} and $10^{23} \frac{electrons}{cm^3}$ and the Fermi energy is of the order of $\varepsilon_F = 5$ eV. The average electron energy in a metal at $0°K$ is thus about 3 eV (compare to <K.E.> of particle in a Maxwell-Boltzmann ideal gas at $300°K$).

$E_c = \frac{m_1}{4m_e} I$

Metals:

- $I \approx$2 eV and $m_e \approx \frac{1}{2000}$ amu
- $E_c = \frac{m_1 2[eV]}{4\frac{1}{2000}[amu]} \Rightarrow E_c = 1000 m_1\,[amu]\,[eV] \Rightarrow E_c = m_1\,[amu]\,[keV]$

For an example, Cu: $m_1 = 63.54$ amu

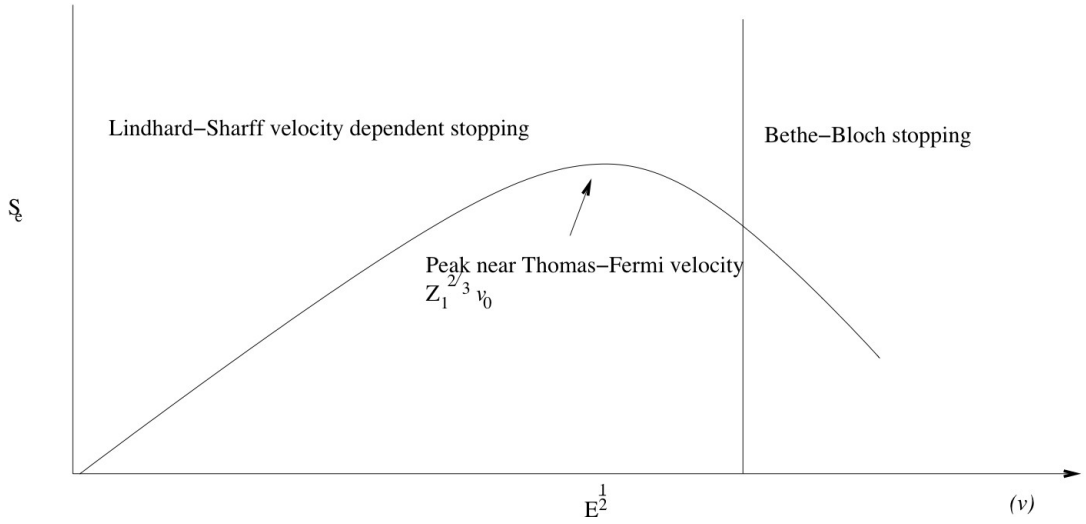

Figure D.24: Electronic Stopping vs. Projectile Energy E

- $E_c^{Cu} = 63.54$ keV
- $E_1 \gg 63$ keV electronic stopping dominates
- $E_1 \ll 63$ keV nuclear stopping dominates

D.0.10 Energy Loss vs. Stopping Power or Stopping Cross-section

Energy loss: $\left(\frac{-dE}{dx}\right)$with typical units: $\left[\frac{eV}{\text{Å}}\right]$ or $\left[\frac{keV}{nm}\right]$

Stopping power (S) or Stopping Cross-section (ε) with typical units: $[eV \cdot cm^2]$

$S = \int T d\sigma = \frac{1}{\rho}\frac{dE}{dx}$ remember ρ is atomic density

$\therefore \left(\frac{dE}{dx}\right) = \rho \int T d\sigma$ where $d\sigma\,(E, T)$

D.0.11 Electronic Stopping vs. Projectile Energy E

D.0.11.1 Bethe-Bloch Stopping:

Projectile (m_1, E) particle moves through target so fast that the velocity of the projectile, v_1, is large compared to the speed of the electrons in its innermost orbit = $Z_1 v_\circ$ ($v_\circ$ = Bohr velocity). The particle is effectively stripped of electrons and moves ads a bare ion through the medium. Also, all target electrons can be ionized.

D.0.11.2 Lindhard-Scharff "velocity-dependent" stopping:

The projectile moves so slowly that it retains all of its own electrons *and* it can only ionize the outermost electrons in the target.

D.0.11.3 In between:

The projectile charges scales as $Z_1^{eff} = \frac{v_1}{v_\circ} Z^{\frac{1}{3}}$

ASIDE about particle velocities

The Bohr velocity (the velocity of an electron in a ground state H atom):

$v_\circ = \frac{e^2}{\hbar} = \frac{\hbar}{m_e a_B} = 2.187690 \cdot 10^8 \frac{cm}{s} \approx 2.28 \cdot 10^8 \frac{cm}{s}$

a_B is the Bohr radius

$a_B = \frac{(\hbar c)}{e^2 E_\circ} = \frac{\left(1973 eV \cdot \text{Å}\right)^2}{14.4 eV \cdot (0.511 MeV)} \approx 0.529$ where $E_\circ$ is the rest energy electron

$c = 2.997925 \cdot 10^{10} \frac{cm}{s}$

$\frac{v_\circ}{c} = \frac{1}{137}$ which is the *fine structure constant*

$v_F =$ Fermi velocity = velocity of e^-s at top of conduction band in a metal.

Statement: For most solids $v_F \approx v_\circ$

Fermi velocity ≈ Bohr velocity

$v = \sqrt{\frac{2E}{m}} = \sqrt{\frac{2[eV]\cdot 1.60210\cdot 10^{-19}\frac{J}{eV}}{m[amu]\cdot 1.6605655\cdot 10^{-27}\frac{kg}{amu}}}\left[\frac{m}{s}\right]$

$v = 1.389095\cdot 10^{6}\sqrt{\frac{E[eV]}{m[amu]}}\left[\frac{cm}{s}\right]$

$v_F = \sqrt{\frac{2\varepsilon_F}{m_e}}$ where $\varepsilon \approx 5$ eV and $m_e = 5.488\cdot 10^{-4} amu$

$v_F = 1.326\cdot 10^{8}\frac{cm}{s}$ *and* $v_\circ = 2.2\cdot 10^{8}\frac{cm}{s}$. *Similar magnitude!*

Yes, Fermi velocity is of the order of Bohr velocity. How about the velocity of a 10 keV Cu ion?

$E = 10^{4} eV$

$m_{Cu} = 63.54 amu$

$v_{Cu} = 1.389095\cdot 10^{6}\sqrt{\frac{10^{4}[eV]}{63.54 amu}}\left[\frac{cm}{s}\right] = 1.74\cdot 10^{7}\frac{cm}{s}$.

This is considered a low velocity ion. $v_i \ll v_F$.

$v = 1.389095\cdot 10^{6}\sqrt{\frac{E[eV]}{m[amu]}}\left[\frac{cm}{s}\right] = 1.389095\cdot 10^{6}\sqrt{\frac{E[keV]\cdot 10^{3}\frac{eV}{keV}}{m[amu]s}}\left[\frac{cm}{s}\right] = 4.3927\cdot 10^{7}\sqrt{\frac{E[keV]}{m[amu]}}\left[\frac{cm}{s}\right]$

$v = 4.3927\cdot 10^{7}\sqrt{\left(\frac{E}{m}\right)\left[\frac{keV}{amu}\right]}\left[\frac{cm}{s}\right]$ where $\left[\frac{keV}{amu}\right]$ is also $\left[\frac{keV}{nucleaon}\right]$

Solve for $\frac{E}{m}$ for $v = v_\circ$

$\left(\frac{E}{m}\right)\left[\frac{keV}{amu}\right]\left[\frac{kev}{nucleon}\right] = \left(\frac{2.2\cdot 10^{8}\left[\frac{cm}{s}\right]}{4.3927\cdot 10^{7}}\right)^{2}$

$\left(\frac{E}{m}\right)_{v=v_\circ} = 25\left[\frac{keV}{amu}\right]$ or $\left[\frac{kev}{nucleon}\right]$

$< 25\left[\frac{keV}{amu}\right]$ is considered very low velocity ion.

D.0.12 Velocity regimes

1. Very low velocity ions:

$v_1 < v_F$ (or $v_\circ$), i.e. $\left(\frac{E}{m}\right) < 25\left[\frac{keV}{amu}\right]$ or $\left[\frac{keV}{nucleon}\right]$

$\Rightarrow$ energy loss $\propto$ ion velocity (Lindhard-Scharff)

2. Very high velocity ions:

$v_1 > 3v_F$ (or $v_\circ$), i.e. $\left(\frac{E}{m}\right) > 200\left[\frac{keV}{amu}\right]$ or $\left[\frac{keV}{nucleon}\right]$

$\Rightarrow$ Bethe-Bloch stopping (or mixture)

Example: Swift heavy ion irradiation, 120 MeV $^{107}Ag \approx 100\frac{keV}{amu}$

$S_e = 24.1\frac{keV}{nm}$

$S_n = 0.12\frac{keV}{nm}$

$v = 4.3927 \cdot 10^7\sqrt{\left(\frac{E}{m}\right)\left[\frac{keV}{amu}\right]}\frac{cm}{s}$

$\left(\frac{E}{m}\right) = 200\frac{keV}{amu}$

$v\left(\frac{cm}{s}\right) = 4.3927 \cdot \sqrt{200} = 6.21 \cdot 10^8\frac{cm}{s}$

with $v_\circ = 2.2 \cdot 10^8\frac{cm}{s} \Rightarrow \frac{6.21 \cdot 10^8\frac{cm}{s}}{2.2 \cdot 10^8\frac{cm}{s}} = 2.8$

Calculate Speed of Innermost Electrons:

$mv_nr_n = n\hbar$ quantized angular momentum

$v_n = \frac{n\hbar}{mr_n}$

$r_n = n^2r_1$

$v_n = \frac{n\hbar}{mn^2r_1} = \frac{\hbar}{mnr_1}$

$r_1 = \frac{a_B}{Z}$

$v_n = \frac{\hbar}{mn\frac{a_B}{Z}} = \frac{\hbar}{mna_B}Z = \frac{\hbar}{ma_B}\frac{Z}{n}$

The speed of electrons in the innermost orbit is v_1

$v_1 = \frac{\hbar}{ma_B}Z = v_\circ Z$ where $\frac{\hbar}{ma_B} = v_\circ = \frac{e^2}{\hbar}$

More accurate is the Thomas-Fermi description of multi-electron atom. Basic scaling relationship:

$v_e \propto Z^{\frac{2}{3}}$

So, for a projectile ion to travel at "Thomas-Fermi" velocity, need:

$\underbrace{v_1 = Z^{\frac{2}{3}} v_\circ = Z^{\frac{2}{3}} \frac{e^2}{\hbar}}$

This is the *peak* in the electronic stopping curve. Calculate energy equivalent of a single nucleon traveling at the Thomas-Fermi velocity:

$v = 4.3927 \cdot 10^7 \sqrt{\left(\frac{E}{m}\right)\left[\frac{keV}{amu}\right]} = v_{T-F} = Z_1^{\frac{2}{3}} v_\circ = 4.3927 \cdot 10^7 \sqrt{\left(\frac{E}{m}\right)\left[\frac{keV}{amu}\right]}$

$\left(\frac{E}{m}\right)_{v=v_{T-F}} = \left(\frac{Z^{\frac{2}{3}} 2.3 \cdot 10^8 \left[\frac{cm}{s}\right]}{4.3927 \cdot 10}\right)^2 \left[\frac{keV}{amu}\right] = Z_1^{\frac{4}{3}} \cdot 25 \left[\frac{keV}{amu}\right]$ or $\left[\frac{keV}{nucleon}\right]$

Peak in electronic stopping curve for Cu:

$\left(\frac{E}{m}\right)_{v=v_{T-F}} = (29)^{\frac{4}{3}} \cdot 25 \left[\frac{keV}{amu}\right] = 89 \left[\frac{keV}{amu}\right]$

$E = 89 \frac{keV}{amu} \cdot 63.54 amu = 5661 keV = 5.66 MeV$

$v_{T-F}^{Cu} = Z_1^{\frac{2}{3}} v_\circ = (29)^{\frac{2}{3}} (2.2 \cdot 10^8) \frac{cm}{s} = 2.08 \cdot 10^9 \frac{cm}{s} = 9.44 v_\circ$

Bethe-Bloch Stopping

Electronic stopping at high energies. Projectile is stripped of its electrons. The projectile ion interacts with target electrons via pure Coulombic interactions:

$V(r) = \frac{Z_1 Z_2 e^2}{r}$ in esu units. For an electron, $Z_2 = 1 \Rightarrow V(r) = \frac{Z_1 e^2}{r} = \frac{K}{r}$ where $K = Z_1 e^2$.

$d\sigma(E,T) = \frac{\pi K^2 \frac{m_1}{m_2}}{E} \frac{dT}{T}$ where $m_2 = m_e \ll m_1$.

$d\sigma(E,T) = \frac{\pi Z_1^2 e^4 \frac{m_1}{m_e}}{E} \frac{dT}{T}$

Stopping Power:

$S_e(E) = \int_{T_{min}}^{T_{max}} T d\sigma(E,T)$

$T_{min} = I =$ binding energy of electron ionization potential

$T_{max} = \Lambda E = \frac{4 m_1 m_2}{(m_1+m_2)^2} E = \frac{4 m_1 m_e}{(m_1+m_e)^2} E \approx 4 \frac{m_e}{m_1} E$

$S_e(E) = \frac{\pi Z_1^2 e^4 \frac{m_1}{m_e}}{E} \int_{T=I}^{T=4\frac{m_e}{m_1}E} \frac{dT}{T}$

$S_e(E) = \frac{\pi Z_1^2 e^4 \frac{m_1}{m_e}}{E} lm\left(\frac{4\frac{m_e}{m_1}E}{I}\right)$

Interestingly, this is within a factor of two of the correct, quantum mechanical derivation of Bethe-Bloch stopping:

$S_e(E) = \frac{2\pi Z_1^2 e^4 \frac{m_1}{m_e}}{E} ln\left(\frac{4E}{\frac{m_1}{m_e}\bar{I}}\right)$ where $\bar{I}$ = the average e^- ionization potential. Quantum mechanical analysis reveals:

$\bar{I} = kZ_2$ where $k \approx 10$, k is known as Bloch's constant.

$\left(\frac{-dE}{dx}\right) = \rho S(E)$ and $\left(\frac{-dE}{dx}\right)_e = \rho_e S_e(E)$

At the energies where Bethe-Bloch stopping is relevant, all electrons can be ionized. $\therefore$ $\rho_e =$ electron density of target $= \rho_a Z_2$ where ρ_a is the atomic density of target.

$\left(\frac{-d\varepsilon}{dx}\right)_e = \frac{2\pi Z_1^2 Z_2 e^4 \rho_a \frac{m_1}{m_e}}{E} ln\left(\frac{4E}{\frac{m_1}{m_e}(kZ_2)}\right)$remember $k \approx 10$.

D.0.13 Bethe Range:

$R_{Bethe} = \int_{E=E}^{E=0} \frac{dE}{\left(\frac{-dE}{dx}\right)_e}$

Let $c_1 = \pi Z_1^2 Z_2 e^4 \rho_z \frac{m_1}{m_e}$ and $c_2 = \frac{4}{\frac{m_1}{m_e} Z_2}$

$R_{Bethe} = \frac{1}{c_1} \int_E^0 \frac{EdE}{ln(c_2 E)}$

D.1 Lindhard-Scharff Velocity-Dependent Stopping:

D.1.1 Electronic stopping at low energies

Consider a projectile ion, max m_1, velocity $\vec{v}_{10}$, impinging head-on into an electron with mass m_e and oppositely-directed velocity vector $\vec{v}_{e0}$ (Figure D.25).

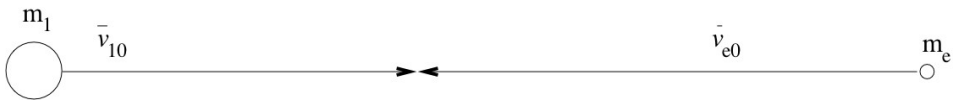

Figure D.25: Head on collision with electron

Energy of $e^{-}s$ very near the Fermi surface: $E_F \approx 5eV$. Fermi velocity, v_F, is of the order of $v_\circ = 2.2 \cdot 10^8 \frac{cm}{s.}$. At these low energies, the velocity of the projectile ion is very much less than the Bohr (or Fermi) velocity. So $\vec{v}_{10}$ is a short vector compared to $\vec{v}_{e0}$. Also, at these velocities, only target electrons very near the Fermi level can be "ionized" (i.e. promoted to empty states). We're considering first the maximum possible energy transfer to a target electron. So the vector diagram should look more like Figure D.26.

Figure D.26: Maximum energy transfer to electron

In a head-on collision, the outgoing particles are collinear with the incoming particles. ∴we can ignore vector quantities, just keep track of magnitudes (Figure D.27).

Figure D.27: Vectors reduced to magnitudes due to head-on collisions being co-linear

1) Subtract velocity of CM:

$u = \frac{m_1}{m_1+m_e} v_{10} - \frac{m_e}{m_1+m_e} v_{e0} \approx v_{10} - \frac{m_e}{m_1} v_{e0}$ when $(m_e \ll m_1)$

$v_{10}^{cm} - v_{10} - \left(v_{10} - \frac{m_e}{m_1} v_{e0}\right) = \frac{m_e}{m_1} v_{e0}$

$v_{e0}^{cm} = -v_{eo} - \left(v_{eo} - \frac{m_e}{m_1} v_{e0}\right) = -v_{10} - \left(1 - \frac{m_e}{m_1}\right) v_{e0} \approx -\left(v_{10} + v_{e0}\right)$

2) CM interaction (velocities always anti-parallel; magnitudes don't change (Figure D.28).

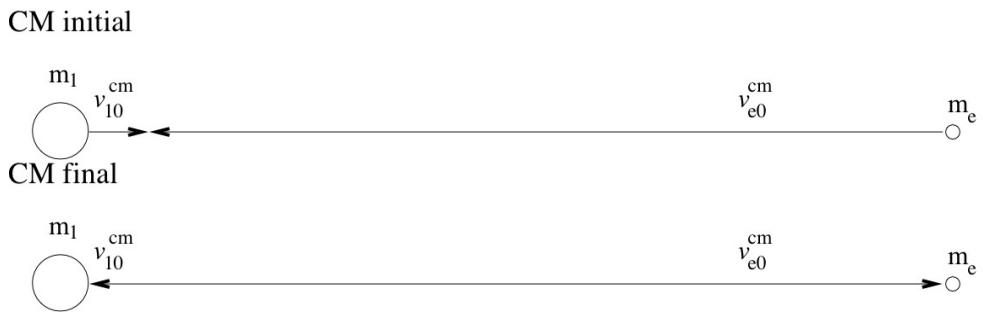

Figure D.28: Center of mass coordinate before and after collision

$v_{1f}^{cm} = -\frac{m_e}{m_1} v_{e0}$

$v_{ef}^{cm} = v_{10} + v_{e0}$

3) Add velocity of CM to convert to lab coordinates

$v_{1f} = -\frac{m_e}{m_1} v_{e0} + v_{10} - \frac{m_e}{m_1} v_{e0} = v_{10} - 2\frac{m_e}{m_1} v_{e0}$

$v_{ef} = v_{10} + v_{eo} + v_{10} - \frac{m_e}{m_1} v_{e0} = 2v_{10} + \left(1 - \frac{m_e}{m_1}\right) v_{e0} \approx 2v_1 + v_{e0}$

Calculate change in target electron velocity:

$\triangle v_e = v_{ef} - v_{e0} = 2v_{10} + v_{e0} - v_{e0}$

$\triangle v_e = 2v_{10}$

Calculate change in kinetic energy of target electron:

$T_0 = \frac{1}{2} m_e v_{e0}^2$

$T_f = \frac{1}{2} m_e \left(2v_{10} + v_{e0}\right)^2 = \frac{1}{2} m_e \left(4v_{10}^2 + 2v_{10}v_{e0} + v_{e0}^2\right)$

$\triangle T = T_f - T_0 = \frac{1}{2} m_e \left(4v_{10}^2 + 2v_{10}v_{e0}\right)$

$\triangle T \approx m_e v_{10} v_{e0}$ for $v_{10} \ll v_{eo}$

So, $\triangle v_e = 2v_{10}$ maximum

$\langle \triangle v_e \rangle \approx v_{10}$ average

Most metals supply one electron to the conduction band. $n_e^{cond} = \rho_a$ (ρ_a is the atomic density). But not all of these electrons can be excited to empty states. The effective electron concentration (available for "ionization") is:

$n_e^{eff} \approx \frac{\langle \triangle v_e \rangle}{v_F} n_e^{cond}$

$n_e^{eff} = \frac{v_{10}}{v_F} \rho_a$

Now, fix a coordinate system to the projectile ion m_1. m_1 "sees" a flux of target electrons impinging on it. This flux produces an electron "drag."

Electron drag on projectile ion:

$\left(-\frac{dE}{dx}\right)_e \left[\frac{eV}{\mathring{A}}\right] = \triangle E \left[\frac{eV}{e^-(scatt.event)}\right] \frac{I_e \left[\frac{e^-}{\mathring{A}^2 \cdot s}\right]}{v_{10} \left[\frac{\mathring{A}}{s}\right]} \sigma_e \left[\frac{\mathring{A}^2}{e^- \cdot scatt.events}\right]$ which gives (energy loss per second) per distance traveled per second.

Current of effective electrons (I_e):

$I_e = n_e u_{relative}$ where $u_{relative} = v_{10} + v_{e0}$ (coordinate system fixed on m_1)

$I_e = n_e \left(v_{10} + v_{e0}\right) \approx n_e v_{e0}$ for $v_{10} \ll v_{e0}$

Change in energy of projectile after scattering $(\triangle E)$:

$v_{1f} = v_{10} - \frac{2m_e}{m_1} v_{e0}$

$E_{1f} = \frac{1}{2} m_1 \left(v_{10} - \frac{2m_e}{m_1} v_{e0}\right)^2 = \frac{1}{2} m_1 \left(v_{10}^2 - 4\frac{m_e}{m_1} v_{10} v_{e0} + \left[4\left(\frac{m_e}{m_1}\right)^2 v_{e0}\right]\right)$

where $\left[4\left(\frac{m_e}{m_1}\right)^2 v_{e0}\right] \approx 0$ as $m_e \ll m_1$.

$E_{10} = \frac{1}{2} m_1 v_{10}^2$ and $\triangle E = E_{1f} - E_{10}$

$\triangle E = -2 m_e v_{10} v_{e0}$

$\left(\frac{-dE}{dx}\right)_e = \triangle E \frac{I_e}{v_{10}} \sigma_e = -2 m_e v_{10} v_{e0} \frac{n_e v_{e0}}{v_{10}} \sigma_e = -2 m_e v_{e0}^2 \sigma_e n_e = -2 m_e v_{e0}^2 \sigma_e \left(\frac{v_{10}}{v_F} \rho_a\right)$

$v_{e0} \approx v_F$

$\left(\frac{-dE}{dx}\right)_e = -2\sigma_e \rho_a v_F v_{10}$ where $v_{10}$is velocity dependent stopping. But $v_{10} = \sqrt{\frac{2E}{m_1}} \Rightarrow \left(\frac{-dE}{dx}\right)_e = kE^{\frac{1}{2}}$. This is Lindhard-Scharff stopping [185].

(LSS)

$S_e(E) = \frac{1}{\rho}\left(-\frac{dE}{dx}\right)_e = k' E^{\frac{1}{2}}$

$S_{eij}(E) = 3.8455 \cdot 10^{-15} \frac{Z_i^{\frac{7}{6}} Z_j}{\left(Z_i^{\frac{2}{3}} + Z_j^{\frac{2}{3}}\right)^{\frac{3}{2}}} \sqrt{\frac{E[keV]}{m_i[amu]}} \left[\frac{eV \cdot cm^2}{atom}\right]$

D.1.2 LSS Theory: Energy-Partitioning

Goal: Calculate number of displacements per PKA =$\nu(E)$

Later on, $\nu(E)$ will be used alternatively to represent "damage energy"

D.1.3 One component derivation

Assume mono-atomic target, species *i*. Assume projectile same species *i*. $Z =$ atomic # target and projectile (Z_1 and Z_2).

$P_a(T, T+dT)$ =(probability of atomic collision within *dx*, with recoil between *T*, *T+dT*) = $\rho_a dx$ (projected atom density of "areal density")$d\sigma(E,T)$(differential cross-section for projectile energy E, to produce recoil energy T)

$P_e(T_e, T_e+dT_e)$ = (probability of electron scattering within *dx*, with electron recoil between $T_e, T_e+dT_e = \rho_a dx \underbrace{d\sigma_e(E,T_e)}$ (differential electron scattering cress-section projectile energy E producing ionized electron energy T_e.

$P_\circ$ = (probability in dx of no collision) = $1-\int_0^E P_a - \int_0^{\Lambda_e E} P_e = 1-\rho_a dx \int_0^E d\sigma(E,T) - \rho_a dx \int_0^{\Lambda_e} d\sigma(E.T_e) = 1-\rho(\sigma(E)+\sigma_e(E))$ where $\sigma(E)$ is the total nuclear cross-section and $\sigma_e(E)$ is the total electronic cross-section.

D.1.4 Conservation Law

$\nu(E) = \int_0^E [\nu(E-T)+\nu(T)] P_a + \int_0^{\Lambda_e E} \nu(E-T_e) P_e + P_\circ \nu(E)$

How to think about this:

Imagine that within *dx* only one thing can happen: PKA with energy E collides with atom and imparts a specific energy T to the recoil (Figure D.29).

Now two particles travel into slab *dx* adjacent to the initial slab. Each particle can displace atoms. One displaces a number $\nu(E-T)$, the other a number $\nu(T)$. Our conser-

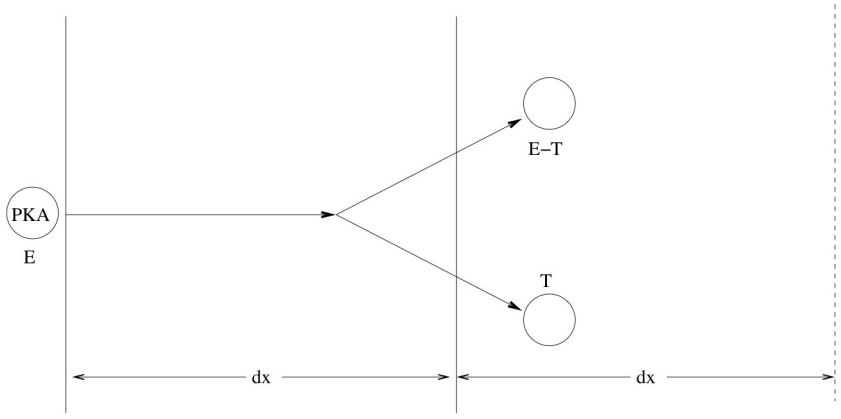

Figure D.29: Conservation of momentum between target atom and PKA

vation law assumes r $\nu(T)$ and $\nu(E-T)$ are independent and sum to the total number of displacements induced by the initial PKA, $\nu(E)$. So: $\nu(E) = \nu(E-T) + \nu(T)$.

Now imagine that only tow things can happen inside *dx*:

1. the previous atomic collision transferring energy T
2. an electron collision with energy transfer T_e

Assume the probabilities are P_a and P_e. Then, into the second slab, we either have 2 subsequent displacements $\nu(E-T)$ and $\nu(T)$; or we have one particle that produced subsequent displacements $\nu(E-T_e)$.

The first two must be weighted by P_a. The last quantity must be weighted by P_e. Then, by our conservation law:

$\nu(E) = \nu(E-T) + \nu(T)\,P_a + \nu(E-T_e)\,P_e$

Continue this reasoning for all possible scattering events and all recoil energies T, T_e and these sums become integrals and the conservation law is as written on the previous page.

Replacing probabilities with cross-sections:

$\nu(E) =$

$\rho_a dx \int_0^E [\nu(E-T) + \nu(T)]\, d\sigma(E,T) +$

$\rho_a dx \int_0^{\Lambda_e E} \nu(E-T_e)\, d\sigma_e(E,T_e) +$

$[1 - \rho_a dx(\sigma(E)) + \sigma_e(E)]\, \nu(E)$

$\nu(E)$ cancels on both sides and upon rearrangement, the areal density $\rho_a dx$ drops out:

$[\sigma(E) + \sigma_e(E)]\, \nu(E) =$

$\int_0^E [\nu(E-T) + \nu(T)]\, d\sigma(E,T) + \int_0^{\Lambda_e E} \nu(E-T_e)\, d\sigma_e(E,T_e)$

Now, we can simplify the second term on the right-hand side by observing that for atom-electron collisions energy transfer efficiency is very poor. $\Rightarrow T_e \ll E$

So we expand $\nu(E-T_e)$ in a Taylor's series and retain two terms.

$\nu(E-T_e) = \nu(E) - T_e \frac{d\nu}{dE}$ or $\nu(E) - T_e\nu'$ for $T_e \ll E$

$\therefore \int_0^{\Lambda_e E} \nu(E-T_e)\, d\sigma_e(E,T_e) =$

$\int_0^{\Lambda_e E} \nu(E)\, d\sigma_e(E,T_e) - \int_0^{\Lambda_e E} \nu' T_e d\sigma_e(E,T_e)$ as $\nu(E)$ and ν' have no T_e dependence.

$= \nu(E) \int_0^{\Lambda_e E} d\sigma_e(E,T_e) - \nu' \int_0^{\Lambda_e E} T_e d\sigma_e(E,T_e)$

But $\int_0^{\Lambda_e E} d\sigma_e(E,T_e) = \sigma_e(E)$ Total electronic stopping cross-section!!

and $\int_0^{\Lambda_e E} T_e d\sigma_e(E,T_e) = S_e(E) = \frac{1}{\rho}\left(\frac{dE}{dx}\right)_e$ Electronic stopping power!!

So, $\int_0^{\Lambda_e E} \nu(E-T_e)\, d\sigma_e(E,T_e) = \nu(E)\, \sigma_e(E - \nu' S_e(E))$

Substitute this back into the conservation equation.

$[\sigma(E) + \sigma_e(E)]\, \nu(E) = \int_0^E [\nu(E-T) + \nu(T)]\, d\sigma(E,T) + \sigma_e(E)\, \nu(E) - S_e(E)\, \nu'$

Rearranging:

$$\nu(E) + \frac{S(E)}{\sigma(E)} \quad \nu' \quad = \frac{1}{\sigma(E)} \int_0^E [\nu(E-T) + \nu(T)]\, d\sigma(E,T)$$

$$\Uparrow$$

$$\frac{d\nu}{dE}$$

This is the famous LSS *integrodifferential* equation.

Note: since $\int_0^E \nu(E)\, d\sigma(E,T)\, dT = \nu(E)\,\sigma(E)$ the LSS-ID equation is often rewritten:

$\int_0^E [\nu(E-T) + \nu(T) - \nu(E)]\, d\sigma(E,T) - S_e(E)\,\nu' = 0$

Consider a *hard-sphere* interaction potential:

$d\sigma(E,T) = \frac{dT}{\Lambda E}\sigma(E)$ with a mono-atomic solid and self-ion giving $m_1 = m_2$ and $\Lambda = 1$

$\frac{d\sigma(E,T)}{\sigma(E)} = \frac{dT}{E}$

LSS-ID equation becomes:

$\nu(E) + \frac{S_e(E)\nu'}{\sigma(E)} = \frac{1}{E}\underbrace{\int_0^E [\nu(E-T) + \nu(T)]\, dT}$ If the integral is split into two parts, you discover that they are equal. Prove that:

$\int_0^E \nu(E-T)\, dT = \int_0^E \nu(T)\, dT$

Proof:

$\int_0^E \nu(E-T)\, dT$

Change of variables: Let

$$T' = E - T$$

$$dT' = -dT$$

$$T = 0 \quad \Rightarrow \quad T' = E$$

$$T = E \quad \Rightarrow \quad T' = 0$$

$\int_0^E \nu(E-T)\, dT = -\int_{T'=E}^{T'=0} \nu(T')\, dT' = \int_0^E \nu(T')\, dT'$

Q.E.D.

So the hard-sphere LSS-ID equation becomes:

$\nu(E) + \frac{S(E)}{\sigma(E)}\nu' = \frac{2}{E}\int_0^E \nu(T)\, dT$ *(for hard-sphere)*

D.1.5 Kinchin-Pease (KP) approximation:

Kinchin and Pease made two important assumptions:

1. two-body interactions are hard sphere

2. electronic stopping is ignored below E_c

Inserting assumption 2. into our hard sphere LSS-ID equation ($S_E(E) = 0$), we find

$\nu(E) = \frac{2}{E}\int_0^E \nu(T)\,dT$ for hard-sphere

Trick! Multiply this equation by E and then differentiate both sides with respect to E:

$E\nu(E) = 2\int_0^E \nu(T)\,dT$

$\frac{d}{dE}(E\nu) = 2\frac{d}{dE}\int_0^E \nu(T)\,dT$

$\nu(E)\frac{dE}{dE} + E\frac{d\nu}{dE} = 2\int_0^E d\nu(T)\frac{dT}{dE}$ but $\frac{dE}{dE} \Rightarrow 0$ and $\frac{dT}{dE} \Rightarrow 0$

$E\nu' = 2\nu(E) - \nu(E)$

$E\frac{d\nu}{dE} = \nu$ Solve this differential equation

$\frac{d\nu}{\nu} = \frac{dE}{E}$

$\int \frac{d\nu}{\nu} = \int \frac{dE}{E}$

$ln(\nu) = ln(E) + ln(C) = ln(CE)$

$\nu(E) = CE$ Solution

$\nu(E) = CE = \frac{2}{E}\int_0^E \nu(T)\,dT$

We can evaluate undetermined constant C, in a Kinchin-Pease sense, if we introduce the concept of a threshold displacement energy $\Rightarrow E_d$.

$0 < E < E_d : \nu(E) = 0$

Energy E is insufficient to generate even a single displacement.

$E_d \leq E \leq 2E_d$: $\nu(E) = 1$

This is the *replacement* collision regime: The PKA displaces one atom, but then runs out of energy to continue propagating through the lattice. It replaces the knock-on atom in the lattice and expends the remainder of its energy as heat.

So, by definition, at $E = 2E_d$

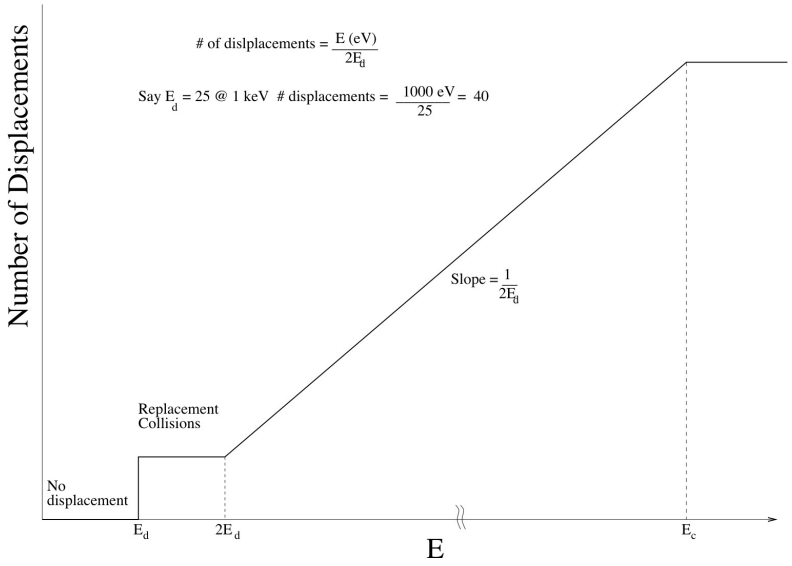

Figure D.30: KP displacement model

$\nu(E = 2E_d) = 1$ but $\nu(E) = CE$, so for $E = 2E_d : C2E_d = 1$

$C = \frac{1}{2E_d}$

So, finally we can write

$2E_d < E < E_c : E_c = \underset{(amu)}{M} \; [keV]$

$\nu(E) = \frac{E}{2E_d}$

Putting all the energy regimes together, we generate the Kinchin-Pease (K-P) displacement model (Figure D.30)

$\nu(E)$ = # of displacements.

Lindhard noted that $\nu(E)$ need not be interpreted as number of displacements/PKA. It could also represent energy transfer to, not displacement of, lattice atoms.

Then E_d need not enter the calculation. $\nu(E)$ increases continuously from $E = 0$ in $\nu(E) + \frac{S(E)}{\sigma(E)}\nu' = \frac{1}{\sigma(E)} \int_0^E [\nu(E - T) + \nu(T)] \, d\sigma(E, T)$, calling $\nu(E)$ the "damage" energy.

- $\nu(E)$ = energy transferred to lattice atoms in ballistic collisions
- $\eta(E) =$ electronic energy transfer
- $E = \nu(E) + \eta(E)$
- $\frac{\nu(E)}{E}$ is the fraction of the total energy expended on nuclear collisions $\equiv$ damage efficiency.

LSS used a Thomas-Fermi screened Coulomb potential to solve the damage energy integrodifferential equation, i.e.. $V(r) = \frac{K}{r}e^{-\frac{r}{a}} = \frac{Z_1 Z_2 e^2}{r}e^{-\frac{r}{a}}$

$a = \frac{\left(a\pi^2\right)^{\frac{1}{3}} 2^{\frac{7}{3}} a_B}{\sqrt{Z_1^{\frac{2}{3}}+Z_2^{\frac{2}{3}}}} = \frac{0.8853 a_B}{\sqrt{Z_1^{\frac{2}{3}}+Z_2^{\frac{2}{3}}}}$ Thomas-Fermi screening radius with a_B= Bohr radius $= 0.529\text{Å}$

LSS related this potential to a differential atomic scattering cross-section given by:

$d\sigma = \pi a^2 \frac{dT}{2t^{\frac{3}{2}}} f\left(t^{\frac{1}{2}}\right)$

$f\left(t^{\frac{1}{2}}\right)$ was called the universal scattering function *calculated numerically* (so this is not really an analytical formula).

- $t = \varepsilon^2 \frac{T}{T_m}$ and $T_m = \Lambda E$ with *E* = initial energy and *T* = recoil energy. $0 \leq T \leq T_m$
- $\Lambda = \frac{4 m_1 m_2}{(m_1+m_2)^2}$ the kinetic efficiency factor
- m_1 = mass of scattered particle
- m_2 = mass of recoiling particle
- $\varepsilon = \frac{m_2}{m_1+m_2} E \left(\frac{Z_1 Z_2 e^2}{a}\right)^{-1}$ the reduced energy (dimensionless)
- Z_1 = atomic number of scattered particle
- Z_2 = atomic number of recoiling particle

- a = screening radius
- $f\left(t^{\frac{1}{2}}\right)$ is a function that depends on the assumed form of the screening function
- $t^{\frac{1}{2}} \propto \hat{r}_{\circ}$ (distance of closest approach in a head–on (b = 0) collision)

Winterbon, Sigmund, and Sanders (WSS) (1970) [182], developed a now famous analytical approximation formula for the universal scattering function $f\left(t^{\frac{1}{2}}\right)$ WSS:

$f\left(t^{\frac{1}{2}}\right) = \frac{\lambda' t^{\frac{1}{6}}}{\left[1+\left(2\lambda' t^{\frac{2}{3}}\right)^{\frac{2}{3}}\right]^{\frac{3}{2}}}$ with $\lambda' = 1.309$

Lindhard, Nielsen, Scharff, and Thompson (1963) [186], developed a comprehensive formula for the damage energy:

$\nu(\varepsilon) = \frac{\varepsilon}{1+k\cdot g(\varepsilon)}$ with ε = reduced energy and k is the electronic stopping power proportionality factor.

$\left(\frac{dE}{dx}\right)_e = kE^{-\frac{1}{2}}$. $\nu(\varepsilon) = \frac{\varepsilon}{1+k\cdot g(\varepsilon)}$ is the reduced damage energy. $\nu(E) = \frac{\varepsilon}{1+k\cdot g(\varepsilon)}$ damage energy. k is the electronic stopping proportionality factor.

Universal function $g(\varepsilon)$:

Numerical approximation to $g(\varepsilon)$ introduced by Robinson of Norgett, Robinson, and Torrens (1975) [187, 188]:

$g(\varepsilon) = 3.4008\varepsilon^{\frac{1}{6}} + 0.40244\varepsilon^{\frac{3}{4}} + \varepsilon$ with ε = LSS reduced energy

NRT modified Kinchin-Pease formula:

$N_d = \left[\frac{displacements}{PKA}\right] = \xi\frac{\nu(E)}{2E_d}$ with $\xi =$ displacement efficiency factor ≈ 0.8 (Sigmund 1969).

Let $E_d = 40eV$ and $\xi = 0.8$

$N_d = \frac{\nu(E)[eV]}{2(40)[eV]}\left[\frac{displacements}{PKA}\right]$

$N_d = \frac{1}{100}\nu(E)\,[eV]$

or $\quad\quad$ $\left[\frac{displacements}{PKA}\right] \Rightarrow$ same as $\left[\frac{SKA}{PKA}\right]$

$N_d = 10\nu(E)\,[keV]$

LSS equation for damage energy $\nu(E)$

$$\int_0^E [\nu(E-T) + \nu(T) - \nu(E)]\,\sigma(E,T)\,dT - S_e(E)\,\nu' = 0$$

Assume *T* is small compared to E. Then, from a Taylor's expansion,

$$\nu(E-T) \approx \nu(E) - T \underbrace{\frac{d\nu}{dE}}_{\nu'}$$

Substitute into LSS we find:

$$\nu(E)\int_0^E \sigma(E,T)\,dT - \nu'(E)\underbrace{\int_0^E T\sigma(E,T)\,dT}_{X} +$$

($\nu(E)\int_0^E \sigma(E,T)\,dT$: $\nearrow$ $Cancel$!!!; $\nu'(E)\int_0^E T\sigma(E,T)\,dT$: $Cancel$!!! $\uparrow$)

$$\int_0^E [\nu(T) - \nu(E)]\,\sigma(E,T)\,dT - S_e(E)\,\nu' = 0$$

Where *X* is recognizable as the nuclear stopping power:

$S_n(E) = \frac{1}{N}\left(\frac{dE}{dx}\right)_n = \int_0^E T\sigma(E,T)\,dT$!!

$(S_n(E) + S_e(E))\,\nu' = \int_0^E \nu(T)\,\sigma(E,T)\,dT$

$d\nu(E) = \frac{dE}{S_n(E)+S_e(E)}\int_0^E \nu(T)\,\sigma(E,T)\,dT$

$$\nu(E) = \int_0^{E'} \underbrace{\frac{dE'}{S_n\left(E'\right) + S_e\left(E'\right)}}\int_0^{E'} \nu(T)\,\sigma\left(E',T\right)dT$$

In that $S\left(E'\right)$ =total stopping power.

This equation will even work for a projectile ion different from target ion *j* (mono-atomic target *j*), so long as expressions for the scattering cross-section and the stopping

powers can be written down:

$$\nu_i(E) = \int_0^{E'} \frac{dE'}{\underbrace{S_n^{ij}\left(E'\right) + S_e^{ij}\left(E'\right)}_{S_{ij}\left(E'\right)}} \int_0^{\Lambda_{ij}E'} \nu_j(T)\,\sigma_{ij}\left(E', T\right) dT$$

$$\nu_i(E) = \int_0^{E'} \frac{dE'}{S_{ij}\left(E'\right)} \Downarrow$$

We can get $\nu_j(T)$ from $\nu(T) = \frac{T}{1+k\cdot g(\varepsilon)}$ where $g(\varepsilon) = 3.4008\varepsilon^{\frac{1}{6}} + 0.40244\varepsilon^{\frac{3}{4}} + \varepsilon$.

D.1.6 Kinetic Rate Theory I

Computer simulation of interstitials, vacancies and interstitial clusters/loops as a function of irradiation time and for different damage rates.

[189, 190]

Radiation damage accumulation in many materials not susceptible of amorphization (e.g. metals, ceramics (ionic-bonding, non-covalently bonded materials), proceeds by defect accumulation. Microstructural changes $\Rightarrow$ introduction of dislocation loops, defect clusters, voids, bubbles, etc.

Material integrity and performance depends on rate of accumulation of extended defects.

Rates are dependent on mobilities of point defects: interstitials and vacancies.

During irradiation:

Point defect concentration is dependent on production rate of interstitials and vacancies.

Displacement damage produces Frenkel defects: Frenkel pair = interstitial + vacancy. The number of Frenkel pairs = $N_\circ\sigma\varphi t$ where $N_\circ$ is the atomic density $\left[\frac{atoms}{cm^3}\right]$, σ is the cross-section for atomic displacement $[cm^2]$, φ is the ion flux $\left[\frac{ions}{cm^2\cdot s}\right]$(ions, neutrons, electrons), and t is the irradiation time $[s]$.

Concentration of point defects:

- $C_i = conc.interstitials = \frac{N_i}{N_\circ}$
- $C_v = conc.vacancies = \frac{N_v}{N_\circ}$

By definition of Frenkel pair, assuming no other reactions, $C_i = C_v$.

Mobility of point defects.

- $M_i =$ mobility of interstitials
- $M_v =$ mobility of vacancies

Interstitials are mobile at low temperature, vacancies are mobile at high temperature.

Low Temperature Kinetic Rate Theory Models

Mobility of interstitials only.

P is the production rate of Frenkel pairs D

$\frac{dC_i}{dt} = P - [\ \underbrace{F\left(C_i, C_v, M_i\right)}$

(annihilation of interstitials due to i-v recombination)

$- \underbrace{G\left(C_i, C_s, M_i\right)}$

(annihilation of interstitials at *sinks*)

$- \underbrace{H\left(C_i, C_i, M_i\right)}$

(annihilation due to the formation of di-interstitials (nucleation of interstitial clusters))

$- \underbrace{J\left(C_i, C_L, C_{iL}, M_i\right)}\ ]$

(annihilation of interstitials at growing interstitial cluster/loops)

Aside 1

Comments on the Production rate (*P*)

The production rate should scale

1. as the number of lattice sites, $N_\circ$
2. as the magnitude of irradiating flux, ρ
3. as the "damage cross-section", σ

σ should be proportional to the damage energy, $\nu(E)$ (LSS) according to earlier lectures. And this should convert to number of Frenkel pairs (FP) per PKA, via the modified Kinchin-Pease, NRT (Norgett, Robinson, Torrens) equations:

$N_{NRT} = \frac{0.8\nu(E)}{2E_d}$ (# of Frenkel pairs per PKA)

But N_{NRT} represents the total number of point defects produced in the collisional phase of the cascade. Many of these do not survive beyond a few picoseconds.

One annihilation mechanism for these collisional phase point defects is the *Spontaneous Recombination Volume* (SRV) mechanism. If a vacancy defect and an interstitial defect (split interstitial above) are found with a few nearest neighbor distances of one another, they will spontaneously recombine (annihilate).

The production of a stable FP requires separating an interstitial atom from its vacancy suitably far to avoid spontaneous recombination. SRV determines the energy required for a displacement *and* the maximum concentration of defects that can me stored in a lattice. A mechanism for transporting interstitial atoms beyond the SRV is called the *Replacement Collision Sequence* (RCS) One atom replaces the next sequentially along a close-packed row. The RCS terminates with the last atom in the chain being ejected into an interstitial

site. At low energies, RCSs determine the cross-sections for creating FPs. Lengths of RCSs determine the probability that a defect can escape from its vacancy once it becomes mobile.

Defect Production Efficiency, ξ

$\xi(T) = \frac{\nu(T)}{\nu^{KP}(T)}$ and $\xi(T) = \frac{N_F}{N_{NRT}}$

where $\nu(T)$ is the surviving damage function and $\nu^{KP}(T)$ is the instantaneous function. N_F is the surviving defects and N_{NRT} is the instantaneous defects predicted from the modified Kinchin-Pease equation.

Damage efficiency $\Downarrow$ as $\Uparrow$

Light ions are much more effective at producing retained damage compared to heavy ions (in metals!). Defect production efficiency falls off very rapidly from unity with energy near the displacement energy, and approaches an asymptotic value $\xi \approx \frac{1}{3}$ at high energies.

Thermal spikes may explain the high energy effects (i.e. lost damage efficiency)

Aside 2

Important additional comments about interstitials, vacancies and FPs in metals.

In the absence of irradiation:

$\Rightarrow$ *Thermal Disorder*

Entropic introduction of equilibrium concentrations of point defects with $\Uparrow$ temperature. Many people often consider an interstitial atom as having been produced by the transfer of an atom from a normal site to an interstitial site, thus resulting in a one-to-one correspondence between the concentrations of vacancies and interstitials. *This is not the case!* The vacancy concentration need bear no relation to the concentration of interstitials, since the surface may act as a source or sink for vacancies. The vacancy concentration

varies with temperature according to:

$C_v = \frac{n_V}{N_\circ} = e^{\left(\frac{\triangle S_{fv}}{k}\right)} e^{\left(\frac{-\triangle H_{fv}}{kT}\right)}$

The interstitial concentration varies similarly:

$C_i = \frac{n_i}{N_\circ} = e^{\left(\frac{\triangle S_{fi}}{k}\right)} e^{\left(\frac{-\triangle H_{fi}}{kT}\right)}$

$\triangle S_v$ and $\triangle S_i$ are relatively small and can be neglected.

Atom(interior of crystal) = Atom(surface) $\triangle H_v$

Atom(surface) = Atom(interstitial) $\triangle H_{fi}$

For Cu:

$\frac{\triangle H_{fi}}{\triangle Hfv} \approx 7$

$\frac{C_v}{C_i} \approx e^{\left(\frac{\triangle H_{fi} - \triangle H_{fv}}{kT}\right)}$ At 1000 K $\frac{C_v}{C_i} \approx 10^{39}$!!

Thermal disorder can be attributed to vacancies (This should not be surprising for close-packed metals-interstices in the lattice aren't very big). The concept of vacancy-induced thermal disorder was first proved in a famous experiment by Simmons and Baluffi [191]: The volume thermal expansion coefficient, α, of a crystal can be written:

$\alpha = \frac{\left(\frac{\delta V}{V}\right)}{\delta T} = 3\frac{\left(\frac{\delta l}{l}\right)}{\delta T}$

It is also proportional to $3\frac{\triangle a}{a}$ where *a* is a reference lattice parameter *but* $3\frac{\triangle a}{a}$ is not necessarily equal to $3\frac{\triangle l}{l}$. From an elastic model, one can deduce changes in total volume *V* and lattice parameter *a* due to atomic concentrations $C_i$and/or $C_v$of interstitials and vacancies:

$\left(\frac{\triangle V}{V}\right)_i = 3\left(\frac{\triangle l}{l}\right)_i = 3\left(\frac{\triangle a}{a}\right)_i - C_i$

$\left(\frac{\triangle V}{V}\right)_v = 3\left(\frac{\triangle l}{l}\right)_v = 3\left(\frac{\triangle a}{a}\right)_v + C_v$

The corrective terms C_i and C_v take into account the fact that the interstitial atom is removed from the surface and placed in the bulk, while to create the vacancy, an atom is removed (subtracted) from the bulk and placed (added) on the surface. These equations show that when point defects are created, the expression $\left(\frac{\triangle V}{V}\right) - 3\left(\frac{\triangle a}{a}\right)$ should be *positive*

for vacancies and *negative for interstitials*. The Simmons-Baluffi result here proves that thermal disorder is due to vacancies. From their results, estimates of C_v at the melting point are:

$Al\,(T = T_m) : C_v = 9.4 \cdot 10^{-4}$

$Ag\,(T = T_m) : C_v = 1.7 \cdot 10^{-4}$

But under irradiation conditions we produce an athermal, non-equilibrium, population of interstitials that greatly exceeds the thermal equilibrium concentration. Even though the formation energy for the interstitial is large, the kinetic energies involved in ballistic collisions greatly exceed this formation energy.

In Cu:

$E_{fi} = 4 - 5eV\ E_{mi} = 0.05 - 0.25eV$

$E_{fv} = 1 - 1.5eV\ E_{mv} = 0.8 - 1.2eV$

Note that interstitials are much more mobile than vacancies despite the fact that $E_{fv} < E_{fi}$. This is because $E_{mi} \ll E_{mv}$. This can be understood quantitatively from the fact that in close-packed metals, interstitials are nowhere very stable, thus need less energy to break through to a neighboring equilibrium site.

Mobility Proportional to Diffusivity

$D = \delta^2 \nu e^{\frac{\triangle S_f + \triangle S_m}{k}} e^{\frac{-\left(\triangle H_f + \triangle H_m\right)}{kT}}$

δ is the jump distance and ν is the vibrational frequency, usually take as Debye frequency $\nu \approx 10^{13} - 10^{14} s^{-1}$.

Einstein formula for random walk diffusing from point source:

$D = \frac{1}{6}\Gamma\delta^2\,[time^{-1}]\,[length^2] = \left[\frac{cm^2}{s}\right]$ Γ is the jump frequency

fcc metal at T_m (self-diffusion):

$D \approx 10^{-8}\frac{cm^2}{s}$

$\delta \approx 10^{-8} cm$

$\Gamma = 6 \cdot \frac{10^{-8}}{10^{-16}} = 6 \cdot 10^{8} s^{-1}$ or $\approx$ 100 million jumps per second. But! Only one jump every 10^{5} oscillations, even at the melting point.

Yoshida and Kiritani:

Equation 3:

$\frac{dC_i}{dt} = P\left(1 - C_v\right)\left(1 - Z_1 C_v\right) - \left(Z_1 M_i C_v C_i\right) - M_i C_s C_i - 2 Z_2 M_i C_i^2 - Z_3 M_i \left(C_{iL} C_L\right)^{\frac{1}{2}} C_I$

Can we derive this?

I. Assume no sinks are available for point defect annihilation.

$i - v$ pairs are created at rate: $P = \sigma\rho$

Turn on flux ρat *t* = 0. For small *t*:

$\frac{dN_i}{dt} = \frac{dN_v}{dt} = N_\circ P$

$dN_i = N_\circ P dt$

$\int dN_i = N_\circ P \int dt$

$N_i = 0$ @ $t = 0 \Rightarrow c = 0$

$N_i\left(t\right) = N_\circ P t = N_\circ \sigma \rho t = N_v\left(t\right)$

II. As N_i and N_v increase the number of occupied atomic sites at which primary damage (Frenkel pair formation) can take place decreases. The number of available sites in the lattice at any time *t* is given by:

$N_\circ - N_v\left(t\right)$

The probability of hitting an undisturbed lattice site is given by:

$\frac{N_\circ - N_v}{N_\circ} = 1 - C_v$ where $C_v = \frac{N_v}{N_\circ}$

Multiply this probability by $N_\circ$ to find the revised formation rate of *i-v* pairs.

$\frac{dN_i}{dt} = \frac{dN_v}{dt} = \left(1 - C_v\right) N_\circ P$ or $\frac{dC_i}{dt} = \frac{dC_v}{dt} = \left(1 - C_v\right) P$

Since $C_i = C_v$ at any time *t*:

$\frac{dC_i}{1 - C_i} = P dt$

$-\frac{d(1-C_i)}{1-C_i} = Pdt$

$-\int dln\,(1-C_i) = P\int dt$

$-ln\,(1-C_i) = Pt + c\; C_i = 0\ @\ t = 0 \Rightarrow c = 0$

$1 - C_i = e^{-Pt}$

$C_i\,(t) = 1 - e^{-Pt} = C_v\,(t)$

t_e is the characteristic time associated with *i-v* saturation.

$C_i = 1 - e^{-\frac{t}{t_e}}$

$t_e = \frac{1}{P} = \frac{1}{\sigma\rho}$

This exponential dependence of *i-v* concentration is good for large *t*.

III. Athermal or low-T instantaneous annihilation of interstitials

An interstitial, upon birth, can be annihilated by a pre-existing lattice vacancy in the near vicinity of the newly-born interstitial.

If a pre-existing vacancy and a newly-born interstitial cohabitate a volume V_1 containing Z_1atomic sites, they will instantaneously recombine with an efficiency of unity, $\eta_1 = 1$.

- # of sites in lattice affected by recombination mechanism $= Z_1 N_v$
- probability that an interstitial, upon birth, resides within a recombination volume $= \frac{Z_1 N_v}{N_\circ} = Z_1 C_v$.
- probability that an interstitial, upon birth, does *not* reside wit a recombination volume $= 1 - Z_1 C_v$

Modified interstitial creation rate

$\frac{dN_i}{dt} = \underbrace{(1 - Z_1 C_v)}\,(1 - C_v)\,N_\circ P$

This probability modifies the creation rate as a prefactor.

$\frac{dC_i}{dt} = (1 - Z_1 C_v)(1 - C_v) P$

This is also the modified vacancy creation rate. $\frac{dC_V}{dt} = (1 - Z_1 C_v)(1 - C_v) N_\circ P$.

Also, assuming no other interstitial sinks, we have $C_i = C_v$

and $\therefore \frac{dC_i}{dt} = (1 - Z_1 C_i)(1 - C_i) P$.

Solve by separation of variables:

$\frac{dC_i}{(1-C_i)(1-Z_1 C_i)} = Pdt$

$g(y)\, dy = f(t)\, dt$

$\int g(y)\, dy = \int f(t)\, dt + \tilde{c}$

$\int \frac{dy}{(a+by)(c+dy)} = Pt + \tilde{c}$

let $y = C_i$, $a = 1$, $b = -1$, $c = 1$, $d = -Z_1$

$\int \frac{dy}{u \cdot v}$ where $u = a + by$ and $v = c + dy$

Integral tables:

$\int \frac{dy}{u \cdot v} = \frac{1}{k} ln\left(\frac{v}{u}\right)$ with $k = ad - bc = -Z_1 - (-1) = 1 - Z_1$

$ln\left(\frac{v}{u}\right) = ln\left(\frac{c+dy}{a+by}\right) = ln\left(\frac{1-Z_1 C_i}{1-C_i}\right)$

$\frac{1}{1-Z_1} ln\left(\frac{1-Z_1 C_i}{1-C_i}\right) = Pt + \tilde{c}$

$\frac{1-Z_1 C_i}{1-C_i} = e^{\tilde{c}(1-Z_1)} e^{(1-Z_1)Pt}$

@ $t = 0$ and $C_i = 0 \Rightarrow 1 = e^{\tilde{c}(1-Z_1)}$. For arbitrary Z_1, must have $\tilde{c} = 0$.

$\frac{1-Z_1 C_i}{1-C_i} = e^{(1-Z_1)Pt}$

$1 - Z_1 C_i = e^{(1-Z_1)Pt} - C_i e^{(1-Z_1)Pt}$

$\left(e^{(1-Z_1)Pt} - Z_1\right) C_i = e^{(1-Z_1)Pt} - 1$

$C_i(t) = \frac{e^{(1-Z_1)Pt} - 1}{e^{(1-Z_1)Pt} - Z_1}$

For $Z_1 = 0$ (no instantaneous recombination)

$Z_1 \to 0$

$C_i(t) = \frac{e^{Pt} - 1}{e^{Pt}} = 1 - \underbrace{e^{-Pt}}$

$e^{-Pt}$from solution from part II.

So we found the solution of $\frac{dC_i}{dt} = (1 - C_i)(1 - Z_1 C_i) P$ is $C_i(t) = \frac{e^{-(Z_1+1)Pt} - 1}{e^{-(Z_1+1)Pt} - Z_1}$

We should note that when $C_i$is small the differential equation can be approximated as follows.

$\frac{dC_i}{dt} = (1 - C_i)(1 - Z_1 C_i) P = (1 - C_i - Z_1 C_i + Z_1 C_i^2) P =$

$(1 - (1 + Z_1) C_i + Z_1 C_i^2) P$

But for $C_i \ll 1$, $Z_1 C_i^2 \ll (1 + Z_1) C_i$ So we can write:

$\frac{dC_i}{dt} \approx (1 - (1 + Z_1) C_i) P$

$\frac{dC_i}{1-(1+Z_1)C_i} = Pdt$

$dln(1 - (1 + Z_1) C_i) = \frac{(1+Z_1)dC_i}{1-(1+Z_1)C_i}$

$-\frac{1}{1+Z_1} \int_{C_i(t=0)}^{C_i} dln(1 - (1 + Z_1) C_i) = P \int_0^t dt$

$-\frac{1}{1+Z_1} ln(1 - (1 + Z_1) C_i) = pt$

$1 - (1 + Z_1) C_i = e^{-(1+Z_1)Pt}$

$C_i \approx \frac{1}{(1+Z_1)} \left(1 - e^{-(1+Z_1)Pt}\right)$ for small C_i

$C_v = C_i = \frac{1}{(1+Z_1)} \left(1 - e^{-(1+Z_1)Pt}\right)$

D.1.7 Chemical Rate Theory

Summary of results to date:

Production rate of Frenkel Pairs (FP) in electron irradiated experiments:

$P \approx 10^{-4} s^{-1}$

Rate of FP production in neutron irradiation much lower:

$P \approx 10^{-7} s^{-1}$

This is why ion and electron experiments are called “accelerated damage” or accelerated aging: experiments.

Point Defect Mobilities ($M_{i,v}$ or $\Gamma_{i,v}$)

The jump frequency scales as $\Gamma_{i,v} = \nu_\circ e^{-\frac{E_{m(i,v)}}{kT}}$ where $E_{m(i,v)}$ is the activation energy for migration for interstitials or vacancies, respectively.

$\nu_\circ$ is taken as the Debye frequency $\nu_\circ \approx 10^{13} s^{-1}$

★ Don't need formation energies in radiation damage problems.

Yoshida-Kiritani give $E_{m(i,v)}$ for Au:

$E_{mi} = 0.15eV$

$E_{mv} = 0.70eV$

Interstitials much more mobile than vacancies (10^{10} vs.10^2 at 300K)

T = 0 K Solutions

1. No mobility of point defects

2. $C_i = C_v$ always

General solution:

$C_i(t) = \frac{e^{(1-Z_1)Pt}-1}{e^{(1-Z_1)Pt}-Z_1}$ 1)

Z_1 is the spontaneous *i-v* recombination volume (SRV) (in units of # of lattice sites) ≡"cross-section" for *i-v* annihilation.

For small C_i, 1) becomes $C_i = \frac{1}{1+Z_1}\left(1 - e^{-(1+Z_1)Pt}\right)$ 2)

For $Z_1 = 0$, 1) becomes $C_i = 1 - e^{-Pt}$ 3)

Aside: This page has been corrected from previous notes. I had this equation written wrong.

So we found the solution of $\frac{dC_i}{dt} = (1 - C_i)(1 - Z_1 C_i) P$ is $C_i(t) = \frac{e^{(1-Z_1)Pt} - 1}{e^{(1-Z_1)Pt} - Z_1}$.

We should note that when C_i is small the differential equation can be approximated as follows:

$\frac{dC_i}{dt} = (1 - C_i)(1 - Z_1 C_i) P =$

$(1 - C_i - Z_1 C_i + Z_1 C_i^2) P = (1 - (1 + Z_1) C_i + Z_1 C_i^2) P$

But for $C_i \ll 1$, $Z_1 C_i^2 \ll (1 + Z_1) C_i$.

So we can write:

$\frac{dC_i}{dt} \simeq (1 - (1 + Z_1) C_i) P$

$\frac{dC_i}{1-(1+Z_1)C_i} = Pdt$

$dln(1 - (1 + Z_1) C_i) = \frac{-(1+Z_1)dC_i}{1-(1+Z_1)C_i}$

$-\frac{1}{1+Z_1} \int_{C_i(t=0)}^{C_i} dln(1 - (1 + Z_1) C_i) = P \int_0^t dt$

$-\frac{1}{1+Z_1} ln(1 - (1 + Z_1) C_i) = Pt$

$1 - (1 + Z_1) C_i = e^{-(1+Z_1)Pt}$

so $C_i \simeq \frac{1}{(1+Z_1)} \left(1 - e^{-(1+Z_1)Pt}\right)$ for small C_i.

$C_v = C_i = \frac{1}{(1+Z_1)} \left(1 - e^{-(1+Z_1)Pt}\right)$

$P \approx 10^{-4}$ $Z_1 \approx 10^2$ $t_0 \approx \frac{1}{PZ_1} = \frac{1}{10^{-2}} = 100$

Let $Z_1 = 100$ and $P = 10^{-4}$

Equation 2) becomes $C_i = \frac{1}{101} \left(1 - e^{-\frac{101t}{10^4}}\right)$

Log-Log vs. Linear-Linear plots

Concentration saturates in $10^3 s$ at $C_i \approx 10^{-2}$

General solution: Equation 1)

$C_i(t) = C_v(t) = \frac{e^{(1-Z_1)Pt} - 1}{e^{(1-Z_1)Pt} - Z_1}$

The larger Z_1 (the SRV) the lower the saturation concentration of the FPs (steady-state value) and the faster steady-state is reached. The general solution only really applies for $Z_1 > 1$, C_i is undefined.

T > 0K Solutions

1) Mobilities of point defects are finite.

$\Gamma_i \gg \Gamma_v > 0$

2) $C_i = C_v$

★ This is only true when you only allow *i-v* recombination as a point defect annihilation mechanism.

In this case,

$C_i(t) = C_v(t) = \frac{e^{\sqrt{-q}t} - 1}{\frac{s}{r-\sqrt{-q}}\left(e^{\sqrt{-q}} - \frac{r-\sqrt{-q}}{r+\sqrt{-q}}\right)}$

where:

- $q = -4Z_1 P\Gamma - (1 + Z_1)^2$
- $r = (1 + Z_1) P$
- $s = 2Z_1 (P - \Gamma)$
- $\Gamma = \Gamma_i + \Gamma_v \approx \Gamma_i$
- $P = 10^{-4} s^{-1}$
- $Z_1 = 100$
- $\Gamma_i = 10^{10} s^{-1}$
- $\Gamma_v = 10^2 s^{-1}$

Both Γ's are good for $T \approx 300K$.

Note that $C_i = C_v$reaches an extremely small saturation concentration. $C_i \approx 10^{-8}$ and reaches steady-state in an extremely short time $\approx 10^{-3}s$. Turning on defect mobility has a huge effect on CRT.

IV

The next level of complication is to also allow interstitials and vacancies to move around in the crystal.

In moving, there are two possibilities: Interstitials can annihilate with vacancies or vice versa, as they meet one another.

IVa

Let's take one possibility at a time. Let's assume moving interstitials can annihilate with vacancies, whenever they enter a volume V_1 containing Z_1 sites where a vacancy resides.

Assume the jump frequency of an interstitial is given by $\Gamma_i = \nu e^{\frac{-E_m^i}{kT}}$ where $E_m^i =$ migration energy of the interstitial and $\Gamma_i =$the number of sites visited by a single, random-walking interstitial per unit time. Then, the fraction of sites in the lattice visited by interstitials per unit time is $\frac{\Gamma_i N_i}{N} = \Gamma_i C_i$.

But $Z_1 N_v$ of these N sites are unstable sites for interstitials, so as each interstitial walks it will be annihilated with each new step with a probability of $\frac{Z_1 N_v}{N} = Z_1 C_v$. So the annihilation rate of interstitials due to there motion is $Z_1 \Gamma_i C_v C_i$. So the modified rate of interstitials is:

$\frac{dC_i}{dt} = (1 - C_i)(1 - Z_1 C_i) P - Z_1 \Gamma_i C_v C_i$

Similarly, since we've introduced no mechanisms that violate this assumption, we are free to set $C_i = C_v$ so that

- $\frac{dC_i}{dt} = (1 - C_i)(1 - Z_1 C_i) P - Z_1 \Gamma_i C_v C_i$
- $\frac{dC_v}{dt} = (1 - C_v)(1 - Z_1 C_v) P - Z_1 \Gamma_i C_v C_i$ everywhere C_i and C_v are interchangeable.

★ Note! Because $Z_1 \Gamma_i$is so large compared to $Z_1 P$ (ordinarily), most authors just reduce the first term to P. This is because the the second annihilation term completely dominates the $(1 - Z_1 C_v)$ effects. [So, you never see the saturation predicted by the first term - you never even get close by many orders of magnitude]

Solve the new differential equation analytically:

$\frac{dC_i}{dt} = (1 - C_i)(1 - Z_1 C_i) P - Z_1 \Gamma_i C_v C_i = (1 - C_i)(1 - Z_1 C_i) P - Z_1 \Gamma_i \underbrace{C_i^2}$ (*key* substitution)

$\frac{dy}{dx} = (1 - y)(1 - \alpha y)\beta - \gamma y^2 = (1 - y - \alpha y + \alpha y^2)\beta - \gamma y^2 = \beta - (1 + \alpha)\beta y +$

$\alpha = Z_1$

$\alpha\beta y^2 - \gamma y^2$ Here, $\beta = P$

$\gamma = Z_1 \Gamma_i$

$\frac{dy}{dx} = \beta - \delta y + \epsilon y^2$ With $\delta = (1 + \alpha)\beta$

$\epsilon = \alpha\beta - \gamma$

$\int \frac{dy}{\beta - \delta y + \epsilon y^2} = \int dx$

CRC integration tables A-119 #109 [78]: Forms containing $a+by+cy^2$, $Y = a+by+cy^2$ and $q = 4ac - b^2$

- $\int \frac{dy}{Y} = \frac{2}{\sqrt{q}} tan^1 \left(\frac{2cy+b}{\sqrt{q}} \right)$ for $q > 0$
- $\int \frac{dy}{Y} = \frac{-2}{\sqrt{-q}} tanh^{-1} \left(\frac{2cy+b}{\sqrt{-q}} \right)$ or $\frac{1}{\sqrt{-q}} ln \left(\frac{2xy+b-\sqrt{-q}}{2cy+b+\sqrt{-q}} \right)$ for $q < 0$

If $q = 0$, there are different integral forms.

In our example:

$q = 4ac - b^2 = 4\beta\epsilon - \delta^2 = 4P(\alpha\beta - \gamma) - (1-\alpha)^2\beta^2 = 4P(Z_1P - Z_1\Gamma_i) - (1+Z_1)^2P^2$

- $= 4Z_1P^2 - 4Z_1P\Gamma_i - (1 + 2Z_1 + Z_1^2)P^2$
- $= 4Z_1P^2 - P^2 - 2Z_1P^2 - Z_1^2P^2 - 4Z_1^2P\Gamma_i = 2Z_1P^2 - (1+Z_1^2)P^2 - 4Z_1P\Gamma_i$
- $= (-1 + 2Z_1 + Z_1^2)P^2 - 4Z_1P\Gamma_i$
- $= (1 - Z_1)(Z_1 - 1)P^2 - 4Z_1P\Gamma_i$

Take $P = 10^{-4}$, $Z_1 = 10^2$ and $\Gamma_i = 10^{10}$, then

$q = (1 - 10^2)(10^2 - 1)10^{-8} - 4 \cdot 10^2 \cdot 10^{-4} \cdot 10^{10}$

$\approx -10^{-4} - 4 \cdot 10^8$

$\approx -4 \cdot 10^8$

So, q is a huge negative quantity in our problem, with little possibility that we can change this result by variation of parameters.

We will use the logarithm form of the solution.

$$\int \frac{dy}{Y} = \frac{1}{\sqrt{-q}} ln\left(\frac{2xy+b-\sqrt{-q}}{2cy+b+\sqrt{-q}}\right) \text{ with } \begin{array}{ll} a = \beta & \alpha = Z_1 \\ b = -\delta & \beta = P \\ c = \epsilon & \gamma = Z_1\Gamma_i \\ & \delta = (1-\alpha)\beta \\ & \epsilon = \alpha\beta - \gamma \end{array} \text{ and}$$

$q = (1 - Z_1)(Z_1 - 1)P^2 - 4Z_1P\Gamma_i$

$-q = 4Z_1P\Gamma_i + (1 - Z_1)(1 - Z_1)P^2$

$-q = 4Z_1P\Gamma_i + (1 - Z_1)^2P^2$

$\frac{1}{\sqrt{-q}} ln\left(\frac{2\epsilon y+(-\delta)-\sqrt{-q}}{2\epsilon y+(-\delta)+\sqrt{-q}}\right)$
$\frac{1}{\sqrt{-q}} ln\left(\frac{2(\alpha\beta-\gamma)y-(1+\alpha)\beta-\sqrt{-q}}{2(\alpha\beta-\gamma)y-(1+\alpha)\beta+\sqrt{-q}}\right)$
$\frac{1}{\sqrt{-q}} ln\left(\frac{2(Z_1P-Z_1\Gamma_i)-(1+Z_1)P-\sqrt{-q}}{2(Z_1P-Z_1\Gamma_i)-(1+Z_1)P+\sqrt{-q}}\right)$
$\frac{1}{\sqrt{-q}} ln\left(\frac{2Z_1(P-\Gamma_i)y-(1+Z_1)P-\sqrt{-q}}{2Z_1(P-\Gamma_i)y-(1+Z_1)P+\sqrt{-q}}\right)$

We used *s* earlier, but for now we will use $\wp$.

$\wp = 2Z_1\left(P-\Gamma_i\right)$ and $r = (1+Z_1P)$

Then we have :

$\frac{1}{\sqrt{-q}} ln\left(\frac{\wp C_i-r-\sqrt{-q}}{\wp C_i-r+\sqrt{-q}}\right) = t+k$
$\left(\frac{\wp C_i-r-\sqrt{-q}}{\wp C_i-r+\sqrt{-q}}\right) = e^{\sqrt{-q}k}e^{\sqrt{-q}t}$

boundary conditions $C_i = 0$ @ $t = 0$

$e^{\sqrt{-q}k} = \frac{-r-\sqrt{-q}}{-r+\sqrt{-q}}$
$k = \frac{1}{\sqrt{-q}} ln\left(\frac{-r-\sqrt{-q}}{-r+\sqrt{-q}}\right)$
$\frac{\wp C_i-r-\sqrt{-q}}{\wp C_i-r+\sqrt{-q}} = e^{\sqrt{-q}\frac{1}{\sqrt{-q}} ln\left(\frac{-r-\sqrt{-q}}{-r+\sqrt{-q}}\right)}e^{\sqrt{-q}t} = e^{ln\left(\frac{-r-\sqrt{-q}}{-r+\sqrt{-q}}\right)}e^{\sqrt{-q}t}$
$\frac{\wp C_i-r-\sqrt{-q}}{\wp C_i-r+\sqrt{-q}} = e^{ln\left(\frac{-r-\sqrt{-q}}{-r+\sqrt{-q}}\right)}e^{\sqrt{-q}t}$
$\frac{\wp C_i-(r+\sqrt{-q})}{\wp C_i-(r-\sqrt{-q})} = e^{ln\left(\frac{r+\sqrt{-q}}{r-\sqrt{-q}}\right)}e^{\sqrt{-q}t}$

$$a = \wp$$

$\frac{ay-b}{ay-d} = f\left(x\right)$ $\quad b = r+\sqrt{-q}$

$$d = r-\sqrt{-q}$$

$$f\left(x\right) = \frac{r+\sqrt{-q}}{r-\sqrt{-q}}e^{\sqrt{-q}t}$$

$ay-b = af\left(x\right) - df\left(x\right)$

$y = f\left(x\right)y - \frac{d}{a}f\left(x\right) + \frac{b}{a}$

$\left(1-f\left(x\right)\right)y = -\frac{d}{a}f\left(x\right) + \frac{b}{a}$

$y = \frac{-\frac{d}{a}f(x)+\frac{b}{a}}{1-f(x)}$

$C_i = \frac{-\frac{r-\sqrt{-q}}{\wp}\frac{r+\sqrt{-q}}{r-\sqrt{-q}}e^{\sqrt{-q}t}+\frac{r+\sqrt{-q}}{\wp}}{1-\frac{r+\sqrt{-q}}{r-\sqrt{-q}}e^{\sqrt{-q}t}} = \frac{-\frac{r+\sqrt{-q}}{\wp}e^{\sqrt{-q}t}+\frac{r+\sqrt{-q}}{\wp}}{1-\frac{r+\sqrt{-q}}{r-\sqrt{-q}}e^{\sqrt{-q}t}} = \frac{-\frac{1}{\wp}\left(e^{\sqrt{-q}t}-1\right)}{1-\frac{1}{r-\sqrt{-q}}\left(e^{\sqrt{-q}t}-\frac{r-\sqrt{-q}}{r+\sqrt{-q}}\right)}$

$C_i = \frac{e^{\sqrt{-q}t}-1}{\frac{\wp}{r-\sqrt{-q}}\left(e^{\sqrt{-q}t}-\frac{r-\sqrt{-q}}{r+\sqrt{-0q}}\right)}$

Remember that $\wp$ was called *s* earlier in the notes.

$-q = 4Z_1 P\Gamma_i + (1 - Z_1)^2 P^2$

$\wp = 2Z_1 (P - \Gamma_i)$

$r = (1 + Z_1) P$

If we turn off the mobility of interstitials, i.e., $\Gamma_i = 0$, this expression must reduce to the result of part III, namely

$C_i = \frac{e^{(1-Z_1)Pt}-1}{e^{(1-Z_1)Pt}-Z_1}$ For $\Gamma_i = 0$, $-q = (1 - Z_1)^2 P^2$ with $\sqrt{-q} = (1 - Z_1) P$, $\wp = 2Z_1 P$, $r = (1 + Z_1) P$

$$C_i = \frac{e^{(1-Z_1)Pt}-1}{\frac{\frac{2Z_1P}{\underbrace{(1+Z_1)P-(1-Z_1)P}_{P+Z_1P-P+Z_1P}}}{2Z_1P}\left(e^{(1-Z_1)Pt}-\frac{\overbrace{(1+Z_1)P-(1-Z_1)P}^{2Z_1P}}{\underbrace{(1+Z_1)P+(1-Z_1)P}_{P+Z_1P+P-Z_1P}}\right)}$$

$$= \frac{e^{(1-Z_1)Pt}-1}{e^{(1-Z_1)Pt}-\frac{2Z_1P}{2P}}$$

$\therefore C_i = \frac{e^{(1-Z_1)Pt}-1}{e^{(1-Z_1)Pt}-Z_1}$ Yes! It works!

IVb

Now lets allow vacancy motion as well as interstitial motion and mutual annihilation. So we still have the condition $C_i = C_v$. This is the last level of complication we can go to which is completely soluble without reverting to numerical calculations. (because after this we will have the possibility of $C_i \neq C_v$, in which case we will have 2 simultaneous differential equations, one for $\frac{dC_i}{dt}$ and one for $\frac{dC_v}{dt}$).

Let $\Gamma_v = \nu e^{-\frac{E_m^v}{kT}}$ be the jump frequency of a vacancy.

Fraction of sites visited by vacancies: $\frac{\Gamma_v N_v}{N} = \Gamma_v C_v$

Probability of annihilation by walking: $\frac{Z_1 N_i}{N} = Z_1 C_i$

Annihilation rate of *vacancies* and *interstitials* due to vacancy $Z_1 \Gamma_v C_i C_v$

Modified rate equation for interstitial and vacancy motion and annihilation: (remembering that $C_i = C_v$)

$\frac{dC_i}{dt} = (1 - C_i)(1 - Z_1 C_i) P - Z_1 \Gamma_i C_i C_v - Z_1 \Gamma_v C_i C_v$

$\frac{dC_i}{dt} = (1 - C_i)(1 - Z_1 C_i) P - Z_1 (\Gamma_i + \Gamma_v) C_i C_v$

and since $C_i = C_v$

$\frac{dC_i}{dt} = \frac{dC_v}{dt} = (1 - C_i)(1 - Z_1 C_i) P - Z_1 (\Gamma_i + \Gamma_v) C_i^2$

So the same solution holds as in IVa except we can write $\Gamma = \Gamma_i + \Gamma_v$ in place of Γ_i.

$$-q = 4 Z_1 P \Gamma + (1 - Z_1)^2 P^2$$

$$\wp = 2 Z_1 (P + \Gamma)$$

$$r = (1 + Z_1) P$$

$$\Gamma = \Gamma_i + \Gamma_v$$

$C_v = \frac{e^{\sqrt{-q}t} - 1}{\frac{\wp}{r - \sqrt{-q}} \left(e^{\sqrt{-q}t} - \frac{r - \sqrt{-q}}{r + \sqrt{-q}} \right)}$ as

V

The next level of complication is to allow with the interstitial and vacancy motion the possibility that

a) interstitials can bind with other interstitials forming di-interstitials (nuclei of interstitial loops)

b) vacancies can bind with other vacancies forming di-vacancies (nuclei of vacancy loops/voids)

Let's take a) first

Va

Now, we can no longer assume $C_i - C_v$ because when two interstitials bind to form a di-interstitial, *two* interstitials are annihilated, but the vacancy concentration is unchanged.

We'll assume that di-interstitials are only formed by the migration of interstitials, not by the instantaneous creation mechanism of part III. We've already shown that this mechanism is completely swamped by the motion mechanism.

Imagine a volume V_2 encompassing a number of lattice sites Z_2 in which two interstitials combine with an efficiency $\eta_2 = 1$. The probability of annihilation of a moving interstitial by another interstitials in its vicinity is:

$\Gamma_i C_i Z_2$ such that:

- Γ_i is the number of sites visited by and interstitials per unit time
- C_i is the probability a given site is occupied by and interstitial
- Z_2 is the number of capture sites surrounding a given site
- the product $C_i Z_2$ is the probability that a given site is unstable for the survival of an interstitial

The formation rate is actually $\sqrt{2}$ time this product since the "rms relative jump rate" is required because both interstitials are in motion.

$\frac{dN_{ii}}{dt} = \left(\sqrt{2} Z_2 \Gamma_i C_i\right) N_i$ or $\sqrt{2} Z_2 \Gamma_i C_i^2$

We'll also assume that vacancy mobility is low again, so that we don't have to consider di-vacancy formation. So $\Gamma = \Gamma_i + \Gamma_v \approx \Gamma_i$

The annihilation rate of interstitials is twice the formation rate of di-interstitials, because two interstitials are used to create one di-interstitials. So instead of one differential equation, we have three simultaneous differential equations.

Notice here that we can no longer substitute $(1 - C_i)$ for ***C***

$\frac{dC_i}{dt} = (1 - C_v)(1 - Z_1 C_v) P - Z_1 \Gamma_i C_v C_i - 2\sqrt{2} Z_2 \Gamma_i C_i^2$

$\frac{dC_v}{dt} = (1 - C_V)(1 - Z_1 C_V) P - Z_1 \Gamma_i C_v C_i$

$\frac{dC_{ii}}{dt} = \sqrt{2} Z_2 \Gamma_i C_i^2$

So now we have 3 simultaneous equations, the analytic solution to which is unlikely to be found. But now we'll employ the Yoshida-Kiritani methods of finding an approximate formula for various regimes. the procedure goes something like this:

Because Γ_i is so high relative to other terms, the $(1 - C_i)(1 - Z_1 C_i)$ effect never has a chance to show its effect because the *i-v* annihilation mechanism totally dominates it with a much higher rate $Z_1 \Gamma_i C_v$ or for vacancies, $Z_1 \Gamma_i C_i$.

So we will approximate as follows :

$(1 - C_i)(1 - Z_1 C_i) P = (1 - (1 + Z_1) C_i + Z_1 C_i^2) P \approx P$ The same approximation holds for vacancies.

So, we'll rewrite the simultaneous differential equations as:

$\frac{dC_i}{dt} = P - (Z_1 \Gamma_i C_v) C_i - \left(2\sqrt{2} Z_2 \Gamma_i C_i\right) C_i$

$\frac{dC_v}{dt} = P - (Z_1 \Gamma_i C_i) C_v$

$\frac{dC_{ii}}{dt} = \frac{dC_L}{dt} = \sqrt{2} Z_2 \Gamma_i C_i C_i$

Now, we will work out approximate solutions at various times as follows:

At very small *t*, concentrations of *i* and *v* are so small that the annihilation terms can have no effect. So, interstitial and vacancy concentrations simply grow at a constant rate *P*.

At very small *t*: $C_i = Pt$ and $C_v = Pt$

Aside

For interstitials:

Notice that the i-v annihilation mechanism term has the following effects on C_i:

$\frac{dC_i}{dt} \propto -\left(Z_1 \Gamma_i C_v\right) C_i$

This is the well-known exponential population relation $C_i \propto e^{-\frac{t}{t_\circ}}$ where $t_\circ = \frac{1}{Z_1 \Gamma_i C_v}$. So, this tells us that the *i-v* annihilation mechanism has a characteristic time at which this mechanism kicks in. When is this?

Well C_v is a function of time, so this characteristic time is also a function of time.

$C_v = Pt$ so $t_\circ = \frac{1}{Z_1 \Gamma_i P t}$

for

$$Z_1 = 10^2$$

$$\Gamma_i = 10^{10}$$

$$P = 10^{-4}$$

$$Z_1 \Gamma_i P = 10^8$$

then $t_\circ = \frac{10^{-8}}{t}$

So at 10^{-8} seconds, $t_\circ = 1$second and at 1 second $t_\circ = 10^{-8}$ second. In one second, this characteristic rate for the *i-v* mechanism has changed by 8 orders of magnitude! So *i-v* annihilation is going to be an important mechanism within a very short time (due to the huge magnitude of Γ_i.

Because of the huge magnitude of Γ_i, when the *i-v* mechanism kicks in it will completely dominate the production rate, so that $\frac{dC_i}{dt} \Rightarrow 0$, i.e. the situation becomes production rate limited - the *i-v* mechanism is 100% efficient at eliminating any newly created *i-v* pairs.We'll assume that until this occurs the concentrations C_i and C_v rise linearly, but eventually $Z_1 \Gamma_i C_v C_i$ matches P.

$P = Z_1 \Gamma_i C_v C_i$, as $\frac{dC_i}{dt} \Rightarrow 0$. In fact, at this stage $C_i = C_v = Pt$

We can write $P = Z_1 \Gamma_i C_i^2$

So $C_i = \sqrt{\frac{P}{Z_1 \Gamma_i}}$. This is the maximum concentration C_i. This occurs at $Pt = \sqrt{\frac{P}{Z_1 \Gamma_i}}$, $t = \sqrt{\frac{1}{Z_1 \Gamma_i P}}$

Now, in our old model, at about $t = \sqrt{\frac{1}{Z_1\Gamma_i P}}$ both C_i and C_v would saturate at the concentration $\sqrt{\frac{P}{Z_1\Gamma_i}}$ and we would be done. C_i and C_v would remain constant with time. But we've added a glitch here - we've added the binding of interstitials to one another. This will cause C_i to either:

1. saturate at a lower value
2. decrease after $t > \sqrt{\frac{1}{Z_1\Gamma_i P}}$

and it will allow C_v to continue to decrease after $t > \sqrt{\frac{1}{Z_1\Gamma_i P}}$ due to the self-annihilation of interstitials.

Before we continue to discuss the glitch, let's note that from our set of simultaneous differential equations, the one thing we can calculate at this point is the total number of interstitial loop nuclei (i.e. di-interstitials) that have nucleated between $t = 0 \Rightarrow t = \sqrt{\frac{1}{Z_1\Gamma_i P}}$.

$\frac{dC_{ii}}{dt} = \frac{dC_L}{dt} = \sqrt{2}Z_2\Gamma_i C_i^2$ but $C_i = Pt$ (note that Yoshida-Kiritani do not include the factor $\sqrt{2}$)

$\frac{d\acute{C}_L}{dt} = \sqrt{2}Z_2\Gamma_i P^2 t^2$

$C_L = \sqrt{2}Z_2\Gamma_i P^2 \frac{t^3}{3}\Big|_{t=0}^{t=\sqrt{\frac{1}{Z_1\Gamma_i P}}}$

$C_L = \frac{\sqrt{2}}{3}Z_2 Z_1^{-\frac{3}{2}}\Gamma_i^{-\frac{1}{2}}P^{\frac{1}{2}}$ This gives concentration of loops up to $t = \sqrt{\frac{1}{Z_1\Gamma_i P}}$. This is also the same as Yoshida-Kiritani except for $\sqrt{2}$, $C_L = \frac{1}{3}\sqrt{\frac{2\left(\frac{Z_2}{Z_1}\right)^2 P}{Z_1\Gamma_i}}$at $t = \sqrt{\frac{1}{Z_1\Gamma_i P}}$.

Now for the glitch. After $t = \sqrt{\frac{1}{Z_1\Gamma_i P}}$, vacancies will continue to increase instead of stay constant, and interstitials will decrease, rather than stay constant, due to the annihilation of interstitials by one another to form loops.

Now for the key step: The Kiritani-Yoshida trick. The vacancy concentration can't

continue to increase as *Pt* because the *i-v* annihilation mechanism suppresses C_v somewhat after $t = \sqrt{\frac{1}{Z_1\Gamma_i P}}$.

★Key Step But C_v can continue to increase at a rate proportional to P, modified by a factor representing the difference between an interstitial self-annihilation (to form interstitial loop nuclei) to these annihilated by vacancies. This factor is indicative of the probability of vacancy survival due to the sparcity of interstitials which are dissipated by another mechanism.

This factor or probability is simply given by the ratio of the "rates: of i-i annihilation to i-v annihilation, i.e. to $\frac{2\sqrt{2}\Gamma_i Z_2 C_i}{Z_1\Gamma_i C_v}$.

So, after the rate of increase of vacancies after $t = \sqrt{\frac{1}{Z_1\Gamma_i P}}$ is simply $\frac{dC_v}{dt}$=$\frac{2\sqrt{2}Z_2 C_i}{Z_1 C_v}P$.

But for $t > \sqrt{\frac{1}{Z_1\Gamma_i P}}$ let's assume C_i is "constant":

★★ Kurt's key step $C_i = \sqrt{\frac{P}{Z_1\Gamma_i}}$, validity is questionable[2]

So, $\frac{dC_v}{dt}$=$\frac{2\sqrt{2}Z_2 C_i}{Z_1 C_v}P = \frac{\sqrt{2}Z_2 P^{\frac{3}{2}}}{Z_1^{\frac{3}{2}}\Gamma_i^{\frac{1}{2}}}\frac{1}{C_v} = 2\sqrt{2}\sqrt{\frac{Z_2^2 P^3}{Z_1^3\Gamma_i}}\frac{1}{C_v}$

$C_v dC_v = 2\sqrt{2}\sqrt{\frac{Z_2^2 P^3}{Z_1^3\Gamma_i}}dt$, let $\alpha = 2\sqrt{2}\sqrt{\frac{Z_2^2 P^3}{Z_1^3\Gamma_i}}$

$\frac{C_v^2}{2} = \alpha t + k$

At $t = \sqrt{\frac{1}{Z_1\Gamma_i P}}$ $C_v = \sqrt{\frac{P}{Z_1\Gamma_i}}$, so $k = \frac{P}{2Z_1\Gamma_i} - \frac{\alpha}{\sqrt{Z_1\Gamma_i P}}$

So $C_v = \sqrt{2\alpha + \frac{P}{Z_1\Gamma_i} - \frac{2\alpha}{\sqrt{Z_1\Gamma_i P}}}$

$C_v = \left(2\sqrt{2}\sqrt{\frac{4Z@_2P^3}{Z_1^3\Gamma_i}}t + \frac{P}{Z_i\Gamma_i} - 2\sqrt{2}\sqrt{\frac{4Z_i^2P^2}{Z_1^4\Gamma_i^2}}\right)^{\frac{1}{2}} = \left(2\sqrt{2}\sqrt{\frac{4Z@_2P^3}{Z_1^3\Gamma_i}}t + \frac{P}{Z_i\Gamma_i} - \frac{4\sqrt{2}Z_2P}{Z_1^2\Gamma i}\right)^{\frac{1}{2}}$

[2]★★ There's a problem with this assumption C_L actually peaks at $t = \sqrt{\frac{1}{Z_1\Gamma_i P}}$ and gradually diminishes thereafter. So the rest of this calculation assumes that C_i diminishes very gradually. It is fair to assume $\frac{dC_i}{} \approx 0$, $P - Z_1\Gamma_i C_v C_i \approx P - Z_1\Gamma_i C_v^2 = 0$, $C_i = \sqrt{\frac{P}{Z_1\Gamma_i}}$. Note this last step further assumes we can write $C_v = C_i$.

$$\bigstar C_v = \underbrace{\left(2\sqrt{2}\sqrt{\frac{4\left(\frac{Z_2}{Z_1}\right)^2 P^3}{Z_1\Gamma_i}t + \frac{P - 4\sqrt{2\left(\frac{Z_2}{Z_1}\right)}}{Z_1\Gamma_i}} \right)^{\frac{1}{2}}}$$

At large *t* where $\left(\frac{Z_2}{Z_1}\right) P\sqrt{\frac{2P}{Z_1\Gamma_i}} \gg \frac{P\left(1-4\sqrt{2}\left(\frac{Z_2}{Z_1}\right)\right)}{Z_1\Gamma_i}$, $C_v \approx \left(4\left(\frac{Z_2}{Z_1}\right) P\sqrt{\frac{2P}{Z_1\Gamma_i}}\right)^{\frac{1}{2}} t^{\frac{1}{2}}$, Note that this equation ($\bigstar$) reduces to $C_v = \sqrt{\frac{P}{Z_1\Gamma_i}}$ if you set $Z_2 = 0$ i.e. if you turn off the di-interstitial formation mechanism. This is the saturation value of $C_v$if the i-v annihilation mechanism operates.

Now let's calculate the interstitial concentration after $t > \frac{1}{\sqrt{Z_1\Gamma_i P}}$.

Once the *i-v* annihilation mechanism overtakes the surface annihilation mechanism, since the interstitial mobility is still much higher than the production rate, an equilibrium is established between the production rate P and the *i-v* annihilation rate, so that C_i is almost constant, and we can write:

$\frac{dC_i}{dt} \approx 0$ so

$\frac{dC_i}{dt} \approx P - \underbrace{Z_1\Gamma_i C_v C_i}_{} \approx 0$

We are assuming this mechanism of annihilation dominates all others i.e. $Z_1\Gamma_i C_v \gg 2\sqrt{2}Z_2\Gamma_i C_i$.This is true for $Z_1 \approx Z_2$ since $C_v C_i$ at large _____.

So $P = Z_1\Gamma_i C_v C_i$ and $C_i = \frac{P}{Z_1\Gamma_i}\frac{1}{C_v}$

$C_i = \frac{P}{Z_1\Gamma_i}\left(4\left(\frac{Z_2}{Z_1}\right) P\sqrt{\frac{2P}{Z_1\Gamma_i}}t + \frac{P\left(1-4\sqrt{2}\right)\left(\frac{Z_2}{Z_1}\right)}{Z_1\Gamma_i}\right)^{-\frac{1}{2}}$ for $t > \frac{1}{\sqrt{Z_1\Gamma_i P}}$

At very large t $4\left(\frac{Z_2}{Z_1}\right) P\sqrt{\frac{2P}{Z_1\Gamma_i}t} \gg \frac{P\left(1-4\sqrt{2}\left(\frac{Z_2}{Z_1}\right)\right)}{Z_1\Gamma_i}$

$C_i \approx \left(\frac{P^2}{Z_1^2\Gamma_i^2}\sqrt{\frac{Z_1\Gamma_i}{2P}}\frac{Z_1}{4Z_2P}\right)^{\frac{1}{2}} t^{-\frac{1}{2}} = \left(\frac{P}{4Z_1Z_2\Gamma_i^2}\right)^{\frac{1}{2}} t^{-\frac{1}{2}}$=

$\left(\frac{1}{4}\sqrt{\frac{P^2Z_1\Gamma_i}{Z_1^2Z_2^2\Gamma_i^4 2P}}\right)^{\frac{1}{2}} t^{-\frac{1}{2}} = \frac{1}{2}\left(\sqrt{\frac{P}{2Z_1Z_2^2\Gamma_i^3}}\right)^{\frac{1}{2}} t^{-\frac{1}{2}}$

$C_i = \frac{1}{2}\left(\frac{2Z_1Z_2^2\Gamma_i^3}{P}\right)^{-\frac{1}{4}} t^{-\frac{1}{2}}$ *at large t.*

The last thing to calculate is the additional amount of loops nucleated after $t = \frac{1}{\sqrt{Z_1\Gamma_i P}}$. We have already shown that up to $t = \frac{1}{\sqrt{Z_1\Gamma_i P}}$ we nucleate $C_L = \frac{\sqrt{2}}{3}Z_2 Z_1^{-\frac{3}{2}}\Gamma_i^{-\frac{1}{2}}P^{\frac{1}{2}} =$

$\frac{1}{3}\sqrt{\frac{2Z_2^2P}{Z_1^3\Gamma_i}}$ loops.

$C_L = \frac{1}{3}\sqrt{\frac{2\left(\frac{Z_2}{Z_1}\right)^2P}{Z_1\Gamma_i}}$ at $t = \frac{1}{\sqrt{Z_1\Gamma_iP}}$.

But at $t = \frac{1}{\sqrt{Z_1\Gamma_iP}}$ when $Z_1\Gamma_iC_vC_i$ becomes equal to P we have a new expression for

$C_i = \frac{P}{Z_1\Gamma_i}\left(4\left(\frac{Z_2}{Z_1}\right)P\sqrt{\frac{2P}{Z_1\Gamma_i}}t + \frac{P\left(1-4\sqrt{2}\left(\frac{Z_2}{Z_1}\right)\right)}{Z_1\Gamma_i}\right)^{-\frac{1}{2}}$ which we can place into

$\frac{dC_L}{dt} = \frac{dC_{ii}}{dt} = \sqrt{2}Z_2\Gamma_iC_i^2$

Let's say that $\alpha = \sqrt{\frac{2\left(\frac{Z_2}{Z_1}\right)^2P}{Z_1\Gamma_i}}$ at $\beta = \frac{P\left(1-4\sqrt{2\left(\frac{Z_2}{Z_1}\right)}\right)}{Z_1\Gamma_i}$

Then $C_L = \frac{\alpha}{3}$ at $t = \frac{1}{\sqrt{Z_1\Gamma_iP}} = \tau$ and $C_i = \frac{P}{Z_1\Gamma_i}\left(4\alpha Pt + \beta\right)^{-\frac{1}{2}}$

Let $\gamma = \frac{P}{Z_1\Gamma_i}$ and $\delta = 4\alpha P$

$C_i = \gamma\left(\delta t + \beta\right)^{-\frac{1}{2}}$

$\frac{dC_L}{dt}$=$\sqrt{2}Z_2\Gamma_iC_i^2$, let $\epsilon = \sqrt{2}Z_2\Gamma_i$

$\frac{dC_L}{dt} = \epsilon C_i^2 = \frac{\epsilon\gamma^2}{\delta t+\beta}$ for $t > \frac{1}{\sqrt{Z_1\Gamma_iP}}$

$dC_L = \epsilon\gamma^2\frac{dt}{\delta t+\beta}$, $dln\left(\delta t+\beta\right) = \frac{\delta dt}{\delta t+\beta}$

$\int dC_L = \frac{\epsilon\gamma^2}{\delta}\int dln\left(\delta t+\beta\right)$

$C_L = \frac{\epsilon\gamma^2}{\delta}ln\left(\delta t+\beta\right) + k$

$C_L = \frac{\alpha}{3}$at $t = \tau = \frac{1}{\sqrt{Z_1\Gamma_iP}}$ and $k = \frac{\alpha}{3} - \frac{\epsilon\gamma^2}{\delta}ln\left(\delta\tau+\beta\right)$

$C_L = \frac{\epsilon\gamma^2}{\delta}ln\left(\delta t+\beta\right) + \frac{\alpha}{3} - \frac{\epsilon\gamma^2}{\delta}ln\left(\delta\tau+\beta\right)$

$\bigstar C_L = \frac{\gamma^2}{\frac{\delta}{\epsilon}}ln\left(\frac{\delta t+\beta}{\delta\tau+\beta}\right) + \frac{\alpha}{3}$

$\alpha = \sqrt{\frac{2\left(\frac{Z_2}{Z_1}\right)^2P}{Z_1\Gamma_i}}$ dimensionless

$\beta = \frac{\left(\left(1-4\sqrt{\left(\frac{Z_2}{Z_1}\right)P}\right)\right)}{Z_1\Gamma_i}$ dimensionless

$\gamma = \frac{P}{Z_1\Gamma_i}$ dimensionless

$\delta = 4\alpha P$ dimension of *rate*

$\epsilon = \sqrt{2}Z_2\Gamma_i$ dimension of *rate*

$\frac{\delta}{\epsilon} = \frac{4\alpha}{\sqrt{2}}\frac{P}{Z_2\Gamma_i}$ dimensionless

$\tau = \frac{1}{\sqrt{Z_1 \Gamma_i P}}$ dimension of *time*

for large t, $\frac{\delta t}{\delta\tau+\beta} \gg \frac{\beta}{\delta\tau+\beta}$

$C_L = \frac{\gamma^2}{\frac{\delta}{\epsilon}} ln\left(\frac{\delta}{\delta\tau+\beta} t\right)$

This is as far as this model can go.

★★ In Kurt's 6^{th} progressive step we find the results equivalent to the Kiritani-Yoshida thick-film, low T case.

VI

We'll skip the notion that vacancies can bind with other vacancies, and continue the derivation that is valid at low-T where only interstitials are mobile. In the last treatment (part V and Va), we did not consider the growth of the interstitial loop nuclei, i.e. the accumulation of interstitials at di-interstitials. As these loops grow, the number of sites in the crystal where interstitial annihilation can occur increases. This number of sites is proportional to the total length of interstitial loops, which we'll call L, since interstitials are absorbed at the perimeter of loops at the position of the edge dislocation.

The total length of interstitial loops is proportional $L \propto \sqrt{N_L N_{iL}}$ where N_{iL} is the total number of interstitials that have been absorbed by growing loops. One can verify this relationship as follows:

Examples A), B) and C) below: keeping the number of interstitials incorporated in loops constant

Imagine a crystal with N lattice sites

- N = # lattice sites

- a = spacing between sites
- N_P = # of lattice sites on the perimeter of interstitial loops
- N_L = # of interstitial loops
- N_{iL} = # of interstitials contained within N_L loops

Example:

$N_L = 4$

$N_{iL} = 4 \cdot 10^2 = 400$

$N = 10^4$ and $\sqrt{N} = 100$

A)

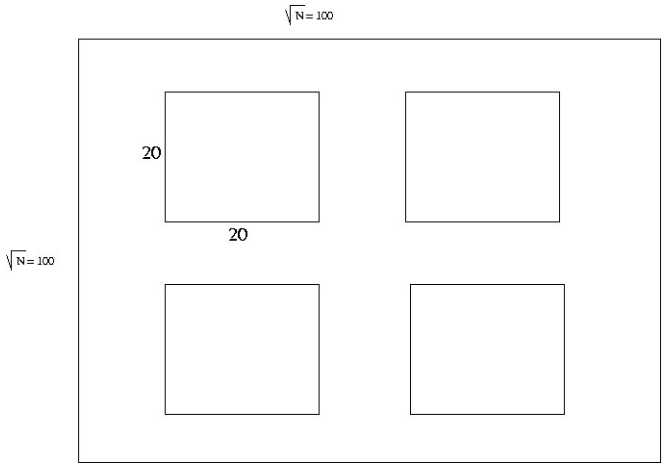

Figure D.31: Four 20 by 20 loops

$N_P = 4 \cdot (4 \cdot 20) = 320$

$N_{iL} = 4\,(20^2) = 1600$

$N_L = 4$

$N = 10^4$

$N_{iL}N_L = 6400$

$\sqrt{N_{iL}N_L} = 80$

B)

Now break each loop into 4 loops:

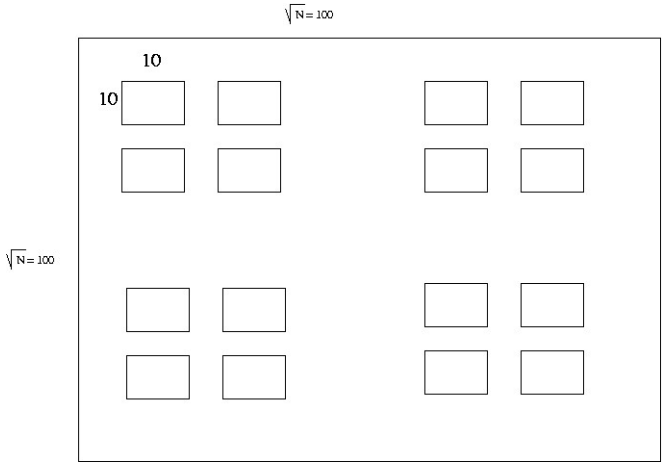

Figure D.32: 16 10 by 10 loops

$N_P = 16 \cdot (4 \cdot 10) = 640$

$N_{iL} = 16 \cdot (10^2) = 1600$

$N_L = 16$

$N = 10^4$

$N_{iL}N_L = 25600$

$\sqrt{N_{iL}N_L} = 160$

C)

Or put all four loops together as one

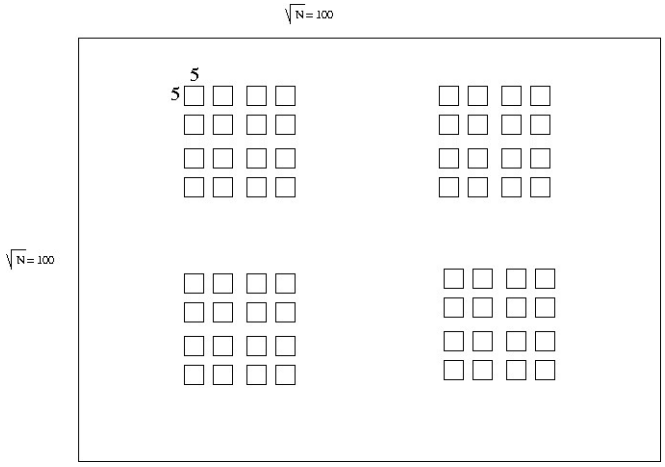

Figure D.33: 64 5 by 5 loops

$N_P = 64 \cdot (4 \cdot 5) = 1280$

$N_{iL} = 64 \cdot (5^2) = 1600$

$N_L = 64$

$N = 10^4$

$N_{iL}N_L = 102400$

$\sqrt{N_{iL}N_L} = 320$

In A), B), and C), N_{iL} was held constant. N_L was increased as N_L^2. N_P increased by a factor of two each time. $\sqrt{N_{iL}N_L}$also increased by a factor of two each time. So, $N_P \propto \sqrt{N_{iL}N_L}$, or $N_P = 4\sqrt{N_{iL}N_L}$.

Example D), E) and F). Keeping the number of loops constant

D)

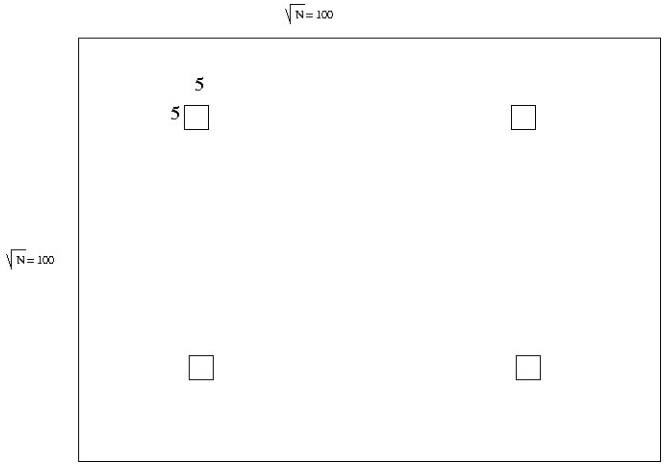

Figure D.34: Four 5 by 5 loops

$N_P = 4 \cdot (4 \cdot 5) = 80$

$N_{iL} = 4 \cdot (5^2) = 100$

$N_L = 4$

$N = 10^4$

$N_{iL}N_L = 400$

$\sqrt{N_{iL}N_L} = 120$

E)

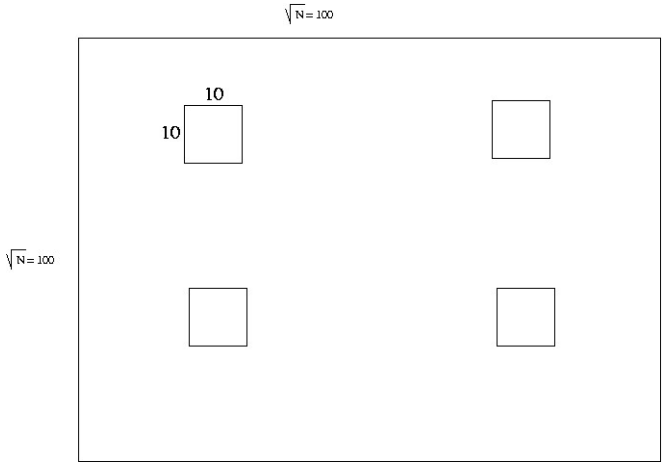

Figure D.35: Four 10 by 10 loops

$N_P = 4 \cdot (4 \cdot 10) = 160$

$N_{iL} = 4 \cdot (10^2) = 400$

$N_L = 4$

$N = 10^4$

$N_{iL}N_L = 1600$

$\sqrt{N_{iL}N_L} = 40$

F)

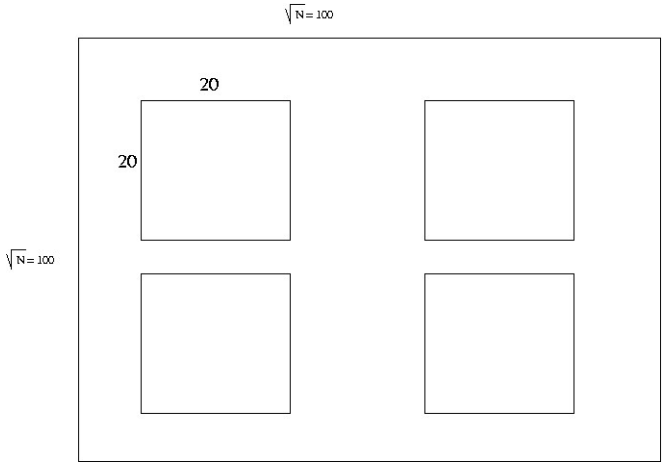

Figure D.36: Four 20 by 20 loops

$N_P = 4 \cdot (4 \cdot 20) = 320$

$N_{iL} = 4 \cdot (20^2) = 1600$

$N_L = 4$

$N = 10^4$

$N_{iL}N_L = 6400$

$\sqrt{N_{iL}N_L} = 80$^2

In D) , E) and F), N_L was held constant, N_{iL} increased as N_{iL}^2, $N_P$and $\sqrt{N_{iL}N_L}$ increased by a factor of 2. So $N_P \propto \sqrt{N_{iL}N_L}$ or $N_P = 4\sqrt{N_{iL}N_L}$.

So we have found that N_P scales as $\sqrt{N_{iL}N_L}$ and exactly $N_P = 4\sqrt{N_{iL}N_L}$. The factor of 4 is a geometrical factor representing square (four-sided) loops in a square lattice, and square lattice sites. We can state that in general:

$N_P = \Omega\sqrt{N_{iL}N_L}$ where Ω is a constant of order unity, proportional to the geometry of the lattice.

So we have found that N_p scales as $\sqrt{N_{iL}N_L}$ and exactly $N_p = 4\sqrt{N_{iL}N_L}$ where the

factor 4 is a geometrical factor representing square (4 sided) loops in a square lattice, and square lattice sites. We could state that in general $N_p = \Omega\sqrt{N_{iL}N_L}$, where Ω is a constant of order unity, proportional to the geometry of the lattice.

Now imagine a volume V_3 containing Z_3sites surrounding the perimeter of an interstitial dislocation loop, wherein if an interstitial enters the volume it is absorbed by the dislocation loop with an efficiency of $\eta_3 = 1$.

The total number of sites in the crystal that are potential sites for interstitial annihilation at interstitial loop perimeter is $Z_3 N_p$, but $N_p = \Omega\sqrt{N_L N_{iL}}$. Remember, N_L is the number of loops, while N_{iL} is the number of interstitials in N_L loops. So the number of sites for absorption of interstitials at loops is $Z_3\Omega\sqrt{N_L N_{iL}}$. So the concentration of these sites is $\frac{Z_3\Omega\sqrt{N_L N_{iL}}}{N} = Z_3\Omega\sqrt{\frac{N_L N_{iL}}{N}} = \underbrace{Z_3\Omega\sqrt{C_L C_{iL}}}$. This concentration is equivalently the probability that a given site in the lattice sits on the perimeter of a dislocation loop. Note that $C_p = \Omega\sqrt{C_L C_{iL}}$.

The probability that a given site in the crystal is visited by an interstitial per unit time is: $\Gamma_i C_i$. So the rate of annihilation of interstitials by this mechanism is $Z_3\Omega\sqrt{C_L C_{iL}}\Gamma_i C_i$.

★★For simplicity we will lump Ω in with Z_3 from here on. Since Z_3 is an unspecified parameter that includes geometric factors. So we have $Z_3\sqrt{C_L C_{iL}}\Gamma_i C_i$. This is the annihilation rate of interstitials by the loop growth mechanism.

We can also write and expression or the growth rate of loops:

Assume *a* is the growth distance (atomic spacing, burgers vector, etc.) *du* to the absorption of on interstitial. If the length (circumference) of a dislocation increases by length *a*, the radius must increase by a proportional increment, since for a loop:

$L = 2\pi r$

$ln\,(L) = 2\pi ln\,(r)$

$\left(\frac{dL}{L}\right) = 2\pi\frac{dr}{r}$, Let $dL = a$

$\frac{a}{L} = 2\pi\frac{dr}{r}$

$dr = \frac{r}{2\pi L}a \approx \frac{r}{2\pi(2\pi r)}a = \frac{a}{4\pi^2}$

$dr = \frac{a}{4\pi^2}$

Now, for one site on the perimeter of a given dislocation loop, the probability that *that* site will be visited by an interstitial per unit time is $\Gamma_i C_i$. But the volume V_3 containing Z_3 sites surrounding this site is unstable (i.e. can capture) for an interstitial, so the probability that in interstitial visits this volume is $Z_3\Gamma_i C_i$. Upon capture the circumference increases by a, while the radius increases by an amount $\frac{a}{4\pi^2}$, so $\frac{dr}{dt} = \frac{a}{4\pi^2}Z_3\Gamma_i C_i$. Since $\frac{a}{4\pi^2}$ is a geometric constant of order unity, we will lump it in with Z_3 for now, since Z_3 is an unspecified parameter that includes geometric factors. So we'll write $\frac{dr}{dt} = aZ_3\Gamma_i C_i$.

Now, we can write the following 4 simultaneous differential equations:

- $\frac{dC_i}{dt} = (1 - C_i)(1 - Z_1 C_i)P - Z_1\Gamma_i C_v C_i - 2\sqrt{2}Z_2\Gamma_i C_i^2 - Z_3\sqrt{C_L C_{iL}}\Gamma_i C_i$
- $\frac{dC_v}{dt} = (1 - C_v)(1 - Z_1 C_v)P - Z_1\Gamma_i C_i C_v$
- $\frac{dC_L}{dt} = \frac{dC_{ii}}{dt} = 2\sqrt{2}Z_2\Gamma_i C_i^2$
- $\frac{dr}{dt} = aZ_3\Gamma_i C_i$

Since Γ_i is very large compared to $Z_1 C_i P$ and similar terms, we can write:

$$\begin{aligned}
\tfrac{dC_i}{dt} &= P - (Z_1\Gamma_i C_v)C_i - \left(2\sqrt{2}Z_2\Gamma_i C_i\right)C_i - \left(Z_3\Gamma_i\sqrt{C_L C_{iL}}\right)C_i \\
\tfrac{dC_v}{dt} &= P - (Z_1\Gamma_i C_v)C_i \\
\tfrac{dC_L}{dt} = \tfrac{dC_{ii}}{dt} &= \left(\sqrt{2}Z_2\Gamma_i C_i\right)C_i \\
\tfrac{dr}{dt} &= aZ_3\Gamma_i C_i
\end{aligned}$$

Since $C_i \neq C_v$, an analytical solution is not possible, we must either solve numerically or look at approximate solutions analytically. We've only added one new mechanism - growth of loops - and so much of the analytic results from V are still valid; we have merely

to add the effects of the loop growth mechanism at the time when the rate $\left(Z_3\Gamma_i\sqrt{C_iC_{iL}}\right)$ becomes significant.

The following results from V are valid:

Small *t*:

- $C_i = Pt$
- $C_v = Pt$

At $t = \frac{1}{\sqrt{Z_1\Gamma_iP}}$ C_i peaks at $C_i = \sqrt{\frac{P}{Z_1\Gamma}_i}$

At $t = \frac{1}{\sqrt{Z_1\Gamma_iP}}$ C_v peaks at $C_v = C_i = \sqrt{\frac{P}{Z_1\Gamma}_i}$

At $t = \frac{1}{\sqrt{Z_1\Gamma_iP}}$ C_v peaks at $C_L = C_{ii} = \frac{1}{3}\sqrt{\frac{2\left(\frac{Z_2}{Z_1}\right)^2P}{Z_1\Gamma_i}}$

Now, we can also calculate the "radii" of loops at $t = \frac{1}{\sqrt{Z_1\Gamma_iP}}$

$\frac{dr}{dt} = aZ_3\Gamma_iC_i$ but from $t = 0$ to $t = \frac{1}{\sqrt{Z_1\Gamma_iP}}$, $C_i = Pt$, so for $\frac{dr}{dt} = aZ_3\Gamma_iC_i$,

$$r = aZ_3\Gamma_iP\frac{t^2}{2}\Bigg|_{\substack{t=\frac{1}{\sqrt{Z_1\Gamma_iP}}\\ t=0}} = \frac{a}{2}\frac{Z_3\Gamma_iP}{Z_1\Gamma_iP}$$

At $t = \frac{1}{\sqrt{Z_1\Gamma_iP}}$, $r = \frac{1}{2}\frac{Z_2}{Z_2}a$

Now beyond $t > \frac{1}{\sqrt{Z_1\Gamma_iP}}$, we must use the Kiritani-Yoshida *trick* again. Vacancies continue to increase at a rate proportional to P modified by the ratio of the rate of interstitial annihilation by mechanisms other than *i-v* rate of interstitial annihilation by the *i-v* mechanism. This ratio is indicative of the fraction of vacancies that survive annihilation. Last time for this ratio we used $\frac{2\sqrt{2}Z_2\Gamma_iC_i}{Z_1\Gamma_iC_v}$ but this time we'll use $\frac{Z_3\Gamma_i\sqrt{C_LC_{iL}}}{Z_1\Gamma_iC_v}$ because $Z_3\Gamma_i\sqrt{C_LC_{iL}} \approx Z_3\Gamma_iC_p \gg 2\sqrt{2}Z_2\Gamma_iC_i$ assuming $Z_3 \approx 2\sqrt{2}Z_2$

We're saying here that for $t > \frac{1}{\sqrt{Z_1\Gamma_iP}}$, $C_p \gg C_i$, and at $t = \frac{1}{\sqrt{Z_1\Gamma_iP}}$, $C_i = \sqrt{\frac{P}{Z_1\Gamma_i}}$. Let's estimate C_p at this time.

C_p at $t = \frac{1}{\sqrt{Z_1\Gamma_iP}}$

$C_p \approx \sqrt{C_LC_{iL}}$

$C_L\left(t=\frac{1}{\sqrt{Z_1\Gamma_i P}}\right)=\frac{1}{3}\sqrt{\frac{2\left(\frac{Z_2}{Z_1}\right)^2 P}{Z_1\Gamma_i}}$

$C_{iL}\approx C_L\frac{\pi r^2}{a^2}$

$r\left(t=\frac{1}{\sqrt{Z_1\Gamma_i P}}\right)=\frac{1}{2}\left(\frac{Z_3}{Z_2}\right)a$

$C_{iL}\left(t=\frac{1}{\sqrt{Z_1\Gamma_i P}}\right)=\frac{1}{3}\sqrt{\frac{2\left(\frac{Z_2}{Z_1}\right)^2 P}{Z_1\Gamma_i}}\frac{1}{4}\left(\frac{Z_3}{Z_2}\right)^2$

$C_p\approx\sqrt{C_L C_{iL}}=\frac{1}{3}\sqrt{\frac{2\left(\frac{Z_2}{Z_1}\right)^2 P}{Z_1\Gamma_i}}\frac{1}{2}\left(\frac{Z_3}{Z_2}\right)=\frac{\sqrt{2}}{6}\left(\frac{Z_2}{Z_1}\right)\left(\frac{Z_3}{Z_2}\right)\sqrt{\frac{P}{Z_1\Gamma_i}}$

$C_p\left(t=\frac{1}{\sqrt{Z_1\Gamma_i P}}\right)=\frac{\sqrt{2}}{6}\left(\frac{Z_3}{Z_1}\right)\sqrt{\frac{P}{Z_1\Gamma_i}}\approx\sqrt{\frac{P}{Z_1\Gamma_i}}$ for $Z_1\approx Z_3$

$C_i\left(t=\frac{1}{\sqrt{Z_1\Gamma_i P}}\right)=\sqrt{\frac{P}{Z_1\Gamma_i}}$

So, actually $C_p\approx C_i$, they are the same order of magnitude at $t=\frac{1}{\sqrt{Z_1\Gamma_i P}}$. But after $t=\frac{1}{\sqrt{Z_1\Gamma_i P}}$, $C_i$can only fall due to enhanced annihilation because C_P continues to grow as loops grow. So after $t>\frac{1}{\sqrt{Z_1\Gamma_i P}}$ the limiting rate ratio that we want in order to consider survival of vacancies is:

(rate of interstitial annihilation at loops)/(rate of interstitials annihilated by *i-v* recombination = $\frac{Z_3\Gamma_i\sqrt{C_L C_{iL}}}{Z_1\Gamma_i C_v}$. Note that Γ_i cancels. So we can write that after $t=\frac{1}{\sqrt{Z_1\Gamma_i P}}$,

★★ *Key Step!* $\frac{dC_v}{dt}=\frac{Z_3\sqrt{C_L C_{iL}}}{Z_1 C_v}$

Now for a second key step ★★:

Consider that loop absorption of interstitials is the dominant mechanism of interstitial annihilation after $t\approx\frac{1}{\sqrt{Z_1\Gamma_i P}}$, out pacing loop nucleation which is given by $C_L=C_{ii}$.

So the increase in vacancy concentration after this time is given by the amount of interstitials absorbed at loops, i.e.

★★$C_{iL}=C_v$

This is strictly true only after some elapsed time after $t=\frac{1}{\sqrt{Z_1\Gamma_i P}}$ such that $C_{iL}=C_v\gg\frac{C_{iL}\left(t=\frac{1}{\sqrt{Z_1\Gamma_i P}}\right)}{C_v\left(t=\frac{1}{\sqrt{Z_1\Gamma_i P}}\right)}$

But actually this is still quite a good approximation at $t=\frac{1}{\sqrt{Z_1\Gamma_i P}}$ since we've al-

ready shown that at this time $C_i = C_v = \sqrt{\frac{P}{Z_1\Gamma_i}}$ and $C_{iL} = \frac{\sqrt{2}}{12}\left(\frac{Z_2}{Z_1}\right)\left(\frac{Z_3}{Z_2}\right)\sqrt{\frac{P}{Z_1\Gamma_i}} = \frac{\sqrt{2}}{12}\left(\frac{Z_3}{Z_1}\right)\sqrt{\frac{P}{Z_1\Gamma_i}}$.

So assuming $\frac{\sqrt{2}}{12}\left(\frac{Z_3}{Z_1}\right) \approx 1$, $C_v \approx C_{iL}$ at $t = \frac{1}{\sqrt{Z_1\Gamma_i P}}$.

So if we assume $C_{iL} = C_v$, then $\frac{dC_v}{dt} = \frac{Z_3}{Z_1}\frac{\sqrt{C_L C_v}}{C_v}P = \frac{Z_3}{Z_1}P\sqrt{\frac{C_L}{C_v}}$.

We're not done yet! We still have $C_L$to consider. Yoshida-Kiritani introduce a 3rd key step.

★★ Key Step 3

>From numerical simulation, they observe that $C_L$typically does not change much after $t = \frac{1}{\sqrt{Z_1\Gamma_i P}}$, so they assume after this time C_L is *constant*!!

$C_L - C_L\left(t = \frac{1}{\sqrt{Z_1\Gamma_i P}}\right) = \frac{1}{3}\underbrace{\sqrt{\frac{2\left(\frac{Z_2}{Z_1}\right)^2 P}{Z_1\Gamma_i}}}$

We formally called this constant α. Thus we can finally write the differential equation:

$\frac{dC_v}{dt} = \frac{Z_3}{Z_1}P\frac{\sqrt{\frac{\alpha}{3}}}{C_v^{\frac{1}{2}}}$ for $t > \frac{1}{\sqrt{Z_1\Gamma_i P}}$ and $\alpha = \sqrt{\frac{2\left(\frac{Z_2}{Z_1}\right)^2 P}{Z_1\Gamma_i}}$

$C_v^{\frac{1}{2}}dC_v = \frac{Z_3}{Z_1}P\sqrt{\frac{\alpha}{3}}dt$

$\frac{2}{3}C_v^{\frac{3}{2}} = \frac{Z_3}{Z_1}P\sqrt{\frac{\alpha}{3}}t + k$ at $t = \frac{1}{\sqrt{Z_1\Gamma_i P}}$ $C_v = \sqrt{\frac{P}{Z_1\Gamma_i}}$

$k = \frac{2}{3}\left(\left(\frac{P}{Z_1\Gamma_i}\right)^{\frac{1}{2}}\right)^{\frac{3}{2}} - \frac{Z_3}{Z_1}P\sqrt{\frac{\alpha}{3}}\frac{1}{\sqrt{Z_1\Gamma_i P}} = \frac{2}{3}\left(\frac{P}{Z_1\Gamma_i}\right)^{\frac{3}{4}} - \sqrt{\frac{\alpha}{3}}\left(\frac{Z_3}{Z_1}\right)\sqrt{\frac{P}{Z_1\Gamma_i}}$

$C_v^{\frac{3}{2}} = \frac{3}{2}\frac{Z_3}{Z_1}\sqrt{\frac{\alpha}{3}}Pt + \frac{2}{3}\left(\frac{P}{Z_1\Gamma_i}\right)^{\frac{3}{4}} - \sqrt{\frac{\alpha}{3}}\left(\frac{Z_3}{Z_1}\right)\sqrt{\frac{P}{Z_1\Gamma_i}}$

$C_v = \left(\frac{2}{3}\left(\frac{Z_3}{Z_1}\right)\sqrt{\frac{\alpha}{3}}Pt + \frac{2}{3}\left(\frac{P}{Z_1\Gamma_i}\right)^{\frac{3}{4}} - \sqrt{\frac{\alpha}{3}}\left(\frac{Z_3}{Z_1}\right)\sqrt{\frac{P}{Z_1\Gamma}}\right)^{\frac{2}{3}}$

where $\frac{\alpha}{3} = C_L$ and $\alpha = \sqrt{\frac{2\left(\frac{Z_2}{Z_1}\right)^2 P}{Z_1\Gamma_i}}$

At large t $\frac{3}{2}\frac{Z_3}{Z_1}\sqrt{\frac{\alpha}{3}}Pt \gg \frac{2}{3}\left(\frac{P}{Z_1\Gamma_i}\right)^{\frac{3}{4}} - \sqrt{\frac{\alpha}{3}}\left(\frac{Z_3}{Z_1}\right)\sqrt{\frac{P}{Z_1\Gamma}}$

$C_v \approx \left(\frac{3}{2}\left(\frac{Z_3}{Z_1}\right)\sqrt{\frac{\alpha}{3}}P\right)^{\frac{2}{3}}t^{\frac{2}{3}}$ but $C_L = \frac{\alpha}{3}$

$C_v \approx \left(\frac{3}{2}\left(\frac{Z_3}{Z_1}\right)C_L^{\frac{1}{2}}P\right)^{\frac{2}{3}}$ same as Kiritani-Yoshida.

Now, the majority of the interstitials introduced at rate *P* are still *disappearing to vacancies*. So we can write

$\frac{dC_i}{dt} \approx P - Z_1\Gamma_i C_v C_i \approx 0$

$P = Z_1\Gamma_i C_v C_i$

$C_i = \frac{P}{Z_1\Gamma_i} C_v^{-1}$

So $C_i = \frac{P}{Z_1\Gamma_i}\left(\frac{2}{3}\left(\frac{Z_3}{Z_1}\right)\sqrt{\frac{\alpha}{3}}Pt + \frac{2}{3}\left(\frac{P}{Z_1\Gamma_i}\right)^{\frac{3}{4}} - \sqrt{\frac{\alpha}{3}}\left(\frac{Z_3}{Z_1}\right)\sqrt{\frac{P}{Z_1\Gamma}}\right)^{-\frac{2}{3}}$

with $\frac{\alpha}{3} = C_L$ and $\alpha = \sqrt{\frac{2\left(\frac{Z_2}{Z_1}\right)^2 P}{Z_1\Gamma_i}}$

at large *t* $C_i \approx \frac{P}{Z_1\Gamma_i}\left(\frac{3}{2}\left(\frac{Z_3}{Z_1}\right)\sqrt{\frac{\alpha}{3}}C_L^{\frac{1}{2}}P\right)^{-\frac{2}{3}} t^{-\frac{2}{3}} \approx \left(\left(\frac{P}{Z_1\Gamma_i}\right)^{\frac{3}{2}}\right)^{\frac{2}{3}}\left(\frac{2}{3}\left(\frac{Z_1}{Z_3}\right)\frac{1}{C_L^{\frac{1}{2}}P}\right)^{\frac{2}{3}} t^{-\frac{2}{3}}$

$\approx \left(\frac{2}{3}\right)^{\frac{2}{3}}\left(\frac{Z_1 P^{\frac{3}{2}}}{Z_1^{\frac{3}{2}} Z_3 \Gamma_i^{\frac{3}{2}} C_L^{\frac{1}{2}} P}\right)^{\frac{2}{3}} t^{-\frac{2}{3}} \approx \left(\frac{2}{3}\right)^{\frac{2}{3}}\left(\frac{P^{\frac{1}{2}}}{Z_1^{\frac{1}{2}} Z_3 \Gamma_i^{\frac{3}{2}} C_L^{\frac{1}{2}} P}\right)^{\frac{2}{3}} t^{-\frac{2}{3}}$

$C_i \approx \left(\frac{2}{3}\right)^{\frac{2}{3}}\left(\frac{P}{Z_1 Z_3^2 \Gamma_i^3 C_L}\right)^{\frac{1}{3}} t^{-\frac{2}{3}}$ (at large *t*). Same as Yoshida-Kiritani.

We've already assumed the number of loop nuclei remains constant at

$C_L = \frac{\alpha}{3} = \frac{1}{3}\sqrt{\frac{2\left(\frac{Z_2}{Z_1}\right)^2 P}{Z_1\Gamma_i}}$ after $t = \frac{1}{\sqrt{Z_1\Gamma_i P}}$.

So the last thing to calculate is the relationship for loop radii!

$\frac{dr}{dt} = aZ_3\Gamma_i C_i$ and $r = \frac{1}{2}\frac{Z_3}{Z_2 a}$ at r $t = \frac{1}{\sqrt{Z_1\Gamma_i P}}$.

We'll only calculate this at large : where $C_i \approx \left(\frac{2}{3}\right)^{\frac{2}{3}}\left(\frac{P}{Z_1 Z_3^2 \Gamma_i^3 C_L}\right)^{\frac{1}{3}} t^{-\frac{2}{3}}$

$\frac{dr}{dt} = \underbrace{aZ_3\Gamma_i\left(\frac{2}{3}\right)^{\frac{2}{3}}\left(\frac{P}{Z_1 Z_3^2 \Gamma_i^3 C_L}\right)^{\frac{1}{3}}}\, t^{-\frac{2}{3}}$

Call this whole constant Σ

$\frac{dr}{dt} = \Sigma t^{-\frac{2}{3}} + k$

$r = \Sigma\frac{t^{-\frac{2}{3}+\frac{3}{3}}}{-\frac{2}{3}+\frac{3}{3}} = \Sigma\frac{t^{\frac{1}{3}}}{\frac{1}{3}} = 3\Sigma t^{\frac{1}{3}} + \underbrace{k}$ Forget about *k*

★ Important result!

$r \propto 3aZ_3\Gamma_i\left(\frac{2}{3}\right)^{\frac{2}{3}}\left(\frac{P}{Z_1 Z_3^2 \Gamma_i^3 C_L}\right)^{\frac{1}{3}} t^{\frac{1}{3}}$ at large . Loop radius or loop diameter scales with cube root of time.

Finally, even though we assumed C_L = constant in order to calculate C_v, C_i and r

at long times, we can now introduce these results onto $\frac{dC_L}{dt} = \frac{dC_{ii}}{dt} = \left(\sqrt{2}Z_2\Gamma_i C_i\right)C_i$ to obtain, by this iteration or feedback technique, a more correct form for C_L. At large *t*:

$C_i \approx \left(\frac{2}{3}\right)^{\frac{2}{3}}\left(\frac{P}{Z_1 Z_3^2 \Gamma_i^3 C_L}\right)^{\frac{1}{3}} t^{-\frac{2}{3}}$

$\frac{dC_L}{dt} = \sqrt{2}Z_2\Gamma_i\left(\frac{2}{3}\right)^{\frac{4}{3}}\left(\frac{P}{Z_1 Z_3^2 \Gamma_i^3 C_L}\right)^{\frac{2}{3}} t^{-\frac{4}{3}} = \sqrt{2}\left(\frac{2}{3}\right)^{\frac{4}{3}}\left(\frac{Z_2^{\frac{3}{2}}}{Z_1 Z_3^2}\right)^{\frac{2}{3}}\left(\frac{P\Gamma_i^{\frac{3}{2}}}{\Gamma_i^{\frac{6}{2}}}\right)^{\frac{2}{3}} C_L^{-\frac{2}{3}} t^{-\frac{4}{3}}$

$= \underbrace{\sqrt{2}\left(\frac{2}{3}\right)^{\frac{4}{3}}\left(\frac{Z_2^{\frac{3}{2}}}{Z_1 Z_3^2}\right)^{\frac{2}{3}}\left(\frac{P}{\Gamma_i^{\frac{3}{2}}}\right)^{\frac{2}{3}}}\, C_L^{-\frac{2}{3}} t^{-\frac{4}{3}}$

call this X.

$\frac{dC_L}{dt} = X C_L^{-\frac{2}{3}} t^{-\frac{4}{3}}$

$\int C_L^{\frac{2}{3}} dC_L = X \int t^{-\frac{4}{3}} dt$

$\frac{C_L^{\frac{2}{3}+\frac{3}{3}}}{\frac{2}{3}+\frac{3}{3}} = X\frac{t^{-\frac{4}{3}+\frac{3}{3}}}{-\frac{4}{3}+\frac{3}{3}} + k$

$\frac{3}{5}C_L^{\frac{5}{3}} = -3Xt^{-\frac{1}{3}} + k$

Now $C_L = \frac{1}{3}\sqrt{\frac{2\left(\frac{Z_2}{Z_1}\right)^2 P}{Z_1\Gamma_i}}$, which we will now call C_L^* at $t = \frac{1}{\sqrt{Z_1\Gamma_i P}}$, which we will now call τ.

- $C_L^* = \frac{\sqrt{2}}{3}\frac{Z_2}{Z_1^{\frac{3}{2}}}\frac{P^{\frac{1}{2}}}{\Gamma_i^{\frac{1}{2}}}$
- $\tau = Z_1^{-\frac{1}{2}}\frac{P^{-\frac{1}{2}}}{\Gamma_i^{\frac{1}{2}}}$

$k = \frac{3}{5}C_L^{*\frac{5}{3}} + 3Xt^{-\frac{1}{3}}$

$\frac{3}{5}C_L^{\frac{5}{8}} = \frac{3}{5}C_L^{*\frac{5}{8}} + 3\frac{X}{\tau^{\frac{1}{3}}} - 3Xt^{-\frac{1}{3}}$

$C_L = \left[\frac{5}{3}\left(\frac{3}{5}C_L^{*\frac{5}{3}} + 3\frac{X}{\tau^{\frac{1}{3}}} - \underbrace{3Xt^{-\frac{1}{3}}}\right)\right]^{\frac{3}{5}}$

But as $t \Rightarrow \infty$ this term vanishes, so

$C_L^{\infty} = \left(C_L^{*\frac{5}{3}} + \frac{5X}{\tau^{\frac{1}{3}}}\right)^{\frac{3}{5}} =$

$\left[\left(\frac{\sqrt{2}}{3}\right)^{\frac{5}{3}}\left(\frac{Z_2}{Z_1^{\frac{3}{2}}}\right)^{\frac{5}{3}}\left(\frac{P^{\frac{1}{2}}}{\Gamma_i^{\frac{1}{2}}}\right)^{\frac{5}{3}} + 5\sqrt{2}\left(\frac{2}{3}\right)^{\frac{4}{3}}\left(\frac{Z_2^{\frac{3}{2}}}{Z_1 Z_3^2}\right)^{\frac{2}{3}}\left(\frac{P}{\Gamma_i^{\frac{3}{2}}}\right)^{\frac{2}{3}}\left(Z_1^{-\frac{1}{2}}\right)^{-\frac{1}{3}}\left(\frac{P^{-\frac{1}{2}}}{\Gamma_i^{\frac{1}{2}}}\right)^{\frac{3}{5}}\right]$

$= \left[\left(\frac{\sqrt{2}}{3}\right)^{\frac{5}{3}}\frac{Z_2^{\frac{5}{3}}}{Z_1^{\frac{15}{6}}}\frac{P^{\frac{5}{6}}}{\Gamma_i^{\frac{5}{6}}} + 5\sqrt{2}\left(\frac{2}{3}\right)Z_1^{\frac{4}{3}}\frac{Z_2}{Z_1^{\frac{2}{3}}Z_3^{\frac{4}{3}}}\frac{P^{\frac{2}{3}}}{\Gamma_i}Z_1^{\frac{1}{6}}\frac{P^{\frac{1}{6}}}{\Gamma_i^{-\frac{1}{6}}}\right]^{\frac{3}{5}} =$

$$\left[\left(\frac{\sqrt{2}}{3}\right)^{\frac{5}{3}}\frac{Z_2^{\frac{5}{3}}}{Z_1^{\frac{5}{2}}}+5\sqrt{2}\left(\frac{2}{3}\right)^{\frac{4}{3}}\frac{Z_2}{Z_1^{\frac{2}{3}}Z_3^{\frac{4}{3}}}\right]^{\frac{3}{5}}\frac{P^{\frac{15}{30}}}{\Gamma_i^{\frac{15}{30}}}$$

$$C_L^{\infty}=\left[5\sqrt{2}\left(\frac{2}{3}\right)^{\frac{4}{3}}\frac{Z_2}{Z_1^{\frac{2}{3}}Z_3^{\frac{4}{3}}}+\left(\frac{\sqrt{2}}{3}\right)^{\frac{5}{3}}\frac{Z_2^{\frac{5}{3}}}{Z_1^{\frac{5}{2}}}\right]^{\frac{3}{5}}\frac{P^{\frac{1}{2}}}{\Gamma_i^{\frac{1}{2}}}$$

This is the same as Yoshida-Kiritani! $P^{\frac{1}{2}}$ is the experimentally observed *intensity* dependence.

Appendix E

Mathematical Solutions for Interstitial Sizes

The size of the interstitial sites within the NaCl lattice are tied to the radii of the two constituents. The NaCl lattice is, by definition, an fcc lattice with all of its octahedral interstices filled by the opposing atom. The fcc lattice has eight octahedral sites and eight tetrahedral sites. The NaCl lattice has only the eight tetrahedral sites available. There are 16 distorted tetrahedral sites formed by the sides of the octahedral sites, yet these are smaller than any other and thus less likely to be considered. A vacancy, however, may be considered an octahedral interstice on one of the fcc sublattice. Figure E.1 shows an illustration of the NaCl lattice. Atom connections to illustrate the octahedral and tetrahedral interstices. Note the eight tetrahedral interstices adjacent to the corners.

The octahedral interstices are filled with a true 1:1 ratio of elements. Figure E.2 shows both an open tetrahedral interstice and a filled octahedral interstice. Figure E.2 b) shows the interpenetrating tetrahedron formed by the two elements. Note the {111} plane shown in shaded red.

The size of the interstices is dependant upon the geometry of the system, which is dependant upon the radii of the atoms forming the lattice. It has been considered and explained elsewhere that the zirconium atom is considered the large atom and thus produces the "hard-sphere packing" that leads to the lattice. As such, the zirconium dominates the geometry of the interstices and forms the basis for the size.

The solutions for the interstitial radius for both octahedral and tetrahedral interstices is

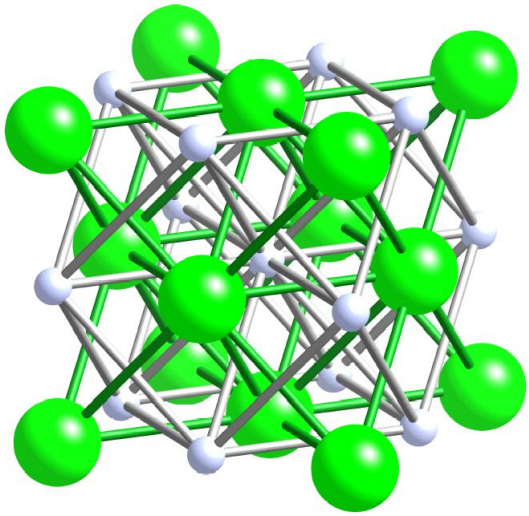

Figure E.1: NaCl Lattice

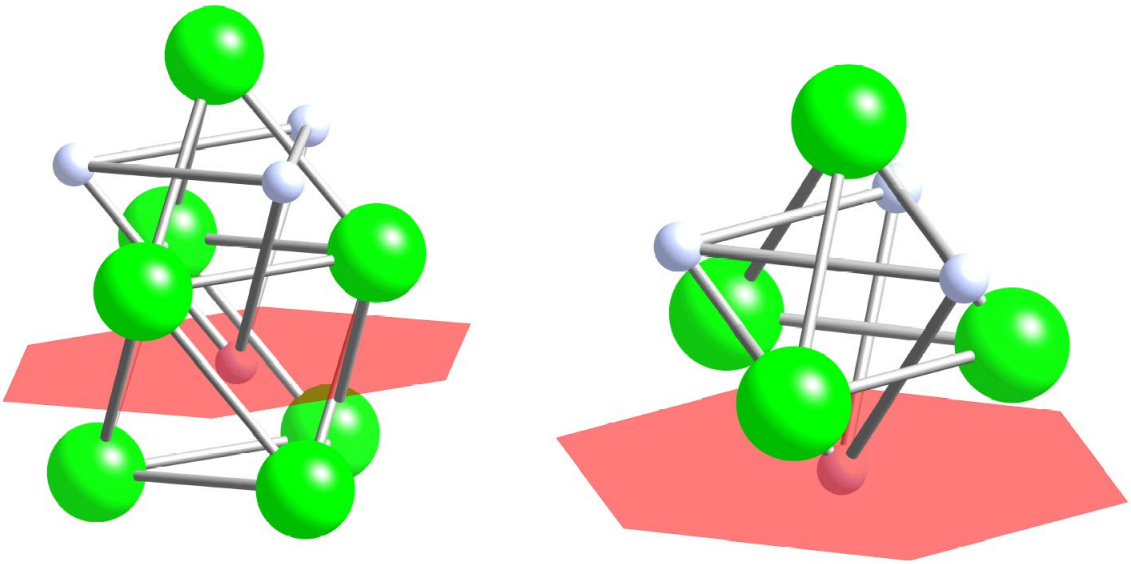

(a) Octahedral interstice filled by light blue sphere. Note this forms the tip of one tetrahedron while the sides of the octrhedron form part of the other. 111 plan shown in shaded red.

(b) Interpenetrating tetrehedra shown with respect to the 111 plane.

Figure E.2: Octahedral and Tetrahedral Interstices

based on the logic that;

- the interstice is the center of the geometry formed by the close-packed and bonded atoms
- that the maximum radius is from the center of the interstice to the closest atom that it may touch

As such, the center is found for the two geometries.

Octahedral

The octahedral site may be imagined as the center of a perfect square that joins four opposing corners (atom centers) of the octahedron. Since the 6 corners that make the octahedron are of the same element, the octahedron is symmetric. Figure E.3 shows an idealized octahedron with square marked of in its center. Each edge length is two radii as the atoms just touching. The square is bisected twice to produce four perfect triangles (each having angles of 45°. 45° and 90°. For ease of calculation, any one of these triangles may be bisected again, producing two smaller triangles with the same angles. In Figure E.3 this is highlighted in red. Each side of this triangle has a length of "*r*", or one radius of an atom. The hypotenuse is then $r\sqrt{2}$. This is the distance from any corner to the center, as shown by the blue highlighted triangle. Thus, the largest interstitial radii is the distance from the center to the radius along the bisected triangle edge, or $r\sqrt{2} - r$ or $r\left(\sqrt{2} - 1\right) = 0.4142r$. Since the Zr atoms are considered the large and thus touching atoms, they produce an interstitial radius of the size Å, which is approximately the calculated size of the nitrogen atomic radius.

Calculating the size of the nitrogen octahedron would produce similar results, with the radius of Zr fitting into the interstice. This exercises shows vacancy size with respect to the

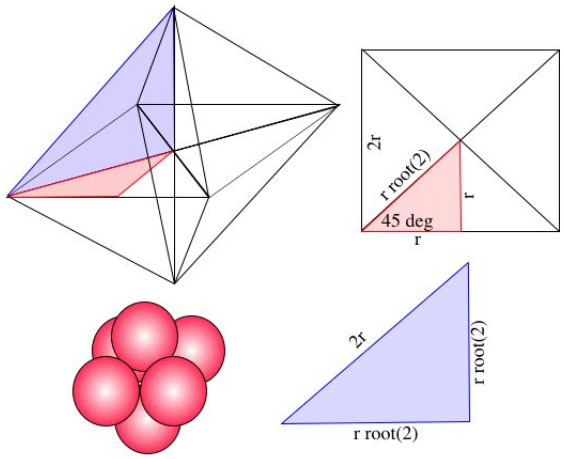

Figure E.3: Octahedron

octahedral radius, minus lattice relaxation effects. It is also a simple basis for the derivation of the tetrahedral interstice radii.

Tetrahedron A tetrahedron is composed of four joined equilateral triangles joined at four opposing corners. The logic is as follows:

- set a base triangle and find its center
- this allows a second triangle to be formed giving the total height of the tetrahedron.
- from opposing side, bisect and find its center

form a triangle from the corner to the opposing center. This forms two sets of similar triangles. By solving systematically, the intersection formed by two base to height lines is found at their intersections. This is the center of the tetrahedron. The maximum interstitial radii is then found by subtracting the center from base height and radius from the total height.

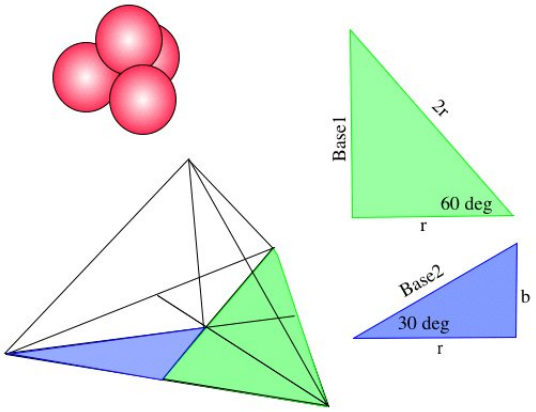

Figure E.4: Tetrahedral Base

Algorithm 12 Solutions for the Tetrahedral Base

$Base1 = \sqrt{(2r)^2 - (r)^2} = \sqrt{4r^2 - r^2} = \sqrt{r^2(4-1)} = r\sqrt{3}$ or $= 2r \cdot Sin(60°) = r\sqrt{3}$
$Base2 = \frac{r}{Cos(30°)}$
$b = Base2 \cdot Sin(30°) = \frac{r}{\sqrt{3}}$

Figure E.4 shows an idealized tetrahedron (corners at atom centers) with its base bisected three times to produce multiple triangles. Each side (and base) is an equilateral triangle with three angles of 60. Bisecting any one of these produces two triangles with angles of 30°, 60°and 90°. This is shown as the green and blue highlighted triangles in Figure E.4.

The edge of the tetrahedron is two radii, just touching, and as such the known lengths are labeled in Figure E.4. Solutions required are "*Base1*", the bisected base length, and "*Base2*", the distance from the corner to the base center, and "*b*", the distance from the center of the base to the center of the edge. Algorithm 15 shows the base equations.

With base center and lengths defined, tetrahedron can be viewed from its side, corner to opposing side as shown in Figure E.5. The figure shows a triangle, highlighted by red,

Algorithm 13 Tetrahedron Height

$$Height = \sqrt{(2r)^2 - Base2^2} = \sqrt{4r^2 - \frac{r^2}{Cos^2(30°)}} = \sqrt{r^2\left(4 - \frac{1}{Cos^2(30°)}\right)} = r\sqrt{\left(4 - \frac{1}{Cos^2(30°)}\right)} = 2r\sqrt{\frac{2}{3}}$$

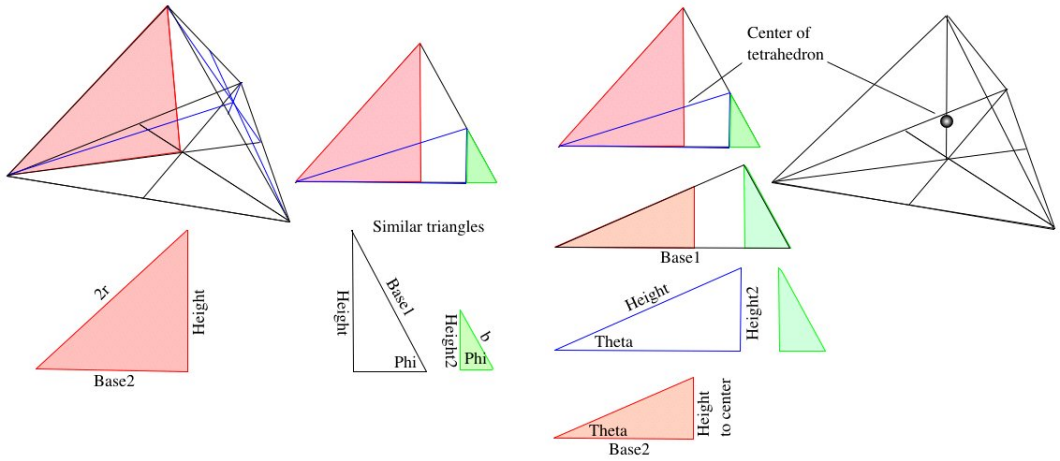

(a) Height and similar triangles used to solve for half of the center problem

(b) Similar triangles used from solutions found previous. Intersection with center (blue and red triangles) is the center of tetrahedron.

Figure E.5: Tetrahedron Height and Center

formed by the edge from corner to top and to the center of the base. Known dimensions are shown to be *2r* as the edge and he bottom as *"Base2"*. The height on the y axis is the distance from the base center to the top. Two other triangles are shown, one in white and one in green. These are both formed by the opposing face that has been bisected (blue lines) with a line drawn from its center to the opposing corner. The two triangles, white and green, are similar triangles in that they share the same angles.

The white triangle has a height of "*Height*", being the same solution as the red triangle. The hypotenuse is Base1, solved above. Thus the solution of the angle "*Phi*" is a Sine relation. The green triangle has hypotenuse "*b*" and angle "*Phi*", and thus Height2 is solved by trigonometry.

Algorithm 14 Solution to White and Green Similar Triangles

$Phi = Sin^{-1}\left(\frac{Height}{Base1}\right) = Sin^{-1}\left(\frac{2r\sqrt{\frac{2}{3}}}{r\sqrt{3}}\right) Height2 = b \cdot Sin\left(Phi\right) = \frac{r}{\sqrt{3}}\frac{2r\sqrt{\frac{2}{3}}}{r\sqrt{3}} = r\frac{2}{3}\sqrt{\frac{2}{3}}$

Algorithm 15 Solutions for the Orange and Blue Similar Triangles

$Theta = Sin^{-1}\left(\frac{Height2}{Height}\right)$

$(Height - to - center) = Base2 \cdot Tan\left(Theta\right) = \frac{r}{Cos(30°)} \cdot Tan\left(Sin^{-1}\left(\frac{r\frac{2}{3}\sqrt{\frac{2}{3}}}{2r\sqrt{\frac{2}{3}}}\right)\right)$

$= \frac{r}{Cos(30°)} \cdot Tan\left(Sin^{-1}\left(\frac{\frac{2}{3}}{2}\right)\right) = \frac{r}{Cos(30°)} \cdot Tan\left(Sin^{-1}\left(\frac{1}{3}\right)\right)$

A check of validity is the ratio of the total height, "Height", to "Height-to-center".

$Ratio = \frac{(Height-to-center)}{Height} = \frac{Base2 \cdot Tan(Theta)}{Height} = \frac{\frac{r}{Cos(30°)} \cdot Tan\left(Sin^{-1}\left(\frac{1}{3}\right)\right)}{2r\sqrt{\frac{2}{3}}}$

Setting $r = 1$, the ratio checks at $\frac{1}{4}$, or the distance from the base to t
he center of a tetrahedron is a quarter of the total height. This checks with literature.

Figure E.5 (b shows the edge view with a third triangle defined by a blue outline. This triangle is the distance form the Opposing face center to the corner, and to the beginning of the green triangle (forming a right triangle). This triangle has a hypotenuse of "*Height*" and height of "*Height2*" and an angle of *"Theta*". Again, Theta can be solved for by trigonometry. The orange triangle shown, which is formed by the intersection of the blue triangle with the large red triangle produces again a similar triangle sharing the angle "*Theta*". It has a base of "Base2", which by tangent relation with "*Theta*", gives opposing side, the "*Height to center*". This is the center of the tetrahedron.

The radius of the interstitial is thus the distance from the top (any corner) to the center minus the radius of the corner atom. Algorithm 16 shows this along with the combined solution based only on the radius of the corner atoms. This is only applicable if all four corners have atoms of the same size, which produces the symmetric tetrahedron solved for. As can be observed in Figure E.6, the interstitial is small relative to the atoms that make up the tetrahedron.

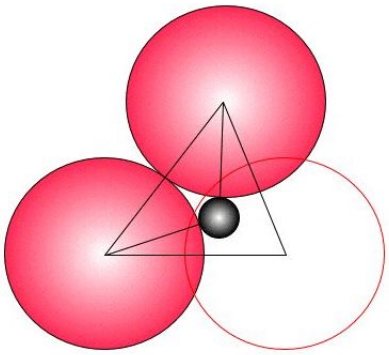

Figure E.6: Tetrahedral Interstitial Radial Size with Respect to Corner Atom Radii

Algorithm 16 Solution for the Tetrahedral Interstitial Radius

$Radius_{interstitial} = Height - (Height - to - center) - r = Height - Base2 \cdot Tan\left(Sin^{-1}\left(\frac{Height2}{Height}\right)\right) - r$

$Radius_{interstitial} = 2r\sqrt{\frac{2}{3}} - \frac{r}{Cos(30°)} \cdot Tan\left(Sin^{-1}\left(\frac{1}{3}\right)\right) - r$

$Radius_{interstitial} = r\left(r\sqrt{\frac{2}{3}} - \frac{1}{Cos(30°)} \cdot Tan\left(Sin^{-1}\left(\frac{1}{3}\right)\right) - 1\right)$

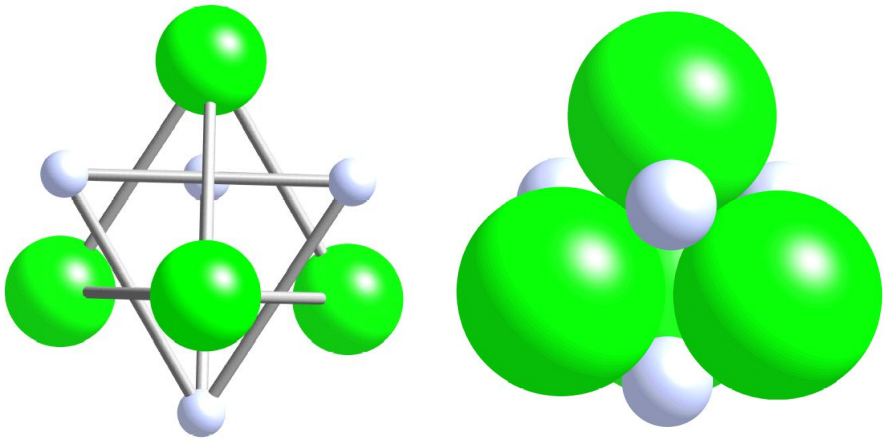

(a) Ball and stick model of the ZrN tetrahedral interstial site. This islocated at the center of both interpenetrating tetrahedra.

(b) Space filled view. Note for persective that the nitrogen atoms have no part in determining the interstitial size.

Figure E.7: Interpenetrating Tetrahedrons of Zr and N (green and grey respectively)

Yet, as can be observed in Figure E.7, the tetrahedron are formed by both nitrogen and zirconium atoms. Nitrogen has a much smaller atom yet has to be spaced apart from other nitrogen atoms to assume the same fcc sublattice that fits within the zirconium sublattice. Figure E.7 shows that it in fact shares the open tetrahedral interstice as the two tetrahedron are interpenetrating. By solving for the distance between the tops of both tetrahedron, it was found that each $\{111\}$ plane of atoms are $\frac{1}{3}$ this distance from each other, and as such, the center of each tetrahedron are equal. Since the radius of the nitrogen is so much smaller than the zirconium, it dominates the size of the tetrahedral interstitial. By assuming that $r = 1.6145$Å, the calculated size of the zirconium atom, the maximum hard-sphere interstitial radius for the tetrahedral site is 0.363Å. Figure E.7 shows the ball-and-stick model and a more realistic filled space based on radii of zirconium and nitrogen calculated.

Bibliography

[1] IBM, "World Power Usage," www.ibm.com (2002).

[2] Peter Beck, *Prospects and Stratagies of Nuclear Power*, Earthscan Publications Inc., London, UK (1994).

[3] EIA, "System for the Analysis of Global Energy Markets (2003)," www.eia..com (2003).

[4] T. Ogawa, A. Ohmichi, T .and Maeda, Y. Arai and Y. Suzuki, *Journal of Alloys and Compounds* **224**(1) 55 (1995).

[5] T. Sato R.G. Haire T. Ogawa, F. Kobayashi, *Journal of Alloys and Compounds* **271** 347 (1998).

[6] M. Burghartz, G. Ledergerber, H. Hein, R.R. Van, der Laan and R.J.M. Konings, *Journal of Nuclear Materials* **288**(2-3) 233 (2001).

[7] M. Streit, F. Ingold, M. Pouchon, L.J. Gauckler and .J.P. Ottaviani, *Journal of Nuclear Materials* **319** 51 (2003).

[8] H. Kleykamp, *Journal of Nuclear Materials* **275**(1) 1 (1999).

[9] Hj. Matzke, *Journal of Nuclear Materials* **30** 107 (4 1969), Copyright (c) 2002 Elsevier Science B.V.

[10] C. D. Bowman, *Annual Review of Nuclear and Particle Sciences* **48** 505 (Dec 1998).

[11] J. Rydberg G. Choppin and J.O. Liljenzin, *Radio and Nuclear Chemistry*, Pergamon Press, 3rd edn. (2002).

[12] John R. Lamarch, *Introduction to Nuclear Reactor Theory*, Addison Wesley, Reading, Ma (1966).

[13] C. T. Walker and G. Nicolaou, *Journal of Nuclear Materials* **218**(2) 129 (1995).

[14] Y. Kurata, T. Takizuka, T. Osugi and H. Takano, *Journal of Nuclear Materials* **301**(1) 1 (2002).

[15] D.E. Beller, G..J Van, Tuyle, D. Bennett, G. Lawrence, K. Thomas, K. Pasamehmetoglu, N. Li, D. Hill, J. Laidler and P. Fink, *Nuclear Instruments and Methods in Physics Research Section A-Accelerators Spectrometers Detectors and Associated Equipment* **463**(3) 468 (2001).

[16] *Accelerator-based gamma neutron transmutation of radionuclides as a new technology for the nuclear fuel cycle*, vol. Particle Accelerator Conference. Proceedings of the. Dallas, TX, USA IEEE (1995).

[17] K. Tsujimoto, T. Sasa, K. Nishihara, T. Takizuka and H. Takano, *Progress in Nuclear Energy* **37**(1-4) 339 (2000).

[18] T. Sasa, T. Nishida, T. Takizuka, O. Sato and N. Yoshizawa, *Progress in Nuclear Energy* **32**(3-4) 485 (1998).

[19] K. Tsukada, I. Nishinaka, N. Shinohara, S. Ichikawa, Y. Nagame, K. Sueki, H. Nakahara, T. Ohtsuki and M. Tanikawa, *The European Physical Journal A* **2**(2) 153 (1998).

[20] Y.S. Kim G.L. Hofman, *AAA Fuels Handbook*, Argon National Laboratory (2001).

[21] J. S. Wan, E. J. Langrock, W. Westmeier, P. Vater, R. Brandt, J. Adam, A. Balabekian, V. P. Bamblevski, M. Yu Barabanov, V. Bradnova, P. Chaloun, V. G. Kalinnikov, V. A. Krasnov, M. I. Krivopustov, B. A. Kulakov, V. P. Perelygin, V. S. Pronskikh, A. A. Solnyshkin, A. N. Sosnin, V. I. Stegailov, V. M. Tsoupko-Sitnikov, G. Modolo, R. Odoj, S. R. Hashemi-Nezhad and M. Zamani-Vallasiadou, *Journal of Radioanalytical and Nuclear Chemistry* **247**(1) 151 (2001).

[22] R.J.M. Konings, R. Conrad, G. Dassel, B. J. Pijlgroms, J. Somers and E. Toscano, *Journal of Nuclear Materials* **282**(2-3) 159 (Dec).

[23] R.J.M. Konings, K. Bakker, J. G. Boshoven, H. Hein, M. E. Huntelaar and R. R. van, der Laan, *Journal of Nuclear Materials* **274**(1-2) 84 (1999).

[24] DOE-HDBK-1019/1-93, *Nuclear Physics and Reactor Theory*, vol. I and II of *Department of Energy Fundamentals Handbook*, Integrated Publishing (1993).

[25] D.R. Olander, *Fundamentals Aspects of Nuclear Fuel Elements*, Technical Information Center, Office of Public Affaris, Energy Reaseach and Development Administration, Oak Ridge, Tn (1976).

[26] Cyriel Wagemans, *The Nuclear Fission Process*, CRC Pess (1991).

[27] Hj. Matzke, *Science of Advanced LMFBR Fuels*, North Holland, Amsterdam (1986).

[28] Y.W. Lee, H.S. Kim, S.H. Kim, C.Y. Joung, S.H. Na, G. Ledergerber, P. Heimgartner, M. Pouchon and M. Burghartz, *Journal of Nuclear Materials* **274**(1-2) 7 (1999).

[29] M. Burghartz, H. Matzke, C. Leger, G. Vambenepe and M. Rome, *Journal of Alloys and Compounds* **271** 544 (1998).

[30] G. Ledergerber, C. Degueldre, P. Heimgartner, M. A. Pouchon and U. Kasemeyer, *Progress in Nuclear Energy* **38**(3-4) 301 (2001).

[31] G. Ledergerber, *Fuel and Energy Abstracts* **43**(4) 257 (2002).

[32] D. R. Olander and P. Van, Uffelen, *Journal of Nuclear Materials* **288**(2-3) 137 (2001).

[33] D. R. Olander and P. Van, Uffelen, *Journal of Nuclear Materials* **300**(2-3) 277 (2002).

[34] Louis E. Toth, *Transition Metal Carbides and Nitrides*, vol. 7 of *Refractory Materials: A series of Monographs*, Academic Press, New York (1971).

[35] H. Blank, "Fabrication of carbide and nitride pellets and the nitride irradiations NILOC I and NILOC II," Tech. rep., DOE (1989).

[36] Z.X. Song, X.H. Ju and K.W. Xu, *Acta Metallurgica Sinica* **38**(7) 723 (2002).

[37] W.S. Williams, *JOM-Journal of the Minerals, Metals and Materials Society* **49**(3) 38 (1997).

[38] D.H. Gregory, A. Bowman, C.F. Baker and D.P. Weston, *Journal of Materials Chemistry* **10**(7) 1635 (2000).

[39] D.H. Gregory, P.M. O'Meara, A..G Gordon, D.J. Siddons, A.J. Blake, M.G. Barker, T.A. Hamor and P.P. Edwards, *Journal of Alloys and Compounds* **317** (2001).

[40] D.H. Gregory, *Coordination Chemistry Reviews* **215** 301 (2001).

[41] D.H. Gregory, *Journal of the Chemical Society-Dalton Transactions* **3** 259 (1999).

[42] J.C. Grossman, A. Mizel, M. Cote, M.L. Cohen and S.G. Louie, *Physical Review B* **60**(9) 6343 (1999).

[43] L. Benco, *Journal of Solid State Chemistry* **111**(2) 440 (1994).

[44] E.K. Storms, A.L. Giorgi and E.G. Szklarz, *Journal of Physics and Chemistry of Solids* **36**(7-8) 689 (1975).

[45] M. Oden, *Journal of Materials Research* **12**(8) 2134 (Aug 1997).

[46] P. Li and J.M. Howe, *Acta Materialia* **50**(17) 4231 (2002).

[47] P. Li and J.M. Howe, *Material Research Society Symposium Proceedings* **779** 141 (2003).

[48] P. Scott N. Kalstsoyannis, *The f elements*, no. 76 in Oxford Chemistry Primers, Oxford Science Publications (1999).

[49] M. Takano, A. Itoh, M. Akabori and T. Ogawa, *Journal of Alloys and Compounds* **327**(1-2) 235 (2001).

[50] M. Takano, A. Itoh, M. Akabori, T. Ogawa, M. Numata and H. Okamoto, *Journal of Nuclear Materials* **294**(1-2) 24 (2001).

[51] V.V. Ogorodnikov and Y.J. Rogovoi, *Inorganic Materials* **29**(4) 591 (1993).

[52] Ogawa T., *Journal of Alloys and Compounds* **203**(1-2) 221 (1994).

[53] A. J. Perry, A. J. Nelson, D. L. Williamson, D. Rafaja, V. Valvoda and B. D. Sartwell, *Journal of Vacuum Science and Technology A* **10**(4) (1992).

[54] A. Straboni, L. Pichon and T. Girardeau, *Surface and Coatings Technology* **125**(1-3) 100 (2000).

[55] H.M. Benia, M. Guemmaz, G. Schmerber, A. Mosser and J.C. Parlebas, *Applied Surface Science* **200**(1-4) 231 (2002).

[56] D. Arias L. Gribaudo and J. Abriata, *Journal of Phase Equilibria* **15**(4) 441 (1994).

[57] R. F. Domagal, D. J. McPherson and M. Hansen, *Transactions of the American Institute of Mining and Metallurgical Engineers* **206**(2) 98 (1956).

[58] L. Brewer, *Science* **161**(3837) 115 (1968).

[59] S.T. Oyama, *Catalysis Today* **15**(2) 179 (Jun 1992).

[60] S.T. Oyama, J.C. Schlatter, J.E. Metcalfe and J.M. Lambert, *Industrial and Engineering Chemistry Research* **27**(9) 1639 (1988).

[61] S.T. Oyama, *Catalysis Today* **15**(2) 179 (1992).

[62] S. Ramanathan and S. T. Oyama, *Journal of Physical Chemistry* **99**(44) 16365 (Nov 1995).

[63] S.T. Oyama, *Journal of Solid State Chemistry* **96**(2) 442 (1992).

[64] Weie Wang and D. R. Olander, *Journal of Alloys and Compounds* **224**(1) 153 (1995).

[65] P. Li and J.M. Howe, *Acta Materialia* **51**(5) 1261 (2003).

[66] M. Sauvage and E. Parthe, *Acta Crystallographica Section A* **A 28** 607 (Nov 1972).

[67] L. I. Johansson, *Surface Science Reports* **21** 5 (1995).

[68] L.I. Johansson and H.I.P. Johansson, *Nitrides and Oxynitrides* **325-3** 335 (2000).

[69] A.L. Ivanovskii, V.M. Zainullina and S.V. Okatov, *Journal of Structural Chemistry* **41**(4) 553 (2000).

[70] A.I. Gusev, *Zhurnal Neorganicheskoi Khimii* **24**(12) 3177 (1979).

[71] A.F. Guillermet, J. Haglund and G. Grimvall, *Physical Review B-Condensed Matter* **48**(16) 11673 (1993).

[72] A.F. Guillermet and K. Frisk, *Journal of Alloys and Compounds* **203**(1-2) 77 (1994).

[73] P.T. Dawson, *Surface and Interface Analysis* **17**(6) 335 (1991).

[74] Jeremy K. Burdett, *Chemical Bonding in Solids*, Oxford University Press, New York (1995).

[75] W.E. Garner, *Chemistry of the solid state*, Academic Press (1955).

[76] P.R. LeClair, *Titanium Nitride Thin Films by the Electron Shower Process*, Master's thesis, Massachusetts Institute of Technology (1998).

[77] E.K. Storms, *A critical review of refractories*, Los Alamos Scientific Laboratory (1964).

[78] D.R. Lide, ed., *Handbook of Chemistry and Physics*, CRC Press, 73rd edn. (1992).

[79] E.K. Storms, *High Temperature Science* **7**(2) 103 (1975).

[80] S.H. Jhi, J. Ihm, S.G. Louie and M.L. Cohen, *Nature* **399**(6732) 132 (1999).

[81] S.H. Jhi, S.G. Louie, M..L Cohen and J. Ihm, *Physical Review Letters* **86**(15) 3348 (2001).

[82] A. J. Perry, B. D. Sartwell, V. Valvoda, D. Rafaja, D. L. Williamson and A. J. Nelson, *Journal of Vacuum Science and Technology A* **10**(4) 1446 (Jul-Aug 1992).

[83] D. Zanghi, A. Traverse, M.D.M. Alves, T. Girardeau and J.P. Dallas, *Nuclear Instruments and Methods in Physics Research Section B-Beam Interactions with Materials and Atoms* **155** 416 (1999).

[84] M.L. Taubin, *Atomnaya Energiya* **69**(3) 176 (1990).

[85] M.L. Taubin, *Soviet Atomic Energy* **69**(3) 765 (1990).

[86] A. J. Perry and D. E. Geist, *Nuclear Instruments and Methods in Physics Research Section B: Beam Interactions with Materials and Atoms* **127-128** 967 (1997).

[87] A.J. Perry, Y.P. Sharkeev, D.E. Geist and S.V. Fortuna, *Journal of Vacuum Science and Technology A Vacuum Surfaces and Films* **17**(4) 1848 (1999).

[88] D. Rafaja, V. Valvoda, A. J. Perry and J. R. Treglio, *Surface and Coatings Technology* **92**(1-2) 135 (1997).

[89] A. J. Perry, J. R. Treglio, V. Valvoda and D. Rafaja, *Journal of Vacuum Science and Technology A* **13**(3) 1067 (May-Jun 1995).

[90] A. J. Perry, *Materials Science and Engineering A* **253**(1-2) 310 (Sept 1998).

[91] A. J. Perry, J. R. Treglio, J. P. Schaffer, J. Brunner, V. Valvoda and D. Rafaja, *Surface and Coatings Technology* **66**(1-3) 377 (Aug 1994).

[92] A. J. Perry and D. E. Geist, *Nuclear Instruments and Methods in Physics Research Section B-Beam Interactions with Materials and Atoms* **127** 967 (May 1997).

[93] A. J. Perry, V. Valvoda and D. Rafaja, *Vacuum* **45**(1) 11 (Jan 1994).

[94] A. J. Perry, R. R. Manory, R. Nowak and D. Rafaja, *Vacuum* **49**(2) 89 (Feb 1998).

[95] I. Pollini, A. Mosser and J.C. Parlebas, *Physics Reports-Review Section of Physics Letters* **355**(1) 1 (2001).

[96] Y. P. Sharkeev, A. J. Perry and S. V. Fortuna, *Surface and Coatings Technology* **109**(1-3) 419 (Oct 1998).

[97] S. J. Zinkle, *Journal of Nuclear Materials* **219** 113 (1995).

[98] T. Yano, H. Miyazaki and T. Iseki, *Journal of Nuclear Materials* **230**(1) 74 (1996).

[99] T. Yano, K. Ichikawa, M. Akiyoshi and Y. Tachi, *Journal of Nuclear Materials* **283** 947 (2000).

[100] S.J. Zinkle and C. Kinoshita, *Journal of Nuclear Materials* **251** 200 (1997).

[101] S. O. Kucheyev, J. S. Williams and S. J. Pearton, *Materials Science and Engineering: R: Reports* **33**(2-3) 51 (2001).

[102] S. O. Kucheyev, J. S. Williams, J. Zou, C. Jagadish and G. Li, *Nuclear Instruments and Methods in Physics Research Section B: Beam Interactions with Materials and Atoms* **175-177** 214 (2001).

[103] S. O. Kucheyev, J. S. Williams, J. Zou, C. Jagadish and G. Li, *Nuclear Instruments and Methods in Physics Research Section B: Beam Interactions with Materials and Atoms* **178**(1-4) 209 (2001).

[104] S. O. Kucheyev, J. S. Williams, J. Zou, G. Li, C. Jagadish and A. I. Titov, *Nuclear Instruments and Methods in Physics Research Section B: Beam Interactions with Materials and Atoms* **190**(1-4) 782 (2002).

[105] C. Liu, A. Wenzel, B. Rauschenbach, E. Alves, A. D. Sequeira, N. Franco, M. F. da, Silva, J. C. Soares and X. J. Fan, *Nuclear Instruments and Methods in Physics Research Section B: Beam Interactions with Materials and Atoms* **178**(1-4) 200 (2001).

[106] M. Uhrmacher M. Restle U. Vetter L. Ziegeler H. Hofsass T. Gehrke K. Jarrendahl R.F. Davis C. Ronning, M. Dalmer, *Journal of Applied Physics* **87**(5) 2149 (2000).

[107] S. B. Qadri, B. Molnar, M. Yousuf and C. A. Carosella, *Nuclear Instruments and Methods in Physics Research Section B-Beam Interactions with Materials and Atoms* **v.190** 878 (2002).

[108] S.J. Zinkle, *Nuclear Instruments and Methods in Physics Research Section B-Beam Interactions with Materials and Atoms* **91**(1-4) 234 (1994).

[109] S.J. Zinkle and L.L. Snead, *Nuclear Instruments and Methods in Physics Research Section B-Beam Interactions with Materials and Atoms* **116**(1-4) 92 (1996).

[110] S.J. Zinkle, V.A. Skuratov and D.T. Hoelzer, *Nuclear Instruments and Methods in Physics Research Section B-Beam Interactions with Materials and Atoms* **191** 758 (2002).

[111] W.J. Weber, R.C. Ewing, C.R.A. Catlow, T.D. delaRubia, L.W. Hobbs, C. Kinoshita, H. Matzke, A.T. Motta, M. Nastasi, E.K.H. Salje, E.R. Vance and S.J. Zinkle, *Journal of Materials Research* **13**(6) 1434 (1998).

[112] H. Kleykamp, *Journal of Nuclear Materials* **300** 273 (2002).

[113] Y. Ito, K. Yasuda, R. Ishigami, M. Sasase, S. Hatori, K. Ohashi, S. Tanaka and A. Yamamoto, *Nuclear Instruments and Methods in Physics Research Section B: Beam Interactions with Materials and Atoms* **191**(1-4) 530 (2002).

[114] J. D. Hunn, R. E. Stoller and S. J. Zinkle, *Journal of Nuclear Materials* **219** 169 (1995).

[115] K.M. Beardmore and N. Gronbech-Jensen, *Physical Review E* **57**(6) 7278 (1998).

[116] K.M. Beardmore and N. Gronbech-Jensen, *Nuclear Instruments and Methods in Physics Research Section B-Beam Interactions with Materials and Atoms* **153**(1-4) 391 (1999).

[117] K.M. Beardmore, ed., *Direct simulation of ion beam induced stressing and amorphization of silicon* (1999).

[118] J.W. Mayer M. Nastasi and J.K. Hirvonen, *Ion Solid Interactions: Fundamentals and Applications*, Cambridge University Press, London, UK (1996).

[119] T. Wiss C. Ronchi, *Journal of Applied Physics* **92**(10) 5837 (2002).

[120] U.L. Littmarck J.F. Ziegler, J.P. Bierzack, *The Stopping Power of and Range of Ions in Solids*, Peragamon Press, New York (1985).

[121] W.H. Hocking, R.A. Verrall and I.J. Muir, *Journal of Nuclear Materials* **294**(1-2) 45 (2001).

[122] J. Maier, *Angewadte Chemie-International Edition in English* **32**(3) 313 (1993).

[123] J. Maier, *Angewadte Chemie-International Edition in English* **32**(4) 528 (1993).

[124] M.A. Pouchon, M. Dobeli, C. Degueldre and M. Burghartz, *Journal of Nuclear Materials* **274**(1-2) 61 (1999).

[125] M.A. Pouchon, M. Dobeli, C. Degueldre and M. Burghartz, *Journal of Nuclear Materials* **274**(1-2) 61 (August 1999).

[126] P. Losonen, *Nuclear Engineering and Design* **201**(2-3) 139 (2000).

[127] P. Losonen, *Nuclear Engineering and Design* **203**(2-3) 273 (2001).

[128] P. Losonen, *Journal of Nuclear Materials* **280**(1) 56 (2000).

[129] P. Losonen, *Nuclear Engineering and Design* **196**(2) 161 (2000).

[130] P. Losonen, *Journal of Nuclear Materials* **304**(1) 29 (2002).

[131] J.P. Hiernaut and C. Ronchi, *Journal of Nuclear Materials* **294**(1-2) 39 (2001).

[132] P. Hermansson and A.R. Massih, *Journal of Nuclear Materials* **304**(2-3) 204 (2002).

[133] P. Shewman, *Diffusion in Solids*, The Minerals, Metals and Materials Society, 2nd edn. (1989).

[134] M.E. Glicksman, *Diffusion in Solids: Field Theory, Solid-State Principals, and Applications*, John Wiley and Sons (2000).

[135] R.E. Voskoboinikov and A.E. Volkov, *Journal of Nuclear Materials* **297**(3) 262 (2001).

[136] R.E. Voskoboinikov and A.E. Volkov, *Journal of Nuclear Materials* **282**(1) 66 (2000).

[137] A.I. Volkov, A.E .and Ryazanov, *Journal of Nuclear Materials* **273**(2) 155 (1999).

[138] A. Sarce, *Journal of Nuclear Materials* **288**(2-3) 130 (2001).

[139] E. K. Storms, *Journal of Nuclear Materials* **158** 158 (1988).

[140] N. M. Ghoniem, *Journal of Nuclear Materials* **174** 168 (Nov 1990).

[141] N. M. Ghoneim, S. Sharafat, J. M. Williams and L. K. Mansur, *Journal of Nuclear Materials* **117** 96 (1983).

[142] P. M. G. Damen, A. van Veen, H. Matzke, H. Schut, J. A. Valdez, C. J. Wetteland and K. E. Sickafus, *Journal of Nuclear Materials* **306**(2-3) 180 (Dec).

[143] Hj. Matzke and J.L. Whitton, *Canadian Journal of Physics* **44** 995 (May 1966).

[144] J. G. Desmaison and W. W. Smetzer, *Journal of the Electrochemical Society* **122**(3) 354 (Mar 1975).

[145] J. G. Desmaison, *Journal of the Electrochemical Society* **124**(1) 152 (Jan 1977).

[146] J.R. Morris and K.M. Ho, *Physical Review B* **63**(22) 224116 (2001).

[147] Bruker Inc., "www.bruker-axs.co.uk/products.asp," internet (2004).

[148] B. Carter D.B. Williams, *Transmission Electron Microscopy*, Plenum Press, New York (1996).

[149] J.W. Edington, *Interpretation of Transmission Electron Micrographs*, no. 3 in Monographs in Practical Electron Microspcopy in Material Science, MacMillan Press (1975).

[150] J.M. Howe S. S. Sharma, K.T. Moore, *Philosophical Magazine* **83**(1) 31 (2003).

[151] S.J. Skrzypek, A. Baczmanski, W. Ratuszek and E. Kusior, *Journal of Applied Crystallography* **34** 427 (2001).

[152] S.R. Stock B.D. Cullity, *Elements of X-Ray Diffraction*, Prentice Hall, 3rd edn. (2001).

[153] M. Meyer R.C. Birtcher T.R. Allen J. Gan, R.S. Fielding, "Heavy Ion and Neutron Irradiation for Candidate Materials in Gen-IV Reactor System," Afci gen-iv working group, DOE (Oct 2003).

[154] J. Gan R.S. Fileding, "GFR Fuel (Dispersion) Fuel Status," Doe report, DOE (2004).

[155] B.L. Eyre, *The Journalof Physics F: Metal Physics* **3** 422 (1973).

[156] J.W. Edington, *Practical Electron Microscopy in Materials Science*, TechBooks (1976).

[157] K. E. Sickafus, J. M. Wills and N. W. Grimes, *Journal of the American Ceramics Society* **82**(12) 3279 (Dec).

[158] K. E. Sickafus, N. Yu and M. Nastasi, *Journal of Nuclear Materials* **304** 237 (8 2002).

[159] K. E. Sickafus, C. J. Wetteland, N. P. Baker, N. Yu, R. Devanathan, M. Nastasi and N. Bordes, *Materials Science and Engineering A* **253**(1-2) 78 (Sep 1998).

[160] K. E. Sickafus, A. C. Larson, N. Yu, M. Nastasi, G. W. Hollenberg, F. A. Garner and R. C. Bradt, *Journal of Nuclear Materials* **219** 128 (Mar).

[161] K.J. McClellan K. Wheeler I. Han, P. Peralta, *JOM* **56**(11) 255 (Nov 2004).

[162] T. Donomae T. Yano M. Akiyoshi, K. Ichikawa, *Journal of Nuclear Materials* **307-311** 1305 (2002).

[163] E. Atar, H. Cimenoglu and E.S. Kayali, *Surface and Coatings Technology* **162**(2-3) 167 (2003).

[164] H. Hasegawa, A. Kimura and T. Suzuki, *Journal of Vacuum Science and Technology A-Vacuum Surfaces and Films* **18**(3) 1038 (2000).

[165] C. Hazelton, J. Rice, L.L. Snead and S.J. Zinkle, *Journal of Nuclear Materials* **253** 190 (1998).

[166] T. Iseki, M. Tezuka, C. S. Kim, T. Suzuki, H. Suematzu and T. Yano, *Journals of Nuclear Science and Technology* **30**(1) 68 (JAN 1993).

[167] J. Musil and H. Polakova, *Surface and Coatings Technology* **127**(1) 99 (2000).

[168] Th. Hartmann K. Yasuda J.A. Valdez P. Chodak M. Nastasi R.A. Verrall K.E. Sickafus, Hj. Matske, *Journal of Nuclear Materials* **274**(1-2) 66 (1999).

[169] K. Fukumoto K. Nakai K. Shinhara C. Kinoshita, H. Abe, *Ultramicroscopy* **39** 205 (1991).

[170] S.H. Jhi, S.G. Louie, M.L. Cohen and J.W. Morris, *Physical Review Letters* **87**(7) 075503 (2001).

[171] S.H. Jhi and J. Ihm, *Physical Review B-Condensed Matter* **56**(21) 13826 (1997).

[172] E.T. Lileodden P. Anderson J.T. Wyrobek W. W. Gerberich, J. Nelson, *Acta Materialia* **55**(9) 3585 (1995).

[173] K.B. Yoder D.E. Kramer and W.W. Gerberich, *Philisophical Magazine* **81**(8) 20333 (2001).

[174] "www.shef/ac/uk/chemistry/orbitron," internet (2003).

[175] "www.chm.davidson.edu/ChemistryApplets/AtomicOrbitals/," internet (2003).

[176] V.L. Indenbom B.K. Vainshtein, V.M. Fridkin, *Structure of Crystals (3rd Edition)*, Springer Verlag, Berlin, (3rd edition) edn. (1995).

[177] G.S. Zhdanov, *Crystal Physics*, Academic Press, New York (1965).

[178] L. Minervini, *Atomistic Simulations of Defective Oxides*, Ph.d, Imperial College, Technology and Medicine, Imperial College, London, UK (July 2000).

[179] J.M. Howe P. Li, *Foundations of Crystallography* **A59** 584 (2003).

[180] I.V. Afanasyev-Charkin, R.M. Dickerson, D.W. Cooke, B.L. Bennett, V.T. Gritsyna and K.E. Sickafus, *Journal of Nuclear Materials* **289**(1-2) 110 (Feb).

[181] J.B. Sanders K.B. Winterbon, P. Sigmund, *Kgl. Dan. Vidensk. Selsk.* **37**(14) (1970).

[182] K.B. Winterbon, P. Sigmund and J.B. Sanders, *Kgl. Dan. Vidensk. Selsk.* **37: 14**((1970)) (Mat.-Fys. Medd.).

[183] G. H. Kinchin and R. S. Pease, *Reports on Progress in Physics* **18** 1 (1955).

[184] H.E. Schioett J. Lindhard, M. Scharff, *Kgl. Danske Videnskab. Selskab. Mat. Fys. Medd.* **33**(14) 1 (1963).

[185] M. Lindhard, J.; Scharff, *Physical Review* **124** 128 (Oct 1961).

[186] M. Scharff P.V. Thomsen J. Lindhard, V. Nielsen, *Kgl. Danske Videnskab., Selskab. Mat. Fys. Medd.* **33**(10) 1 (1963).

[187] I. M. Torrens M. H. Norgett, M. T. Robinson, *Nuc. Eng. Design* **33**(33) 91 (1975).

[188] I.M. Torrens M.J. Norgett, M.T. Robinson, *Nuclear Engineering and Design* **33**(1) 50 (1975).

[189] C. Kinoshita, K. Hayashi and S. Kitajima, *Nuclear Instruments and Methods in Physics Research, Section B (Beam Interactions with Materials and Atoms)* **229**(2/3) 209 (1984).

[190] N. Yoshida and M. Kiritani, *Journal of the Physical Society of Japan* **35**(5) 1418 (1973).

[191] R. O. Simmons and R. W. Balluffi, *Physical Review* **117**(1) 52 (1960).


Los Alamos
NATIONAL LABORATORY
EST.1943